UNIVERSITE DE BLIDA 1
Faculté de Technologie
Département d'Electronique

THESE DE DOCTORAT
en Electronique

Power Management in Islanded and Grid-Connected Microgrids

Par

Ahmed BENDIB

Devant le jury composé de :

Rafik BRADAI	**MC A, Université de Blida 1**	**Président**
Kamel KARA	**Professeur, Université de Blida 1**	**Rapporteur**
Aissa CHOUDER	**Professeur, Université de M'Sila**	**Co-Rapporteur**
Aissa KHELDOUNE	**Professeur, Université de Boumerdès**	**Examinateur**
Badia AMROUCHE	**MC A Université de Blida 1**	**Examinatrice**
Linda HASSAINE	**DR, CDER, Bouzareah-Alger**	**Examinatrice**

Blida, le 09 juin 2021

ملخص:

تعرف الشبكة المصغرة (MG) عموما على أنها شبكة توزيع ذات جهد منخفض أو متوسط تشتمل على مصادر توليد متنوعة متوزعة، عناصر تخزين الطاقة وكذا أحمال يمكن التحكم فيها. و هذه الشبكات يمكنها ان تكون متصلة او منفصلة (مستقلة) عن الشبكة الرئيسية. هيكل التحكم، والذي يتكون من طبقات التحكم الأولي، الثانوي والثالثي، تم اقتراحه من أجل هذه الشبكات المصغرة. تعد طبقات التحكم الثانوية والثالثية ضرورية من أجل استعادة المعلمات الرئيسية للشبكة الصغيرة (التردد والسعة) الى قيمها المطلوبة، التزامن مع الشبكة، وكذا إدارة تدفق الطاقة بين الشبكة المصغرة والشبكة الرئيسية. طبقات التحكم هذه عاموما تحتوي على وحدة PLL أو FLL من اجل استخراج المعاملات المفتاحية لجهد الشبكة المصغرة، وهذه الوحدات جد حساسة لاضطرابات كل من الحمل والشبكة، وخاصة العنصر المستمر (DC-offset) والذي قد يتواجد في جهد دخلها. هذه المشكلة، والتي يمكن أن تتسبب في ظهور تذبذبات ذات تردد أساسي في مخراجات PLLs (او FLLs)، قد تؤثر على أداء طبقات التحكم، وبالتالي، استقرار الشبكة المصغرة المستقلة أو المرتبطة بالشبكة الرئيسية. على الرغم من أنه تم اقتراح حلول للتعامل مع هذه المشكلة في بعض الأعمال، خاصةً في حالة الأنظمة أحادية الطور، الا انه لم يتم التطرق لدمج هذه الوحدات في طبقات التحكم المذكورة. لذلك، فإن تصميم مخططات المتحكمين المعنيين بادراج هذه الوحدات، والتي قد تساهم في تحسين أداء النظام أمر لابد منه. علاوة على ذلك، يعد ضمان استقرار مثل هذه الشبكات المصغرة التي تتضمن طبقات التحكم المذكورة، أمرًا مهمًا، وهو الأمر الذي يتطلب نماذج رياضية دقيقة من أجل التحليل الفعال لاستقرار النظام وكذا تصميم متحكم مناسب.

تركز هذه الأطروحة على تصميم تقنيات تحكم ثانوية وثلاثية، اعتمادا على طريقة SOGI-FLL المُحسَّنة والتي يمكنها ازالة العنصر DCوكذا تأثيراته، تطوير طرق نمذجة دقيقة، وكذا تقديم طريقة ممنهجة من أجل ضبط معاملات التحكم المقترحة. تقنيات التحكم المصممة تم اقتراحها من أجل الشبكات المصغرة المستقلة وكذا المتصلة بالشبكة. الهدف الرئيسي من التقنيات المقترحة تحقيق إدارة فعالة ومثالية لتدفق الطاقة بين وحدات الطاقة الموزعة في الشبكة المصغرة المستقلة أو بين الشبكة المصغرة والشبكة الرئيسية أثناء الوضع المتصل بالشبكة. التحليل الخاص باستقرار النظام للشبكة المصغرة الذي يتضمن مخططات التحكم المصممة تم تقديمه. كذلك، تم التحقيق من متانة وحدات المتحكمين الثانوي والثالثي المصممة، لتغيرات معلمات النظام. اختبارات عن طريق المحاكاة وتجريب تم انتهاجها من أجل التحقق من فعالية استراتيجيات التحكم المقترحة لشبكة مصغرة مستقلة أحادية الطور وكذا متصلة بالشبكة. توضح النتائج المتحصل عليها فعالية هذه الاستراتيجيات في تحقيق استعادة نموذجية لتردد وسعة الجهد، تزامن سلس، وتدفق مثالي للطاقة في ظل ظروف التشغيل المختلفة.

الكلمات المفتاحية: الشبكات المصغرة أحادية الطور، العاكس ذو متحكم الانخفاض، المتحكم الثانوي، طريقة SOGI-FLL، المتحكم الثالثي، النمذجة، تدفق الطاقة المثالي، عملية الضبط، التطبيق التجريبي.

Abstract:

A microgrid (MG) is generally defined as a low or medium voltage distribution network comprising various distributed generation sources, energy storage elements, and controllable loads. A given microgrid can be connected or disconnected to/from the main grid. A hierarchical control architecture consisting of primary, secondary, and tertiary control is often adopted for these microgrids. The secondary control and tertiary control levels are essential for the microgrid key parameters (frequency and amplitude) restoration to their nominal values, for synchronization with the grid, and management of the power flow between the MG and the main grid. However, these control layers often use the phase-locked loop (PLL) or the frequency locked loop (FLL), which are highly sensitive to the load and the grid disturbances, especially to the presence of the DC component in their voltage input. Due to these disturbances, oscillations can occur in the fundamental frequency of the PLLs (FLLs) output. Of course, these oscillations affect the performance of the control layers and therefore the stability of the inverters-based MG and the grid-tied inverters. Despite, some solutions to deal with this issue have been proposed in the literature, especially for the case of single-phase systems, the integration of such techniques into the control layers has not been considered. In this regard, the design of the control schemes based on such techniques, which may lead to the enhancement of the system performance, is imperative. Ensuring the stability of the microgrid systems incorporating the considered control layers is an important task, that requires appropriate mathematical models for effective stability analysis and proper control design.

The present thesis focuses on designing secondary and tertiary control schemes using an Enhanced SOGI-FLL (ESOGI-FLL) that is suitable for the DC offset rejection, developing accurate modeling approaches, and providing systematic guidelines to tune the parameters of the proposed controllers. The case of single-phase droop-operated microgrid during islanded and grid-tied operation modes is considered. The main objective of the developed approaches is to ensure effective and optimal control of the power flow among the distributed generation units inside an islanded MG on one hand, and between the microgrid and the main grid during the grid-connected mode on the other hand. The stability analysis of the microgrid system incorporating the designed control schemes is provided. Furthermore, the robustness of the secondary and the tertiary controllers against the system parameter variations is

investigated. Simulations and experimental tests are conducted to verify the performance of the proposed secondary and tertiary control strategies for single-phase autonomous and grid-tied MGs. The obtained results demonstrate the effectiveness of the developed control approaches in achieving effective frequency and amplitude restoration, seamless synchronization, and optimal power flow control under various operating conditions.

Keywords: Single-phase Microgrid, Droop-controlled VSI, Secondary control, SOGI-FLL method, Tertiary control, Modeling, Optimal power flow, Tuning procedure, Experimental implementation

Résumé:

Un micro-réseau est généralement défini comme un réseau de distribution de basse ou de moyenne tension comprenant diverses sources de production d'énergie distribuées, des éléments de stockage d'énergie et des charges contrôlables. Un micro-réseau peut être connecté ou déconnecté au réseau principal. Une commande hiérarchique constituée de trois niveaux de commande, primaire, secondaire et tertiaire est généralement adoptée pour commander un micro-réseau. Les niveaux de commande secondaire et tertiaire sont essentiels pour la restauration des paramètres clés (fréquence et amplitude) d'un micro-réseau à leurs valeurs nominales, la synchronisation avec le réseau, la gestion de flux de puissance entre le micro-réseau et le réseau principal. Cependant, ces niveaux de commande sont souvent basés sur l'utilisation de la boucle à verrouillage de phase (PLL) ou la boucle à verrouillage de fréquence (FLL). Ces dernières, sont très sensibles aux perturbations de la charge et du réseau, et notamment à la présence de la composante continue DC dans leur tension d'entrée. En présence de ces perturbations, des oscillations dans la fréquence fondamentale de la sortie des PLLs (FLLs) peuvent apparaitre. Ces oscillations peuvent affecter les performances des niveaux de commande et, par conséquent, la stabilité du micro-réseau fonctionnant en mode isolé ou en mode connecté au réseau principal. Bien que certaines solutions pour résoudre ce problème ont été proposées dans la littérature, en particulier pour le cas des systèmes monophasés, l'intégration de telles techniques dans ces niveaux de commande n'a pas été encore envisagée. Par conséquent, la conception de nouvelles stratégies de commande pouvant conduire à l'amélioration des performances du système, est impérative. De plus, assurer la stabilité de ces micro-réseaux incorporant les niveaux de commande considérés est une tâche importante, et nécessite des modèles mathématiques appropriés pour une analyse efficace de stabilité et une conception appropriée des différents niveaux de commande.

La présente thèse s'intéresse à la conception des stratégies de commande de niveaux secondaire et tertiaire, basées sur la méthode SOGI-FLL améliorée (ESOGI-FLL), au développement d'une modélisation précise, et à la présentation d'un guide pour un réglage systématique des paramètres des commandes proposées. Les micro-réseaux monophasés commandés par la méthode de commande de statisme et fonctionnant en mode isolé et en mode connecté au réseau sont considérés dans ce travail. L'objectif principal des approches développées, est d'assurer un contrôle efficace et optimal du flux de puissance entre les sources distribuées incluses dans un micro-réseau autonome d'une part et entre le micro-réseau et le réseau principal en mode connecté d'autre part. L'analyse de stabilité d'un micro-réseau intégrant les niveaux de commande conçus est effectuée. En outre, la robustesse des commandes secondaire et tertiaire vis-à-vis les variations des paramètres du système est envisagée. Des simulations et des essais expérimentaux sont réalisés pour vérifier les performances des stratégies de commande secondaire et tertiaire proposées pour un micro-réseau monophasée autonome et connecté au réseau. Les résultats obtenus démontrent l'efficacité de ces approches de commande dans la restauration de la fréquence et de l'amplitude, la synchronisation sans faille, et la gestion optimale du flux de puissance sous différentes conditions de fonctionnement.

Motclés: Micro-réseau monophasé, Onduleur commandés par la méthode de statisme, Controle secondaire, La méthode SOGI-FLL, Controle tertiaire, Modélisation, Gestion optimale du flux énergitique, Procédure de réglage, Implemnataion expérimentale.

Dedication

To my Mother;

To my Father;

To my brother and sisters;

To my advisor; Kamel KARA; and co-advisor; Aissa CHOUDER; for their supports;

To my professor, Dr. Said BARKAT;

To all my best friends.

Publications

Journal's Paper

- A. Bendib, A. Kherbachi, K. Kara, A. Chouder, S. Barkat, **"New modeling approach of secondary control layer for autonomous single-phase microgrids,"** *Journal of the Franklin Institute*, vol. 356, no. 13, pp. 6842-6874, September 2019.
- A. Kherbachi, A. Chouder, A. Bendib, K. Kara, S. Barkat, **"Enhanced structure of second-order generalized integrator frequency-locked loop suitable for DC-offset rejection in single-phase systems,"** *Electric Power Systems Research*, vol. 170, pp. 348-357, May 2019.

Conferences' Papers

- A. Bendib, A. Kherbachi, K. Kara and A. Chouder, **"Droop controller-based primary control scheme for parallel-connected single-phase inverters in islanded AC microgrid,"** *2017 5th International Conference on Electrical Engineering - Boumerdes (ICEE-B)*, Boumerdes, 2017, pp. 1-6.
- A. Bendib, A. Chouder, K. Kara, A. Kherbachi and S. Barkat, **"SOGI-FLL Based Optimal Current Control Scheme for Single-Phase Grid-Connected Photovoltaic VSIs with LCL Filter,"** *2018 International Conference on Electrical Sciences and Technologies in Maghreb (CISTEM)*, Algiers, 2018, pp. 1-6.
- A. Kherbachi, A. Bendib, K. Kara and A. Chouder, **"ARM-based implementation of SOGI-FLL method for power calculation in single-phase power system,"** *2017 5th International Conference on Electrical Engineering - Boumerdes (ICEE-B)*, Boumerdes, 2017, pp. 1-6.
- A. Kherbachi, A. Chouder, A. Bendib, K. Kara, S. Barkat, **"Experimental Implementation of Droop Control Strategy for Single-Phase Parallel-Connected VSIs Forming Islanded AC Microgrid,"** *2018 International Conference on Electrical Sciences and Technologies in Maghreb (CISTEM)*, Algiers, 2018, pp. 1-6.

Table of Contents

Page

Abstract…… **I**

Dedication…… **III**

Publications…… **IV**

Table of Contents……. **V**

List of Figures…… **VIII**

List of Tables…… **XII**

List of Abbreviation and Symbols…… **XIII**

Chapter 1: Introduction to Microgrid Technology and Control.....**1**

1.1. Introduction 2

1.2. Background and Motivation. 3

1.2.1. Microgrids Definition and Research Interest. 3

1.2.2. Microgrids Classification 4

a. AC Microgrid…… 4

b. DC Microgrid…… 4

c. Hybrid AC/DC Microgrid…… 4

1.2.3. Microgrids Advantages……...6

1.2.4. Microgrids Architecture……6

1.2.5. Motivation 7

1.3. AC Microgrids Hierarchical Control..... 8

1.3.1. Primary Control for AC-MGs 9

1.3.2. Secondary control 17

1.3.3. Tertiary control. 19

1.4. Problem Statement 21

1.5. Literature review of the Secondary and tertiary control strategies in AC MGs..... 21

1.5.1. Secondary control layer 22

1.5.2. Tertiary control layer 24

1.6. Thesis Contributions and Outcomes. 26

1.7. Thesis Organization 27

1.8. Conclusion.....29

Chapter 2: Design and Modeling of Secondary Control Layer for Autonomous Single-Phase Microgrids……...……..……..……30
2.1. Introduction 31
2.2. Control of Single-Phase Islanded AC Microgrids….. 34
2.2.1. Primary Control..... 34
2.2.2. Secondary Control..... 35
2.3. Proposed Modeling Approach of the Secondary Control …..... 36
2.3.1. Modeling Analysis of the ESOGI-FLL… 37
2.3.2. Modeling of the Frequency and Amplitude Restoration Loops 42
2.3.2.1. Voltage Control Loop…..... 42
2.3.2.2. Frequency Control Loop..... 44
2.3.3. Tuning Control Parameters 46
2.3.4. Synchronization Control Loop. 48
2.4. Conclusion…… 50

Chapter 3: Design, Modeling, and Tuning of Tertiary Control for Single-Phase Grid-Tied VSIs-Based MGs…….……..….51
3.1. Introduction..... 52
3.2. The proposed tertiary control scheme for single-phase MG..... 54
3.3. Proposed Modeling approach of the power flow control..... 57
3.3.1. Dynamic phasor modeling based on SOGI-FLL dynamics of the MG power flow…. 58
3.3.1.1. The Expression of the line impedance current. 59
3.3.1.2. The expression of the active and reactive power flows. 61
3.3.1.3. Power flow small-signal model 62
3.3.1.4. Small-signal model of the SOGI-FLL-based power calculation……..…… 64
3.3.2. Accuracy assessment of the obtained models. 66
3.3.2.1. Simulation test. 66
3.3.2.2. Processor-in-the-loop (PIL) test. 68
3.3.3. The open-loop small-signal model of the microgrid power flow. 69
3.3.4. Open-loop model validation…….. 70
3.3.5. The closed-loop small-signal model of microgrid power flow incorporating tertiary control…… 72
3.4. Stability analysis and tertiary control parameter tuning. 75
3.4.1. System stability evaluation to tertiary control parameter variation..... 79
3.4.2. Robustness assessment of the designed controller 81
3.5. Conclusion……..…….. 83

Chapter 4: Numerical Simulation and Experimental Results……...…..…… 84
4.1. Introduction……. 85
4.2. Secondary control……..... 85

4.2.1. Numerical simulation ……..... 85
4.2.2. Experimental results ……..... 89
4.3. Numerical implementation of the tertiary control …..…..... 94
4.4. Conclusion..... 108

Conclusions and Future Works ……..….. 109

Appendices……..……..…. 112

A. Gains of the power flow open-loop model at steady-state …….……...…… 112

B. Model of the secondary control for STM32F4 target in MATLAB/Simulink…….113

Bibliography……..…… 116

List of Figures

Figure **Page**

1.1. Examples of Microgrid projects in several communities …… 4
1.2. Structure of (a) AC microgrid, (b) DC microgrid, and (c) Hybrid AC/DC microgrid……. 5
1.3. Typical structure of an AC Microgrid……..… 7
1.4. Multilevel hierarchical control for AC MGs…… 9
1.5. Schematic diagram of AC MG hierarchical control……. 9
1.6. Configuration of the primary control for droop-controlled VSC based-Microgrid…...… 11
1.7. Block diagram of the power calculation strategy……...……..... 12
1.8. Schematic diagram of the droop control loop…….…...…… 14
1.9. Voltage frequency and amplitude characteristics of the droop control method...…….. 14
1.10. Virtual output impedance; (a) -based droop method (b) implementation by using the SOGI approach.……..……..……...……... 16
1.11. (a) The block diagram of inner control loops, and (b) the equivalent circuit inverter…. 17
1.12. Two main secondary control architectures: (a) Centralized SC, and (b) Distributed SC. 18
1.13. Block diagram of the tertiary control level for a microgrid…….…… 20
2.1. Hierarchical control of two single-phase inverters-based islanded AC microgrid, considering primary control and secondary control based on ESOGI-FLL for parameters estimation. The MG consists of two parallel DG units, in which each DG has its own local controller, connected to a local load and the utility grid at a common AC bus……...… 34
2.2. The hierarchical control scheme for two single-phase inverters-based islanded AC microgrid……. 37
2.3. Model of the restoration control loop based on SOGI-FLL dynamics……. 38
2.4. The Enhanced SOGI-FLL (ESOGI-FLL) scheme ..……. 39
2.5. Phasor representation of the input MG and the direct component MG voltages……... 40
2.6. Transient responses of: (a) the SOGI-FLL and its simplified model (Eq. (8)) for $\Gamma = 40\ s^{-1}$ and $\Gamma = 60\ s^{-1}$, and (b) The SOGI-FLL, and its actual model and simple model (Eq. (15)) for $k = 0.7$ and k = sqrt (2).…….....….……... 42
2.7. Block diagram of the voltage secondary control model…….…….. 43
2.8. Root-Locus plots for: (a) $0.0001 \leq k_{i\text{-}E} \leq 100$ and $k_{p\text{-}E} = 0.01$, and (b) $-1 \leq k_{p\text{-}E} \leq 100$ and $k_{i\text{-}E} = 1.5$…..…….…… 44
2.9. Block diagram of the frequency secondary control model…….……. 45
2.10. Root-Locus plots for: (a) $0.0001 \leq k_{i\text{-}f} \leq 100$ and $k_{p\text{-}f} = 0.01$, and (b) $-0.5 \leq k_{p\text{-}f} \leq 100$ and $k_{i\text{-}f} = 2.6$……..……..…….. 46
2.11. Transient responses of the secondary control models for (a) frequency and (b) amplitude restoration, with three different values of the time delay (τ).……...……. 48
2.12. Block diagram of the synchronization feedback control…….…….. 50
3.1. The tertiary control scheme based on SOGI-FLL for a single-phase microgrid operating in grid-tied mode……... 56

3.2. Simplified block diagram of the power flow control between the grid and the DGs based-MG……. 56
3.3. $f_{MG} - P_g$ and $E_{MG} - Q_g$ tertiary control characteristics……..… 57
3.4. Proposed modeling approach of grid-connected VSI including the tertiary control ..… 58
3.5. The equivalent circuit of single-phase VSI connected to the main AC grid.……..… 60
3.6. Block diagram of the model of the power calculation using the SOGI-FLL algorithm.. 65
3.7. Block diagram of the simulated testbed in MATLAB for the models' validation.…..… 67
3.8. Investigating the accuracy of the actual and the reduced models to frequency variation .67
3.9. Investigating the accuracy of the actual and the reduced models to voltage amplitude variation……. ……. 67
3.10. Block diagram of the real-time implementation based on STM card for models' validation……..… 68
3.11. HIL Transient Performances of the obtained model versus SOG-FLL based-power calculation to frequency variation.……..… 69
3.12. HIL Transient Performances of the obtained model versus SOG-FLL based-power calculation to voltage amplitude variation.……...….. 69
3.13. The open-loop small-signal model of the active and reactive power flow…….…… 70
3.14. Schematic diagram of the implemented system in MATLAB Sim Power system and the HIL setup.…….…….……..… 71
3.15. Simulation study; power's transient responses of the open-loop model and power stage for step-change in the voltage: (a) frequency, and (b) amplitude.…….…….. 71
3.16. HIL real-time implementation; power's transient responses of the open-loop model and the power stage for step-change in the voltage: (a) frequency, and (b) amplitude……..…..…… 72
3.17. Closed-loop model of the MG power flow incorporating tertiary control.……...….. 73
3.18. Block diagram of the closed-loop small-signal model of; (a) the active and (b) reactive power flow control loops…… 76
3.19. Root-Locus plots for (a) 1s ≤ $T_{s\text{-}P}$ ≤ 3.5 s and $T_{s\text{-}Q}$ = 40 s, and (b) Zoom…… 78
3.20. Root-Locus plots for (a) 1s ≤ $T_{s\text{-}Q}$ ≤ 50 s and $T_{s\text{-}P}$ = 3 s, and (b) Zoom..……..…….. 78
3.21. Step response of the active power for $T_{s\text{-}P}$ = 3 s and $T_{s\text{-}Q}$ = 40 s……..…….. 78
3.22. Poles movement when $k_{p\text{-}P}$ varies in the range of, (a) 0.01× $k_{p\text{-}P}$ ≤ $k_{p\text{-}P}$ ≤ 1.2× $k_{p\text{-}P}$, and $k_{i\text{-}P}$ = 1×$k_{i\text{-}P}$, $k_{p\text{-}Q}$ = 3× $k_{p\text{-}Q}$, $k_{i\text{-}Q}$ = 0.5×$k_{i\text{-}Q}$, and (b) Zoom of a pole's movement….. 79
3.23. Poles movement when $k_{p\text{-}P}$ varies in the range of (a) 0.01× $k_{i\text{-}P}$ ≤ $k_{i\text{-}P}$ ≤ 1.1× $k_{i\text{-}P}$ and $k_{p\text{-}P}$ = $k_{p\text{-}P}$, $k_{p\text{-}Q}$ = 3× $k_{p\text{-}Q}$, $k_{i\text{-}Q}$ = 0.5× $k_{i\text{-}Q}$. ……..……..... 80
3.24. Poles' location for $k_{p\text{-}Q}$ changes in the range of (a) 0.1 × $k_{p\text{-}Q}$ ≤ $k_{p\text{-}Q}$ ≤ 10 × $k_{p\text{-}Q}$ and $k_{p\text{-}P}$ = $k_{p\text{-}P}$, $k_{i\text{-}P}$ = $k_{i\text{-}P}$, $k_{i\text{-}Q}$ = 0.5×$k_{i\text{-}Q}$, and (b) Zoom……..……..... 80
3.25. Poles' location for $k_{i\text{-}Q}$ changes in the range of (a) 0.01×$k_{i\text{-}Q}$ ≤ $k_{i\text{-}Q}$ ≤ 1.1×$k_{i\text{-}Q}$, and $k_{p\text{-}P}$ = $k_{p\text{-}P}$, $k_{i\text{-}P}$ = $k_{i\text{-}P}$, $k_{i\text{-}Q}$ = 0.5×$k_{i\text{-}Q}$, and (b) Zoom…… 80
3.26. Active power step response for (a) $k_{p\text{-}P}$ = $k_{p\text{-}P}$, $k_{i\text{-}P}$ = 2× $k_{i\text{-}P}$, $k_{p\text{-}Q}$ = 5× $k_{p\text{-}Q}$, and $k_{i\,Q}$ = 0.5× $k_{i\text{-}Q}$……...……..……..…… 81
3.27. Family of the closed-loop eigenvalues of the obtained global model for line inductance variations; (a) case 01, and (b) Zoom……...…….……...… 81

3.28. Family of the closed-loop eigenvalues of the obtained global model for line inductance variations; (a) case 02, and (b) Zoom…… 84
3.29. Family of the closed-loop eigenvalues of the obtained global model for ω_{MG} variation; (a) case 03, and (b) Zoom…… 84
4.1. Implemented secondary control for a single-phase islanded MG consists of two droop-controlled paralleled VSIs…….…….. 86
4.2. Obtained results in response to case 1……... 88
4.3. Obtained results in response to case 2…….. …… 89
4.4. Obtained results in response to case 3…….…...… 89
4.5. Block diagram of the experimental setup based on ARM Cortex μCs…….. 91
4.6. DGs and CLB: ***(a)*** frequency, ***(b)*** amplitude, ***(c)*** active power, and ***(d)*** reactive power in response test 01……...…… 92
4.7. DGs and CLB: ***(a)*** frequency, ***(b)*** amplitude, ***(c)*** active power, and ***(d)*** reactive power in response to test 2……. 92
4.8. ***(a)*** Grid and CLB voltages and their zooms when: ***(b)*** only the primary control is running, ***(c)*** activating the restoration control, ***(d)*** enabling the synchronization control.……. 93
4.9. Experimental results: ***(a)*** frequency, ***(b)*** amplitude, and ***(c)*** phase angle in response to test 3…… 93
4.10. Scheme of a grid-connected single-phase VSI-based MG system feeding a local load, with the proposed tertiary control-based hierarchical control…… 94
4.11. Simulation results acquired with the designed controller in response to test 1……..… 98
4.12. Responses of the voltage and current in test 1; (a) inverter side, (b) grid side, and (c) Zoom…… 99
4.13. The obtained results in response to grid frequency step change (test 2)…….. 100
4.14. Responses of the voltage and current in test 2; (a) inverter side, (b) grid side…...…. 101
4.15. The obtained results in response to grid voltage sag (test 3)…… 102
4.16. Responses of the voltage and current in test 3; (a) inverter side, (b) grid side, and (c) zoom……..… 103
4.17. The obtained results in response to load variations (test 4)……..… 105
4.18. Responses of the voltage and current in test 4; (a) inverter side, (b) grid side, and (c) zoom……..... 106
4.19. The obtained results in response test 5…… 107
4.20. Responses of the voltage and current in test 5; (a) inverter side, (b) grid side, and (c) zoom……..… 107

List of Tables

Table Page

4.1. Table. 1: Power Stage and Control Parameters……..…. 86

4.2. Table. 2: Experimental Parameters…….……... 90

4.3. Table. 3: Power Stage and Power Flow Control Parameters……..…….….. 96

List of Abbreviations and Symbols

AC	Alternative Current
CLB	Common Load Bus
DC	Direct current
DERs	Distributed Energy Sources
DG	Distributed Generation
ESS	Energy storage System
FLL	Frequency Locked Loop
LPF	Low-Pass Filter
MG	MicroGrid
MSOGI	Multiple Second-Order Generalized Integrator
PID	Proportional-Integral Derivative
PIL	Processor In the Loop
PV	Photovoltaic
PWM	Pulse Width Modulation
SC	Secondary Control
SOGI	Second-Order Generalized Integrator
TC	Tertiary Control
VIL	Virtual Impedance Loop
VSC	Voltage Source Converter
VSI	Voltage Source Inverter

P	Average active power of a DG unit
Q	Average reactive power of a DG unit
v_c	Capacitor filter voltage
k_p, k_i	Coefficient of the PI controller
S	Complex power
$f(\omega)$	DG unit operating frequency
E	DG unit voltage amplitude
$\hat{P}$	Estimated active power
$\hat{Q}$	Estimated reactive power
v_g	Grid voltage
i_L	Inductor filter current
P_g	Injected active power into the main grid
P_g^*	Injected active power reference into the main grid
i_g	Injected current into the main grid
Q_g	Injected reactive power into the main grid
Q_g^*	Injected reactive power reference into the main grid
p	Instantaneous active power
q	Instantaneous reactive power

v_o	Inverter Output voltage
i_o	Inverter output current
$\omega_{cut\text{-}off}$	LPF cut-off frequency
f_{MG}	MG frequency
v_{MG}	MG voltage
E_{MG}	MG voltage Amplitude
z_o	Output impedance of the inverter
ϕ	Phase angle between the MG and the main grid
Ts	Setlling time
L_v, r_v	Virtual inductance and resistance
v_z	Virtual impedance output voltage
H_{SOGI}	Transfer function of the amplitude estimate
G_d	Transfer function of the communication delay
H_{FLL}	Transfer function of the freqeucny estimate
G_{LPF}	Transfer function of the LPF
G_{PI}	Transfer function of the PI controller

Chapter 1:

Introduction to Microgrid Technology and Control

1.1. Introduction

In recent years, due to the worldwide increasing demand for electricity, the trend towards renewable energy sources; particularly Photovoltaics (PV) and wind turbines; has increased at an unexpected pace. The main reasons for this growth are the use of renewable sources to help alleviate the emissions of Co_2 from burning fossil fuel-based electricity production; and achieve a sustainable supply of energy. For instance, the European Union's (EU) energy policy has made it a world leader in the promotion of renewable energy [1], [2], in which the electricity generated from renewable energy reached 50% of the global energy production. Also, the power generation from renewable energy sources in Canada was extended to 30%. Although the use of renewable energy resources brings benefits to the grid environment, one major issue is the direct integration of these resources into the main grid, this challenge is mainly due to their high intermittent generation [3], [4].

The burden on the transmission network has become a great challenge to meet high power demand, especially for remote sites. Therefore, distributed generation (DG) has recently received a significant deal of attention as an effective solution to reduce the stress on the existing and extensive transmission system. The DG concept dates back to the early 1990's, and it mainly depends upon the installation and operation of a portfolio of small size and clean electric power generating units interconnected at nearly any point in the power system [5]. DG units are the emerging micro-generating technologies such as micro-turbines, Internal Combustion (IC) engines, and fuel cells, they also provide high incorporation of renewable energy sources such as solar power and wind power. With this concept, the power can directly flow from the source to the customer without having to pass through the transmission network. Also, it ensures that the loads are served even if the transmission network is down due to any fault. Despite having some benefits thanks to the DG system, many issues should be dealt with. The need for electronic power converters is an issue, which needs to be addressed for the integration of renewable energy resources into the electric grid and play a significant role with the key control objectives [6 – 7]. The lack of inertia of DG units is also considered one of the most important challenges facing these systems. This lack of inertia can lead to a high rate of change of frequency, under power imbalance, and may result in microgrid instability and blackout issues [8]. Furthermore, as mentioned earlier, the output of renewable energy resources fluctuates with the weather conditions, it is also an important issue when DG units are connected to the utility grid [9].

To cope with the above-mentioned issues and utilize distributed RESs more efficiently, the concept of Microgrid was introduced as a new paradigm for the future power distributed generation

systems [10 – 12]. The microgrid architectures are adopted as a groundbreaking technology to meet modern electrical grid challenges such as the rapid increase of power demand, harvesting energy from distributed renewable energy sources, and improving the power quality and reliability of electric supply [13 – 16]. On the other side, MGs can enhance stability, economic optimality, and resiliency in comparison with individual DERs and provide auxiliary services for conventional power systems [17]. These networks are generally consisting of distributed generators based on RESs, distributed energy storage devices along with loads, as well as protection systems and control devices that are capable of operating in both grid-tie and island modes [18].

In this chapter, we give an overview of the electrical energy evolution, after decades of centralization, reoriented towards increased distributed generation and microgrids. Definition and marketing, and classification of a microgrid are presented. Next, the MG hierarchical control is introduced, including primary, secondary, and tertiary control levels as well as the considered problem statement; Additionally, the chapter states a survey review on MG secondary and tertiary control layers design and modeling strategies. Finally, the thesis main contributions, outcomes, and organization are discussed.

1.2. Background and Motivation

This section gives some basic and essential concepts related to microgrid systems and thesis motivation. First, the definition of MG, as well as research projects and investments for MG implementation, are provided. Next, the classification, advantages, and architecture of the MG systems are addressed. Finally, the thesis considered motivation is highlighted.

1.2.1. Microgrids definition and Research Interest

Today, microgrid integrates renewable distributed energy resources, energy storage systems, and adjustable loads, which are expected to maximize flexibility while also decreasing the operation cost of such systems, this is regarded as a promising architecture of the modern electric grid. According to the Microgrid Exchange Group (MEG) of the U.S. Department of Energy (DOE), the microgrid is defined as, "*A group of interconnected loads and distributed energy resources within clearly defined electrical boundaries that acts as a single controllable entity with respect to the grid. A microgrid can connect and disconnect from the grid to enable it to operate in both grid-tied and islanded mode*" [19]. MG has been defined as, "*A network of low voltage power generating units, storage devices and loads capable of supplying a local area such as suburban area, industry or any commercial area with*

electric power and heat" in [20]. Hence, the MG is a low voltage system, which includes RES such as wind turbine and PV, energy storage devices, loads, and converters, interfaces to the grid.

The research efforts and investments in MG applications were increased significantly in recent years. MG projects have been undergoing a boom for the last past few years after proving their value in critical situations. The implementation of these projects in laboratories, as well as real-world experiments, is made in many countries, especially in Europe, the United States, Canada, and Japan [21]. For example, Bornholm island, Santa Rita Jail, Sendai Microgrid, and Hartley Bay projects are built up in Sweden, California, Canada, and Japan, respectively, for MG demonstration in remote sites (see **Fig. 1.1**). From the investment point of view, the International Mining and Resources Conference (IMARC) announces that the global microgrid market was worth US$19.3 billion in 2018 [22]. The market is forecast to reach US$36.3 billion by 2024, which would represent a compound annual growth rate of 10.9% between now and then. In a report, Hitachi, Tokyo, describes microgrids as a worldwide phenomenon. The Asia Pacific will be the dominant region, with 41.3% of the total microgrid revenue. North America is projected to represent 32.5% of the global market share. The cumulative microgrid revenue (calculating the total microgrid asset value) is expected to reach US $164.8 billion by 2024 [23].

Bornholm island Microgrid

Santa Rita Jail Microgrid

Sendai Microgrid

Hartley Bay remote site Microgrid

Fig. 1.1. Examples of Microgrid projects in several communities [21].

1.2.2. Microgrids classification

Generally, the MG network can either operate in a grid-tied mode or a stand-alone mode feeding critical load [24], [25]. In the grid-tied mode, the DG units supply power for the MG while the main grid determines the voltage and the frequency of the system [26]. Thus, the MG components act together as a whole in the point of common coupling to inject/absorb a specified quantity of power to/from the grid. On the other side, during islanded operation, the VSIs control autonomously the local voltage and frequency of the MG and meet the active and reactive power balance between generation and demand [27], [28]. Depending on MG functionalities and type of interconnecting at common bus voltages, MG is classified as AC MGs, DC MGs, and hybrid AC/DC MGs [20].

a. ***AC Microgrid:*** AC MGs are more taken into account due to their challenges in voltage amplitude and frequency controls, both active and reactive power flows, and the correspondence with the present AC distribution networks, which can be clustered into AC MGs and form a new MG mode operation [29]. In an AC microgrid architecture, distributed generators are connected to an AC common bus, as shown in **Fig. 1.2 (a)**. This type of microgrid has mainly two steady states of operation, grid-connected and islanded operation. It also has two transient states, corresponding to the transitions between these steady states. During all these four conditions, the microgrid system must remain stable and maintain the grid code requirement.

b. ***DC Microgrid:*** A DC microgrid has a DC bus where the distributed generators and loads are connected. The DC network is associated with the AC power utility grid via a power electronics inverter, as shown in **Fig. 1.2 (b)**. A DC microgrid can supply AC and DC loads at different voltage levels through power electronic devices. In a DC microgrid, distributed generators are connected to the DC bus-only through a single-stage voltage transformation device [30]. This structure is more economical in cases where there are many DC power sources and loads, such as PV systems and fuel cells. DC MGs have recently gained some researchers' attention due to their higher efficiency and ability to provide more natural power conversion interface with many types of DG units [31]. Also, in the DC microgrid topology, the reactive power flow and harmonic injection do not need to be considered.

c. ***Hybrid AC/DC Microgrid:*** Hybrid MG systems are designed to acquire advantages from both AC and DC microgrid, and the topology contains two separate AC and DC sub-grids [31]. **Fig. 1.2 (c)** illustrates a hybrid AC/DC microgrid which is composed of AC and DC buses and supplies both AC and DC loads. It can be considered as a special form of an AC microgrid considering the DC

network as a power source that is connected to the AC bus through a power electronic inverter. These hybrid AC/DC microgrids are well capable of offering reliable and economical solutions that can probably eradicate the multistage AC-to-DC or DC-to-AC reverse conversions [32]. Also, a hybrid AC/DC can better supply different types of loads. Even though the hybrid AC/DC microgrids have many positive returns, the interconnection of two grid systems having different characteristics showed many serious operational issues over individual microgrids in terms of complexity, control, and protection [33].

Further, extension to the aforementioned microgrid classifications, MGs may also be single- or three-phase systems.

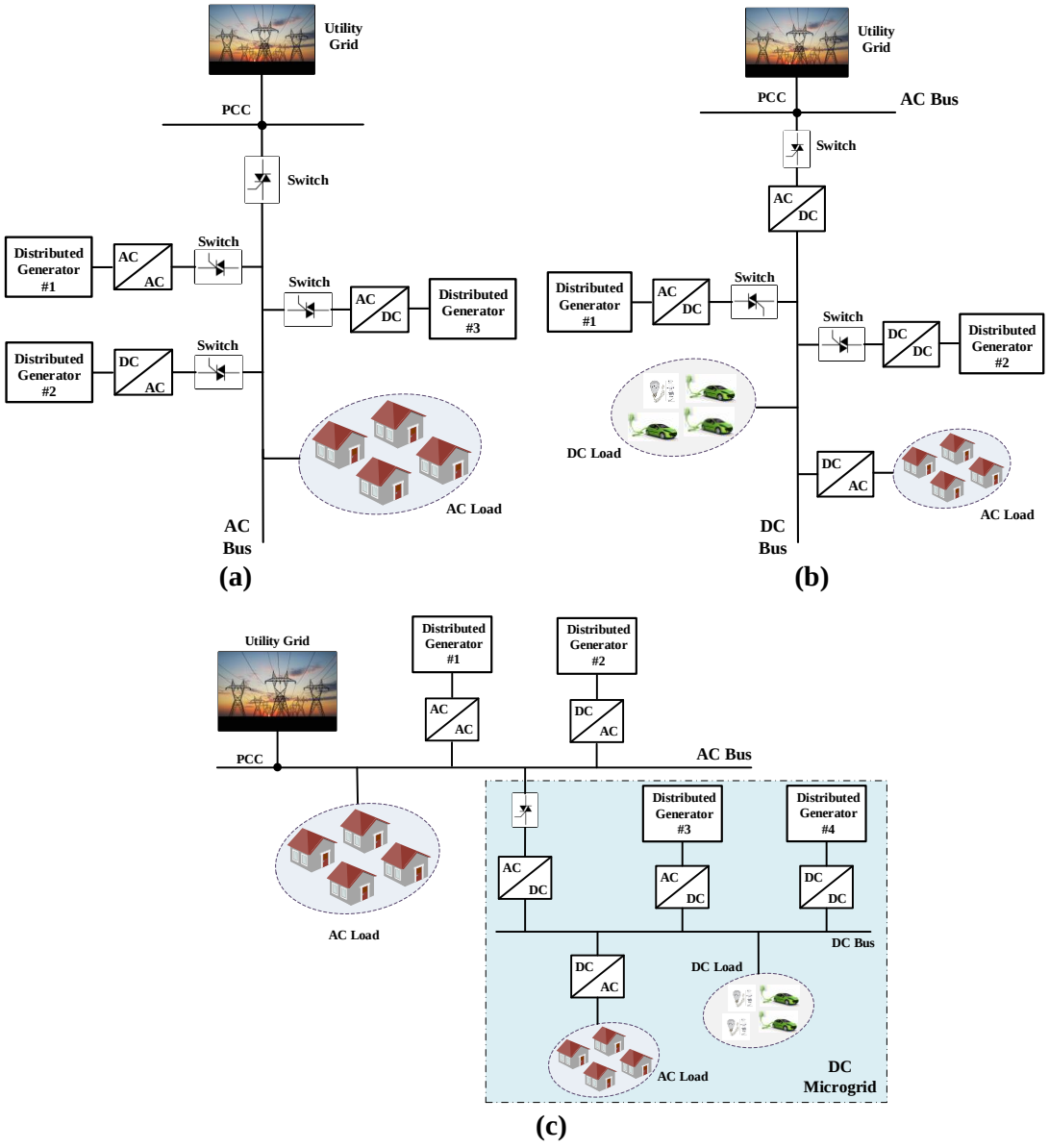

Fig. 1.2. Structure of **(a)** AC microgrid, **(b)** DC microgrid, and **(c)** Hybrid AC/DC microgrid.

1.2.3. Microgrids Advantages

MG topology has offered many benefits to local consumers and distribution systems such as:

- Facilitate distributed generation (DG) and use of renewable energy sources at their original location [34].
- Reduce transmission line losses by making the generation source close to the customer and relieve the need for extensive transmission systems [5].
- Facilitate the maintenance of microgrid devices.
- Increase power quality and improve the overall reliability of the electric supply by providing the ability to disconnect during faults in the microgrid or the utility grid [35].
- Allow easy of use of flexible loads, and ensure more precise matching of production and consumption. This improves the power system efficiency and defers the need for grid reinforcements [36].
- A cost-effective way to facilitate rural electrification, as no main power system is needed to operate the microgrid [20].
- Increase security and tolerance to faults.

For these reasons, the study and investigation of the MG systems are imperative because they are helpful to fulfill the maximization of the above-mentioned advantages.

1.2.4. Microgrids architecture

In AC microgrid, electronic power grid-tied inverters are the key component to interface distributed renewable energy resources or storage devices to low-voltage electrical power grids as well as are required to offer grid support measures [37]. The typical AC microgrid structure is depicted in **Fig. 1.3**, where the MG is connected to the main utility grid via the point of common coupling (PCC) bus and is composed of renewable distributed resources, power electronics components, and energy storage systems and loads. In addition, as seen, the microgrid contains communication infrastructure between the control layers, switches, and metering elements. In this architecture, the DG units are connected in parallel. However, in such networks, the overall system complexity and difficulties concerning system stability are significantly increased. Also, MGs are expected to satisfy some tasks and objectives, such as; DG units' frequency and voltage regulation, power quality, active and reactive power flow, system recovery, energy management, and grid synchronization [38], to ensure safe and proper operation of a microgrid. Furthermore, as MG has the ability to operate connected (i.e., SW1 closed in **Fig. 1.3**) as well as disconnected from the utility grid, the seamless

transition between these operating modes is one of the objectives that should be conceived in a microgrid. As a result, proper operation represents quite a challenge. In this sense, hierarchical control based on control strategies is necessary to guarantee the MG stability and reliability and to achieve optimal MG performance, as well as to satisfy the global control objectives [38], [39 – 42].

1.2.5. Motivation

The rapid progress of the research into the study and the implementation of microgrids conducted to improve the maturity of microgrid technology. In addition, this motivated the need to solve the challenging issues facing microgrids that are rich dynamical systems for design, modeling, control, optimization, and simulation. This thesis presents and discusses the microgrid concept and architecture as well as the corresponding hierarchical control. Furthermore, it covers and investigates, more particularly, the design and modeling related to the hierarchical control-based MG, for the aim of ensuring stable, flexible MG operation. Moreover, stability analysis and tuning procedure of the MG controllers are explored to provide appropriate and robust control that assures optimal dynamic performances of the MG system under various operating conditions.

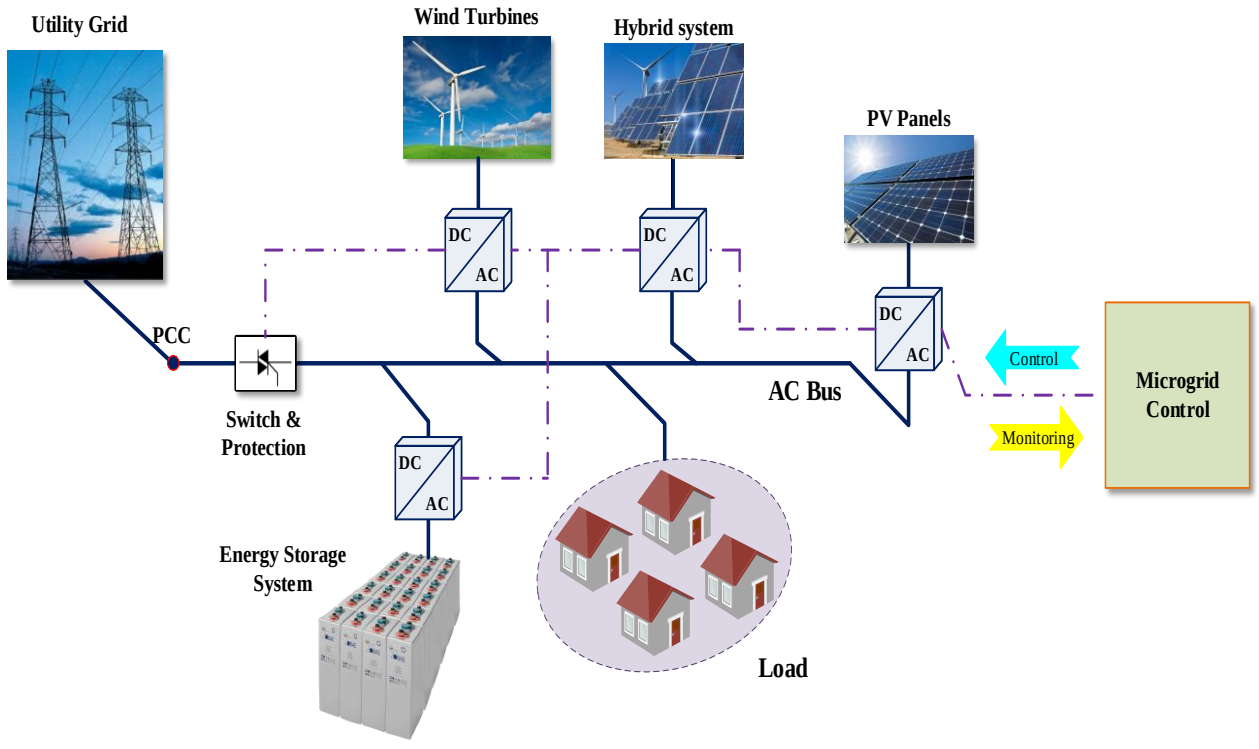

Fig. 1.3. Typical structure of an AC Microgrid.

1.3. AC Microgrids Hierarchical Control

With the development of microgrids, a hierarchical control structure for monitoring AC microgrid has been proposed in [38], where three control levels are considered; primary, secondary, and tertiary control. The block diagram of the multilevel hierarchical control of an AC MG is shown in **Fig. 1.4**. This hierarchical control has been adopted to ensure reliable, proper, and stable MG system operation in the different modes [39]. Also, it has been designed to ensure perspective objectives, such as accurate power-sharing between DG units, improved power quality provided to the customers, proper power flow and management among MG and the utility grid, as well as synchronization process and seamless transition between operation modes. In such a hierarchical control structure, each control layer has the duty of a command level and can supervisory control over lower-level systems. To this end, it is important to ensure that the reference signals from one level to the lower levels will not affect the stability and robustness performance; hence, the bandwidth must be decreased with the control level increase. In addition, each of these levels has objectives and methods of control which are designed and manipulated by different controllers [42], [43].

The schematic diagram of the hierarchical control; includes the three control layers; for parallel-connected VSI formed AC microgrid operating in both grid-connected and islanded modes, this is displayed in **Fig. 1.5**. In this structure, the primary control layer is established as decentralized, it is designed for ensuring power-sharing between DG units and maintain microgrid stability as well. This control level is often based on a droop control approach for the aim of realizing fast power balance in a decentralized manner [44 – 50]. However, the droop-based primary control presents the drawbacks of voltage and frequency deviations as well as inaccurate reactive power-sharing among DG units [38], [43], and [51]. To overcome these drawbacks, the secondary control level; as centralized or distributed controllers; is introduced for both the cancelation of these deviations, and power quality improvement by restoring the microgrid voltage frequency and amplitude to their nominal set points. A further objective of the SC is to synchronize the MG with the main utility grid before performing the connection between them [52]. The tertiary control is generally centralized and is the slowest controller; it is activated when connecting the MG to the main grid. This control level is in charge of managing the bidirectional power flow between the microgrid and the main grid, also the islanding detection mode is considered within the scope of this control level [43]. One should mention that the term energy management system refers to the secondary and tertiary control layers. In the following sub-sections, the basic structures of each control level and their detailed description will be presented.

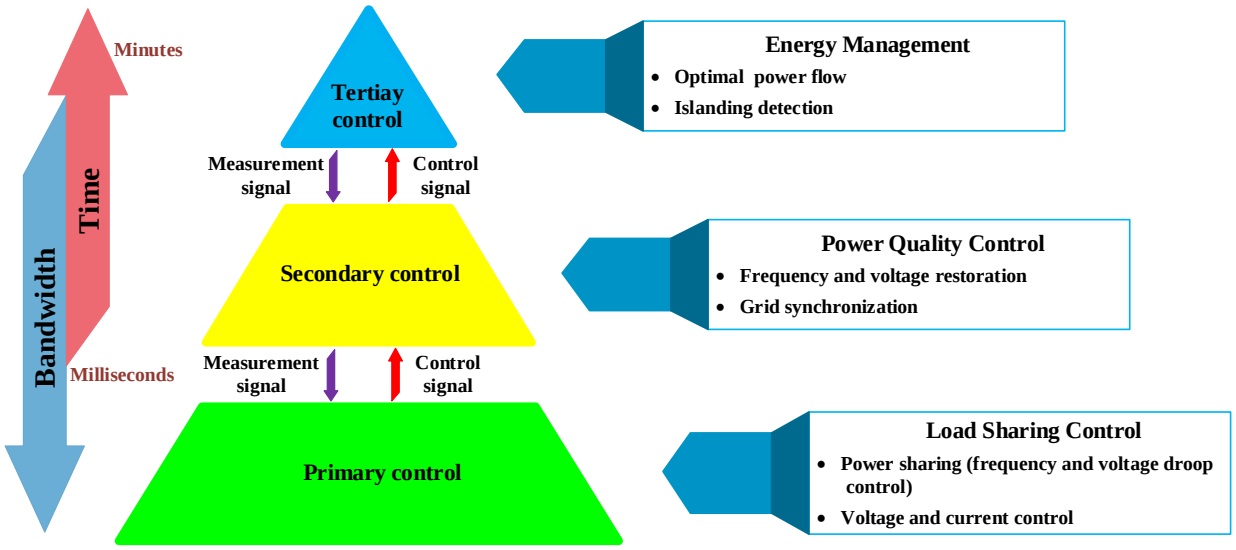

Fig. 1.4. Multilevel hierarchical control for AC MGs.

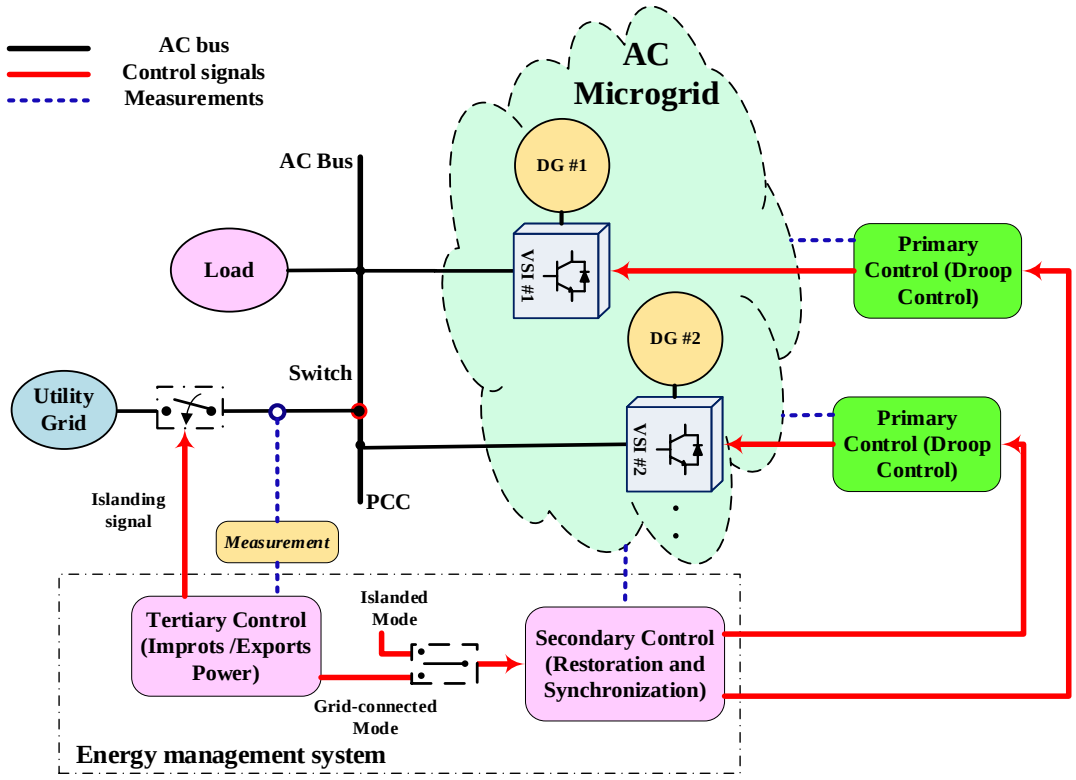

Fig. 1.5. Schematic diagram of AC MG hierarchical control.

1.3.1. Primary Control for AC-MGs

In the MG system, the primary control level is implemented mainly to control the load disturbances [53]. The main goal of this control level is to ensure the MG reliability and improve the

system performance and stability for the local frequency and amplitude control. For instance, the primary control is based only on local measurements and each inverter has its control stage, which allows each DG unit to operate autonomously.

The main control loop of the primary control is based on the droop strategy [45 – 47], [54 – 55]. The droop control is often applied to achieve the active and reactive power share between DG units, corresponding to the loads change by adjusting the voltage and frequency of the VSIs. The basic idea behind the droop method comes from synchronous generators that share any increase in the loads based on their ratings. The instantaneous increase in the power of demand can be compensated by the mechanical power of the rotor. The same idea is utilized in the exciter control of synchronous machines, i.e. the voltage drops when the reactive power is increasing. These two characteristics are implemented in power electronic MGs via the droop functions [48], [56 – 58]. However, even the primary control based on this technique has achieved average power-sharing, it has several drawbacks regarding harmonics sharing. The droop control method is not suitable for sharing current harmonics in the case of VSIs supplying nonlinear loads. Thus, improved schemes of the droop control have been proposed to enhance the harmonics sharing accuracy [58]. One of the effective techniques proposed with the aim of sharing properly the harmonic-current contents includes an additional virtual control loop to adjust the output impedances of the units [59], [60].

The block diagram of the primary control structure based on droop control of multiple VSIs connected in parallel forming MG is shown in **Fig. 1.6**. This scheme comprises current and voltage control loops, virtual impedance loop, droop controller, and power calculation block. The inverter voltage frequency and amplitude stabilization are achieved by current and voltage control loops, while active and reactive power sharing is accomplished by the droop control method. Besides, before the droop control takes place, the power calculation stage uses the output current and voltage mapped into $\alpha\beta$-frame; detected by the SOGI-FLL; to compute the average value of the real and reactive power. Voltage and current control loops are integrated into a single controller, which can significantly improve the dynamic performance of the MG. The virtual impedance loop as an optional loop acts in MGs with mismatched inductive/resistive feeder impedance, in order to improve the power quality and power-sharing accuracy in the MG [61]. These included blocks are described in detail hereafter.

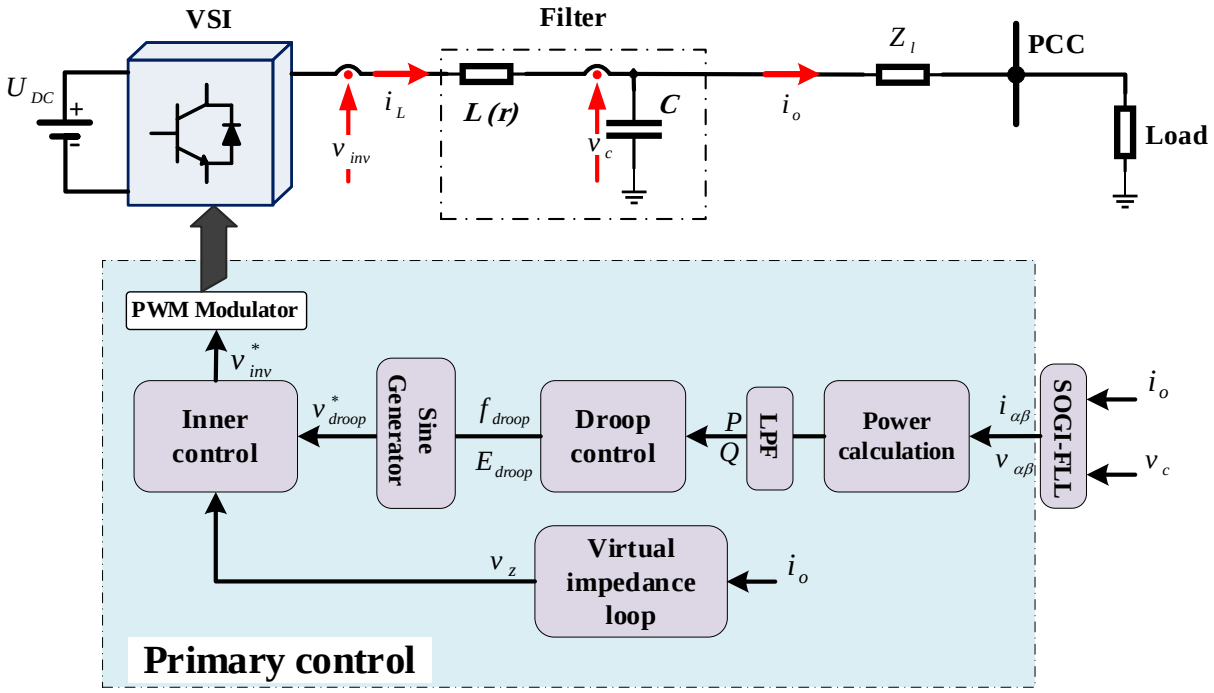

Fig. 1.6. Configuration of the primary control for droop-controlled VSC based-Microgrid.

a- Power calculation block: The power calculation block is introduced into the primary control scheme to calculate the average value of the active and reactive powers. The instantaneous active and reactive powers are generally computed based on their mathematical expressions in $\alpha\beta$ frame or dq frame as a function of output voltage and current $\alpha\beta$ (or dq) components, by using the well-known expressions given by **Eq. (1.1)** (or **Eq. (1.2)**) below, respectively. This purpose can be applied directly for three-phase MG after transforming the three-phase voltages and currents to the $\alpha\beta$ (or dq) reference frame. But, in single-phase systems, an additional unit is needed to generate the orthogonal component (i_β) from the direct current signal, where the active and reactive power can be calculated by using **Eq. (1.3)**. In this sense, several techniques have been adopted to generate the orthogonal component (i_β) from a single current signal, among them, those based on the SOGI scheme.

$$\begin{cases} P = \frac{1}{2}\left(v_{c\alpha} \times i_\alpha + v_{c\beta} \times i_\beta\right) \\ Q = \frac{1}{2}\left(v_{c\alpha} \times i_\alpha - v_{c\beta} \times i_\beta\right) \end{cases} \tag{1.1}$$

$$\begin{cases} P = \frac{1}{2}\left(v_{cd} \times i_d + v_{cq} \times i_q\right) \\ Q = \frac{1}{2}\left(-v_{cd} \times i_q + v_{cq} \times i_d\right) \end{cases} \tag{1.2}$$

where $v_{c\alpha\beta}$, $i_{\alpha\beta}$ are the in-phase and quadrature-phase components of the inverter output voltage and current, respectively.

Fig. 1.7 shows the schematic diagrams of the power calculations for both three- and single-phase systems. It can be seen that after the instantaneous active and reactive powers are determinated, they are passed through a low-pass filter (LPF) to obtain the corresponding average values, in which the transfer function of the LPF can be expressed in the *s*-domain as follows:

$$G_{LPF}(s) = \frac{P}{p} = \frac{\omega_{cut-off}}{s + \omega_{cut-off}} \tag{1.3}$$

where $\omega_{cut-off}$ denotes the cut-off frequency of the LPF which is generally chosen with a very small value to eliminate the inherent harmonics components [62].

The calculated active and reactive power are sent as inputs to the droop controller. For instance, an inappropriate detection of the quadrature version of the inverter current can affect the accuracy of the computed powers and, as a result, degrades the performance of the droop method-based control scheme. To this end, some efforts are done to design an advanced structure of the power calculator that would ensure high averaged power calculation accuracy in single-phase MGs [62].

b- Droop control strategy: In order to avoid circulating current among paralleled VSIs without the need for the communication link between them, the droop control strategy is generally used [38], [39], [52]. This is a kind of collaborative control strategy used to share the active and reactive power between DG units in a cooperative way. The droop control method; also called *P*-*ω* and *Q*-*E* droops; has been proposed to support the parallel connection of multiple voltage sources sharing the critical loads [55], [63]. It ensures that the DG units share the load by drooping the frequency of each VSI with the delivered real power. This allows each generator to share changes in total load in a manner determined by its frequency droop characteristic without the need for a communication link between the DG units. Similarly, a drop in the voltage amplitude (*E*) with reactive power (*Q*) is used to ensure reactive power-sharing.

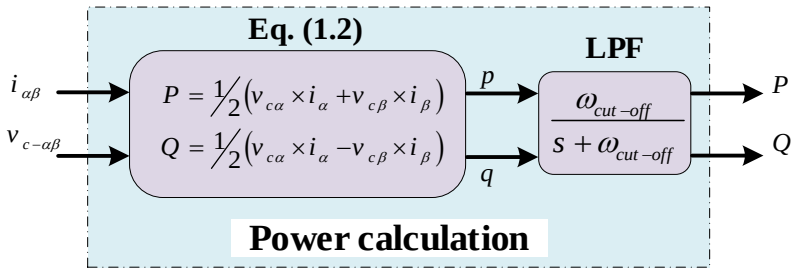

Fig. 1.7. Block diagram of the power calculation strategy.

In the droop control loop, the frequency ω and the amplitude E of the inverter voltage output are fixed according to the average active P and reactive Q powers provided by the VSI to the MG, they can be expressed as:

$$\omega = \omega^* + m\left(P^* - P\right) \tag{1.4}$$

$$E = E^* + n\left(Q^* - Q\right) \tag{1.5}$$

where ω^* and E^* are the frequency and the amplitude of no-load output voltage, respectively. P^* and Q^* are the active and reactive power references, which are set to zero in the case of island operation mode [47]. The control parameters n and m correspond to the slopes of the frequency and amplitude functions, which can be determinated according to the allowed frequency and voltage deviation ($\Delta\omega$ and ΔE) and the maximum active and reactive powers (P_{max} and Q_{max}), respectively. This relationship can be given as follows:

$$m = \Delta\omega \big/ P_{\max}, \quad n = \Delta E \big/ Q_{\max} \tag{1.6}$$

The block diagram of the droop control loop is illustrated in **Fig. 1.8**. According to this figure, the produced frequency and voltage by the droop controller are entered into a sinusoidal signal generator to generate the reference of the output voltage of the VSI, which can be defined by the following equation:

$$v_o^*(t) = E \times \sin\left(\omega \times t\right) \tag{1.7}$$

This determined voltage reference by the droop control is then applied to the input of the inner voltage and current control loops.

Fig. 1.9, illustrates the graphical representation of the droop control characteristics for two VS Is. It can be seen that the droop slopes act as a negative mechanism between P/Q and ω/E, respectively. In addition, it is worth mentioning that the frequency and amplitude in steady-state matches in both VSIs where the same slope parameters coincide, i. e, $n_1=n_2$, and $m_1=m_2$. Hence, a proper active and reactive power sharing supplied by these two DG units is reached.

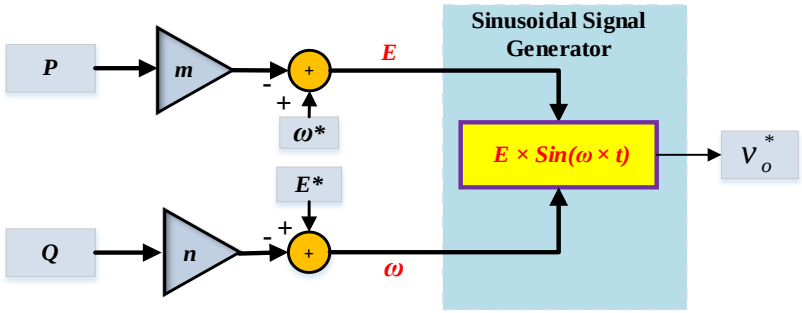

Fig. 1.8. Schematic diagram of the droop control loop.

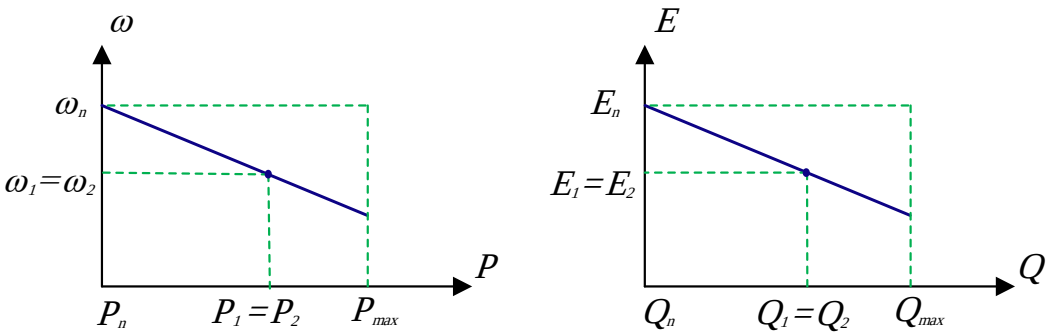

Fig. 1.9. Voltage frequency and amplitude characteristics of the droop control method.

The droop control method presented above is necessary for the operation of MG, especially in islanded mode. However, although this technique achieves real and reactive powers average value share, it has limitations with respect to current sharing since the output current provided by the inverters depends on their output impedance ratios. In addition, harmonic voltage drops due to the flow of harmonic currents induce voltage distortion at the point of common coupling (PCC). This issue can appear in the case of supplying non-linear load by VSIs. Thus, the virtual control loop is integrated into the primary control level for the aim of granting accurate sharing of the current harmonic contents when DG units feeding the non-linear load.

c- Virtual impedance loop: Although the droop control strategy is suitable to share the fundamental active and reactive power between the VSIs, it has limitations when it comes to harmonic current sharing [51], [64], [65]. To this end, the virtual impedance loop is proposed to improve the current sharing between the VSIs by normalizing their output impedance. The virtual output impedance loop consists of a fast control loop which is used to obtain pure inductive equivalent impedance composed of the series connection of the MG impedances seen by the VSI and the virtual impedance (see **Fig. 1.6**, which depicts the equivalent circuit of VSIs with line and virtual impedances). This virtual output impedance is implemented by drooping the output-voltage reference

proportionally to the time derivative of the inverter output current. This effect can increase the inverter output inductive impedance, and consequently increasing the impedance between the VSI and the common bus line, and reducing the circulating current in the MG as well. The virtual inductive output impedance can be implemented by the following expression [66]:

$$z_v(s) = s.\, L_v \tag{1.8}$$

where L_v is the inductor value of the virtual output impedance, and s is the Laplace operator.

Indeed, the virtual output impedance is added to the control loop of each inverter. The block diagram of the programed virtual-output-impedance-based droop control scheme is shown in **Fig. 1.10**. According to this figure, a virtual impedance unit is used to compute the voltage of the virtual output impedance which considers the inverter output current as an input. This virtual impedance voltage is added as an extra term in the output voltage reference; delivered by the droop control loop; as follows:

$$v_o^*(s) = v_{droop}^*(s) - Z_v(s)\, i(s) \tag{1.9}$$

The equation above describes the expression of the output voltage new reference with the corporation of the virtual output impedance.

It is worth mentioning that, as the virtual output impedance is programed as the time derivative of the inverter current, the system becomes highly sensitive to the output current noise and non-linear loads with a high slow rate. To this end, virtual impedance implementation based on the SOGI-QSG scheme has been suggested in the literature as shown in **Fig. 1.10 (b)** [66]. This implementation takes the benefits of the SOGI method features to perform a virtual impedance control scheme that is characterized by; i) less sensitive to the output current noise; ii) avoids performing the time derivative function, iii) achieves better output-voltage total harmonic distortion, and iv) enhances the sharing of nonlinear load [67]. This concept will be adopted in our hierarchical control scheme, where the SOGI-FLL scheme is integrated into all three-control levels.

d- Inner control loops: The inner controllers are required to maintain stable control over the output voltage and current of the inverter, even in the presence of disturbances. This goal can be achieved by setting the output voltage of the inverter to the desired reference. The inner controller that is considered for VSIs includes a voltage loop and an inner current loop. The current and voltage control loops are performed to regulate the output voltage of the inverter and to control the current

while maintaining the system stable. The block diagram of the inner control loops is shown in **Fig. 1.11 (a)**. Both control loops are generally based on the Proportional-Integral (PI) controllers. These controllers manipulate the error between the measured output voltage and inductor current, and their references are provided by the droop controller and the voltage controller, respectively, to produce the commands of the inverter. **Fig. 1.11 (b)** illustrates the equivalent circuit of an inverter, which can be represented by a sinusoidal voltage source and output impedance. Accordingly, the transfer function of the output voltage can be given by [47], [66]:

$$v_g = G_v(P) \quad v_o^{ref} - Z_o(P) \quad i_o \tag{1.10}$$

being $G_v(s)$ the voltage gain and $Z_o(s)$ the output impedance, which can be expressed as follow:

$$\begin{cases} G_v(s) = \dfrac{k_{i-v}k_{i-i}}{C\ L} \cdot \dfrac{1}{s^4 + \dfrac{r + k_{p-i}}{C\ L}s^3 + \dfrac{k_{i-i}}{C\ L}s^2 + \dfrac{k_{i-i}k_{p-v}}{C\ L}s + \dfrac{k_{i-i}k_{i-v}}{C\ L}} \\ Z_o(s) = \dfrac{\dfrac{1}{C}s^2\left(s + \dfrac{r + k_{p-If}}{L}\right)}{s^4 + \dfrac{r + k_{p-i}}{C\ L}s^3 + \dfrac{k_{i-i}}{C\ L}s^2 + \dfrac{k_{i-i}k_{p-v}}{C\ L}s + \dfrac{k_{i-i}k_{i-v}}{C\ L}} \end{cases} \tag{1.11}$$

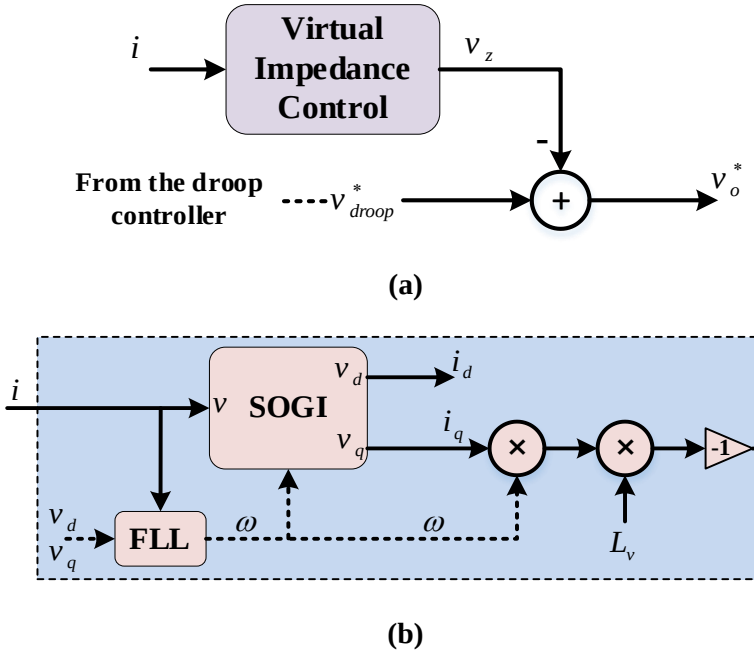

Fig. 1.10. Virtual output impedance; **(a)** -based droop method, **(b)** implementation by using the SOGI approach.

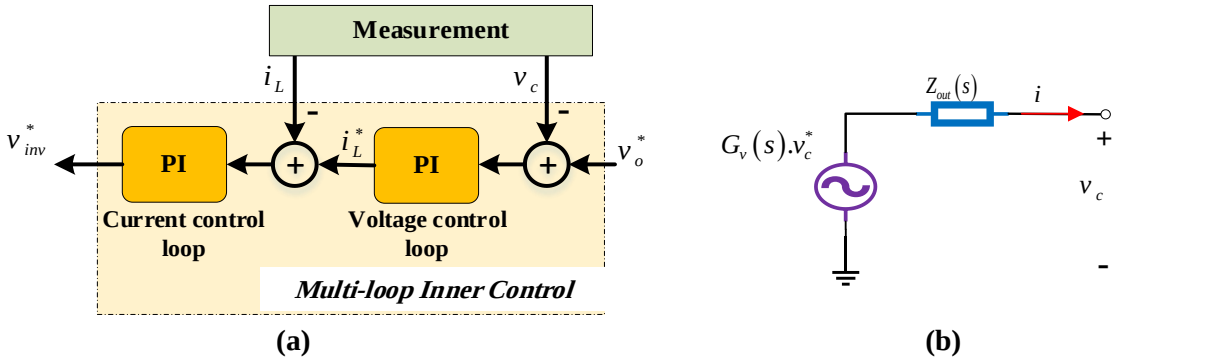

Fig. 1.11. (a) The block diagram of inner control loops, and **(b)** the equivalent circuit inverter.

Consequently, the primary control included the droop control method can ensure accurate power load sharing by controlling voltage frequency and amplitude. However, as aforementioned earlier, steady-state error and frequency and voltage amplitude deviations are the main drawbacks of this control level. In this sense, an additional control level, called secondary control, is addressed to overcome the mentioned issues and eliminate the frequency and voltage deviations [44], [68].

1.3.2. The secondary control layer

The secondary controller; which is our first concern in this thesis; is responsible of removing the frequency and amplitude deviations produced by the VSI virtual inertias and output virtual impedances. In addition, this control takes on the function of synchronizing the microgrid with the main grid before performing the interconnection, i.e., transition from islanded to grid-connected modes. Furthermore, the secondary controller can also act as the Energy Management System (EMS), taking care of power flow and power quality (i.e., suppress circulating currents and harmonic elimination) within the MG, as it is the highest control layer during islanded mode operation [69], [70].

SC can be categorized into centralized and distributed control structures [71]. The schematic diagrams of these two main structures are shown in **Fig. 1.12**. In the centralized SC structure, a central control unit coordinates the DGs and restores the MG frequency and voltages, as illustrated in **Fig. 1.12 (a)**. In this structure, all required parameters, i.e., the DG units frequency and voltage, are generally transmitted via a high data rate communication bus. However, the centralized control structure is suffering from the problem of a single point of failure [71]. In the distributed architecture (**Fig. 1.12 (b)**), each DG unit measures its own frequency and voltage and communicates them to the other DG units. For instance, a peer-to-peer communication network is required to exchange

information between each DG unit and its neighboring units. Either centralized or distributed secondary control measures the voltage frequency and amplitude (ω_{MG} and E_{MG}) and compares them with their references ω_{MG}^{*} and E_{MG}^{*}, then, sends the errors $\partial\omega_{res}$ and ∂E_{res} to all the units to restore the output voltage [44, 72]. For this sense, a proportional and integral (PI) regulator is used, considering the voltage frequency and amplitude deviations as inputs:

$$\partial\omega_{res} = k_{i-f} \times \int \left(\omega_{MG}^{*} - \omega_{MG}\right) dt - k_{p-f} \left(\omega_{MG}^{*} - \omega_{MG}\right) \tag{1.12}$$

$$\partial E_{res} = k_{i-E} \times \int \left(E_{MG}^{*} - E_{MG}\right) dt - k_{p-E} \left(E_{MG}^{*} - E_{MG}\right) \tag{1.13}$$

Moreover, the phase between the grid and the microgrid is measured and sent to all the modules to synchronize the microgrid phase. As shown in **Fig. 1.12**, these control schemes are generally equipped with a PLL. This PLL is integrated to estimate the key parameters (frequency, amplitude, and phase) needed for the secondary control loops.

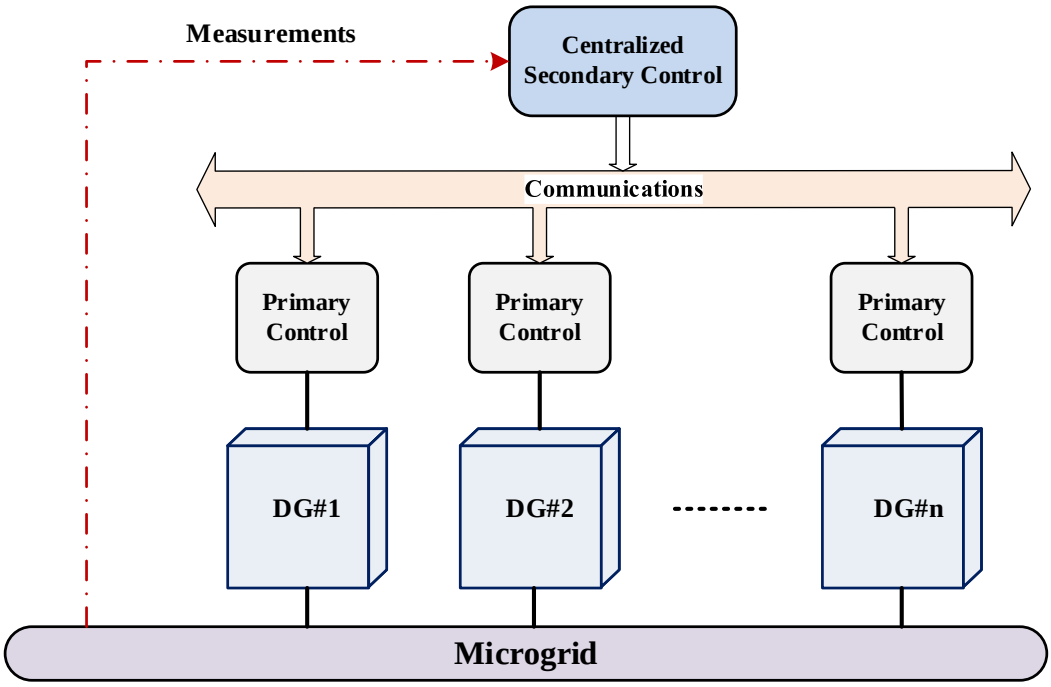

(a)

Fig. 1.12. Two main secondary control architectures: **(a)** Centralized SC and **(b)** Distributed SC.

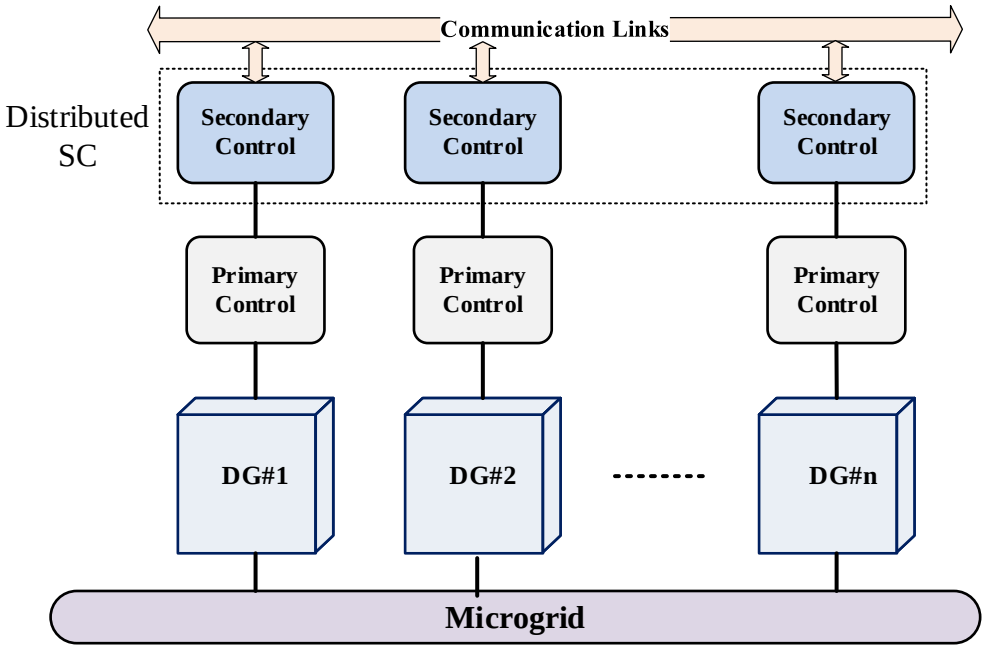

(b)

Fig. 1.12 (suite). Two main secondary control architectures: **(a)** Centralized SC and **(b)** Distributed SC.

1.3.3. The tertiary control layer

The tertiary control level; which is our second point of interest in the present thesis, is designed to regulate the active and reactive power flow between the main grid and the entire microgrid at the PCC, and to provide load balancing [38]. In the grid-connected mode, the microgrid operates by exporting and importing energy to and from the main grid, ensuring the power control flow balance between the MG and the main grid, and supporting the grid services as well. To this end, the tertiary control is introduced as a global central controller for optimal bidirectional control of the active and reactive power flow, power management, and coordination of DG units at optimal set points. More particularly, in microgrid systems interconnected to the utility grid, the main aim of the tertiary control is to manage power flow by enabling any deficit of energy in the microgrid to be supplied by the utility grid as well as by sending any excess of energy in the microgrid to the main grid [43], [73], [74]. Hence, the power flow bidirectionality can be controlled by the tertiary layer, which defines the desired active and reactive power values by providing the voltage amplitude and frequency set points to the lower control levels [40], [74], [75]. **Fig. 1.13** shows the block diagram of the tertiary control level for multiple DG units formed MG connected to the main AC grid. As is illustrated, by measuring the grid current and voltage, the active and reactive power injected to the grid (P_g, Q_g) can be

computed. These quantities are compared with their corresponding desired values P_g^* and Q_g^*, and PI controllers produce the new voltage frequency and amplitude set-points. Hence, by considering active and reactive power flows, the expressions of the tertiary controller can be given as follow [40]:

$$\omega_{MG}^* = \int k_{i-P}\left(P_g^* - P_g\right)dt + k_{p-P}\left(P_g^* - P_g\right) \tag{1.15}$$

$$E_{MG}^* = \int k_{i-Q}\left(Q_g^* - Q_g\right)dt + k_{p-Q}\left(Q_g^* - Q_g\right) \tag{1.16}$$

The obtained frequency and amplitude references are then sent to the secondary control layer for power flow control at the inverter level. In such control level, a PLL is needed for frequency, amplitude, and phase angle estimation of the grid voltage to synchronize the MG with the grid when performing the transition from island to grid-connected modes. It is worth mentioning that the tertiary control actions should be deactivated when islanding mode is detected, i.e., the utility grid is disconnected from the microgrid.

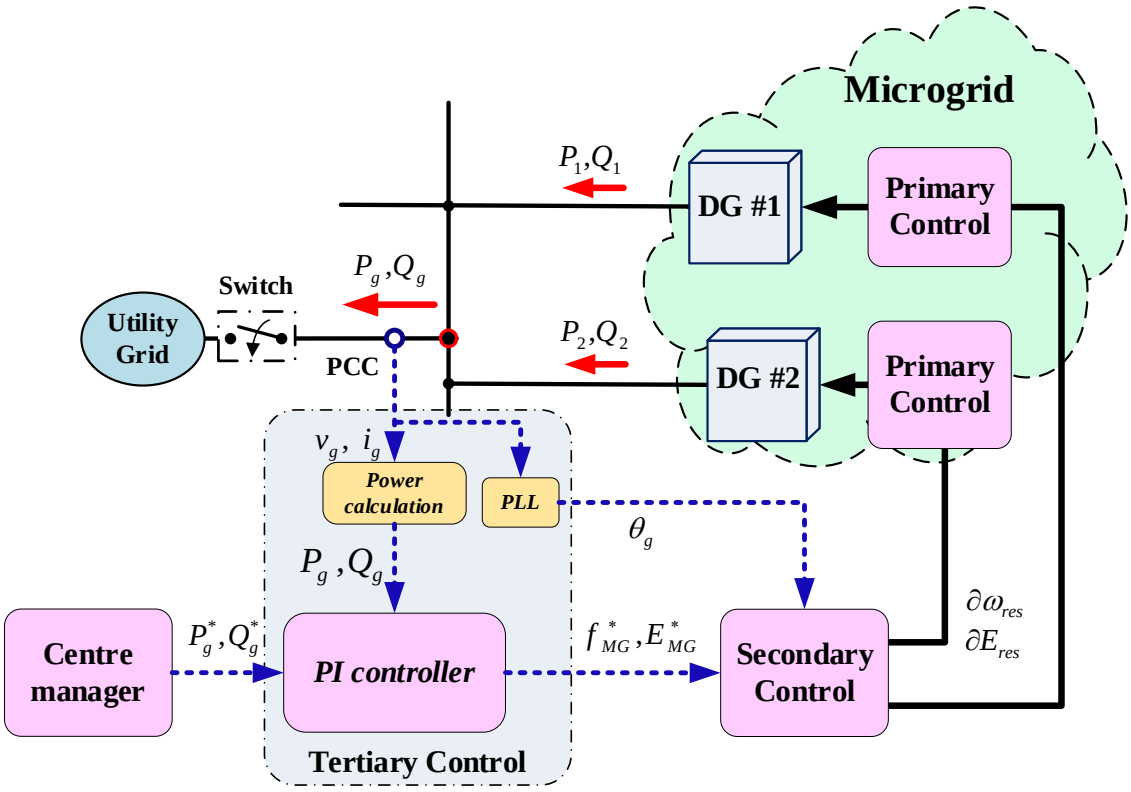

Fig. 1.13. Block diagram of the tertiary control level for a microgrid.

1.4. Problem statement

As discussed above, hierarchical control including primary, secondary, and tertiary control levels have been adopted to achieve microgrid requirements such as power quality, stability, and robustness [39], [76]. Besides, for the aim of improving and evaluating the performance of the microgrid control, different control schemes, modeling, and analysis of these control levels have been proposed. However, the primary control design, modeling, and analysis have gained much research community attention, in which advanced scheme and dynamics performance enhancement of each included stage have been considered for single- and three-phase MGs. On the other side, despite extensive research that has been conducted in designing control strategies for both secondary and tertiary control levels, effective control structures that integrated enhanced estimation schemes cannot be found in the literature review, especially in the case of single-phase MGs. In addition, accurate dynamic modeling, taken into consideration the estimation dynamics, and a comprehensive tuning procedure of these control schemes based-single-phase MG during grid-connected and islanded operation modes are not properly investigated. Hence, these main problems of designing, modeling, and tuning the secondary control and tertiary control layers for single-phase microgrids, which are challenging issues, are addressed in the present research work.

The question is whether the designed secondary and tertiary control schemes as well as the proposed modeling approach including inherent dynamics-based analysis are able to provide a stable and robust operation of MG with enhanced performance?

The given response to this question is that the integration of an enhanced estimation scheme with improved performance can increase the MG robustness and reliability, and provide a system that can respond to changes in load demand and VSIs outputs in an effective manner, without compromising performance and stability. In addition, the development of modeling approach that allows to derive accurate mathematical models can ensure effective evaluation of the MGs stability and the development of control techniques that can accomplish the desired control transient performance. The presented analysis and performance examination as well as the conducted simulation study and experimental tests and their results will validate the effectiveness of the thesis proposal.

1.5. Literature Review of the secondary and tertiary control strategies in AC MGs

This section presents a description of the literature review of the secondary control and tertiary

control layers for droop-controlled VSIs in islanded and grid-tied microgrid, regarding control scheme design and modeling procedures. The related works are analyzed from the control design and modeling approach point of view, taking into consideration related problems as well as the estimation stage performance and dynamics, for single- and three-phase microgrids. In the first subsection, a review of the secondary control design and modeling intended for droop-controlled VSIs interfaced-AC microgrids is discussed. The second subsection presents a review of the design and modeling of tertiary power flow control intended for grid-connected MGs.

1.5.1. The Secondary control layer

The secondary control is in charge of recovering the MG voltage frequency and amplitude to their rated values and perform synchronization with the grid as well. As mentioned earlier, secondary control has been presented by two main architectures, centralized, and distributed intended for three- and single-phase MGs. These architectures have been adopted in various research works, such as in [77] and [72], for centralized and distributed, respectively. In addition, many advanced control techniques have been developed in the literature in order to achieve the secondary control objectives with optimal performance [78 – 80]. Among them, fuzzy logic control [78], H∞ control technique [79] and model predictive control [80], etc... . In the secondary control layer, the communication network is required to send the expected variables to the primary control. This communication network is the main feature that distinguishes between the secondary control architectures. Besides, the effect of the communication delay is the main issue that has been addressed in the literature [81], [82]. The authors in [81] have studied the communication-delay-related stability issue for the distributed secondary frequency and voltage control of three-phase islanded MGs and presented integrated modeling and analysis. Also, references [82] have investigated the impact of communication delay on the system dynamic performance for distributed secondary control intended for single-phase MG.

However, in all the aforementioned works, conventional PLL is generally used to determine the frequency, amplitude, and phase angle of the MG voltage. In fact, the conventional PLL schemes regarding the parameters estimation are highly sensitive to load variation and harmonics issues as well as to DC component disturbance [83]. This effect may severely affect the performance of the frequency and amplitude restoration control loops and as a result, decrease the entire MG system stability. In addition, as PLL involves sine and cosine computing functions, they suffer from implementation complexity, especially, single-phase ones. This issue may complicate the

implementation of secondary control and increase its computational time. Furthermore, the DC component, which may be induced in the input of the PLL, can affect the PLL estimation performance and, as a result, the system stability. To deal with the PLL issues, especially for a single-phase system, SOGI-FLL solution, as well as advanced ones based on SOGI with the capability of DC-offset rejection (ESOGI-FLL [67]), have been proposed in the literature in order to improve the estimation characteristics [84]. These advanced schemes, which are characterized by their implementation simplicity and high DC-offset rejection capabilities, have been presented in various MG applications, and have shown their effectiveness [67]. Although these schemes feature, as well as some researchers, have studied the effect of the PLL in secondary control regarding dynamic performance, no related works for the integration of enhanced estimation scheme in the secondary control layer for droop-controlled VSIs have been adopted in the literature.

In addition, from the modeling point of view, since PLL is involved in the secondary control, it is expected to introduce its estimation dynamics into the frequency and amplitude restoration model. In this regard, small-signal modeling of distributed secondary control for frequency and amplitude restoration of an islanded MG has been presented in [72]. In this paper, the PLL dynamic of the frequency estimate is involved in the frequency restoration model. Where a unity amount is considered for amplitude estimate as feedback in the amplitude restoration model. The same concept is proposed for the centralized secondary control of two three-phase VSIs forming islanded MG in [82], where only the dynamics of the frequency estimation is involved. Similarly, in [85], the authors have modeled the frequency restoration control stage for a three-phase MG, and only the dynamic of the frequency estimation is considered. The researchers in the paper [86] have introduced a first-order transfer function in the model of the frequency restoration control to express the PLL estimation dynamic, while the amplitude restoration model is not presented. For single-phase MG application, only one has been found in the literature [87], which presents the modeling of centralized secondary control. The same concept is adopted for the modeling of the frequency restoration control by introducing the first-order transfer function that is considered for the PLL estimation dynamics. While unity feedback is proposed in the amplitude restoration model. However, the adopted concept may be valid for three-phase applications where the amplitude might be computed in $\alpha\beta$ frame by using the $\alpha\beta$ voltage components. Nevertheless, in single-phase MGs, the amplitude must be estimated as the frequency from a single input voltage. Thus, the amplitude estimate dynamic should be involved in the model of the amplitude restoration control. From this point of view, the obtained models are given

in paper [87] and the analysis based on it is questionable. As a result, the stability of the overall MG system can be compromised. Besides, it is worth mentioning that a comprehensive control design for the tuning of the secondary controller parameters cannot be found in the literature.

1.5.2. The Tertiary control layer

The tertiary control layer is implemented as a centralized controller to manage the power flow between the MG and the grid, which can be enabled by real and reactive power reference tracking capability in all the DG units. This control level is activated when the grid-connected mode is expected. In the research review, the tertiary control has been presented with different control techniques applied to droop-controlled microgrids working on grid-connected mode [40], [88 – 91].

Despite the wide research that has been presented in designing the tertiary control for three-phase grid-connected microgrids, there is still ambiguity regarding single-phase MG. However, in the tertiary control stage, the PLL is often integrated to estimate the key parameters of the grid need by the controller. Furthermore, as the active and reactive powers of the grid are needed, hence, they should be calculated. These powers can be computed in a three-phase system directly according to their expression in $\alpha\beta$ frame (given by **Eq. (1.2)**), followed by LPF to terminate the average active and reactive powers from the instantaneous ones. In single-phase MGs, a power calculation unit with an LPF is generally integrated within the tertiary control level to calculate the average powers, in which the estimation of the voltage orthogonal component is the main issue. Indeed, the integrated LPF, as it is well known, can reduce the dynamic response of the control system [91], hence, degrading the MG stability. In addition, the presence of the DC component in the PLL input signal may affect system stability [67]. Therefore, to deal with these issues, advanced power calculation methods introducing SOGI-based schemes have been presented and have demonstrated their effective performance [92]. Nevertheless, from the literature survey, these structures have not been applied yet in the tertiary control-based grid-tied MG.

Regarding the modeling procedure, the thing that should be mentioned is that the MG power flow modeling intended for the tertiary control level is similar to the one for the droop control since it is performed through line impedances (see Fig. 10). They differ from each other only in the closed-loop control model, where the tertiary controller model is introduced instead of the droop control functions, as well as the input and the output signals of the system. From this regard, various modeling approaches have been developed to derive the small-signal model of the power flow control in the

MG system [88], [91], [93 – 98]. For instance, papers [95] and [6] presents a dynamic phasor modeling approach for a three-phase MG during islanding operation. State-space modeling of MG formed by two VSIs has been given in [97] and [98]. One can observed that most of the stated works have addressed the closed-loop modeling of the MG incorporating the droop control for three-phase systems. Also, the number of works related to the MG power flow modeling incorporating tertiary control in grid-tied MG is significantly reduced, and even more for the case of single-phase MG system. Further, it is worth noting that the researchers in all presented papers have considered active and reactive power decoupling in the control, only the last one has addressed the coupling concept. Adopting the coupling concept may contribute to achieving accurate MG modeling incorporate hierarchical control.

Considering the power calculation point of view, in all these works, a transfer function of a LPF has been proposed to describe the power calculation dynamics into the power flow model [92], [93]. Nevertheless, as mentioned above, an additional block is required to extract the orthogonal component voltage in the case of single-phase MGs, then, its dynamic must be introduced in the control modeling. From our point of view, this concept is often overlooked in the research works presented in the literature review, thus, stability analysis based on the obtained models may not be accurate. In addition, a comprehensive and clear tuning procedure for the proper selection of the tertiary controller parameters cannot be found in the research review. These issues may lead to an inappropriate design of the tertiary control. As a result, the injection of improper power into the grid is expected; as a result, the stability of the overall system may be questionable.

Generally speaking, the ESOGI-FLL method can be introduced in both secondary and tertiary control, especially for single-phase MG applications. This method is an effective solution for the proper estimation of the single voltage key parameters and synchronization process [92]. The ESOGI-FLL is based on a frequency-adjustable resonator, that was implemented by two cascaded integrators working in a closed-loop (see Fig. 5 in chapter. II). In addition, it integrates a frequency observer that adapts the center frequency of the ESOGI to frequency changes. Such scheme is characterized by:

- Precise estimation of filtered voltage fundamental component and its 90◦ phase-shifted version as well as the operating frequency, amplitude, and phase angle.
- Ease implementation and it can filter the input signal without time delay.

- The advantages of fast and accurate signal-tracking capabilities with a high rejection of the input signal disturbances, especially the DC component.
- Robustness to different load disturbances.

In addition to these features, this scheme has a clear mathematical model, which is very useful to be introduced in the MG modeling incorporate hierarchical control for describing the estimates' dynamic.

To deal with the aforementioned control issues and to optimize MG control performance, inspired by the ESOGI-FLL features, the present thesis focus on the design and the modeling of the secondary and tertiary control layers included estimation structure-based ESOGI-FLL. These control layers are interned for droop-controlled MG operating in grid-connected and islanded modes. In addition, in-depth analysis and comprehensive tuning procedures are investigated in this research work. Furthermore, aiming at validating the thesis proposal, the implementation of the complete hierarchical control for single-phase grid-tie and island MG is conducted.

1.6. Main Contributions and outcomes

This thesis proposes an effective and optimal proposal for the design, analysis, and modeling approach of secondary and tertiary control layers intended for single-phase microgrid operating with the droop method during island and grid-tie modes operation. In addition, it develops a comprehensive and clear procedure for the tune of secondary and tertiary controllers' parameters. The performance evaluation of the proposed control approaches is conducted through simulation studies under various operational conditions. Additionally, some experimental tests are presented to validate the effectiveness and robustness of the proposal. The main contributions of the present thesis are summarized below:

a- For the secondary control:

- Designing a secondary control structure based on the ESOGI-FLL scheme intended for single-phase droop-controlled VSIs in islanded MG.
- Developing a new accurate modeling approach of the designed secondary control for frequency and amplitude restoration, taking into account the dynamics of the ESOGI-FLL based-estimation block.
- Introducing the transfer function of FLL, which describes the frequency estimate dynamic into the frequency restoration control loop model.

- Appling dynamic phasor modeling to drive the model of the amplitude estimate to be integrated into the model of the amplitude restoration control loop.
- Studying and analyzing the stability of the MG system incorporating the secondary control layer using the obtained closed-loop models.
- Providing a comprehensive and effective tuning guideline for proper parameter selection of the secondary controllers.
- Assessing the robustness of the designed controllers against load changes and system parameters disturbances based on the obtained models.

b- For the tertiary control:

- The design of an advanced structure for the tertiary control layer equipped by ESOGI-FLL-based-power calculation block for optimal active and reactive power control flows in single-phase grid-tie MG is presented.
- Proposing a dynamic phasor modeling approach to drive an accurate model of the active and reactive power flow for single-phase grid-connected MG incorporating tertiary control. an active and reactive power decoupling control algorithm
- Introducing the dynamics of the ESOGI-FLL-based power calculation into the overall system model.
- Driving an accurate closed-loop state-space model of the power flow control considering active and reactive power coupling.
- Assessing the accuracy of all obtained models under case studies and perform the stability of the whole system.
- Developing an effective control design to tune optimally the parameters of the tertiary controller, which ensures optimal power flows.
- Verifying the robustness of the designed tertiary controller against various disturbances.

1.7. Thesis organization

After giving an introductive description of the microgrid technology and hierarchical control scheme, then, investigating problem statement, introducing a survey of past work focusing on the secondary and tertiary control layer design and modeling and presenting thesis contributions and organization as well, the rest of this thesis is arranged as follows:

Chapter 2 describes, in a detailed manner, the design of the secondary control based on the ESOGI-FLL scheme for two single-phase droop-operated VSIs dominated-islanded AC MG. In

addition, it presents the development of a new modeling approach for the secondary frequency and amplitude control based single-phase MG. In this modeling approach, the dynamics of the frequency and amplitude estimates are taken into consideration in the model of the overall system. Besides, the ESOGI-FLL scheme description, the derivation of its dynamic models regarding frequency and amplitude estimation, and their accuracy examination are provided in this chapter. The system stability analysis and the parameters tuning of the secondary control, as well as robustness assessment, are presented, also, in this chapter. Furthermore, this chapter includes synchronization loop modeling and control design. Finally, the main conclusions of this chapter are given.

Chapter 3 considers the design and modeling of the tertiary control layer for optimal power flow in a single-phase AC microgrid. The dynamic phasor modeling procedure is proposed to derive accurate models for power flow control during the grid-connected mode, and considering active and reactive power coupling. The state-space small-signal model of the open-loop power flow control is obtained and its accuracy is verified. The analysis of the system stability based on a developed closed-loop model for power flow control is provided. A control design guideline based on simplified closed-loop models, which are concluded, is presented to properly choose the control parameters. Finally, the robustness of the tertiary controller is tested against the controller and the system parameters variation as well as load disturbances, and the chapter conclusions are given.

In chapter 4, first, simulation study and experimental implementation of the secondary control layer for a single-phase AC microgrid are provided. A centralized secondary controller is implemented for two parallel-connected droop-controlled VSI forming island MG. Additionally, different tests are conducted and the obtained results are illustrated and discussed in detail. Secondly, a simulation testbed development of a designed tertiary control for importing power from an MG to the grid is realized in this chapter. The effectiveness of the tertiary control is assessed under various grid-tie MG operating conditions. This chapter involves the expected results obtained from the performed tests. The discussion of the obtained result is presented and explained in this chapter. Later, the conclusion of this chapter is provided.

Chapter 5 summarizes the main conclusions of the present thesis. It points out at all the made contributions regarding the design and the modeling of the secondary and tertiary control layer for single-phase AC MG. In addition, a way that the obtained results show how the designed control schemes have improved MG performance as well as validate the thesis purposes.

1.8. Conclusion

This chapter has explored the thesis purpose introduction, background and motivation, MG control, and our focus control level literature reviews, contribution, and organization. First, a general introduction to the future of the electrical power grid, i. e., MG systems, and control are presented. In addition, the hierarchical control strategy proposed for AC microgrids, including primary, secondary, and tertiary levels, was described considering different operating modes. In this chapter, the primary control included the droop method as well as other control loops for microgrid system control, was described in detail. Furthermore, the secondary and tertiary control layers were also, discussed. A review of the literature published on the design and modeling of the secondary and tertiary controls is addressed. The contribution of the thesis regarding the proposed design and modeling approach of the secondary restoration control and the tertiary power flow control is presented. The organization of the present thesis is also given in this chapter.

In the coming chapters, the design of the secondary and tertiary control layers will be proposed. Also, new accurate modeling of the frequency and voltage restoration secondary control and the power flow incorporation tertiary control will be developed. Systems testbeds will be conducted on a simulation study using the MATLAB environment. Finally, the thesis control proposals will be tested in terms of robustness against parameter variation, stability, power quality, and performance enhancement.

Chapter 2:

Design and Modeling of Secondary Control Layer for Autonomous Single-Phase Microgrids

In this chapter, a summary of the first contribution of this thesis is discussed. This contribution is related to the design, modeling, and analysis of the secondary control based on ESOGI-FLL to properly compensate for the voltage amplitude and frequency deviations caused by the inherent characteristics of the droop control strategy in single-phase microgrids (MGs).

2.1. Introduction

Microgrids (MGs) are local electrical networks, which are designed for efficient, reliable, and flexible use of distributed generators (DGs) including renewable energy sources and energy storage devices [98–100]. In such networks, the distributed generators are linked at the point of common coupling (PCC) via power converters enabling MGs to operate either in grid-connected mode or islanded mode [101], [102]. The control of these power converters-based MG must be able to guarantee some objectives such as power-sharing, power quality enhancement, synchronization, and power flow management [6]. Toward this end, hierarchical control consisting of primary, secondary, and tertiary controls is the most adopted scheme in the literature [38, 39], [104]. The primary control is locally implemented to ensure power-sharing among DG units and their stable operation. Whereas, the secondary control is required to compensate for frequency and amplitude deviations caused by the inherent characteristics of the primary control, as well as ensuring power quality enhancement. In addition, when the grid connection mode is expected, microgrid synchronization to the main utility grid is included within the secondary control scope [63]. The tertiary controller deals with the power flow by providing the setpoints to the lower control levels.

The secondary control, intended for frequency and amplitude restoration, has been considered for both single and three-phase AC microgrids [68], [72], [105 – 107]. Two main strategies of the secondary control layer have been reported in the literature; centralized and distributed approaches [93], [108 – 112]. In the centralized control approach, a central controller is responsible for producing the DGs control signals, based on the estimated microgrid parameters, i.e., frequency and amplitude. In this strategy, an underlying communication network is required to communicate the appropriate control signals to the primary control of each DG unit. While the distributed secondary control is locally implemented in each DG with the aim to improve the system reliability. This control strategy requires both local estimates and the measured parameters of interest of the rest of DG units, which are exchanged through a sparse communication network, to produce the required set points to the primary control. The above-mentioned approaches generally use the phase-locked loop (PLL) technique to estimate the frequency and amplitude of the microgrid at the PCC and those of other DG units. In fact, the performance of these PLLs may be

degraded due to the voltage distortions, especially the DC component, which may be caused by different factors in the microgrid voltage [113]. Despite solutions that deal with these issues are available in the literature [114 – 117], no application for these solutions to the secondary control layer has yet been presented.

On the other hand, as the PLL has been considered as an estimator, the dynamic models of the secondary control for frequency and amplitude restoration have been derived by exploiting the small-signal model of the PLL. For instance, Vasquez et al. [44] have modeled the centralized secondary control of a three-phase MG considering the PLL transfer function to express the frequency estimate dynamics in the frequency restoration. While the amplitude estimation is modeled as a unity gain for the amplitude restoration. Similarly, in [118], the PLL model has been used in the frequency recovery model for two different control strategies: model predictive controller and Smith predictor-based PI controller. However, the voltage recovery modeling has not been reported. The same concept has been adopted to model the distributed secondary control for frequency and amplitude restoration in [110], [119], [120]. In [121], a unity voltage feedback has been considered in state-space modeling of a distributed voltage control. It is worth mentioning here that all the available modeling approaches are proposed for three-phase MGs, in which only the frequency estimate dynamic has been taken into account, and the amplitude estimate has been modeled as a unity gain. This concept is valid for three-phase MGs, as the frequency is estimated by the PLL while the amplitude can be computed directly by using the $\alpha\beta$ voltage components that are obtained based on the $abc/\alpha\beta$ coordinate transformation. However, in single-phase MGs, both amplitude and frequency are estimated using the PLL, from a single-phase input voltage. Hence, the estimation dynamics of both of these variables should be taken into consideration in the frequency and amplitude restoration modeling. According to this reason, the authors in [87] have proposed a schematic diagram of the secondary control model for amplitude restoration of a single-phase MG. In fact, a first-order transfer function is introduced to describe the amplitude estimate dynamics. One should note that this is the only paper found in the existing literature which deals with this issue. However, the authors did not mention how this transfer function has been obtained and how its parameter has been selected. This is maybe due to the difficulty of expressing the amplitude estimation dynamics from the PLL's small-signal model. Hence, the analyses of the amplitude restoration control based on this model are not accurate. Consequently, an improper tuning of the control parameters and, then, the stability of the MG can be seriously compromised.

Although the existing literature has addressed extensively the frequency and amplitude restoration in the secondary control layer for three-phase MGs and has covered all the modeling

and control design aspects, there are still blind spots and challenging tasks regarding single-phase MGs. The main challenges related to the secondary control modeling in single-phase MGs, are listed below:

- Lack of precise modeling of microgrid frequency and voltage restoration control, more particularly, due to the unknown dynamics of the involved estimates.
- Lack of a comprehensive tuning procedure for parameter selection of the proportional-integral (PI) controllers involved in the restoration control.

In this chapter, a secondary control scheme based on the Enhanced Second-Order Generalized Integrator-Based Frequency-Locked Loop (ESOG-FLL) scheme suitable for DC offset rejection is presented. Also, an accurate approach to derive small-signal models of the frequency and amplitude voltage at the point of common coupling (PCC) of a single-phase MG by analyzing the dynamics of the ESOGI-FLL is proposed. **Fig. 2.1** shows the hierarchical control of an islanded AC MG, on which the ESOGI-FLL scheme is introduced to estimate accurately the microgrid key parameters. Accordingly, the main features of ESOGI-FLL are explored to get the transfer functions that describe the frequency and amplitude estimates dynamics and to introduce them into the overall secondary control modeling. The main contributions investigated in this chapter are listed hereafter:

i) Dynamic phasor concept-based ESOGI-FLL modeling is proposed to derive the amplitude estimate, dynamic model. The derived model is, then, introduced as feedback in the amplitude restoration control loop.

ii) The linearized model of the frequency locked loop (FLL) is suggested as a frequency estimate model. This model is considered as feedback in the frequency restoration control loop.

iii) The stability analysis of the system and a systematic design process for a proper selection of the restoration controllers' parameters are performed.

iv) The synchronization modeling and control design that enables a seamless transition from islanded mode to grid-connected mode operation are studied.

Simulation and practical experiments of a hierarchical control scheme, including traditional droop control and the proposed secondary control for two single-phase parallel inverters, are implemented to confirm the effectiveness and the robustness of the proposal under different operating conditions. The obtained results validate the proposed modeling approach to provide the expected transient response and disturbance rejection in the MG.

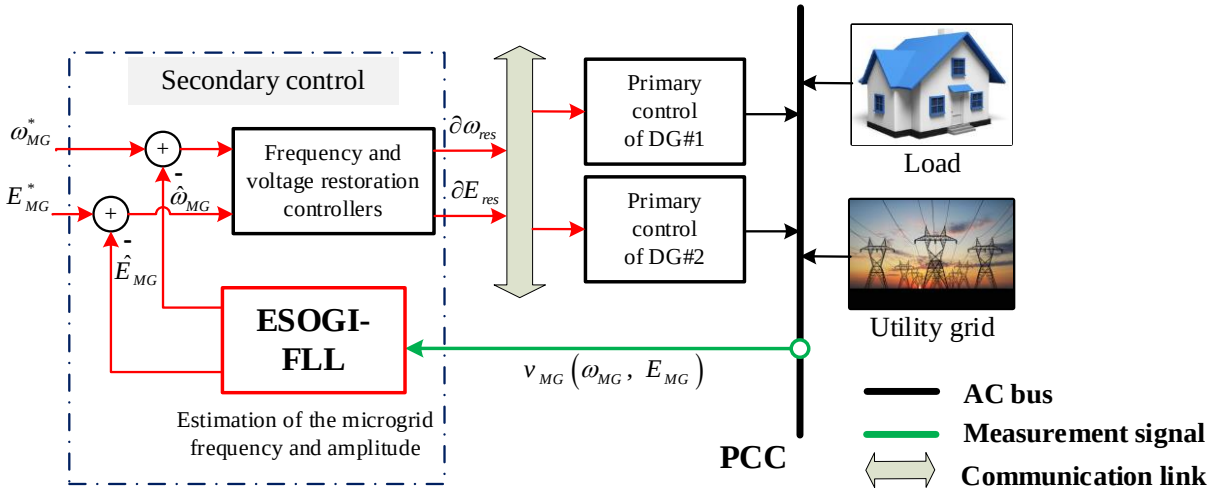

Fig. 2.1. Hierarchical control of two single-phase inverters-based islanded AC microgrid, considering primary control and secondary control based on ESOGI-FLL for parameters estimation. The MG consists of two parallel DG units, in which each DG has its own local controller, connected to a local load and the utility grid at a common AC bus.

The present chapter is organized as follows. Section 2 describes the primary and the secondary controls based on the ESOGI-FLL scheme for an autonomous single-phase AC microgrid. In Section 3, the proposed modeling approach of secondary control for frequency and voltage restoration is provided. In this section, the phasor theory-based SOGI-FLL modeling analysis is developed. Frequency and amplitude restoration modeling and tuning procedure, as well as the synchronization modeling and control design, are also presented in this section.

2.2. The proposed secondary control scheme for Single-Phase Droop-Controlled Islanded Microgrid

In **Fig. 2.2**, it shows the proposed hierarchical control scheme for two parallel-connected single-phase inverters, forming an islanded AC MG. As depicted in **Fig. 2.2**, the power inverters-based DGs share the same AC bus through a line inductive impedance. The local load and the utility grid are also connected to this AC bus. Each DG unit consists of a voltage source inverter (VSI) fed by a DC source and associated with an LC filter allowing high-frequency content cancelation [122]. In this structure, the hierarchical control of the islanded MG is divided into two control levels: primary and secondary.

2.2.1. Primary control

The primary control adopted in this work is based on the droop control method, which is the most employed strategy for islanded AC microgrids [56], [123]. This level is strictly local and is responsible for active and reactive power-sharing between DG units without any communication.

According to **Fig. 2.2**, the primary control layer includes, ESOGI-FLL-based power calculations, droop controller, virtual impedance loop, and voltage and current control loops. The SOGI-FLL scheme is introduced to extract the orthogonal components of the output voltage and current, $v_{\alpha\beta}$ and $i_{\alpha\beta}$, of each DG unit, in order to calculate the average active and reactive powers (P and Q) by using the following expressions [124]:

$$\begin{cases} P_i = \frac{1}{2}\left(\hat{v}_{i\alpha} \times \hat{i}_{i\alpha} + \hat{v}_{i\beta} \times \hat{i}_{i\beta}\right) \\ Q_i = \frac{1}{2}\left(\hat{v}_{i\beta} \times \hat{i}_{i\alpha} - \hat{v}_{i\alpha} \times \hat{i}_{i\beta}\right) \end{cases} \tag{2.1}$$

where: i = 1, 2.

These calculated powers are used by the droop controller to generate the corresponding voltage frequency and amplitude, ω_i, and E_i, according to the droop control functions, given by the following expressions:

$$\begin{cases} \omega_i = \omega^* - mP_i + \partial\omega_{res} \\ E_i = E^* - nQ_i + \partial E_{res} \end{cases} \tag{2.2}$$

where ω^* and E^* are the frequency and amplitude references respectively, m and n are the droop control coefficients. $\partial\omega_{res}$ and ∂E_{res} are the control signals received from the secondary control level in order to compensate for frequency and amplitude deviations.

To produce the voltage reference, v_i^*, across the capacitor of the output filter, the generated sinusoidal voltage using the droop control outputs is compared to the virtual impedance voltage (v_z), as expressed by the following equation:

$$v_i^*(t) = E_i \times \sin\left(\int \omega_i dt\right) - v_{zi}(t) \tag{2.3}$$

The produced reference voltage (v_i^*) is handled by an inner multi-loop control to provide the appropriate PWM pattern for each VSI. More details about the primary control can be found in [126].

2.2.2. Secondary control

As the frequency and voltage at the PCC deviate from their nominal values due to the droop control characteristics, the secondary controller will bring them back to their rated values. The block diagram of the proposed secondary control, implemented in the MG central controller, is shown in **Fig. 2.2**. In this control level, ESOGI-FLL estimates the microgrid's frequency and amplitude, as well as the orthogonal components of both the microgrid and the utility grid. Then,

two control loops; synchronization and restoration are built up. In the synchronization stage, the extracted orthogonal components are used to compute the phase angle difference between the MG and the utility grid and pass through a proportional (P) controller to be matched. The corresponding control signal is used to update the frequency reference in the restoration control loop. In the restoration stage, the estimated frequency and amplitude ($\hat{\omega}_{MG}$, $\hat{E}_{MG}$) are compared to the desired nominal values (ω_{MG}^*, E_{MG}^*) and processed through IP controllers to produce the required adjustments for the actual frequency and amplitude. The produced control signals i.e., $\partial\omega_{res}$ and ∂E_{res}, are sent to the primary control level, via a low bandwidth communication link, to recover the desired nominal values.

The expressions of the frequency and amplitude restoration compensators based on the IP-type controller can be expressed as follow:

$$\partial\omega_{res} = \int k_{i-f}\left(\left(\omega_{MG}^{*} + \partial\omega_{syn}\right) - \omega_{MG}\right)dt - k_{p-f}\ \omega_{MG} \tag{2.4}$$

$$\partial E_{res} = \int k_{i-E}\ \left(E_{MG}^{*} - E_{MG}\right)dt - k_{p-E}\ E_{MG} \tag{2.5}$$

where $k_{p\text{-}f}$, $k_{i\text{-}f}$, and $k_{p\text{-}E}$, $k_{i\text{-}E}$ are frequency and voltage controllers' gains, respectively, $\partial\omega_{syn}$ is the synchronization control signal, which is set to zero when the grid is not present.

In order to analyze the microgrid stability and to select properly the parameters of the frequency and voltage secondary control, accurate dynamic models are developed. The proposed modeling approach to derive these models and the tuning procedure of the control parameters are presented in the next section.

2.3. Proposed Modeling Approach of the Secondary Control

The proposed modeling approach aims to obtain accurate dynamic models of the secondary control for frequency and amplitude restoration of a single-phase AC microgrid. The main idea of the proposed approach is that the frequency and amplitude estimates dynamics of ESOGI-FLL, which should be derived, are exploited in the secondary control modeling. As depicted in **Fig. 2.3**, the restoration control model includes the models of; frequency/amplitude restoration control, communication delay, and ESOGI-FLL frequency and amplitude estimates of the secondary control stage. In addition, the models of droop control, power calculations, and the inner control loops of the primary control stage are introduced in the restoration model. Further, the restoration model includes the line impedance model that describes the frequency and amplitude changes from VSIs to the PCC.

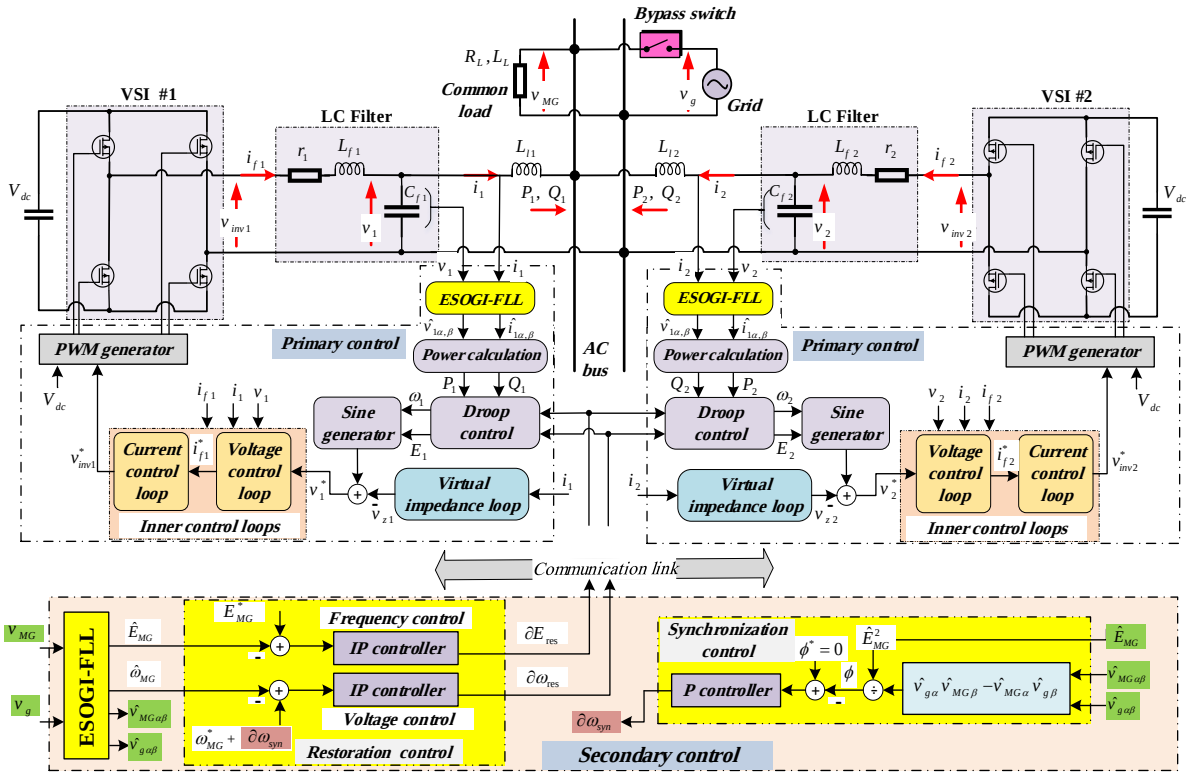

Fig. 2.2. The hierarchical control scheme for two single-phase inverters-based islanded AC microgrid.

The modeling of the ESOGI-FLL scheme is given in the subsection below, where the frequency dynamic is conducted, while a theoretical analysis in the phasor domain is developed to obtain the voltage estimate dynamics. In the second subsection, the modeling of the frequency and amplitude restoration control based on the ESOGI-FLL dynamics is developed, in which the dynamics of the inner controller is assumed to be negligible due to its fast response. Also, the line impedance model is considered negligible in the restoration modeling process. A tuning procedure based on the obtained mathematical models, as well as the synchronization modeling and design analysis are also investigated in other subsections.

2.3.1. Modeling Analysis of the ESOGI-FLL

The ESOGI-FLL scheme is an adaptive second-order filter used to estimate the key parameters of a single-phase input voltage, in which an additional loop for the estimation/rejection of the DC component is introduced [67]. The block diagram of the ESOGI-FLL structure is highlighted in **Fig. 2.4**. It consists of two main blocks; ESOGI-based quadrature signal generator (ESOGI-QSG) and FLL. The ESOGI-QSG block is responsible mainly for extracting the direct and the orthogonal voltage components that may used to calculate the voltage amplitude. While the FLL estimates the operating frequency to be fed to the ESOGI-QSG block. More details about this scheme can be found in [67].

According to **Fig. 2.4**, the closed-loop transfer functions which describe the relationship between the extracted orthogonal components ($\hat{v}_{MG\alpha}$, $\hat{v}_{MG\beta}$) and the input microgrid voltage can be given by:

$$G_{\alpha}(s)=\frac{\hat{v}_{MG\alpha}(s)}{v_{MG}(s)}=k\,\hat{\omega}_{MG}\,\frac{s}{s^{2}+k\,\hat{\omega}_{MG}\,s+\hat{\omega}_{MG}^{2}} \tag{2.6}$$

$$G_{\beta}(s)=\frac{\hat{v}_{MG\beta}(s)}{v_{MG}(s)}=\frac{k\left(\hat{\omega}_{MG}^{2}-\omega_{f}\,s\right)}{s+\omega_{f}}\,\frac{s}{s^{2}+k\,\hat{\omega}_{MG}\,s+\hat{\omega}_{MG}^{2}} \tag{2.7}$$

where *s* is the Laplace variable, $\hat{\omega}_{MG}$ and ω_f are the estimated and the additional block frequencies, respectively, and *k* is the SOGI-QSG gain, which is generally set to $1/\sqrt{2}$ [125].

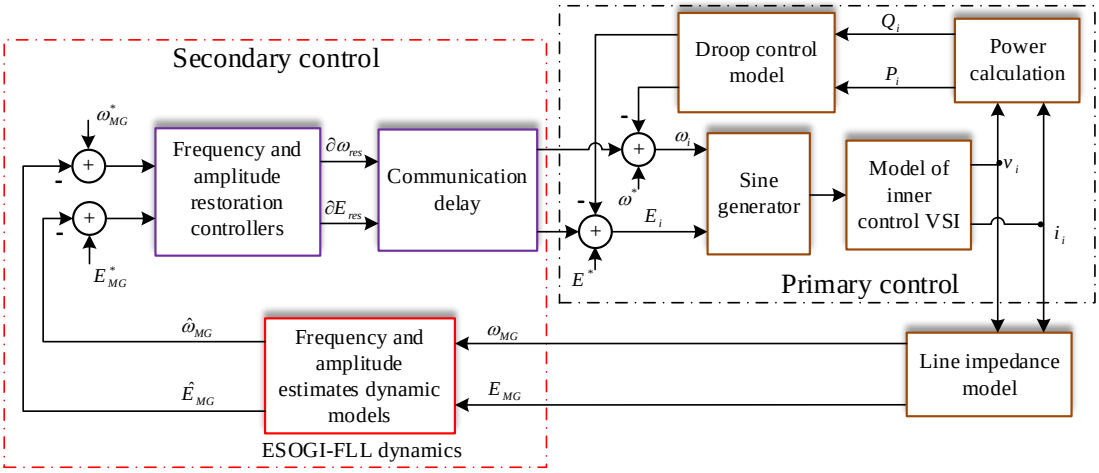

Fig. 2.3. Model of the restoration control loop based on SOGI-FLL dynamics.

It is worth noting that the assumption of no DC component inherent in the inputs of the ESOGI-FLL is considered, hence, the dynamic of FLL-based-SOGI is adopted instead of the dynamic of the FLL-based-ESOGI. Therefore, the simplified transfer function of the FLL frequency adaptation loop is expressed as follows [126]:

$$\hat{\omega}_{MG}=\frac{\Gamma}{s+\Gamma}\,\omega_{MG} \tag{2.8}$$

where ω_{MG} is the input frequency, and Γ is the FLL gain, which is related to the FLL controller gain γ; given in **Fig. 2.4**; by the following expression [126]:

$$\gamma=\frac{k\,\hat{\omega}_{MG}}{\hat{E}_{MG}^{2}}\,\Gamma \tag{2.9}$$

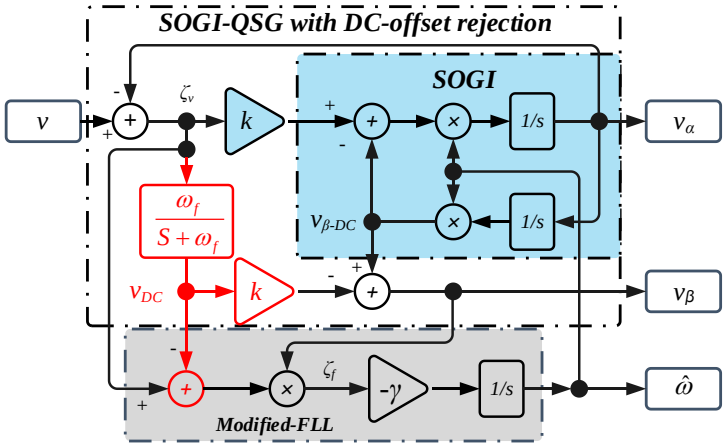

Fig. 2.4. The Enhanced SOGI-FLL (ESOGI-FLL) scheme.

As can be noted, **Eq. (2.8)** which describes the relationship between the input frequency and the estimated one, can be considered as a model for the frequency estimation dynamics. While, for the dynamics of amplitude estimate, theoretical analysis in the phasor domain is developed to derive its corresponding model. The developed analysis is given hereafter.

According to **Eq. (2.6)**, the differential equation describes the direct component $\hat{v}_{MG\alpha}$ dynamics as a function of the input voltage (v_{MG}), can be written as:

$$\ddot{\hat{v}}_{MG\alpha} + k\,\hat{\omega}_{MG}\,\dot{\hat{v}}_{MG\alpha} + \hat{\omega}_{MG}^2\,\hat{v}_{MG\alpha} = k\,\hat{\omega}_{MG}\,\dot{v}_{MG} \tag{2.10}$$

where $\dot{v}_{MG}$ is the first derivative of the input voltage, $\dot{\hat{v}}_{MG\alpha}$ and $\ddot{\hat{v}}_{MG\alpha}$, are the first and the second derivatives of the estimated direct component $\hat{v}_{MG\alpha}$, respectively.

The representation of the input voltage and the direct component voltage in the phasor domain is illustrated in **Fig. 2.5**. Accordingly, the expressions of v_{MG}, $\dot{v}_{MG}$, $\hat{v}_{MG\alpha}$, $\dot{\hat{v}}_{MG\alpha}$ and $\ddot{\hat{v}}_{MG\alpha}$ as a function of its synchronous reference frame components in the phasor domain, under frequency condition (i.e., $\hat{\omega}_{MG} = \omega_{MG}$), can be given by:

$$\begin{aligned}
\bar{v}_{MG} &= \left(v_{MG-d} + jv_{MG-q}\right)e^{j\theta} \\
\dot{\bar{v}}_{MG} &= \left[\dot{v}_{MG-d} + j\dot{v}_{MG-q} + j\,\omega_{MG}\left(v_{MG-d} + jv_{MG-q}\right)\right]e^{j\theta} \\
\bar{\hat{v}}_{MG\alpha} &= \left(\hat{v}_{MG\alpha-d} + j\hat{v}_{MG\alpha-q}\right)e^{j\theta} \\
\dot{\bar{\hat{v}}}_{MG\alpha} &= \left[\dot{\hat{v}}_{MG\alpha-d} + j\dot{\hat{v}}_{MG\alpha-q} + j\,\omega_{MG}\left(\hat{v}_{MG\alpha-d} + j\hat{v}_{MG\alpha-q}\right)\right]e^{j\theta} \\
\ddot{\bar{\hat{v}}}_{MG\alpha} &= \left[\ddot{\hat{v}}_{MG\alpha-d} + j\ddot{\hat{v}}_{MG\alpha-q} + 2j\,\omega_{MG}\left(\dot{\hat{v}}_{MG\alpha-d} + j\dot{\hat{v}}_{MG\alpha-q}\right) - \omega_{MG}^2\left(\hat{v}_{MG\alpha-d} + j\hat{v}_{MG\alpha-q}\right)\right]e^{j\theta}
\end{aligned} \tag{2.11}$$

where j is the imaginary number and θ is the phase angle between the rotating and fixed frames.

By substituting **Eq. (2.11)** into **Eq. (2.10)**, and after some mathematical manipulation, the expressions of $\hat{v}_{MG\alpha-d}$ and $\hat{v}_{MG\alpha-q}$ voltages as a function of the input voltage *dq* components (v_{MG-d} and v_{MG-q}), in the *s*-domain can be obtained as follows:

$$\begin{bmatrix} \hat{v}_{MG\alpha-d} \\ \hat{v}_{MG\alpha-q} \end{bmatrix} = k\,\omega_{MG}\,\frac{\begin{bmatrix} A & B \\ -B & A \end{bmatrix}}{\left(s^2 + k\,\omega_{MG}\,s\right)^2 + \left(k\,\omega_{MG}^2 + 2\omega_{MG}\,s\right)^2} \begin{bmatrix} v_{MG-d} \\ v_{MG-q} \end{bmatrix} \tag{2.12}$$

where:

$$\begin{cases} A = s^3 + k\,\omega_{MG}\,s^2 + 2\omega_{MG}^2\,s + k\,\omega_{MG}^3 \\ B = \omega_{MG}\,s^2 \end{cases}$$

By proposing v_{MG} as a reference in the rotating reference frame, hence, $v_{MGd} = E_{MG}$, $v_{MG-q} = 0$, $\hat{v}_{MG\alpha-d} = \hat{E}_{MG}$ and $\hat{v}_{MG\alpha-q} = 0$, **Eq. (2.12)** becomes:

$$\hat{E}_{MG} = k\,\omega_{MG}\,\frac{\left[s^3 + k\,\omega_{MG}\,s^2 + 2\omega_{MG}^2\,s + k\,\omega_{MG}^3\right]}{\left[s\left(s + k\,\omega_{MG}\right)\right]^2 + \left[\omega_{MG}\left(2s + k\,\omega_{MG}\right)\right]^2} E_{MG} \tag{2.13}$$

This transfer function describes the amplitude estimation dynamics of the ESOGI-FLL.

The obtained actual transfer function, given by **Eq. (2.13)**, is very complex, thus, for the sake of simplicity this transfer function can be approximated as a first-order transfer function based on the analysis of its poles. Hence, the poles of the fourth-order transfer function given by **Eq. (2.13)**, for $-2 \leq k \leq 2$, can be expressed as follow:

$$\begin{cases} P_{1,2} = -\dfrac{k\,\omega_{MG}}{2} - j\,\omega_{MG}\left(1 \pm \sqrt{1 - \left(\frac{k}{2}\right)^2}\right) \\ P_{3,4} = -\dfrac{k\,\omega_{MG}}{2} + j\,\omega_{MG}\left(1 \pm \sqrt{1 - \left(\frac{k}{2}\right)^2}\right) \end{cases} \tag{2.14}$$

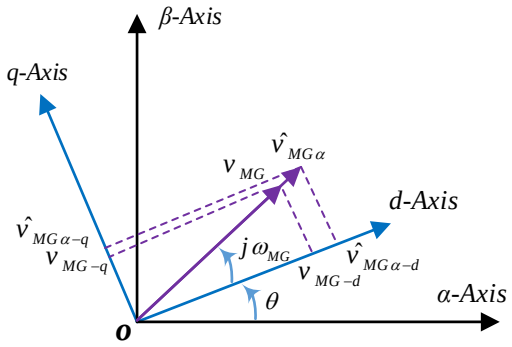

Fig. 2.5. Phasor representation of the input v_{MG} and the direct component $\hat{v}_{MG\alpha}$ voltages.

It can be noticed from these expressions that P_2 and P_4, which have the lowest imaginary part, are the dominant poles. Thus, these poles are taken for the reduced second-order transfer function. Then, the multiplication of the dominant poles (P_2 x P_4) gives a real pole, which is the pole of the simple first-order transfer function. In addition, by setting the steady-state gain to be the same, the simple model that describes the amplitude estimation dynamics of the ESOGI-FLL is given by:

$$\hat{E}_{MG} = \frac{k\,\omega_{MG}/2}{\left(s + k\,\omega_{MG}/2\right)} E_{MG} \tag{2.15}$$

To verify the accuracy of the obtained frequency and amplitude models given by **Eqs. (2.8)**, **(2.13)** and **(2.15)**, a simulation study using the MATLAB/Simulink environment is conducted. In this simulation study, the estimated frequency and amplitude by the ESOGI-FLL are compared with the ones predicted by their models for step changes in the input frequency and amplitude, respectively. The transient responses of the frequency estimate for two different values of the FLL gain Γ are illustrated in **Fig. 2.6 (a)**, while, **Fig. 2.6 (b)** shows the amplitude estimate transient responses for two distinct values of the ESOGI-FLL parameter *k*. From these figures, it can be seen that the obtained models can predict accurately the average dynamic behavior of ESOGI-FLL regarding frequency and amplitude estimation.

The obtained models are useful to be introduced in the restoration control loops for the estimation of microgrid voltage amplitude and frequency.

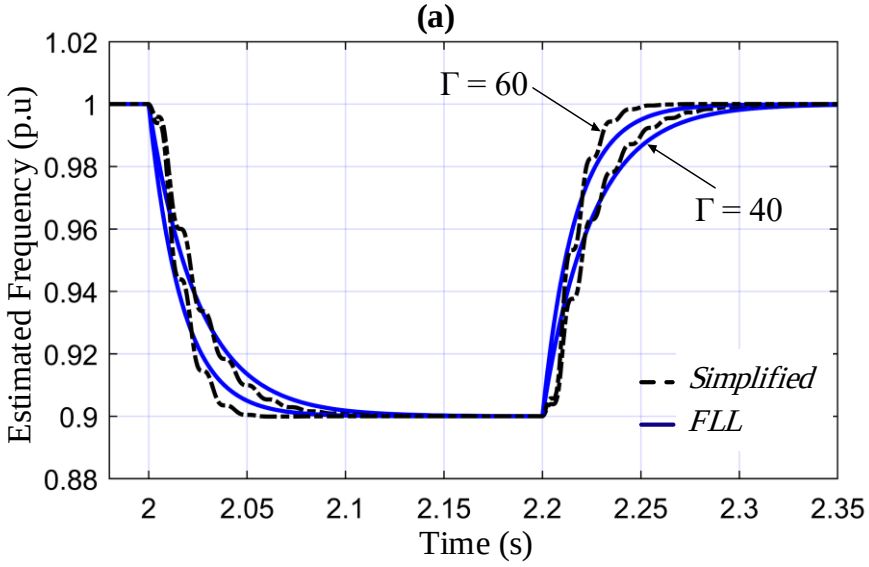

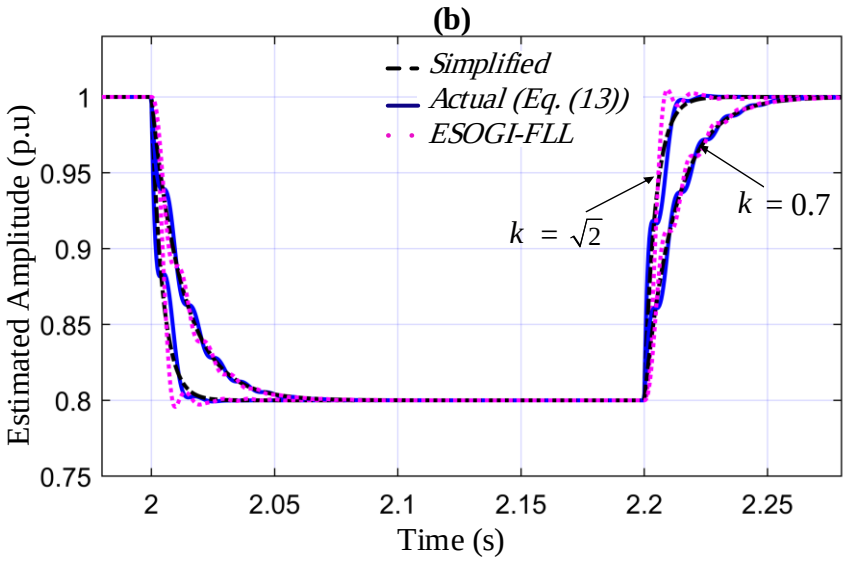

Fig. 2.6. Transient responses of: **(a)** the ESOGI-FLL and its simplified model (**Eq. (2.8)**) for $\Gamma = 40\ s^{-1}$ and $\Gamma = 60\ s^{-1}$, and **(b)** The ESOGI-FLL, and its actual model and simple model (**Eq. (2.15)**) for $k = 0.7$ and $k = \sqrt{2}$.

2.3.2. Modeling of the frequency and amplitude restoration loops

This subsection presents in detail the dynamical modeling of the frequency and amplitude restoration control loops.

2.3.2.1. Voltage control loop

The block diagram of the voltage control model based on the derived simple model, which describes the amplitude estimation dynamics of the ESOGI-FLL, is shown in **Fig. 2.7**. This block diagram is composed of: a droop control model, an IP-type controller followed by a communication line delay (G_d), and the derived simple model (H_{SOGI}) used to extract the microgrid amplitude. According to **Fig. 2.7**, the closed-loop transfer function of the voltage restoration control can be obtained as follows:

$$E_{MG} = \frac{\left[k_{i-E}/s\right]G_d(s)}{1+G_{PI-E}(s)H_{SOGI}(s)G_d(s)}E^*_{MG} - \frac{nG_{LPF}(s)}{1+G_{PI-E}(s)G_d(s)H_{SOGI}(s)}Q \quad (2.16)$$

where the transfer functions are given below:

$$G_{PI-E}(s) = \frac{k_{p-E}s + k_{i-E}}{s} \quad (2.17)$$

$$G_d(s) = \frac{1}{\tau s + 1} \quad (2.18)$$

$$G_{LPF}(s) = \frac{\omega_f}{s + \omega_f} \quad (2.19)$$

$$H_{SOGI}(s) = \frac{k\,\omega_{MG}/2}{\left(s + k\,\omega_{MG}/2\right)} \tag{2.20}$$

where τ is the time delay of the communication link, and G_{LPF} is a low pass filter considered for reactive power calculation with a cutoff frequency $\omega_f = 2\pi\times 20$.

Substituting **Eqs. (2.17)** to **(2.20)** into **Eq. (2.16)**, the complete mathematical form of the voltage control model can be expressed as follows:

$$E_{MG} = \frac{\left(k_{i-E}\,s^2 + a\,k_{i-E}\,s + c\right)}{s^3 + a\,s^2 + b\,s + c}\left[\frac{1}{s\left(\tau s + 1\right)}\right]E^*_{MG} - \frac{n\left(s^2 + a\,s + c/k_{i-E}\right)}{s^3 + a\,s^2 + b\,s + c}\left[\frac{\omega_f}{s + \omega_f}\right]Q \tag{2.21}$$

with the following parameters

$$a = k\,\omega_{MG}/2 + 1/\tau$$
$$b = k\,\omega_{MG}/2\tau\left(1 + k_{p-E}\right)$$
$$c = k_{i-E}\,k\,\omega_{MG}/2\tau$$

The obtained amplitude control model is used to analyze the stability of the MG system for control parameter variation. **Fig. 2.8 (a)** and **(b)** depict a series of root-locus diagrams, showing the evaluation of the characteristic equation eigenvalues for $k_{p\text{-}E}$ and $k_{i\text{-}E}$ variation, respectively. From these figures, it is clearly shown that the system eigenvalues move toward an unstable region when the controller proportional and integral terms increase. Hence, this increases the system oscillations and consequently, the microgrid goes to instability.

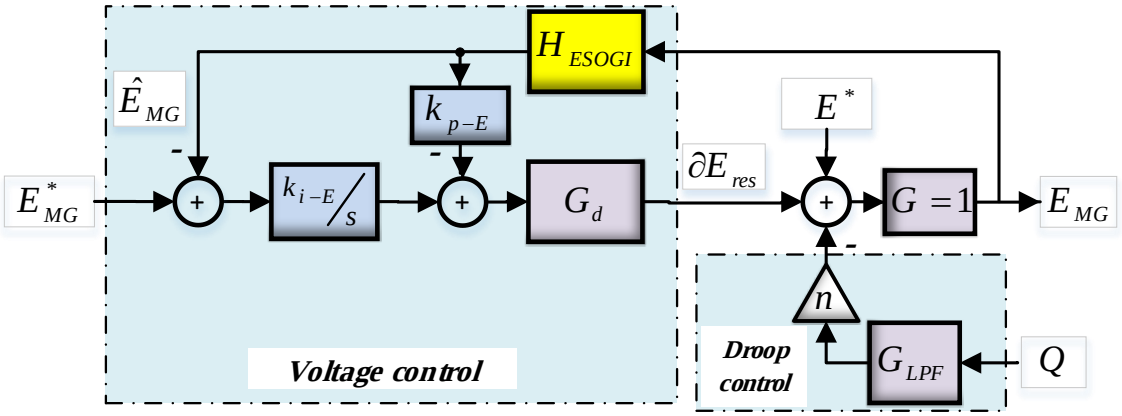

Fig. 2.7. Block diagram of the voltage secondary control model.

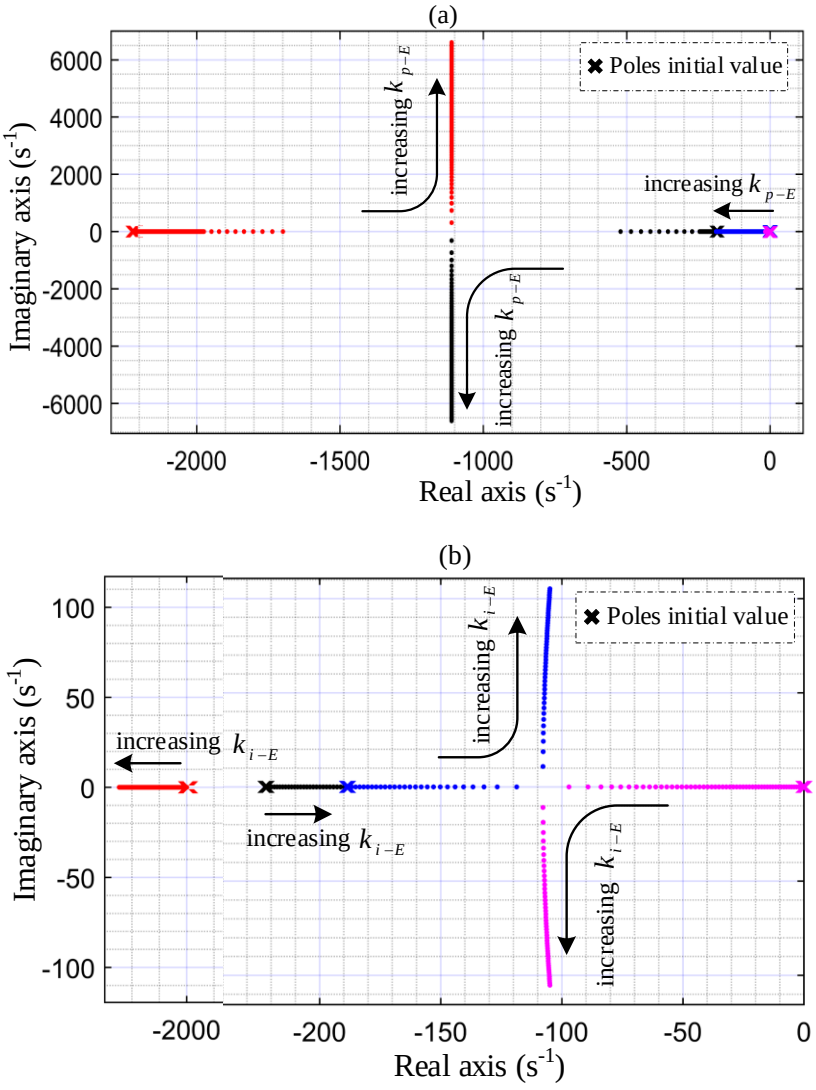

Fig. 2.8. Root-Locus plots for: **(a)** $0.0001 \leq k_{i\text{-}E} \leq 100$ and $k_{p\text{-}E} = 0.01$, and **(b)** $-1 \leq k_{p\text{-}E} \leq 100$ and $k_{i\text{-}E} = 1.5$.

2.3.2.2. Frequency control loop

Fig. 2.9 shows the block diagram of the frequency control model based on the FLL linearized model. This block consists of: a droop control model, the FLL model (H_{FLL}) used to estimate the microgrid frequency, an IP-type controller, and a communication line delay (G_d). According to this figure, the closed-loop transfer function that describes the frequency restoration dynamics can be derived as follows:

$$\omega_{MG} = \frac{\left[k_{i-f}/s\right]G_d(s)}{1+G_{PI-f}(s)G_d(s)H_{FLL}(s)}\omega^*_{MG} - \frac{mG_{LPF}(s)}{1+G_{PI-f}(s)G_d(s)H_{FLL}(s)}P \qquad (2.22)$$

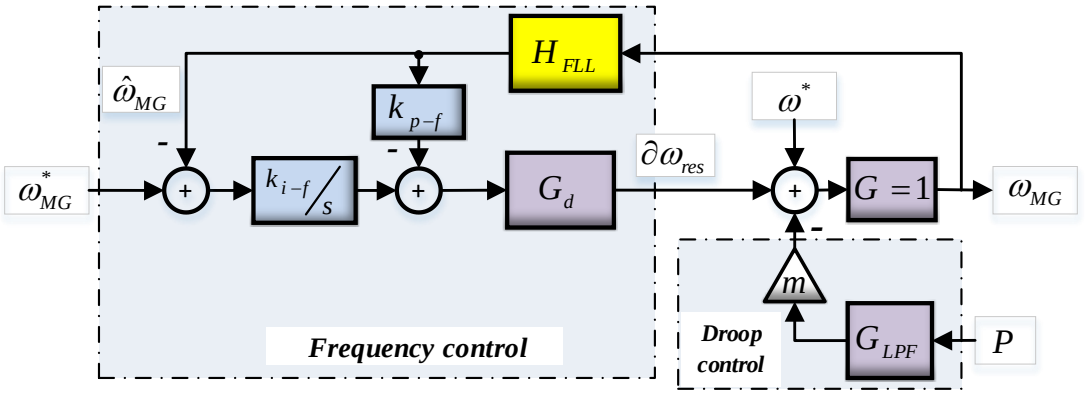

Fig. 2.9. Block diagram of the frequency secondary control model.

where the transfer functions H_{FLL} and $G_{PI\text{-}f}$ are given by:

$$G_{PI-f}(s) = \frac{k_{p-f}\,s + k_{i-f}}{s} \tag{2.23}$$

$$H_{FLL}(s) = \frac{\Gamma}{s+\Gamma} \tag{2.24}$$

By substituting the expression of these transfer functions into **Eq. (2.22)**, the small-signal model of the frequency restoration control can be obtained as follows:

$$\omega_{MG} = \frac{\left(k_{i-f}\,s^2 + a\,k_{i-f}\,s + c\right)}{s^3 + a\,s^2 + b\,s + c}\left[\frac{1}{s(\tau s+1)}\right]\omega^*_{MG} - \frac{m\left(s^2 + a\,s + c/k_{i-f}\right)}{s^3 + a\,s^2 + b\,s + c}\left[\frac{\omega_f}{s+\omega_f}\right]P \tag{2.25}$$

with the following parameters:

$$a = \left(\Gamma + 1/\tau\right)$$
$$b = \Gamma/\tau\left(1 + k_{p-f}\right)$$
$$c = k_{i-f}\,\Gamma/\tau$$

The stability analysis of the microgrid system is performed based on the extracted frequency model. The trajectory of the characteristic polynomial eigenvalues of this model as a function of the frequency control parameters, $k_{p\text{-}f}$, and $k_{i\text{-}f}$, is presented in **Fig. 2.10 (a)** and **(b)**. These figures show that when $k_{p\text{-}f}$ and $k_{i\text{-}f}$ increase the two dominant eigenvalues of the system move toward the unstable region, hence, leads the microgrid to instability issues.

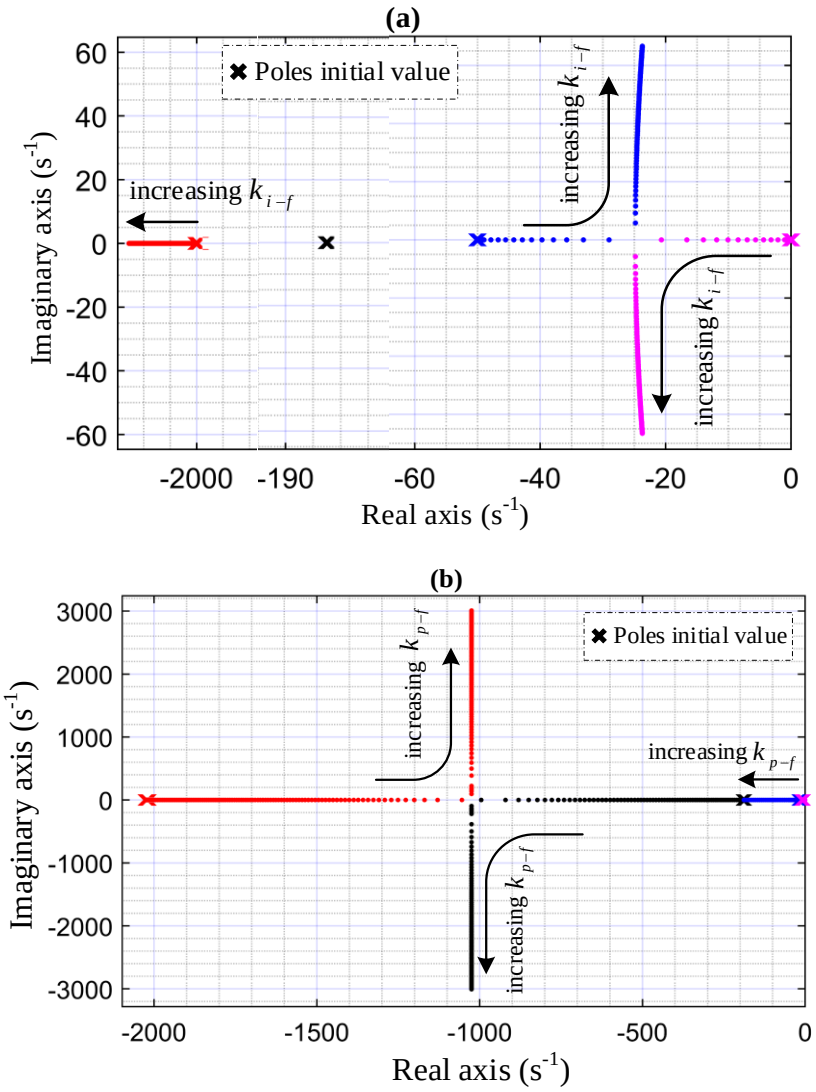

Fig. 2.10. Root-Locus plots for: **(a)** $0.0001 \leq k_{i\text{-}f} \leq 100$ and $k_{p\text{-}f} = 0.01$, and **(b)** $-0.5 \leq k_{p\text{-}f} \leq 100$ and $k_{i\text{-}f} = 2.6$.

2.4. Tuning Control Parameters

To properly select the parameters of the frequency and amplitude restoration control, the following analysis based on the obtained models is developed. According to **Eq. (2.21)** and **Eq. (2.25)**, the transfer functions relating the actual amplitude and frequency to the desired ones can be derived as follow:

$$E_{MG} = \frac{\left(k_{i-E}\, s^2 + a\, k_{i-E}\, s + c\right)}{s^3 + a\, s^2 + b\, s + c}\left[\frac{1}{s\left(\tau s + 1\right)}\right] E^*_{MG} \tag{2.26}$$

$$\omega_{MG} = \frac{\left(k_{i-f}\, s^2 + a\, k_{i-f}\, s + c\right)}{s^3 + a\, s^2 + b\, s + c}\left[\frac{1}{s\left(\tau s + 1\right)}\right] \omega^*_{MG} \tag{2.27}$$

By assuming that the time delay is negligible regarding ESOGI-FLL estimation time and that

the perturbation amount of the droop model is also negligible, hence **Eq. (2.26)** and **Eq. (2.27)** becomes:

$$E_{MG} = \frac{k_{i-E}\, k\,\omega_{MG}/2}{s^2 + k\,\omega_{MG}/2\,(1+k_{p-E})s + k_{i-E}\, k\,\omega_{MG}/2} E^*_{MG} \tag{2.28}$$

$$\omega_{MG} = \frac{\Gamma k_{i-f}}{s^2 + \Gamma(1+k_{p-f})s + k_{i-f}\Gamma}\omega^*_{MG} \tag{2.29}$$

The characteristic polynomials of these transfer functions are:

$$s^2 + \underbrace{k\,\omega_{MG}/2\,(1+k_{p-E})}_{2\zeta_E\ \omega_{n-E}} s + \underbrace{k_{i-E}\, k\,\omega_{MG}/2}_{\omega^2_{n-E}} = 0 \tag{2.30}$$

$$s^2 + \underbrace{k\,\omega_{MG}/2\,(1+k_{p-E})}_{2\zeta_f\ \omega_{n-f}} s + \underbrace{k_{i-E}\, k\,\omega_{MG}/2}_{\omega^2_{n-f}} = 0 \tag{2.31}$$

where ζ and ω_n stand for the damping factor and the natural frequency, respectively.

Accordingly, the expressions of the proportional and integral gains of both amplitude and frequency controllers can be expressed as follow:

$$\begin{cases} k_{p-E} = \dfrac{4\zeta_E\ \omega_{n-E}}{k\,\omega_{MG}} - 1 \\ k_{i-E} = \dfrac{2\omega^2_{n-E}}{k\,\omega_{MG}} \end{cases} \tag{2.32}$$

$$\begin{cases} k_{p-f} = \dfrac{2\zeta_f\ \omega_{n-f}}{\Gamma} - 1 \\ k_{i-f} = \dfrac{2\omega^2_n}{\Gamma} \end{cases} \tag{2.33}$$

Based on the control design concept for deadbeat response proposed in [127], and by selecting a proper value of the damping factor ζ that can ensure, in an optimum way, a tradeoff between overshoot and settling time, the corresponding natural frequency can be determinate relatively to the desired settling time of the control response. Once ζ and ω_n are chosen, the controller parameters can be computed using **Eqs. (2.32)** and **(2.33)**. It is worth mentioning that the value of the damping factor ζ is chosen according to the analysis based on root-locus plots given in **Figs. 2.8** to **2.10**, then, verified according to the transient response of the obtained models.

In order to evaluate the robustness of the designed frequency and amplitude controllers for system parameters variation and under load disturbances, a simulation study in MATLAB/Simulink is carried out. In this study, the transient performances of the obtained

secondary control models in response to step changes in the frequency and amplitude references and active and reactive powers are evaluated, considering three distinct values for the time delay (τ). The obtained results are depicted in **Fig. 2.11 (a)** and **(b)**, and shown the transient response of the frequency and amplitude restoration control, respectively. It can be observed that the proposed control approach is robust against time delay variation and load changes, as amplitude and frequency of the MG are properly restored.

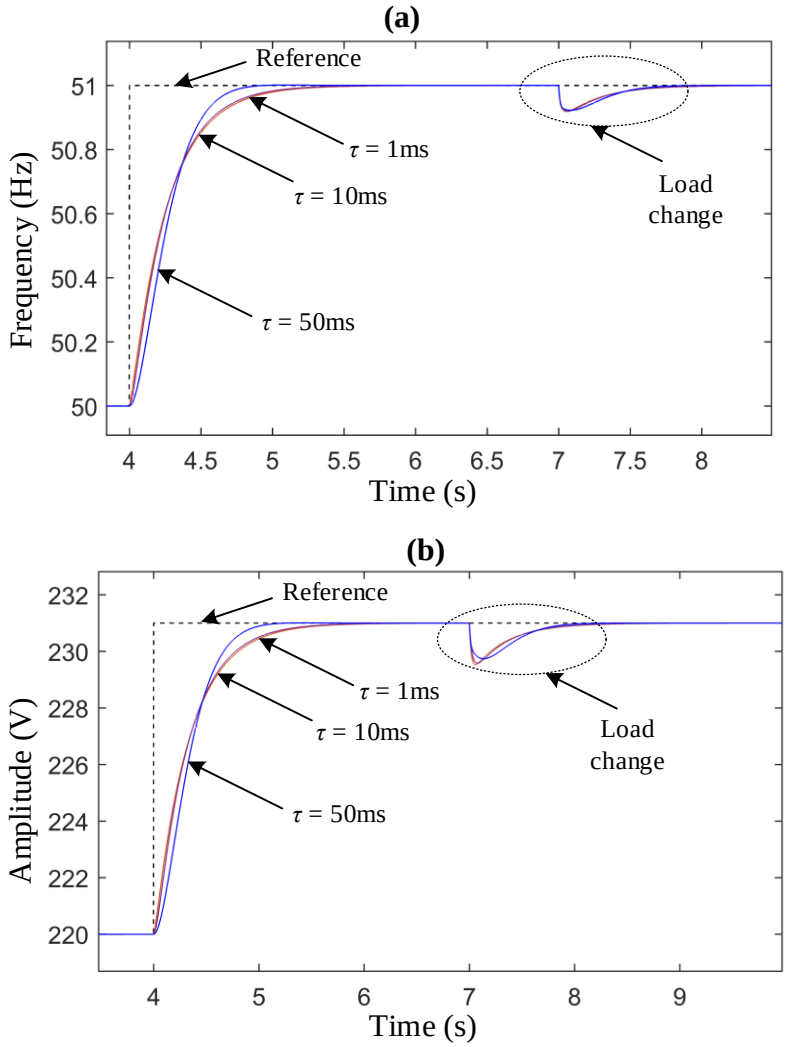

Fig. 2.11. Transient responses of the secondary control models for **(a)** frequency, and **(b)** amplitude restoration, with three different values of the time delay (τ).

2.5. Synchronization control loop

In this subsection, the modeling and control design of the synchronization control loop are presented. The synchronization control scheme is given in **Fig. 2.2**, and it is included within the scope of the secondary control layer. According to **Fig. 2.2**, the expression of the proposed synchronization controller can be given by:

$$\partial\omega_{\text{syn}} = k_{p-\phi}\left(\phi^{*} - \phi\right) \tag{2.34}$$

where $k_{p\text{-}\phi}$ is the proportional gain term of the synchronization controller, ϕ^* is the phase angle reference, which is set to zero, and ϕ is the phase difference between the MG and the main gird.

Actually, the expression of the phase angle difference ϕ can be obtained based on the cross product mathematical formulas. According to the first formula, the cross product of the microgrid and the main grid voltages can be defined by [128]:

$$\left\| \vec{v}_g \times \vec{v}_{MG} \right\| = \hat{V}_g \hat{E}_{MG} \sin(\phi) \tag{2.35}$$

where $\hat{V}_g$ is the estimated voltage amplitude of the main grid.

The second formula of the cross product in the stationary reference frame can be expressed as:

$$\left\| \vec{v}_g \wedge \vec{v}_{MG} \right\| = \hat{v}_{g\alpha} \quad \hat{v}_{MG\beta} - \hat{v}_{MG\alpha} \quad \hat{v}_{g\beta} \tag{2.36}$$

where the $v_{MG\alpha\beta}$ and $v_{g\alpha\beta}$ are the extracted orthogonal components of the microgrid and the main grid voltages.

Subtracting **Eq. (2.35)** from **Eq. (2.36)**, and considering small phase angle variation, i.e., $\sin(\phi) \approx \phi$, the expression of the phase angle difference can be found as follows:

$$\phi = \frac{\hat{v}_{g\alpha}\hat{v}_{MG\beta} - \hat{v}_{MG\alpha}\hat{v}_{g\beta}}{\hat{V}_g \ \hat{E}_{MG}} = \frac{\hat{v}_{g\alpha}\hat{v}_{MG\beta} - \hat{v}_{MG\alpha}\hat{v}_{g\beta}}{\hat{E}_{MG}^2} \tag{2.37}$$

Consequently, **Eq. (2.34)** becomes:

$$\partial\omega_{\text{syn}} = - \ k_{p-\phi} \frac{\hat{v}_{g\alpha}\hat{v}_{MG\beta} - \hat{v}_{MG\alpha}\hat{v}_{\beta-MG}}{\hat{E}_{MG}^2} \tag{2.38}$$

To adjust the parameter ($k_{p\text{-}\phi}$) of the synchronization controller, a model is developed as can be seen in **Fig. 2.12**. This figure depicts the block diagram of the phase angle control, which includes the plant model ($G_\phi(s)$) and the synchronization control model. According to this figure, the closed-loop transfer function of the phase angle control can be derived as follows:

$$\phi = \frac{k_{p-\phi} G_\phi(s)}{1 + k_{p-\phi} G_\phi(s)} \phi^* \tag{2.39}$$

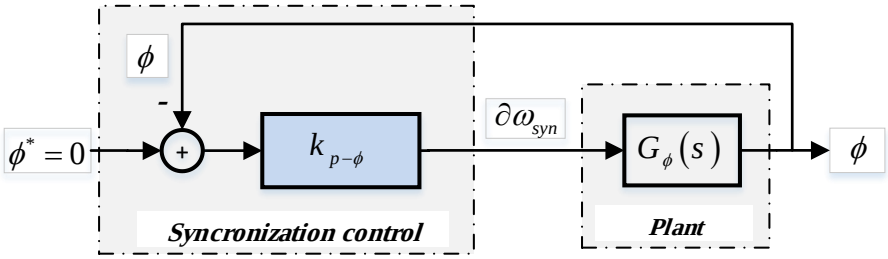

Fig. 2.12. Block diagram of the synchronization feedback control.

where the expression of the plant model G_ϕ(s) is given by:

$$G_\phi(s) = \frac{1}{s} \tag{2.40}$$

Substituting **Eq. (2.40)** into **Eq. (2.39)**, the closed-loop model of the phase angle control can be obtained as follows:

$$\phi = \frac{k_{p-\phi}}{s + k_{p-\phi}} \phi^* \tag{2.41}$$

By applying the first-order control design concept to the transfer function given by **Eq. (2.41)**, the proportional gain $k_{p\text{-}\phi}$ can be calculated using the following expression:

$$k_{p-\phi} = -\frac{1}{T_s} \ln(0.02) \tag{2.42}$$

where T_s is the desired settling time.

2.6. Conclusion

In this chapter, a design of the scheme and a new approach to obtain accurate models of the secondary control based on the ESOGI-FLL for a single-phase microgrid were proposed. The proposed modeling approach exploits the dynamics of the ESOGI-FLL scheme that has served to achieve precise stability analysis of the MG and the proper tuning of the secondary control parameters. A comprehensive guideline for the proper selection of the secondary controllers' parameters was provided. The robustness of the designed control loops to system parameter variations was assessed. The modeling and the design analysis of the synchronization control loop were also carried out, in this chapter, in order to enable the transition from the islanded mode to grid-connected mode. The validation of the proposed control approach will be presented in chapter 4, through simulations and experiments for single-phase parallel-connected VSIs forming islanded microgrid.

Chapter 3:

Design, Modeling, and Tuning of Power Flow Control for Single-Phase Grid-tied VSIs-based MG

This chapter is a summary of the second contribution of this thesis to designing, modeling, analyzing, and tuning tertiary control based on the ESOGI-FLL scheme intended for single-phase VSI based droop-controlled microgrid during the grid-connected operating mode.

3.1. Introduction

Nowadays, microgrids have become an interesting concept for integrating renewable and distributed energy resources and energy storage devices [129], [130]. In addition, MG systems have the ability to work in both autonomous and grid-connected modes of operation. This concept makes the final user able to generate, store, control, and manage part of the energy that will be consumed [40]. To achieve these global tasks, the hierarchical control that includes primary, secondary, and tertiary control levels have been adopted to control and manage the microgrid energy in grid-connected and islanded modes [38, 39], [131]. In islanded operating mode, the primary based on the droop control strategy and the secondary control layers are in charge of regulating the frequency and amplitude of the DGs voltages in order to share the load power demand and proceeding microgrid resynchronization with the main grid as well. While in grid-connected mode, the tertiary control layer; which is our focus; is proposed to bidirectionally control the power flow when the microgrid is connected to the main grid. The active and reactive power flow can be managed by adjusting the frequency and amplitude of the DG units' voltages in the MG according to the load changes at the PCC [39]. Such a tertiary control scheme requires maintaining the stability of the overall system under various disturbances and ensuring optimal power flow between MG and the main grid. To this end, optimal design, as well as effective and accurate modeling, analysis, and parameter tuning of the tertiary control, are essential and challenging issues.

Important research efforts have been made in the literature for designing control schemes, analyzing, and developing mathematical models of power flow control for microgrid during grid-connected operation [94]-[96], [132 – 134]. However, the amount of this literature is considerably reduced if one considers the special case of single-phase grid-connected VSCs for the droop-controlled microgrids. For instance, the design of the tertiary control scheme for microgrids has generally introduced the PLL technique to estimate the required key parameters (frequency, amplitude, and phase) [93], [96], [132]. These parameters are exploited at the tertiary level for the detection of the grid back and the island mode (grid faults), as well as for the synchronization process at the secondary level. The active and reactive powers (P and Q) are another parameter that is needed at the tertiary level and can be calculated based on the measured grid current and voltage in three-phase systems. Whereas, in single-phase applications, an additional block is

required for generating the voltage orthogonal component and, hence, computing *P* and *Q* after using LPF [135]. As it is well-known, the use of LPF may slow down the velocity of the system's transient response. In addition, the control schemes based on conventional PLLs are suffering from implementation complexity and high sensitivity to the grid perturbations and DC component disturbance [135]. A solution that can replace the PLL with LPF is the SOGI-FLL scheme, which has been adopted recently in microgrid control systems for estimating the voltage key parameter [136]. The SOGI-FLL can extract the orthogonal component of a single signal and avoid the need for an additional block in the tertiary control. Furthermore, enhanced SOGI-FLL based-control structures have shown their efficiency in terms of computational burdens and proper estimation of the expected variables with high harmonics and DC component rejection capabilities [92]. Despite these benefits, the integration of the ESOGI-FLL scheme into the tertiary control cannot be found in the existing literature.

On the other hand, as the LPF filter has been included in the power flow control scheme, its dynamic has been introduced in the modeling of microgrid-based control. For instance, the authors in [132] have developed a simple small-signal model of the active and reactive power flow control for single-phase droop-controlled paralleled VSIs in grid-connected MG. In this model, the transfer function of the LPF has been introduced for describing the power calculation dynamics, whereas the tuning of the control parameters has been not considered in this paper. The stability analysis of consensus-based tertiary control has been investigated in paper [137]. Furthermore, the power flow control modeling of parallel-connected VSIs forming islanded MG has been adopted, and the system stability has been investigated, in [93] and [138]. Similarly, the dynamics of the power calculation have been presented by the LPF transfer function. In papers [97], [139], and [140], the power flow state-space models have been developed to investigate microgrid stability. The same concept has been adopted to describe power calculation dynamics. A dynamic phasor modeling approach has been proposed to derive the DG units-based MG small-signal models in [95], [141], and [142]. Brief stability analysis and tuning guidelines are presented in these papers. Here, the transfer function of the LPF is also used for expressing the dynamics of the active and reactive power calculations. The adopted concept may be valid for three-phase systems where the active and reactive power can be directly calculated, but in single-phase, there is need for an additional block for the generation of the orthogonal component, as we mentioned above, therefore, its dynamic should be introduced in the power flow control modeling. As a result, the accuracy of the derived models may be questionable, and the stability of the system should be compromised. Furthermore, one can notice that a comprehensive and effective tuning guideline of the tertiary controller parameters cannot be found in the existing literature review.

To overcome the aforementioned issues, the control structure of the tertiary control based on the ESOGI-FLL scheme for single-phase droop-operated microgrid is proposed. This proposed scheme can improve the performance of the power flow control in view of the provided quantities' quality and computation time burdens. In addition, an accurate dynamic phasor modeling approach and an effective tuning procedure are proposed for a droop-controlled microgrid connected to the main grid incorporating the tertiary controller, in which in-depth MG system stability evaluation and performance enhancement are considered. First, models that describe the active and reactive power calculation dynamics based on ESOGI-FLL is derived by exploiting the dynamics phasor concept. Then, the open-loop model in the state-space form of power flow between a single-phase VSI and the main grid is developed. The accuracy of the derived models is validated based on simulation studies in the MATLAB environment. The closed-loop model of a droop-controller single-phase VSI interfaced main grid including the designed tertiary controller is derived. Using these models, stability analysis and effective tuning guidelines of the single-phase microgrid incorporating tertiary controller are investigated for the proper selection of the control parameters. Also, the robustness assessment of the microgrid system to load disturbances and system parameters variation is carried out using the obtained closed-loop model.

This chapter is organized as follows. In section II, the proposed design and operating principle of the tertiary control layer based on the ESOGI-FLL method for a single-phase grid-connected VSI is given. The proposed dynamic phasor modeling approach of the microgrid power flow is presented in section III. In this section, first, the state-space models of the ESOGI-FLL based-power calculations and the open-loop power flow are derived and validated. Secondly, the closed-loop dynamic model of the tertiary control loop for a VSI connected to the main grid is obtained. MG stability and a control tuning, as well as robustness assessment of the designed controller, are adopted in section IV. Section V summarizes the main conclusions of the present chapter.

3.2. The proposed tertiary control scheme for single-phase MG

As aforementioned, the microgrid can operate autonomously or connected to the main grid. In grid-tied mode, power generation in the microgrid may exceed the local power demand, particularly when the maximum power is to be absorbed from renewable energy sources (energy storage devices). Thus, the excess active and reactive powers are injected into the main AC grid through an inverter and a line impedance. On the other side, when the delivered power in the microgrid is not sufficient for the load demand, the main grid provides power to satisfy the need. The tertiary control level, as a centralized controller, is designed to manage this bidirectional power exchange by controlling the flow of the active and reactive powers between the DG units

based-microgrid and the main grid at the PCC [40]. This power flow can be managed by adjusting the amplitude and frequency of DG units' voltages. Note that this control level has the slowest dynamic response compared to the low-level secondary and primary controls.

Fig. 3.1 shows the structure of a single-phase microgrid in grid-tied operation, including the power stage and the proposed tertiary controller based on the ESOGI-FLL scheme. The load, in this case, is connected to the AC common bus, in which the load power demand is participated equally between the DG units (see **Fig. 3.3**). According to **Fig. 3.1**, the proposed tertiary control scheme includes; an ESOGI-FLL based-power calculation block and a PI controller. The ESOGI-FLL is involved to estimate the direct and quadrature components of the grid voltage and current. These estimated components are used to calculate the active and reactive power of the grid using equation (2.10), given in chapter II. The PI controller adjusts the active and reactive power references of the microgrid according to the corresponding calculated powers P_g and Q_g. Then, the provided frequency and the amplitude voltage amounts in the tertiary control are broadcasted to the secondary control level as updated references of the microgrid, f_{MG}, and E_{MG}.

The expression of the active and reactive power flow control can be obtained as follows [40]:

$$\begin{aligned} \omega_{MG}^{*} &= k_{p-P} \cdot \left(P_g^{*} - P_g \right) + k_{i-P} \cdot \int \left(P_g^{*} - P_g \right) \cdot dt \\ E_{MG}^{*} &= k_{p-Q} \cdot \left(Q_g^{*} - Q_g \right) + k_{i-Q} \cdot \int \left(Q_g^{*} - Q_g \right) \cdot dt \end{aligned} \tag{3.1}$$

in which $k_{p\text{-}P}$, $k_{i\text{-}P}$, $k_{p\text{-}Q}$, and $k_{i\text{-}Q}$ are the control parameters of the tertiary control compensator. $P_g^{*}$and Q_g^{*} are the active and reactive power references of the microgrid (* refers to the reference value of a variable). In island mode, the frequency and amplitude references of the microgrid are set to the nominal values and the active and reactive power are equal to zero ($P_g^{*} = 0$, $Q_g^{*} = 0$). In addition, it is worth noting that the center manager is the one, which is allocated the required grid power references to the DGs units according to the load power demand [131].

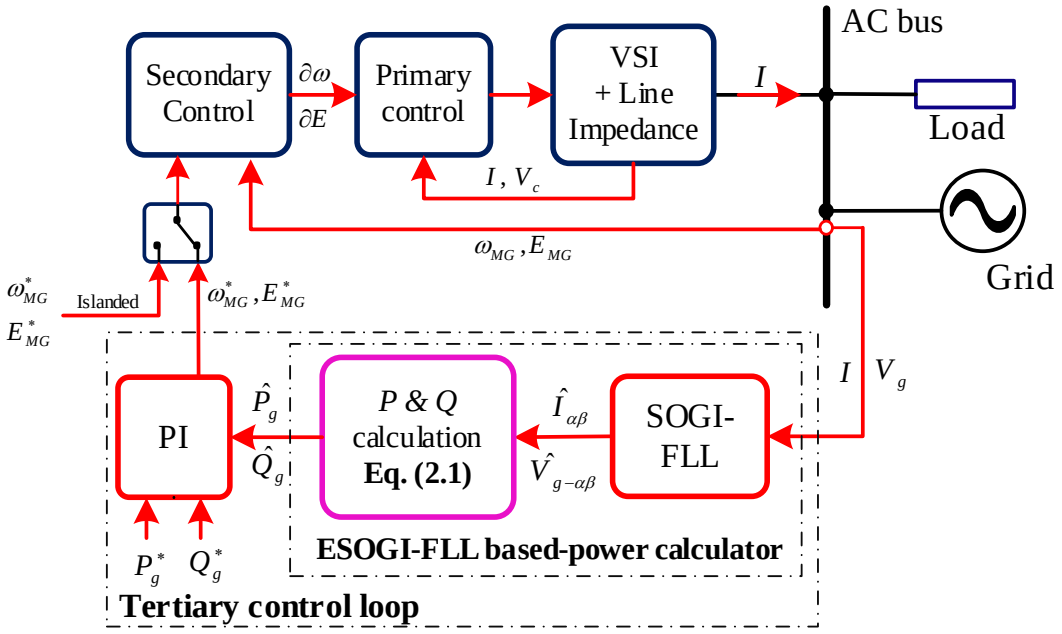

Fig. 3.1. The tertiary control scheme based on ESOGI-FLL for a single-phase microgrid operating in grid-tied mode.

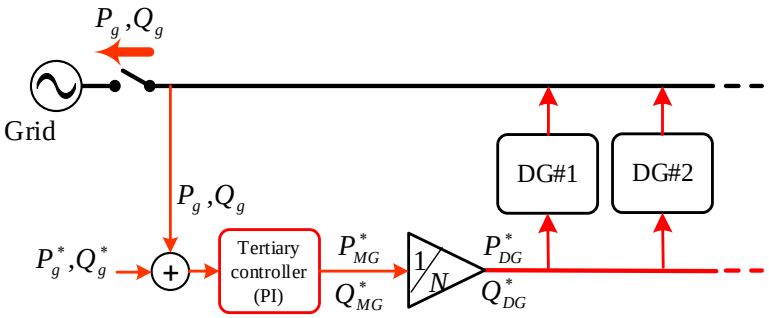

Fig. 3.2. Simplified block diagram of the power flow control between the grid and the DGs-based-MG.

The characteristic of the tertiary control level is described in **Fig. 3.3**, in which depending on the sign of P_g^* and Q_g^*, the active and reactive power flows can be exported or imported independently. As seen, the frequency and amplitude of the grid ($f_g = f_{MG}^*$ and $E_g = E_{MG}^*$) are constants, so that it is represented by horizontal lines. Hence, the amounts of the active and reactive power exchanged between the microgrid and the main grid are determined by the intersection of the droop characteristics of the microgrid and the horizontal lines of the main grid. as a result, the power flows can be controlled by adjusting the microgrid frequency and amplitude references, f_{MG}^* and E_{MG}^* as following:

- If $f_{MG} < f_g$; then the active power amount $P_g < 0$, and the microgrid generates P to the main grid
- While if $f_{MG} > f_g$; then $P_g > 0$, Hence, the microgrid absorbs P from the grid.

The frequency of the microgrid will be determined by the grid so that this action will change the power angle. A similar procedure can be considered for the reactive power Q_g according to the microgrid amplitude reference f^*_{MG}. Besides, by setting $k_{i\text{-}P}$ and $k_{i\text{-}Q}$ to zero in (1), the tertiary control will act as a primary control of the microgrid.

It is worth noting that, when the islanded mode occurs the microgrid is disconnected from the grid for safety and the tertiary control is disabled.

To study the stability of the designed grid-connected microgrid system incorporating tertiary control as well as determinate properly the parameter of the tertiary controller, a mathematical model is needed. Thus, in the next section, an accurate modeling approach based on dynamic phasor is proposed to extract the expected model.

3.3. Proposed Modeling approach for the power flow control

This section aims at developing an accurate small-signal model of a power flow control-based droop-controlled single-phase microgrid by using the dynamic phasor concept. The developed models are able to handle and to evaluate the dynamic behavior active and reactive power of the grid-connected DG units incorporating the tertiary control scheme.

It is worth mentioning that to simplify the analysis, the assumption of no DC component present in the input voltage is considered, hence, the dynamics of the SOGI-FLL scheme are adopted in the becomes mathematical development, instead of the ESOGI-FLL dynamics.

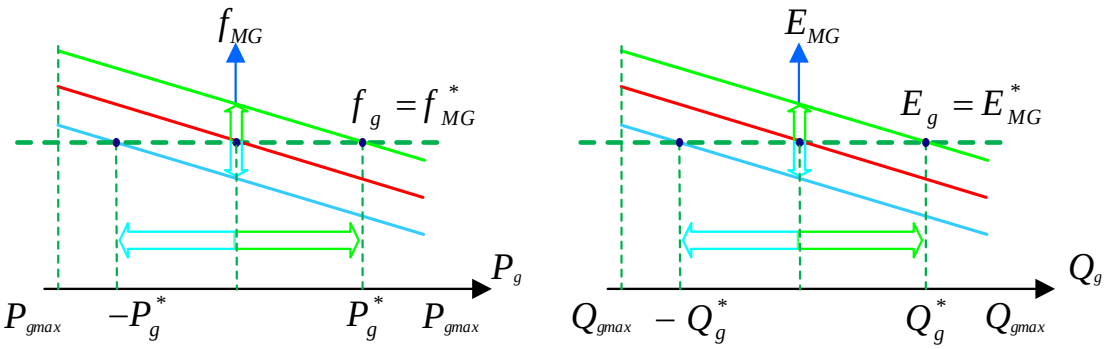

Fig. 3.3. $f_{MG} - P_g$ and $E_{MG} - Q_g$ tertiary control characteristics.

3.3.1. Proposed dynamic phasor modeling based on SOGI-FLL dynamics of the MG power flow

The dynamic phasor concept has been adopted recently for the modeling of the microgrid-based on power converters. For instance, the researchers in [95], [141], and [142] have proposed an approach based on dynamic phasors to reach precise models of the droop-controlled inverters interfaced microgrid. However, in these approaches, a transfer function of a low-pass filter is considered to describe the power calculation dynamics. It is worth mentioning that, this is the adopted concept in all the existing modeling purposes for VSI based-microgrid systems. In fact, this first-order transfer function cannot describe accurately the dynamics of the power calculation, especially for single-phase microgrids. As a result, the obtained models small-signal, unfortunately, cannot perfectly predict the system instabilities.

To overcome this problem, the development of a dynamic phasor modeling approach for grid-connected operation of inverter-based microgrids by exploiting the SOGI-FLL dynamics is presented in this work. The schematic diagram of the proposed model for a single-phase grid-connected microgrid included tertiary control based on SOGI-FLL dynamics is illustrated in **Fig. 3.4**. According to this figure, the power flow model includes the models of; tertiary control, line impedance describes the frequency and amplitude changes of the microgrid, and the SOGI-FLL-based power calculation dynamics. In addition, it integrates the models of the secondary control, primary control, and VSI circuit which are considered negligible. The detailed mathematical analysis of each block, as well as the dynamic phasor modeling approach for achieving the expected small-signal model of the overall system, are presented in subsections below.

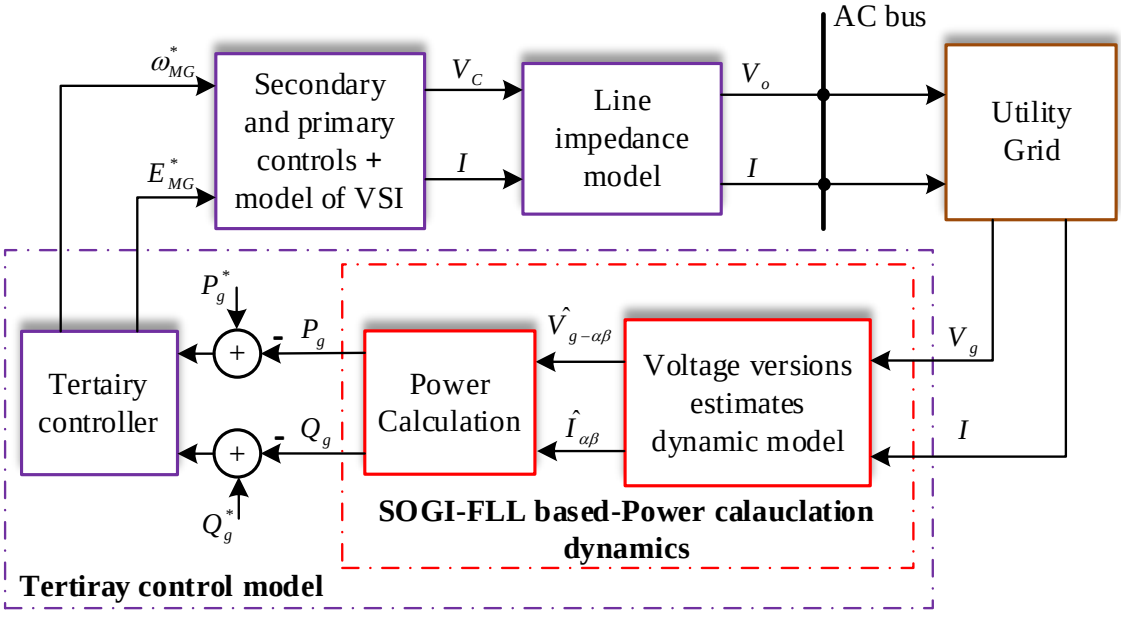

Fig. 3.4. Proposed modeling approach of grid-connected VSI including the tertiary control.

In the grid-tied mode, the AC microgrid is connected to the main utility grid through a tie line impedance at the point of common coupling (PCC) as shown in **Fig. 3.5**, in which the MG is represented by only one DG unit. The VSI is modeled as an AC source with the voltage *E (t)*, where the switching ripples and high-frequency harmonics are assumed neglected. In addition, we assume that the utility AC grid voltage is $V_g \angle 0$.

In this mode, there is a power flow between the DG unit and the main grid. From the circuit shown in **Fig. 3.5**, the complex power, *S*, flowing from the DG unit to the common AC bus can be defined as [105]:

$$S = V_g \times I^* = V_g \angle 0 \left(\frac{V_g \angle 0 - E \angle \varphi}{Z \angle \delta} \right) = P + jQ \tag{3.1}$$

where (*) denotes the complex conjugate operator.

In order to derive the mathematical formulation of both active and reactive powers, the expression of the line impedance current should be determined first.

3.3.1.1. The Expression of the line impedance current (*I*):

To achieve a mathematical formulation that describes the relationship between the inputs, grid and inverter voltage, and phase angle, and the output current of the line impedance. The following analyses based on phasor dynamics for extracting the expression of the line impedance current are demonstrated.

According to the electrical circuit given in **Fig. 3.5**, the following mathematical expression can be derived:

$$E(t) = V_l(t) + V_g(t) = r_l\, I(t) + L_l \frac{dI(t)}{dt} + V_g(t) \tag{3.2}$$

where r_l and L_l are the line impedance resistive and inductive components, respectively.

In the phasor domain, a sinusoidal voltage $V(t) = A.\cos(\omega t + \theta)$; with amplitude (*A*), angular frequency (ω), and initial phase (θ); can be represented by a combination of complex vectors (phasors) as follows [143] :

$$V(t) = \mathrm{Re}\left\{ A \cdot e^{j(\omega t + \theta)} \right\} = \mathrm{Re}\left\{ V_{dq} \cdot e^{j\omega t} \right\} \tag{3.3}$$

where V_{dq} is the resulted vector in the rotating (*dq*) reference frame, given by:

$$V_{dq} = A e^{j\theta} \tag{3.4}$$

and *j* denotes the complex number operator (imaginary).

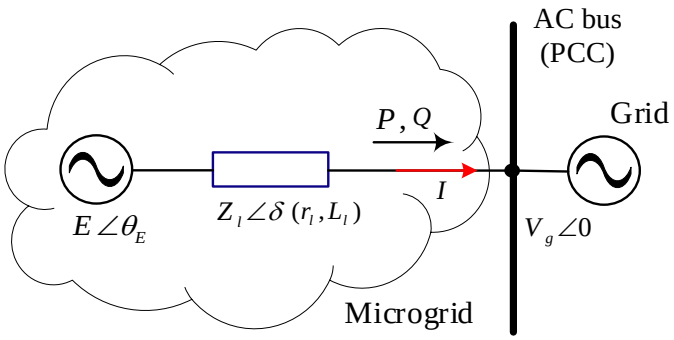

Fig. 3.5. The equivalent circuit of single-phase VSI connected to the main AC grid.

Based on **Eq. (3.3)**, the time derivative of the dynamic phasor *V (t)* produces another phasor, which can be expressed as follows:

$$\frac{d}{dt}V(t)=\mathrm{Re}\left\{\frac{d}{dt}(V_{dq}\cdot e^{j\omega t})\right\}=\mathrm{Re}\left\{\frac{dV_{dq}}{dt}\cdot e^{j\omega t}+j\omega\cdot V_{dq}\cdot e^{j\omega t}\right\} \tag{3.5}$$

Consequently, the expression related the line impedance voltage to the corresponding current can be given by:

$$V_l(t)=L_l\frac{dI(t)}{dt}=\mathrm{Re}\left\{\left(L_l\frac{dI_{dq}}{dt}+j\omega L_l\cdot I_{dq}\right)e^{j\omega t}\right\} \tag{3.6}$$

Based on **Eqs. (3.3)** and **(3.6)**, equation **(3.2)** can be rewritten in *dq* reference frame, after some mathematical manipulation, as follows:

$$E_{dq}=r_l\cdot I_{dq}+L_l\frac{dI_{dq}}{dt}+j\omega L_l\cdot I_{dq}+V_{g-dq} \tag{3.7}$$

Hence, the expression of the output current of the line impedance in the *s*-domain; where *s* is the Laplace operator; can be described by:

$$I_{dq}(s)=\frac{E_{dq}(s)-V_{g-dq}(s)}{L_l\cdot s+r_l+j\omega L_l} \tag{3.8}$$

in which, the inverter and the grid voltages involved in **Eq. (3.8)** can be rewritten in the *abc* reference according to the inverse power-invariant *dq* transformation [144], as follows:

$$\begin{cases}E_{dq}=\left[\sqrt{2}E_{eff}\cdot\sqrt{\dfrac{3}{2}}\right]\angle\varphi=\sqrt{3}E\angle\varphi\\ V_{g-dq}=\left[\sqrt{2}V_{g-eff}\cdot\sqrt{\dfrac{3}{2}}\right]\angle 0=\sqrt{3}V_g\angle 0\end{cases} \tag{3.9}$$

As a result, the expression of the line impedance current can be obtained, in the *s*-domain, as follows:

$$I(s)=\sqrt{3}\frac{\left(E\angle\varphi-V_g\angle 0\right)\left(L_l\cdot s+r_l-j\,\omega L_l\right)}{\left(r_l+L_l\cdot s\right)^2+\left(L_l\omega\right)^2} \tag{3.10}$$

This expression is useful to be exploited for the obtention of the *P* and *Q* power mathematical formulations.

3.3.1.2. The expression of the active and reactive power flow (*P* and *Q*)

By substituting the expression of the line impedance current given by **Eq. (3.10)** into **Eq. (3.1)**, the power flow formulation of the complex power of becomes:

$$S=3\frac{\left(V_gE\cos(\varphi)-V_g^{\,2}-jV_gE\ \sin(\varphi)\right)\left(r_l+L_ls+j\,\omega L_l\right)}{r_l+L_ls^2+\left(\omega L_l\right)^2} \tag{3.11}$$

Consequently, the real and reactive power can be expressed as follows:

$$P=3\frac{r_l+L_ls}{\left(r_l+L_ls\right)^2+\left(L_l\omega\right)^2}\left(V_gE\ \cos(\varphi)-V_g^{\,2}\right)+3\frac{L_l\omega}{\left(r_l+L_ls\right)^2+\left(L_l\omega\right)^2}\cdot V_gE\sin(\varphi) \tag{3.12}$$

$$Q=3\frac{L_l\omega}{\left(r_l+L_ls\right)^2+\left(L_l\omega\right)^2}\left(V_gE\cos(\varphi)-V_g^{\,2}\right)-3\frac{\left(r_l+L_ls\right)}{\left(r_l+L_ls\right)^2+\left(L_l\omega\right)^2}\cdot V_gE\ \sin(\varphi) \tag{3.13}$$

For the sake of simplicity of the coming analysis, the above equations can be rewritten as:

$$P=\frac{r_l+L_ls}{\left(r_l+L_ls\right)^2+\left(L_l\omega\right)^2}u_2+\frac{L_l\omega}{\left(r_l+L_ls\right)^2+\left(L_l\omega\right)^2}u_1 \tag{3.14}$$

$$Q=\frac{L_l\omega}{\left(r_l+L_ls\right)^2+\left(L_l\omega\right)^2}u_2-\frac{\left(r_l+L_ls\right)}{\left(r_l+L_ls\right)^2+\left(L_l\omega\right)^2}u_1 \tag{3.15}$$

with;

$$\begin{cases}u_1=3\cdot V_gE\ \sin(\varphi)\\ u_2=3\left(V_gE\ \cos(\varphi)-V_g^{\,2}\right)\end{cases} \tag{3.16}$$

Thus, the active and reactive power equations (**Eqs. (3.14)** and **(3.15)**) can be written in matrix form as follow:

$$\begin{bmatrix}P\\Q\end{bmatrix}=\frac{\begin{bmatrix}L_l\omega & r_l+L_ls\\ -\left(r_l+L_ls\right) & L_l\omega\end{bmatrix}}{\left(r_l+L_ls\right)^2+\left(L_l\omega\right)^2}\times\begin{bmatrix}u_1\\u_2\end{bmatrix} \tag{3.17}$$

Besides, the above equation can be rewritten as a function of the state variable *x* as follows:

$$\begin{bmatrix} P \\ Q \end{bmatrix} = \begin{bmatrix} L_l\omega & r_l + L_l s \\ -(r_l + L_l s) & L_l\omega \end{bmatrix} \begin{bmatrix} x_1 \\ x_2 \end{bmatrix} \tag{3.18}$$

where the expression related the state variable *x* to the vector *u* can be given by:

$$\begin{bmatrix} x_1 \\ x_2 \end{bmatrix} = \frac{\begin{bmatrix} \left(\frac{1}{L_l}\right)^2 & 0 \\ 0 & \left(\frac{1}{L_l}\right)^2 \end{bmatrix}}{s^2 + 2\frac{r_l}{L_l}\cdot s + \left(\frac{r_l}{L_l}\right)^2 + \omega^2} \begin{bmatrix} u_1 \\ u_2 \end{bmatrix} \tag{3.19}$$

Based on equations given by **(3.18)** and **(3.19)**, the mathematical model of the active and reactive power flow can be presented in state-space form as:

$$\begin{cases} \begin{bmatrix} \dot{x}_1 \\ \ddot{x}_1 \\ \dot{x}_2 \\ \ddot{x}_2 \end{bmatrix} = \begin{bmatrix} 0 & 1 & 0 & 0 \\ -\left(\left(\frac{r_l}{L_l}\right)^2 + \omega^2\right) & -\left(2\frac{r_l}{L_l}\right) & 0 & 0 \\ 0 & 0 & 0 & 1 \\ 0 & 0 & -\left(\left(\frac{r_l}{L_l}\right)^2 + \omega^2\right) & -\left(2\frac{r_l}{L_l}\right) \end{bmatrix} \begin{bmatrix} x_1 \\ \dot{x}_1 \\ x_2 \\ \dot{x}_2 \end{bmatrix} + \begin{bmatrix} 0 & 0 \\ \left(\frac{1}{L_l}\right)^2 & 0 \\ 0 & 0 \\ 0 & \left(\frac{1}{L_l}\right)^2 \end{bmatrix} \begin{bmatrix} u_1 \\ u_2 \end{bmatrix} \\ \begin{bmatrix} P \\ Q \end{bmatrix} = \begin{bmatrix} L_l\omega & 0 & r_l & L_l \\ -r_l & -L_l & L_l\omega & 0 \end{bmatrix} \begin{bmatrix} x_1 \\ \dot{x}_1 \\ x_2 \\ \dot{x}_2 \end{bmatrix} \end{cases} \tag{3.20}$$

where ($\dot{x}$) and ($\ddot{x}$) denote the first and the second derivate of state vector *x*, respectively.

3.3.1.3. Power flow small-signal model

The small-signal model of the power flow can be obtained by considering small disturbances around the state of the equilibrium point, defined by (V_{gn}, E_n, φ_n), of equations **(3.12)**, **(3.13)**, and **(3.16)**. For instance, **Eq. (3.16)** can be linearized and the following expression can be defined as:

$$\begin{bmatrix} \Delta u_1 \\ \Delta u_2 \end{bmatrix} = 3\cdot V_{gn} \begin{bmatrix} E_n\cos(\varphi_n) & \sin(\varphi_n) \\ -E_n\sin(\varphi_n) & \cos(\varphi_n) \end{bmatrix} \begin{bmatrix} \Delta\varphi \\ \Delta E \end{bmatrix} \tag{3.21}$$

where Δ denotes the small deviation of the variable from the equilibrium point.

To simplify the mathematical manipulation, the above equation can be rewritten as follows:

$$\begin{bmatrix}\Delta u_1\\ \Delta u_2\end{bmatrix}=\begin{bmatrix}k_{11} & k_{12}\\ k_{21} & k_{22}\end{bmatrix}\begin{bmatrix}\Delta\varphi\\ \Delta E\end{bmatrix} \tag{3.22}$$

Combining the above equation with the state space form given by **Eq. (3.19)**, the small-signal model of the power flow can be obtained in state-space form as follows:

$$\begin{cases}\begin{bmatrix}\Delta\dot{x}_1\\ \Delta\ddot{x}_1\\ \Delta\dot{x}_2\\ \Delta\ddot{x}_2\end{bmatrix}=\begin{bmatrix}0 & 1 & 0 & 0\\ -\left(\left(\frac{r_l}{L_l}\right)^2+\omega^2\right) & -\left(2\frac{r_l}{L_l}\right) & 0 & 0\\ 0 & 0 & 0 & 1\\ 0 & 0 & -\left(\left(\frac{r_l}{L_l}\right)^2+\omega^2\right) & -\left(2\frac{r_l}{L_l}\right)\end{bmatrix}\begin{bmatrix}\Delta x_1\\ \Delta\dot{x}_1\\ \Delta x_2\\ \Delta\dot{x}_2\end{bmatrix}+\begin{bmatrix}0 & 0\\ \frac{k_{11}}{L_l^2} & \frac{k_{12}}{L_l^2}\\ 0 & 0\\ \frac{k_{21}}{L_l^2} & \frac{k_{22}}{L_l^2}\end{bmatrix}\begin{bmatrix}\Delta\varphi\\ \Delta E\end{bmatrix}\\ \begin{bmatrix}\Delta P\\ \Delta Q\end{bmatrix}=\begin{bmatrix}L_l\omega & 0 & r_l & L_l\\ -r_l & -L_l & L_l\omega & 0\end{bmatrix}\begin{bmatrix}\Delta x_1\\ \Delta\dot{x}_1\\ \Delta x_2\\ \Delta\dot{x}_2\end{bmatrix}\end{cases} \tag{3.23}$$

The parameter of the above-linearized model (E_n and φ_n) can be calculated based on the following mathematical manipulation. When the system operates at its equilibrium points, and from **Eq. (3.16)**, the expression of the corresponding parameters E_n and φ_n can be calculated as follows:

$$\begin{cases}E_n=\sqrt{\left(\frac{1}{3}\frac{u_{1n}}{V_{gn}}\right)^2+\left(\frac{1}{3}\frac{u_{2n}}{V_{gn}}+V_{gn}\right)^2}\\ \varphi_n=-Arctg\left(\frac{u_{1n}}{4u_{1n}+3V_{gn}^2}\right)\end{cases} \tag{3.24}$$

where the expression of the vector u at the equilibrium point as a relation to the nominal value of the active and reactive powers can be determinate according to **Eq. (3.17)** and after set $s = 0$, as follows:

$$\begin{bmatrix}u_{1n}\\ u_{2n}\end{bmatrix}=\left[r_l^2+\left(L_l\omega\right)^2\right]\begin{bmatrix}L_l\omega & r_l\\ -r_l & L_l\omega\end{bmatrix}^{-1}\begin{bmatrix}P_n\\ Q_n\end{bmatrix} \tag{3.25}$$

It is worth mentioning that the fundamental active and reactive powers (P and Q) presented in the small-signal model; given by **Eq. (3.23)**; are calculated based on the estimated output current and voltage components using ESOGI-FLL. Thus, the dynamic model of the power calculation based on the SOGI-FLL dynamics should be integrated into the global small-signal model.

In what comes, a dynamic phasor modeling approach for obtaining the expected power calculation small-signal model based on SOGI-FLL dynamics is developed.

3.3.1.4. Small-signal model dynamics of the SOGI-FLL-based power calculation

In this section, the dynamic phasor modeling procedure of the SOGI-FLL based-power calculation is presented. As mentioned earlier, the average active and reactive powers are calculated by using the ESOGI-FLL estimated outputs corresponding to the fundamental component. The block diagram of the power calculation model including the SOGI-FLL dynamics is presented in **Fig. 3.6**. However, in the stationary and rotating reference frames, the instantaneous active and reactive powers can be calculated as follows:

$$\begin{cases} \hat{P} = \frac{1}{2}(V_{g-\alpha}\cdot\hat{I}_{\alpha} + V_{g-\beta}\cdot\hat{I}_{\beta}) = V_{g-d}\cdot\hat{I}_{d} + V_{g-q}\cdot\hat{I}_{q} \\ \hat{Q} = \frac{1}{2}(-V_{g-\alpha}\cdot\hat{I}_{\beta} + V_{g-\beta}\cdot\hat{I}_{\alpha}) = -V_{g-d}\cdot\hat{I}_{q} + V_{g-q}\cdot\hat{I}_{d} \end{cases} \tag{3.26}$$

In order to derive the mathematical transfer function relating the estimated active and reactive power to the actual ones, the same analysis based on the dynamic phasor modeling presented in chapter II, for the extraction of the amplitude model, is considered [67]. Based on the transfer function of the SOGI-FLL given by **Eqs. (3.27)** to **(3.29)** below; which describes the dynamics of orthogonal components estimated by the SOGI-FLL, to the corresponding input voltage, the expression of the estimated orthogonal components of the output current can be obtained in rotating reference frame as defined in Eq. (3.27).

$$G_{\alpha}(s) = \frac{\hat{v}_{MG\alpha}(s)}{v_{MG}(s)} = k\,\hat{\omega}_{MG}\,\frac{s}{s^2 + k\,\hat{\omega}_{MG}\,s + \hat{\omega}_{MG}^2} \tag{2.27}$$

$$G_{\beta}(s) = \frac{\hat{v}_{MG\beta}(s)}{v_{MG}(s)} = \frac{k\,\hat{\omega}_{MG}^2}{s^2 + k\,\hat{\omega}_{MG}\,s + \hat{\omega}_{MG}^2} \tag{2.28}$$

$$\begin{bmatrix} \hat{I}_d \\ \hat{I}_q \end{bmatrix} = k\,\omega\,\frac{\left[s^3 + k\,\omega s^2 + 2\omega^2 s + k\,\omega^3\right]}{\left[s\left(s + k\,\omega\right)\right]^2 + \left[\omega\left(2s + k\,\omega\right)\right]^2}\begin{bmatrix} I_d \\ I_q \end{bmatrix} \tag{3.29}$$

This transfer function describes the output current estimation dynamics based on the SOGI-FLL scheme.

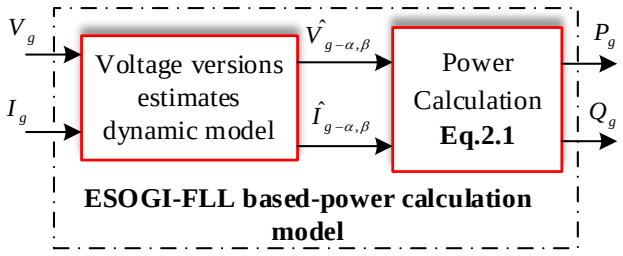

Fig. 3.6. Block diagram of the model of the power calculation using the ESOGI-FLL algorithm.

On the other hand, when considering V_g as a reference in the rotating reference frame (i. e. $V_{g\text{-}q} = 0$), the expressions of the estimated (calculated) active and reactive powers corresponding to the fundamental component can be obtained as:

$$\begin{cases} \hat{P} = V_{g-d} \cdot \hat{I}_d \\ \hat{Q} = -V_{g-d} \cdot \hat{I}_q \end{cases} \tag{3.30}$$

in which the direct version of the grid voltage can be given by the following expression:

$$V_{g-d} = \sqrt{3} \cdot V_g \tag{3.31}$$

Merging **Eqs. (3.29)**, **(3.30)** and **(3.31)**, the transfer function relating the estimated active $\hat{P}$ and reactive $\hat{Q}$ powers to the actual ones (P and Q), can be derived, after some mathematical manipulation, as follows:

$$\begin{cases} \hat{P} = \left(\dfrac{k\omega \cdot s^3 + k^2\omega^2 \cdot s^2 + 2k\omega^3 \cdot s + k^2\omega^4}{s^4 + 2k\omega \cdot s^3 + \left(k^2\omega^2 + 4\omega^2\right)s^2 + 4k\omega^3 \cdot s + k^2\omega^4} \right) P \\ \hat{Q} = \left(\dfrac{k\omega \cdot s^3 + k^2\omega^2 \cdot s^2 + 2k\omega^3 \cdot s + k^2\omega^4}{s^4 + 2k\omega \cdot s^3 + \left(k^2\omega^2 + 4\omega^2\right)s^2 + 4k\omega^3 \cdot s + k^2\omega^4} \right) Q \end{cases} \tag{3.32}$$

This transfer function expresses the model of the active and reactive power estimates dynamics based on the SOGI-FLL algorithm.

Accordingly, the linearized small-signal model dynamics of the power estimate can be presented by:

$$\begin{cases} \Delta\hat{P} = H_p(s) \cdot \Delta P \\ \Delta\hat{Q} = H_q(s) \cdot \Delta Q \end{cases} \tag{3.33}$$

where the transfer functions $H_p(s)$ and $H_q(s)$ denote low-pass filters of fourth-order and are given by:

$$H_p(s) = H_q(s) = \frac{k\omega \cdot s^3 + k^2\omega^2 \cdot s^2 + 2k\omega^3 \cdot s + k^2\omega^4}{s^4 + 2k\omega \cdot s^3 + \left(k^2\omega^2 + 4\omega^2\right)s^2 + 4k\omega^3 \cdot s + k^2\omega^4} \tag{3.34}$$

For easy modeling analysis and control design, the above transfer function ($H_p(s)$) can be approximated to a first-order transfer function. Based on the same mathematical analysis presented in chapter 2, the first-order transfer function corresponds to the one given by **Eq. (3.34)** is:

$$H_p(s) = \frac{\Delta\hat{P}}{\Delta P} = \frac{k\,\omega/2}{s + k\,\omega/2} \tag{3.35}$$

This transfer function describes the reduced small-signal model of the active power calculation dynamics based on the SOGI-FLL.

It is worth noting that unlike the existing approaches; that chose randomly the cut-off frequency of low pass filter used to describe the power calculation dynamics; the cut-off frequency of the reduced model is computed directly when the parameters of the ESOGI-FLL scheme are selected.

3.3.2. Accuracy assessment of the obtained models:

This section aims to validate the obtained models through a simulation study in the MATLAB/ Simulink environment as well as a series of real-time hardware-in-the-loop (HIL) implementation using ARM Cortex Microcontroller.

3.3.2.1. Simulation test

To investigate the accuracy of the derived actual model and the reduced model of the active and reactive power estimate, given by **Eqs. (3.33)** and **(3.35)**, a simulation study in the MATLAB/ Simulink environment is performed considering some standard tests. **Fig. 3.7** shows the block diagram of the test platform simulated in MATLAB, in which, as mentioned earlier, the ESOGI-FLL based-structure is involved for active and reactive power calculations. While, as seen in **Fig. 3.7**, the inputs actual powers of the obtained models are measured in the *αβ* reference frame (**Eq.(2.1)**), in which *abc/αβ* transformation is applied to generated three-phase signals, then, transfer them to the orthogonal *αβ* components. In this simulation study, the calculated active and reactive powers by the ESOGI-FLL-based power calculator are compared to the ones predicted by the obtained models for step changes in the input grid voltage frequency and amplitude. The transient performance of the *P* and *Q* power's estimate for frequency and amplitude changes, respectively are illustrated in **Figs. 3.8** and **3.9**. As shown, the calculated active and reactive powers are varied at t = 0.2 s, corresponding to the voltage frequency and amplitude increase. In addition, one can see that the scopes of the produced powers by the models are matched with the provided powers by the power calculation block. Consequently, the actual and the reduced models, as demonstrated, are able to predict very accurately the ESOGI-FLL based-power calculation

average behavior.

It is worth to menion that, we adopt the calculation of the active and reactive powers in three phase frame because it define the real compution of the expected powers.

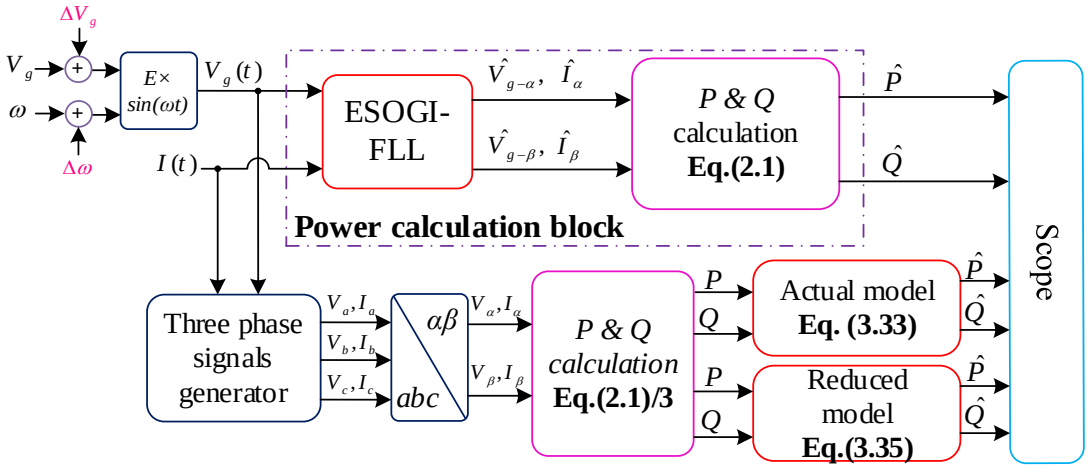

Fig. 3.7. Block diagram of the simulated testbed in MATLAB for the models validation.

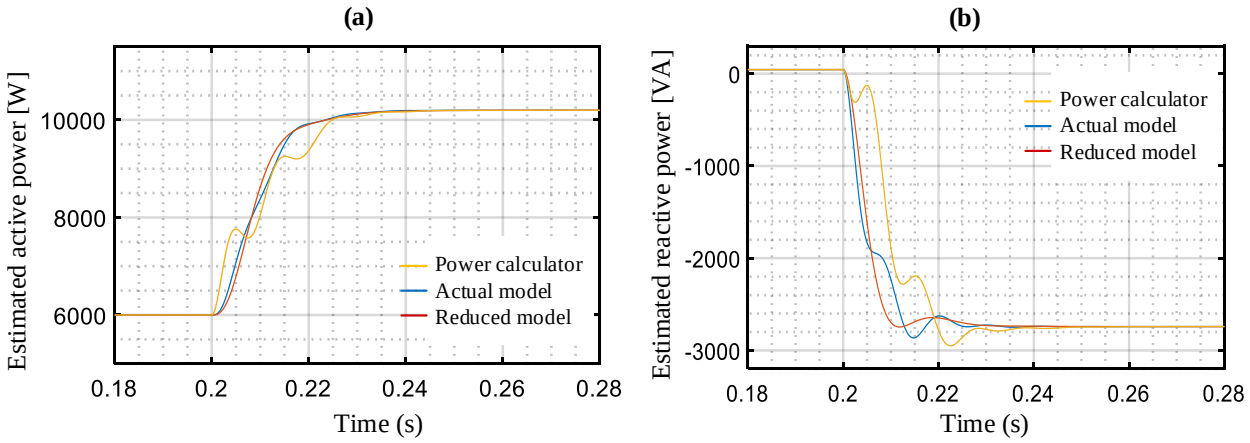

Fig. 3.8. Investigating the accuracy of the actual and the reduced models to *f* variation.

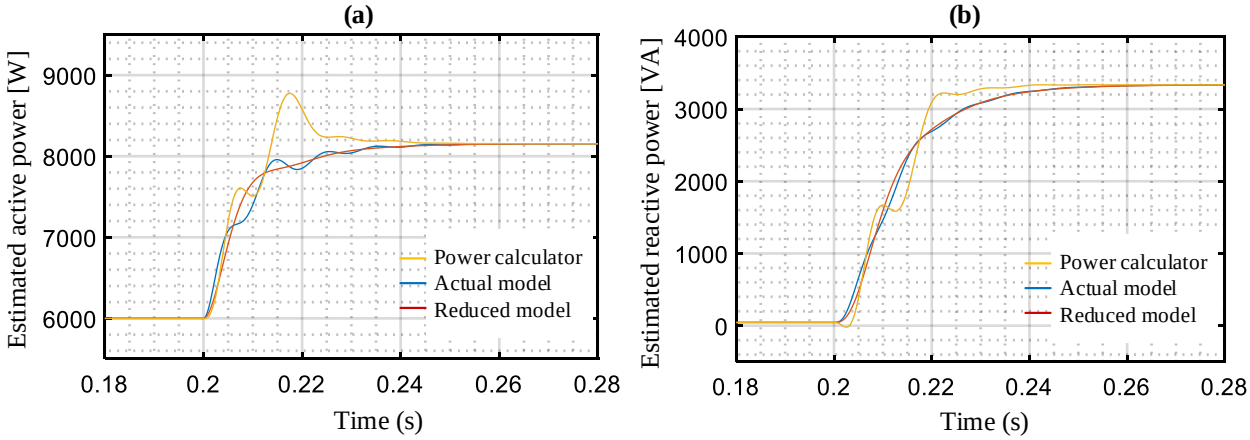

Fig. 3.9. Investigating the accuracy of the actual and the reduced models to *E* variation.

3.3.2.2. Processor-in-the-loop (PIL) test

The investigation of the accuracy of the obtained models in real-time, Processor-in-the-Loop (PIL), based on ARM cortex μC (STM32F4x) is carried out. The schematic diagram of the preformed PIL testbed is illustrated in **Fig. 3.10**. In this scheme, a sinusoidal voltage source with the proposed SOGI-FLL based-power calculation algorithm is implemented in MATLAB/ Sim Power System. While the obtained models are implemented in the STM card. Note that the measured current and voltage are transmitted to the STM card and the produced powers by the card are feedback to the PC through UART (RS 232) to be scoped. The same tests are considered, as before, in which a voltage frequency and amplitude are incensed at t = 0.24 s. **Figs. 3.11** and **3.12** show the obtained results of this investigation. This figure demonstrates the accuracy of the derived actual model and the reduced model in predicting the average transient behavior of the ESOGI-FLL based-power estimation.

As a result, the obtained models are useful to be introduced in the power flow control for describing the active and reactive power calculation dynamics.

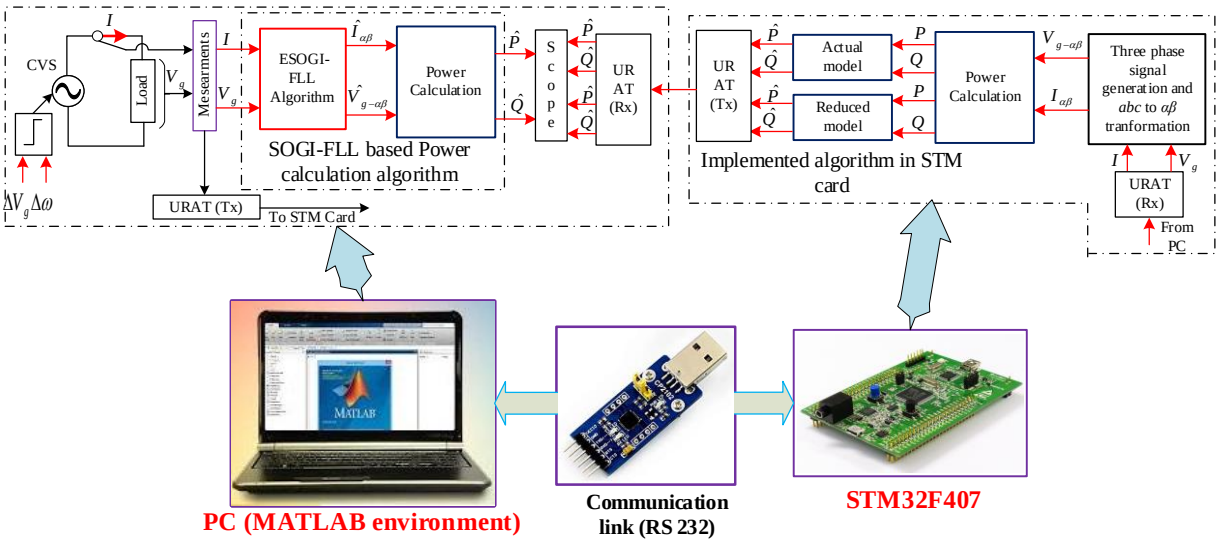

Fig. 3.10. Block diagram of the real-time implementation based on STM card for models validation.

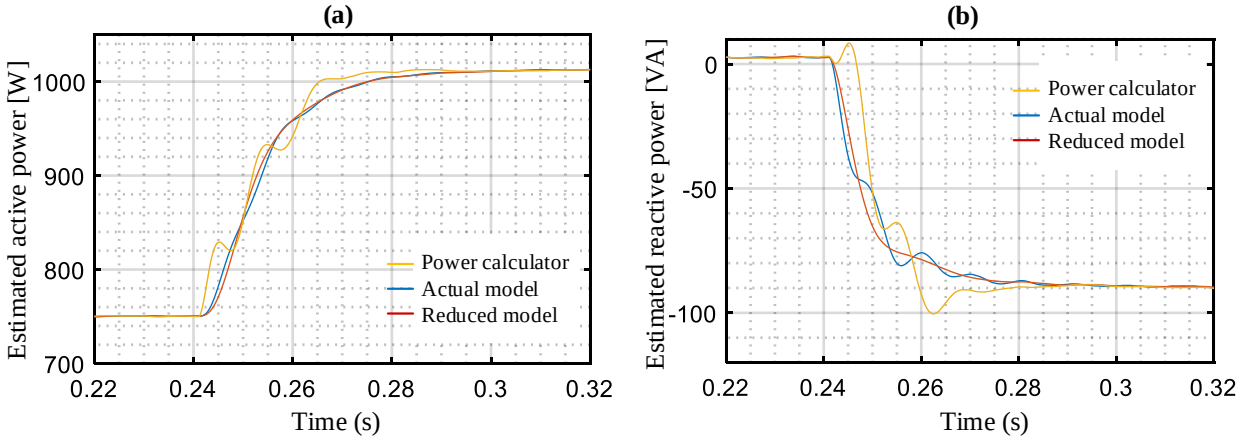

Fig. 3.11. PIL Transient performances of the obtained model versus SOG-FLL based-power calculation to frequency variation.

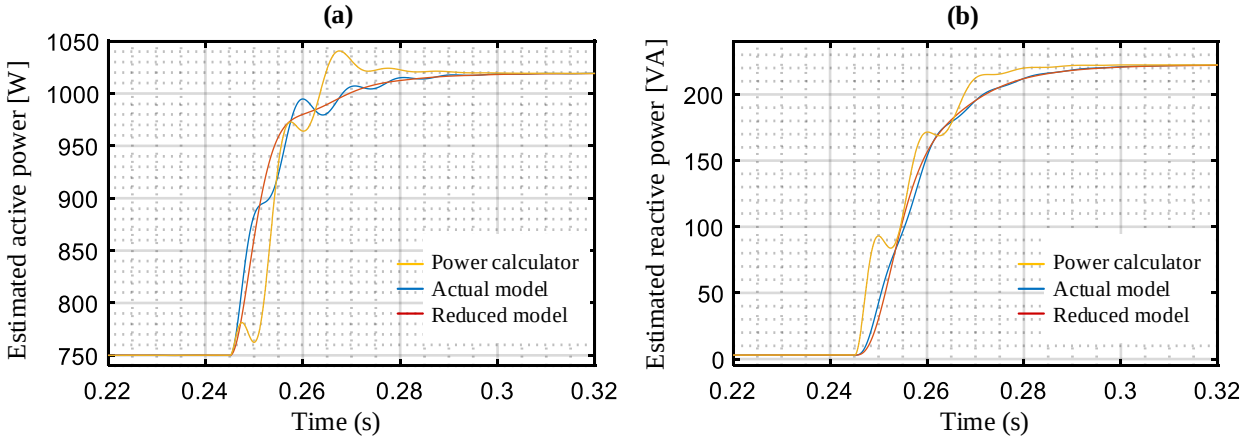

Fig. 3.12. PIL Transient performance of the obtained model versus SOG-FLL based-power calculation to voltage amplitude variation.

3.3.3. The open-loop small-signal model of the microgrid power flow

In this part, the analysis for deriving the open-loop transfer function of the active and reactive power flow of the whole system is presented, in which the active and reactive coupling is considered.

The block diagram of the open-loop small-signal model of the active and reactive power flow is described in **Fig. 3.13**. From this figure, the open-loop model is composed of the power calculation dynamics and the power flow model. Accordingly, by combining the reduced small-signal model describing the power's estimate dynamics, given by **Eq. (3.33)**, and the power flow equation, presented by **Eq. (3.22)**, the open-loop small-signal model of the power flow in state-space form, after some mathematical manipulations, may be obtained as follows:

$$\begin{cases} \begin{bmatrix} \Delta\dot{x}_1 \\ \Delta\ddot{x}_1 \\ \Delta\dddot{x}_1 \\ \Delta\dot{x}_2 \\ \Delta\ddot{x}_2 \\ \Delta\dddot{x}_2 \end{bmatrix} = \begin{bmatrix} 0 & 1 & 0 & 0 & 0 & 0 \\ 0 & 0 & 1 & 0 & 0 & 0 \\ -a_1 & -a_2 & -a_3 & 0 & 0 & 0 \\ 0 & 0 & 0 & 0 & 1 & 0 \\ 0 & 0 & 0 & 0 & 0 & 1 \\ 0 & 0 & 0 & -a_1 & -a_2 & -a_3 \end{bmatrix} \begin{bmatrix} \Delta x_1 \\ \Delta\dot{x}_1 \\ \Delta\ddot{x}_1 \\ \Delta x_2 \\ \Delta\dot{x}_2 \\ \Delta\ddot{x}_2 \end{bmatrix} + \frac{k\,\omega}{2L_l^{\,2}} \begin{bmatrix} 0 & 0 \\ 0 & 0 \\ k_{11} & k_{12} \\ 0 & 0 \\ 0 & 0 \\ k_{21} & k_{22} \end{bmatrix} \begin{bmatrix} \Delta\varphi \\ \delta E \end{bmatrix} \\ \begin{bmatrix} \Delta P \\ \Delta Q \end{bmatrix} = \begin{bmatrix} L_l\omega & 0 & 0 & r_l & L_l & 0 \\ -r_l & -L_l & 0 & L_l\omega & 0 & 0 \end{bmatrix} \begin{bmatrix} \Delta x_1 \\ \Delta\dot{x}_1 \\ \Delta\ddot{x}_1 \\ \Delta x_2 \\ \Delta\dot{x}_2 \\ \Delta\ddot{x}_2 \end{bmatrix} \end{cases} \tag{3.36}$$

in which the parameters, a_1, a_2 and a_3 are given as follows:

$$\begin{cases} a_1 = -k\,\omega/2\left(\left(\dfrac{r_l}{L_l}\right)^2 + \omega^2\right) \\ a_2 = -\left(\dfrac{k\,\omega r_l}{L_l} + \left(\dfrac{r_l}{L_l}\right)^2 + \omega^2\right) \\ a_3 = -\left(2\dfrac{r_l}{L_l} + k\,\omega/2\right) \end{cases} \tag{3.37}$$

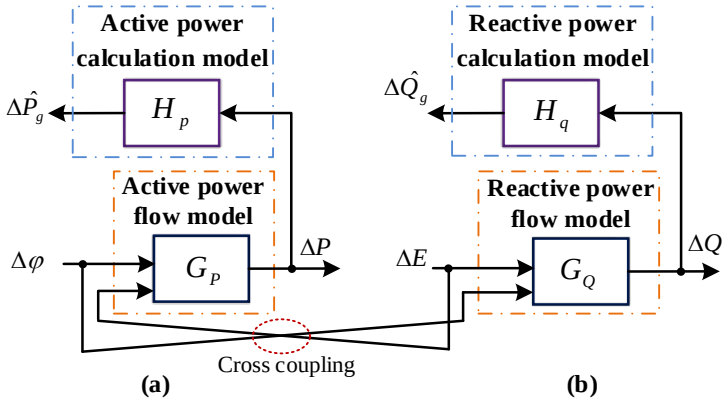

Fig. 3.13. The open-loop small-signal model of the active and reactive power flow.

3.3.4. Open-loop model validation

The accuracy investigation of the open-loop small-signal model for the microgrid power flow is verified under frequency and amplitude voltage variations ($\Delta\varphi$ and ΔE). In this investigation, a simulation study and real-time PIL tests are carried out based on the schematic diagram shown in **Fig. 3.14**. For the simulation study, the constructed scheme that consists of a single-phase VSI connected to the PCC bus with the power-based ESOGI-FLL block and the transfer function of

the obtained model, is implemented in the MATLAB Sim Power System platform. Where the same structure is considered for real-time PIL implementation, in which the power flow model is implemented in the STM card. The results presenting the dynamic performance of the provided powers by the analytic model compared to the ones delivered by the single-phase power stage are shown in **Figs. 3.15** and **3.16**, and prove the model accuracy.

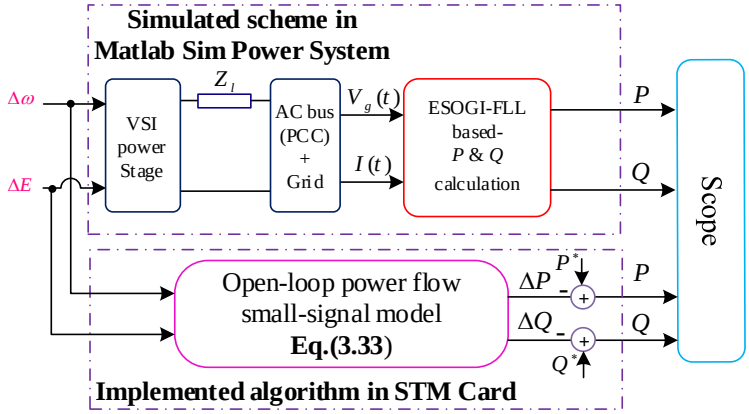

Fig. 3.14. Schematic diagram of the implemented system in MATLAB Sim Power system and the PIL setup.

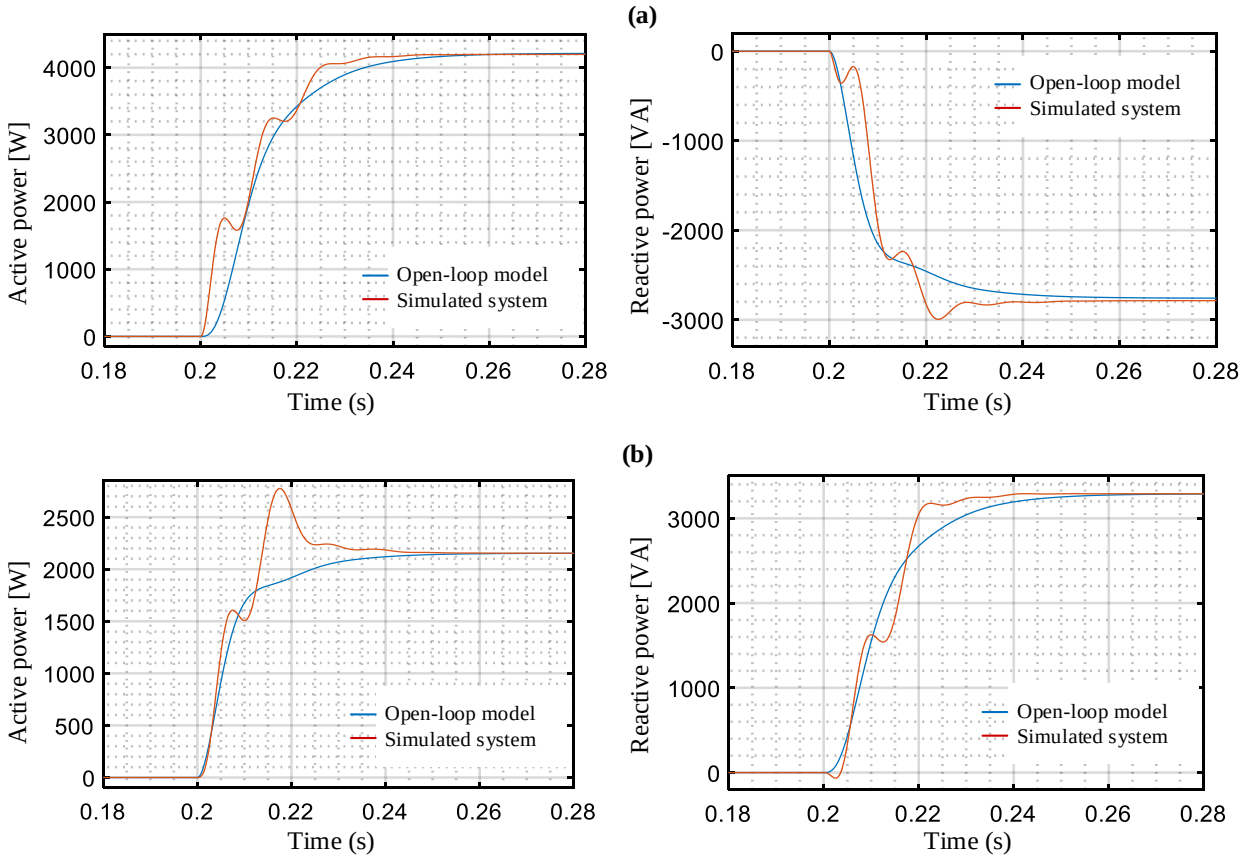

Fig. 3.15. Simulation study; power's transient responses of the open-loop model and power stage for step-change in the voltage: **(a)** frequency, and **(b)** amplitude.

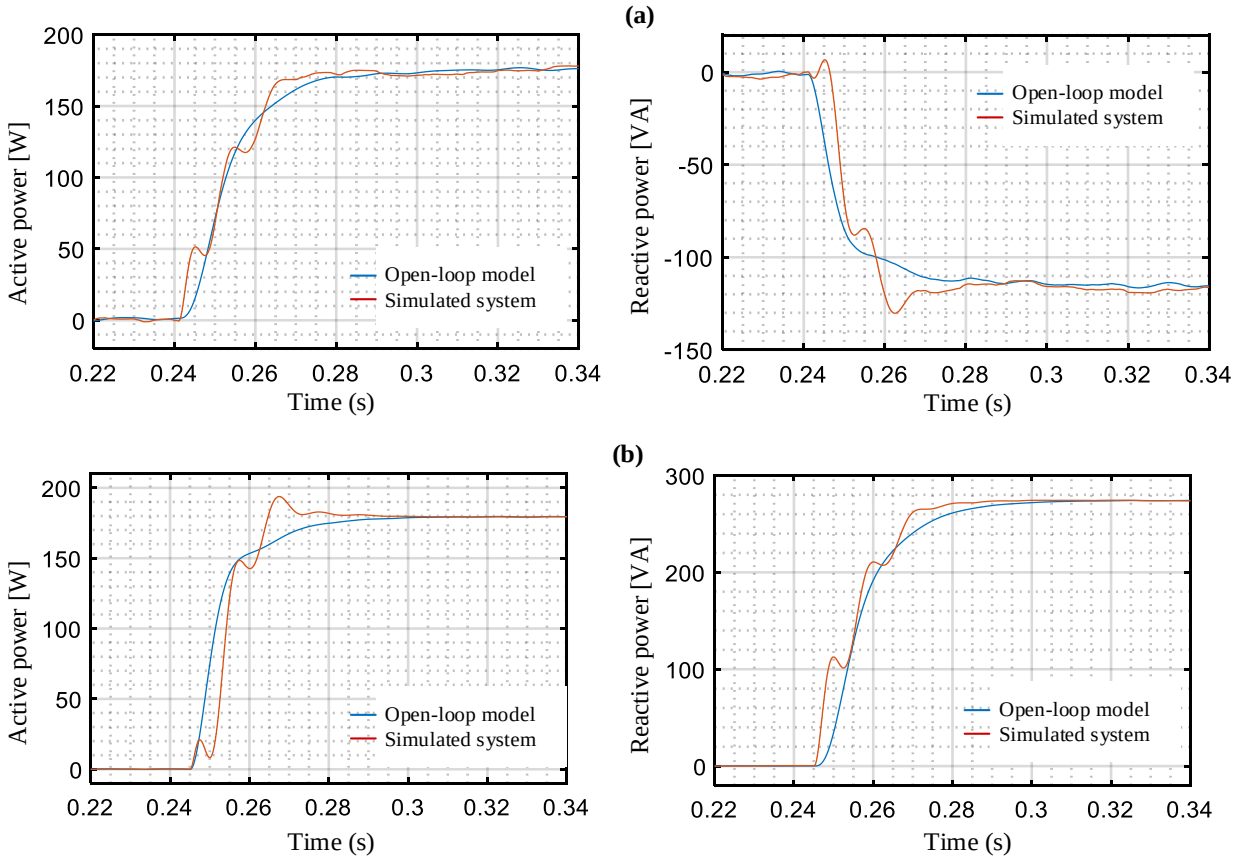

Fig. 3.16. PIL real-time implementation; power's transient responses of the open-loop model and the power stage for step-change in the voltage**; (a)** frequency, and **(b)** amplitude.

The derived model can be used to obtain the closed-loop model of the global power flow system incorporating the tertiary control level. It is worth mentioning that this model can be used, also, for deriving the closed-loop small-signal model of the droop-controlled VSI in autonomous microgrid by including the droop control functions, given by **Eq. (1.13)** in chapter 1.

3.3.5. The closed-loop small-signal model of microgrid power flow incorporating tertiary control

In this section, the closed-loop small-signal model of the considered power flow control loop will be developed to study the system dynamics around a considered operating point.

The power flow control loop is closed by introducing the proposed tertiary control, given above (**Fig. 3.1**), for power reference tracking of a microgrid operating in grid-tied mode. The block diagram of the approximated small-signal model for active and reactive power flow control loops is presented in **Fig. 3.17**. Notice that for the sake of simplicity, the dynamic of the power inverters and its local controller, as well as the secondary dynamics, are assumed to be a unity. In this model, the transfer function *H(s)* is used to describe the dynamics of the SOGI-FLL based-power calculation, C_p and C_Q are the transfer function of the proposed active and reactive power

controllers (Eq. (3.1)), which can be given in *s*-domain by:

$$\begin{cases} C_P(s) = \dfrac{k_{p-P}s + k_{i-P}}{s} \\ C_Q(s) = \dfrac{k_{p-Q}s + k_{i-Q}}{s} \end{cases} \tag{3.38}$$

while *G* is the matrix that related the variations of the active and reactive power to the variations of the voltage frequency and amplitude.

As the active and reactive power variations are coupled to both frequency and amplitude variations, the detailed analysis given below is considered to extract the mathematical formulation of the expected closed-loop model.

First, considering that the active power reference of the grid is equal to zero ($\Delta Q_g^* = 0$), thus, the expressions of the tertiary controller can be rewritten as:

$$\Delta\varphi = C_P(s)\left(\Delta P_g^* - \Delta\hat{P}_g\right) \tag{3.39.a}$$

$$\Delta E = -C_Q(s)\Delta\hat{Q}_g \tag{3.39.b}$$

Secondly, linearizing **Eq. (3.17)** around operating point, the expression relating the active and reactive power to the vector *u* can be derived as follows:

$$\begin{bmatrix} \Delta P \\ \Delta Q \end{bmatrix} = \begin{bmatrix} G_1 & G_2 \\ -G_2 & G_1 \end{bmatrix} \times \begin{bmatrix} \Delta u_1 \\ \Delta u_2 \end{bmatrix} \tag{3.40}$$

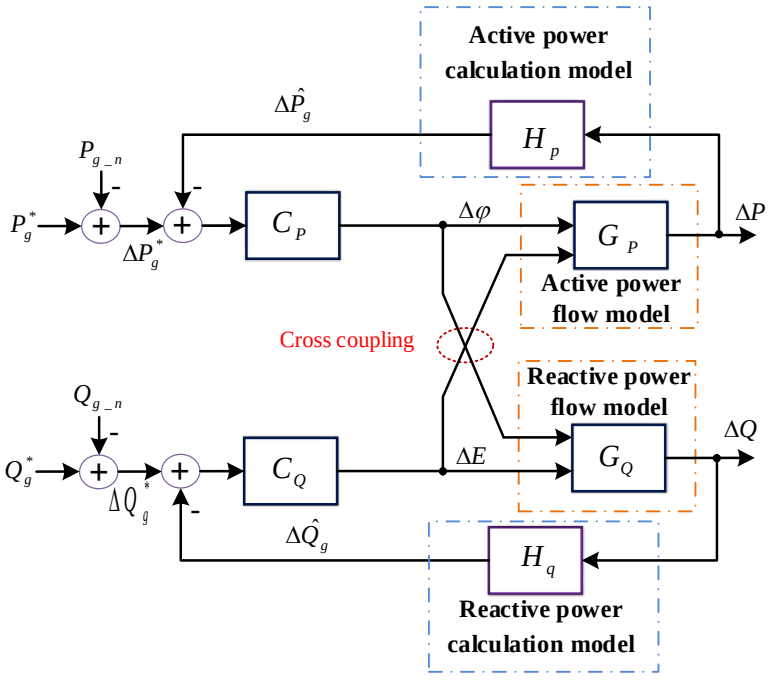

Fig. 3.17. Closed-loop model of the MG power flow incorporating tertiary control.

where G_1 and G_2 are given by:

$$\begin{cases} G_1 = \dfrac{L_l \omega}{r_l^2 + (L_l \omega)^2} \\ G_2 = \dfrac{r_l}{r_l^2 + (L_l \omega)^2} \end{cases} \tag{3.41}$$

Merging **Eq. (3.40)** and **Eq. (3.21)**, the expression relateing small variation of the active and reactive power to frequency and amplitude can be obtained as follows:

$$\begin{bmatrix} \Delta P \\ \Delta Q \end{bmatrix} = \begin{bmatrix} G_1 & G_2 \\ -G_2 & G_1 \end{bmatrix} \begin{bmatrix} k_{11} & k_{12} \\ k_{21} & k_{22} \end{bmatrix} \begin{bmatrix} \Delta\varphi \\ \Delta E \end{bmatrix} \tag{3.42}$$

On the other side, the mathematical formulation describing the dynamics of the actual powers to the estimated ones can be rewritten in matrix form as follows:

$$\begin{bmatrix} \Delta\hat{P} \\ \Delta\hat{Q} \end{bmatrix} = H \begin{bmatrix} \Delta P \\ \Delta Q \end{bmatrix} \tag{3.43}$$

By substituting the above equation, i.e. **Eq. (3.43)**, into **Eq. (3.42)**, the expression of the small variations of the estimated powers corresponding to the frequency and voltage variations can be obtained as follows:

$$\begin{bmatrix} \Delta\hat{P} \\ \Delta\hat{Q} \end{bmatrix} = H \begin{bmatrix} G_1 & G_2 \\ -G_2 & G_1 \end{bmatrix} \begin{bmatrix} k_{11} & k_{12} \\ k_{21} & k_{22} \end{bmatrix} \begin{bmatrix} \Delta\varphi \\ \Delta E \end{bmatrix} = \begin{bmatrix} G_{11} & G_{12} \\ G_{21} & G_{22} \end{bmatrix} \begin{bmatrix} \Delta\varphi \\ \Delta E \end{bmatrix} \tag{3.44}$$

Based on this equation and **Eq. (3.39.b)**, the transfer function relating the variations of the amplitude to the frequency can be represented by:

$$\Delta E = \frac{G_{21}}{\left(G_{22} + \dfrac{1}{C_Q}\right)} \Delta\varphi \tag{3.45}$$

By substituting in **Eq. (3.44)**, the transfer function describing the dynamics of the active power to the frequency variations can be given by:

$$\Delta\hat{P} = \left(G_{11} + \frac{G_{21} G_{12}}{\left(G_{22} + \dfrac{1}{C_Q}\right)} \right) \Delta\varphi \tag{3.46}$$

Consequently, the closed-loop small-signal model of the active power flow control can be expressed by:

$$\Delta\hat{P} = \frac{C_P\left(G_{11} + \frac{G_{21}G_{12}}{\left(G_{22} + \frac{1}{C_Q}\right)}\right)}{1 + C_P\left(G_{11} + \frac{G_{21}G_{12}}{\left(G_{22} + \frac{1}{C_Q}\right)}\right)}\Delta P^* \tag{3.47}$$

As a result, the matrixial form of the closed-loop small-signal model of the active and reactive power flow control as a function of the included transfer functions can be derived as follows:

$$\begin{bmatrix}\Delta\hat{P}\\ \Delta\hat{Q}\end{bmatrix} = \left(1 + H\begin{bmatrix}G_1 & G_2\\ -G_2 & G_1\end{bmatrix}\begin{bmatrix}k_{11} & k_{12}\\ k_{21} & k_{22}\end{bmatrix}\begin{bmatrix}C_P & 0\\ 0 & C_Q\end{bmatrix}\right)^{-1} H\begin{bmatrix}G_1 & G_2\\ -G_2 & G_1\end{bmatrix}\begin{bmatrix}k_{11} & k_{12}\\ k_{21} & k_{22}\end{bmatrix}\begin{bmatrix}C_P & 0\\ 0 & C_Q\end{bmatrix}\left(\begin{bmatrix}\Delta P^*\\ \Delta Q^*\end{bmatrix}\right) \tag{3.48}$$

The closed-Loop model defined by equation **Eq. (3.47)** is useful to study the stability of grid-connected microgrid incorporating the tertiary controller.

3.4. Stability analysis and tertiary control parameter tuning

In this section, stability analysis and effective tuning guidelines for the proposed tertiary controller by using the obtained closed-loop model are investigated. Also, the robustness of the designed tertiary controller is verified under system parameters variations and load disturbances as well.

First, before starting to realize the expected analysis, it is worth noting that it is very difficult to perform the stability analysis based on the derived closed-loop model; where the active and reactive powers are coupled. More particularly, it is not easy to perform analyses with arbitral vast variations of four parameters for both active and reactive controllers ($k_{p\text{-}P}$, $k_{i\text{-}P}$, $k_{p\text{-}Q}$, and $k_{i\text{-}Q}$). Thus, an approach for deriving an approximated small-signal model, easy and effective tuning procedures are proposed. This adopted approach allows to define approximately the amount of the controller parameters ($k_{p\text{-}P}$, $k_{i\text{-}P}$, $k_{p\text{-}Q}$, and $k_{i\text{-}Q}$) corresponding to the desired rate of the response time (T_s) and limit their variations.

Based on **Fig. 3.18**, an approximated small-signal model can be conducted, as shown in **Fig. 3.18**, in which the dynamics of the power stage are assumed unity and that the active and reactive

powers are decoupled. From this figure, the closed-loop small-signal model of the power flow control ($\Delta\hat{P}_g$ -to ΔP_g^*) can be expressed by:

$$\begin{cases} \Delta\hat{P}_g = \dfrac{G_P(s)\big|_{s=0} C_P(s) H_p(s)}{1+G_P(s)\big|_{s=0} C_P(s) H_p(s)} \cdot \Delta P_g^* \\ \Delta\hat{Q}_g = \dfrac{G_Q(s)\big|_{s=0} C_Q(s) H_p(s)}{1+G_Q(s)\big|_{s=0} C_Q(s) H_q(s)} \cdot \Delta Q_g^* \end{cases} \tag{3.49}$$

where the transfer function $G_P(s)\big|_{s=0}$ defines the at the steady-state (see appendix 01).

Accordingly, the characteristic equations of these transfer function after some mathematical manipulation can be given by:

$$\begin{cases} s^2 + \underbrace{k\omega/2\left(1+G_P(s)\big|_{s=0} k_{p-P}\right)}_{2\zeta_P\,\omega_{n-P}} s + \underbrace{G_P(s)\big|_{s=0} k_{i-P}\, k\omega/2}_{\omega_{n-P}^2} = 0 \\ s^2 + \underbrace{k\omega/2\left(1+G_Q(s)\big|_{s=0} k_{p-Q}\right)}_{2\zeta_Q\,\omega_{n-Q}} s + \underbrace{G_Q(s)\big|_{s=0} k_{i-Q}\, k\omega/2}_{\omega_{n-Q}^2} = 0 \end{cases} \tag{3.50}$$

By matching these equations with the desired responses of a second-order characteristic equation and applying the same tuning procedure proposed to determinate the secondary controller parameters'; in chapter II; the parameter of the tertiary controller can be expressed, as a function of the desired response time, as follows:

$$\begin{cases} k_{p-P} = \left(4.82\dfrac{4\zeta_P}{k\omega T_{s-P}} - 1\right) \Big/ G_P(s)\big|_{s=0} \\ k_{i-P} = \dfrac{2(4.82)^2}{G_P(s)\big|_{s=0}\, k\omega T_{s-P}^2} \end{cases}, \quad \begin{cases} k_{p-Q} = \left(4.82\dfrac{4\zeta_Q}{k\omega T_{s-Q}} - 1\right) \Big/ G_Q(s)\big|_{s=0} \\ k_{i-Q} = \dfrac{2(4.82)^2}{G_Q(s)\big|_{s=0}\, k\omega T_{s-Q}^2} \end{cases} \tag{3.51}$$

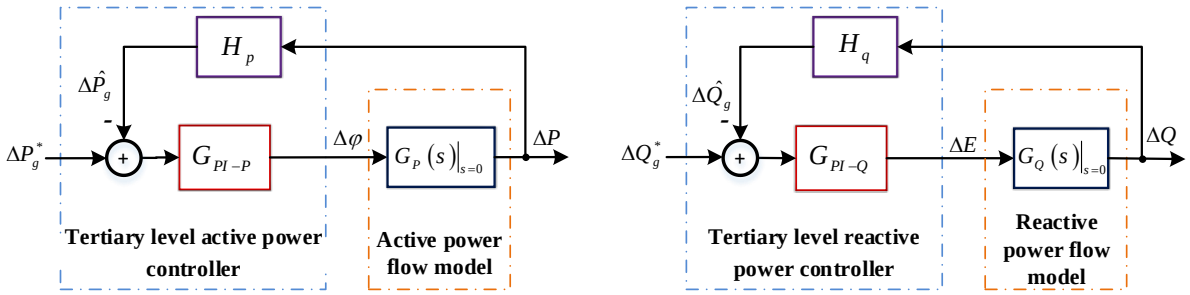

(a) **(b)**

Fig. 3.18. Block diagram of the closed-loop small-signal model of; **(a)** the active and **(b)** reactive power flow control loops.

After choosing the optimum value of the damping factor ξ (ξ = 0.7 in our case), the roots of the characteristic equation of the obtained model (**Eq. (3.47)**) are evaluated as a function of the desired settling time (T_s). The following tests are considered:

1) Test 01: the settling time of the active power transient response, $T_{s\text{-}P}$ is varied from 1s to 3.5s, and of the reactive power control is fixed to 40s, i. e., $T_{s\text{-}Q}$ = 40seconds.
2) Test 02: $T_{s\text{-}P}$ = 3s, while the reactive power settling time is varied from 1s to 50s.

The results given in **Figs. 3.19** and **3.20**, showing the location of the roots of the model's characteristic equation (**Eq. (3.47)**) in the complex *s*-plane corresponding to test 01 and test 02, respectively. The red arrows depict the poles' increasing trend. As is seen in **Fig. 3.19**, a pair of complex poles and a real pole move towards the positive real axis, when increasing $T_{s\text{-}P}$. Hence, it makes the system less damped towards instability if $T_{s\text{-}P}$ > 3.4s. In addition, one can observe that a pair of complex poles are located in the positive real part when $T_{s\text{-}P}$ < 1s, and moves toward the negative real axis after $T_{s\text{-}P}$ increases. Consequently, the stability of the system is assured if $T_{s\text{-}P}$ belongs to the range of 1s < $T_{s\text{-}P}$ < 3.4s. According to **Fig. 3.20**, it can be noticed that the increase of $T_{s\text{-}Q}$ shifts a pair of complex poles from the positive real axis to the negative one, making the system stable as long as $T_{s\text{-}Q}$ is superior to the value 35s ($T_{s\text{-}P}$ > 35s). As a result, when the $T_{s\text{-}Q}$ increases, it makes the system response grow rapidly, and the stability margin increase.

Fig. 3.21 illustrates the transient step response of the system active power for the desired settling time $T_{s\text{-}P}$ = 3 s and $T_{s\text{-}Q}$ = 40 s. One can observe from this figure that the system responds with a settling time $T_{s\text{-}P}$ = 85 s and without overshoots. In addition, it can be noticed that the obtained settling time is not the same as the choosen ones, because the preformed analysis is based on the extracted simplified model. It is worth noting, according to this analysis, that the ratio between the settling time of the active power and the reactive power should be; almost; multiple of ten, i. e. $T_{s\text{-}Q}$ = 10 × $T_{s\text{-}P}$.

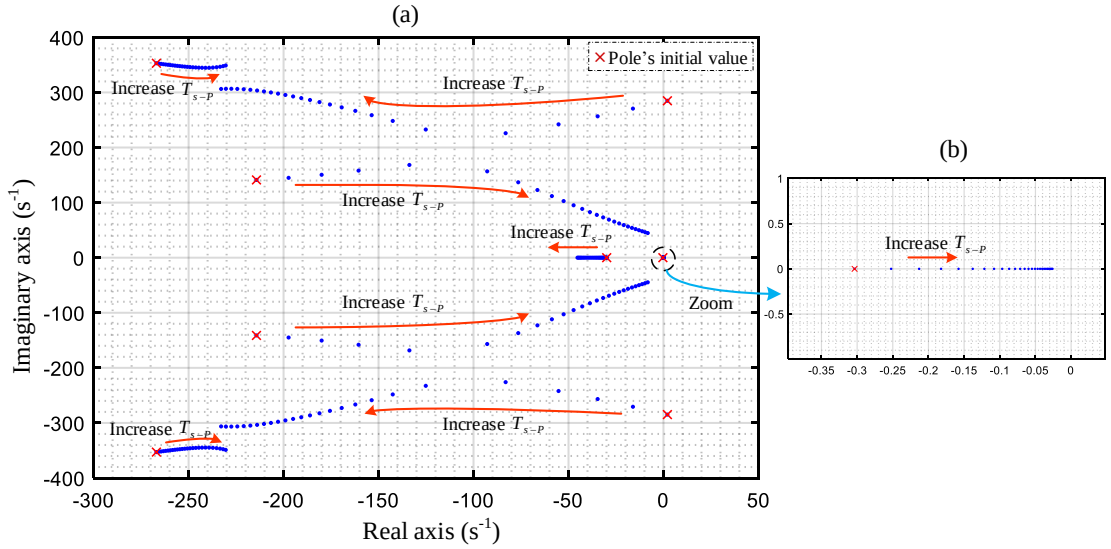

Fig. 3.19. Root-Locus plots for **(a)** 1s ≤ $T_{s\text{-}P}$ ≤ 3.5s and $T_{s\text{-}Q}$ = 40s, and **(b)** Zoom.

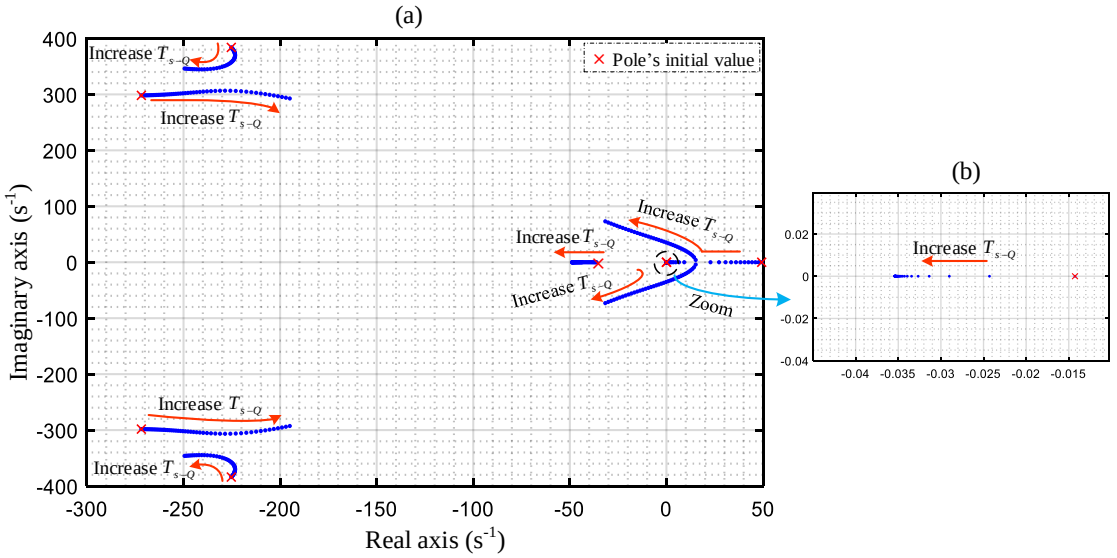

Fig. 3.20. Root-Locus plots for **(a)** 1s ≤ $T_{s\text{-}Q}$ ≤ 50s and $T_{s\text{-}P}$ = 3s, and **(b)** Zoom.

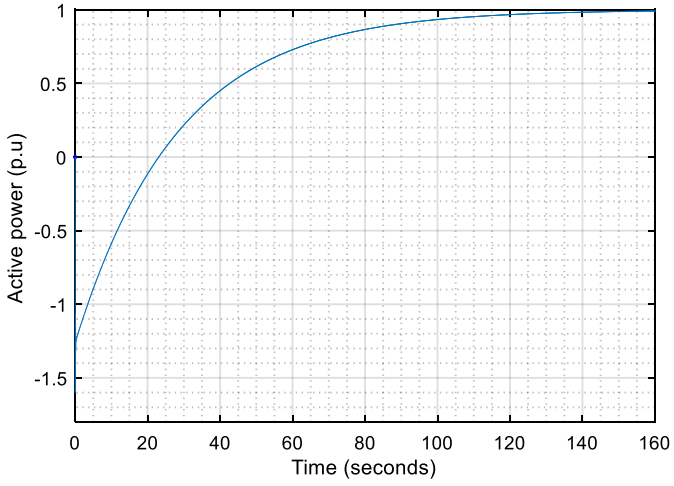

Fig. 3.21. Step response of the active power for $T_{s\text{-}Q}$ = 3s and $T_{s\text{-}Q}$ = 40s.

In what is coming, the stability analysis under the tertiary controller gains, $k_{p,}$ and k_i, variations are adopted to select; on optimum way; the value of the controller parameters.

3.4.1. System stability evaluation to tertiary control parameter variation

In order to evaluate the system stability of the grid-connected VSC, simulation tests are performed. In these tests, the characteristic equation roots of the obtained actual model (**Eq. (3.47)**) are evaluated to controller parameter variations ($k_{p\text{-}P}$, $k_{i\text{-}P}$, $k_{p\text{-}Q}$, and $k_{i\text{-}Q}$), taking into consideration their values chosen earlier. The trajectory of the roots of the closed-loop model to the controller parameter variation is shown in **Figs. 3.22** -to **3.25**. According to the roots' evaluation in **Figs. 3.22** and **3.23**, one can observe that a pair of complex conjugate poles move towards the unstable region as $k_{p\text{-}P}$ and $k_{i\text{-}P}$ increase, hence, leading the grid-tied microgrid system to instability issues. On the other hand, the poles' movement of **Fig. 3.24**, show that when $k_{p\text{-}Q}$ increases a real pole and a conjugate complex pair, those near to the origin, shift towards the unstable region. While from **Fig. 3.25**, one can see that by increasing $k_{i\text{-}Q}$ all the poles shift towards the stable region only the real pole moves to the unstable region, as a result, moving the system towards instability.

The transient performance of the actual closed-loop model for the chosen controller parameter is given in Fig. 26. In this figure, the active power transient response to step response is illustrated for $k_{p\text{-}P} = k_{p\text{-}P}$, $k_{i\text{-}P} = 2\times\ k_{i\text{-}P}$, $k_{p\text{-}Q} = 5\times\ k_{p\text{-}Q}$, and $k_{i\text{-}Q} = 0.5\times\ k_{i\text{-}Q}$. One can notice that the system responds with a settling time of 100s and without overshoots.

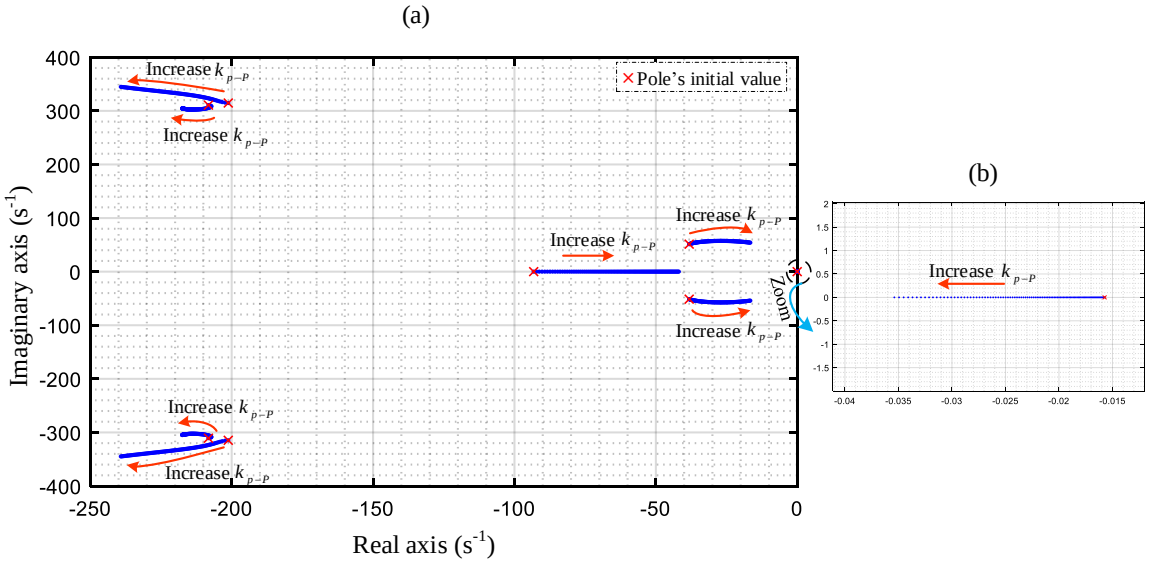

Fig. 3.22. Poles movement when $k_{p\text{-}P}$ varies in the range of, **(a)** $0.01\times\ k_{p\text{-}P} \leq k_{p\text{-}P} \leq 1.2\times\ k_{p\text{-}P}$, and $k_{i\text{-}P} = 1\times k_{i\text{-}P}$, $k_{p\text{-}Q} = 3\times\ k_{p\text{-}Q}$, $k_{i\text{-}\ Q} = 0.5\times k_{i\text{-}Q}$, and **(b)** Zoom of a pole's movement.

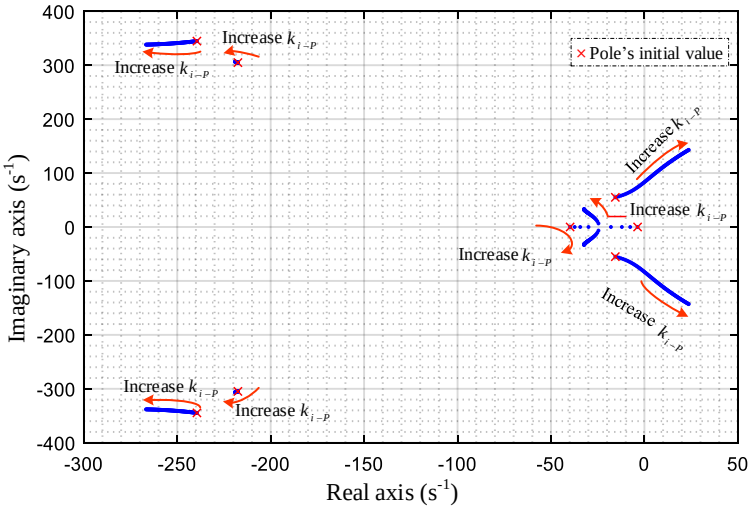

Fig. 3.23. Poles movement when $k_{p\text{-}P}$ varies in the range of $0.01\times k_{i\text{-}P} \le k_{i\text{-}P} \le 1.1\times k_{i\text{-}P}$ and $k_{p\text{-}P} = k_{p\text{-}P}$, $k_{p\text{-}Q} = 3\times k_{p\text{-}Q}$, $k_{i\text{-}Q} = 0.5\times k_{i\text{-}Q}$.

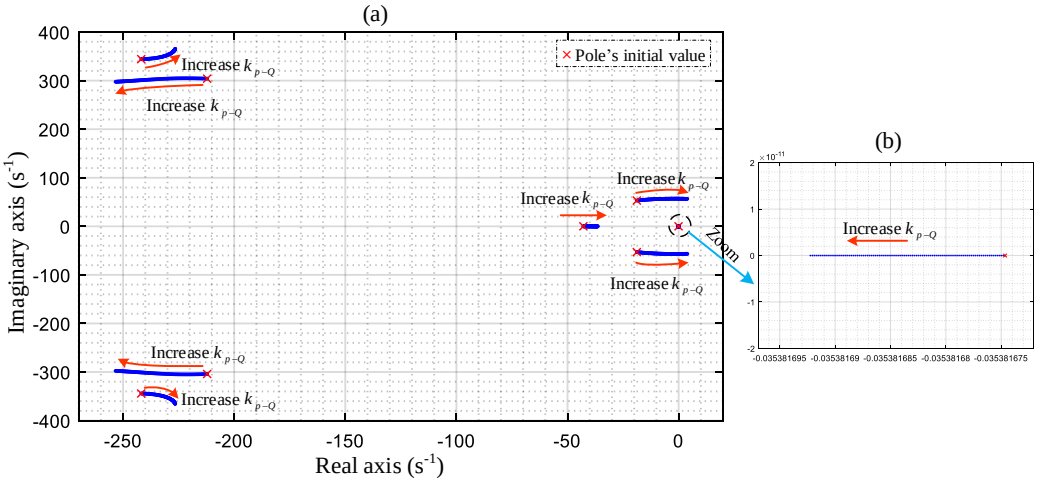

Fig. 3.24. Poles location for $k_{p\text{-}Q}$ changes in the range of $0.1 \times k_{p\text{-}Q} \le k_{p\text{-}Q} \le 10 \times k_{p\text{-}Q}$ and $k_{p\text{-}P} = k_{p\text{-}P}$, $k_{i\text{-}P} = k_{i\text{-}P}$, $k_{i\text{-}Q} = 0.5\times k_{i\text{-}Q}$ **(a)**, with zoom **(b)**.

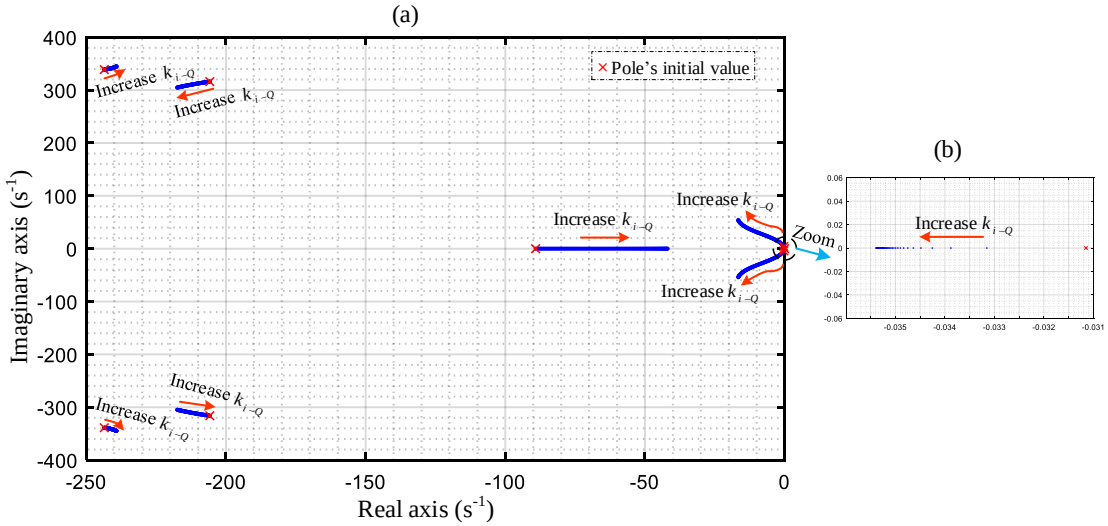

Fig. 3.25. Poles location for $k_{i\text{-}Q}$ changes in the range of $0.01\times k_{i\text{-}Q} \le k_{i\text{-}Q} \le 1.1\times k_{i\text{-}Q}$, and $k_{p\text{-}P} = k_{p\text{-}P}$, $k_{i\text{-}P} = k_{i\text{-}P}$, $k_{i\text{-}Q} = 0.5\times k_{i\text{-}Q}$ **(a)**, with zoom **(b)**.

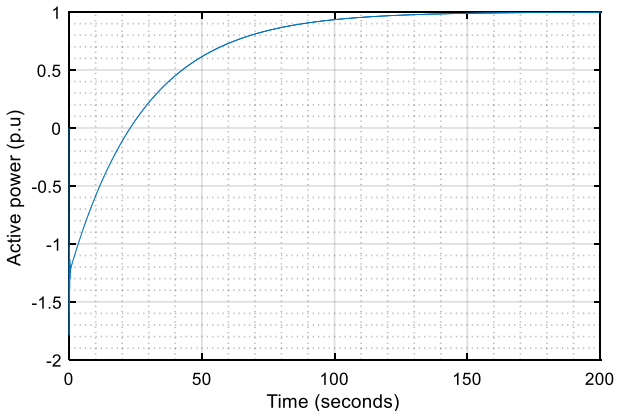

Fig. 3.26. Active power step response for $k_{p\text{-}P} = k_{p\text{-}P}$, $k_{i\text{-}P} = 2\times\ k_{i\text{-}P}$, $k_{p\text{-}Q} = 5\times\ k_{p\text{-}Q}$, and $k_{i\text{-}Q} = 0.5\times\ k_{i\text{-}Q}$.

3.4.2. Robustness assessment of the designed controller

To verify the robustness of the designed tertiary controller, simulation tests are carried out in MATLAB based on the obtained closed-loop power flow model. In this simulation study, the controller is tested against system parameter variations that are considered negligible in the adopted purpose. The following case studies are performed:

- Case 1: when the line resistance (r_l) varied in the range of $0.1\times\ r_l \leq r_l \leq 5\times r_l$
- Case 2: when the line inductance (L_l) varied in the range of $0.1\times\ L_l \leq L_l \leq 10\times\ L_l$
- Case 3: the microgrid frequency (ω_{MG}) varied in the range of $0.1\times\ \omega_{MG} \leq \omega_{MG} \leq 2\times\omega_{MG}$.

It is worth noting that the values of r_l, L_l, and ω_{MG} are set to 200Ω, 10mH, and 50Hz, respectively.

The roots evaluation of the closed-loop model characteristic equation when varying the resistance (r_l) and inductance (L_l) of the interconnected line, as well as the microgrid operating frequency (ω_{MG}) is illustrated in **Fig. 3.27**, **3.28**, and **3.29**, respectively. According to these figures, it is clearly shown that the microgrid system is stable for a specified values' range of the considered parameter. One can observe in **Fig. 3.27**, that the microgrid is stable in the range where the line resistance r_l belongs to the interval $0.7\times r_l$ to $4.6\times r_l$. Where two poles move to the positive real side of the *s*-plane; i. e make the system unstable; if the values of r_l are out of this range. One can see in **Fig. 3.28**, when the line inductance L_l values belong to the range $0.9\times L_l < L_l$, the microgrid is still stable. Nevertheless, out of this range, the poles move to the unstable region and as a result, the microgrid stability is questionable. From **Fig. 3.29**, one can notice when the value of the operating frequency is changed in the range of $0.6\times\omega_{MG} < \omega_{MG}$, the system is stable, and else, it indicates unstable conditions for the system. Consequently, the obtained results confirm the robustness of the designed controller versus a wide range of the system parameters.

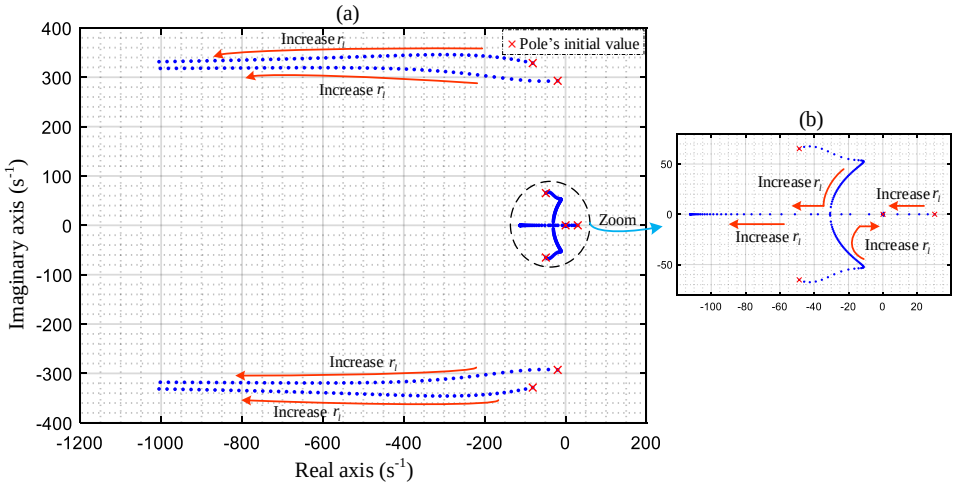

Fig. 3.27. Family of the closed-loop eigenvalues of the obtained global model for line inductance variations; (a) case 01, and (b) Zoom.

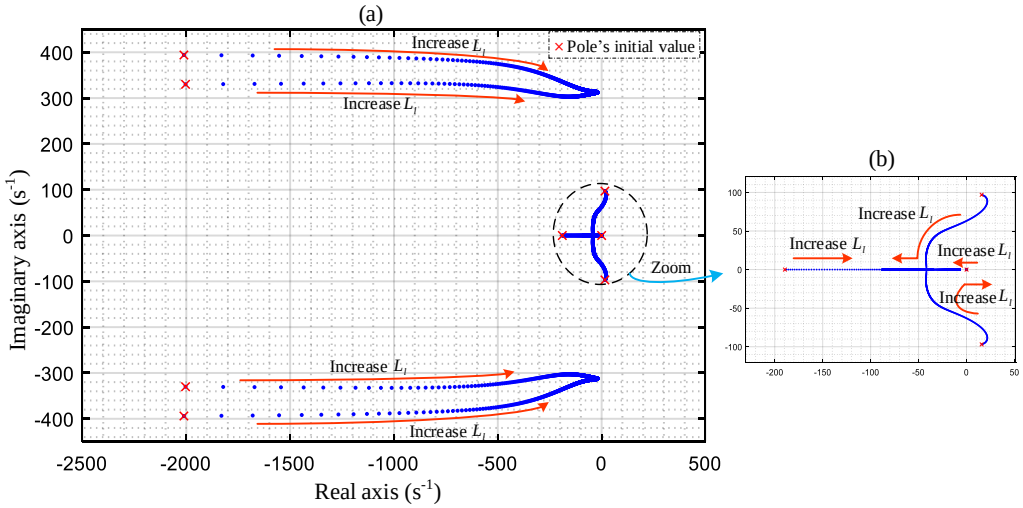

Fig. 3.28. Family of the closed-loop eigenvalues of the obtained global model for line inductance variations; **(a)** case 02, and **(b)** Zoom.

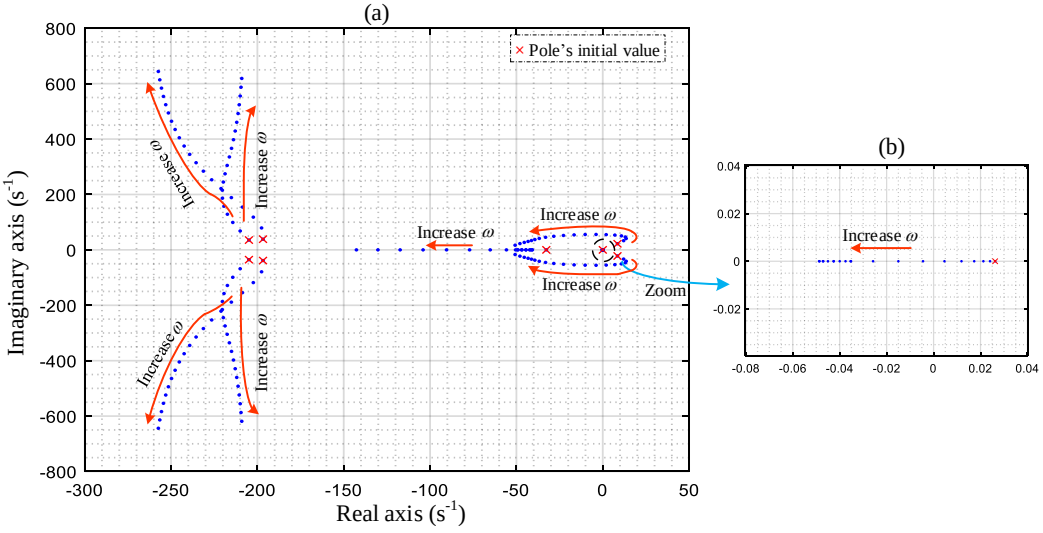

Fig. 3.29. Family of the closed-loop eigenvalues of the obtained global model for ω_{MG} variation; **(a)** case 03, and **(b)** Zoom.

3.5. Conclusion

Phasor dynamic modeling, analysis, and control design of the tertiary control based on the ESOG-FLL scheme for a single-phase droop-controlled microgrid during grid-connected mode are developed, in this chapter. The proposed modeling approach based on the dynamic phasor concept is adopted to derive an accurate model of the active and reactive power flow between the grid and the microgrid. Besides, the dynamic of the active and reactive power calculations, which are included in the obtained model, are extracted by exploiting the SOGI-FLL scheme functions. The accuracy of all the obtained models for predicting the dynamic behavior of the corresponding block is verified. By using the obtained closed-loop model, stability analysis, and a comprehensive tuning guideline are developed to select properly the parameters of the tertiary controller. The obtained results corroborate that the proposed power flow modeling approach is a useful and reliable tool for analyzes, planning, design, and control for a single-phase microgrid. Besides, it confirms the necessity of including the power estimate dynamics in the power flow modeling. Furthermore, the study shows that the designed controller ensures the power flow between the grid and the microgrid's good performance regarding transient response and steady-state solution.

The simulation tests suggested for validating the proposed approach-based designed tertiary controller are reported in the following chapter.

Chapter 4:

Numerical Simulations and Experimental Implementation

This chapter presents simulations and experimental implementation that validate the performance and the robustness of the proposed secondary and tertiary control strategies intended for single-phase droop-controlled AC microgrid. In addition, it provides the results obtained corresponding to performed case studies and practical tests, and discussions as well.

4.1. Introduction

In microgrids, the focus of researchers is on developing and optimizing algorithms and hardware that improve the control system performance and making their adoption viable and highly advantageous. To test and evaluate the efficacy of these developed approaches, simulations, as well as real-time experiments, are generally established. In the present chapter, the test of the performance of the proposed control strategies, in the previous chapters, through simulation study, and real-time validation for different operating modes of single-phase VSIs-based microgrid are addressed. The main idea behind these simulations is to demonstrate the performance of the designed controls in terms of voltage and frequency restoration, load sharing capabilities, grid synchronization, and optimal power flow during island and grid-tie mode operation.

Considering the suggested control approaches, the present chapter is categorized into two parts. The performance evaluation of the proposed secondary control for single-phase VSIs forming MG is explored in the first part, which in turn is classified into two subsections. The first subsection provides the simulation studies based on MATLAB/Simulink environment, the obtained results, and discussions. While, in the second subsection, the experimental setup of the designed secondary control applied to an autonomous microgrid formed by two DGs is described. Also, this subsection gives the results and the respective discussions.

The second part of this chapter presents the simulations of the tertiary control approach for grid-connected MG. The designed controller is applied for the power flow control of single-phase grid-tied VSIs. Different case studies and tests are carried out under load disturbances and various grid operating conditions. Moreover, the obtained results and discussions are highlighted.

4.2. Secondary control

Simulation studies and experimental tests of the secondary control layer intended for single-phase autonomous MG are presented in this section.

4.2.1. Numerical Simulation

In the present section, a simulation study, under MATLAB/Sim Power System environment, is carried out in order to assess the effectiveness and the robustness of the proposed secondary

control approach. As illustrated in **Fig. 4.1**, the structure of a system test of an islanded microgrid is built up. The constructed microgrid consists of two DG units with the same power rate (2.5 kW), feeding a local inductive load (40Ω, 1mH). The secondary control parameters are selected according to the presented tuning process so that its response is ten times slower than the primary control. The parameters taken in the simulation study are reported in **Table. 1** it is worth mentioning that a DC component of the percentage of 5% from the voltage fundamental component is considered in the measurement devices.

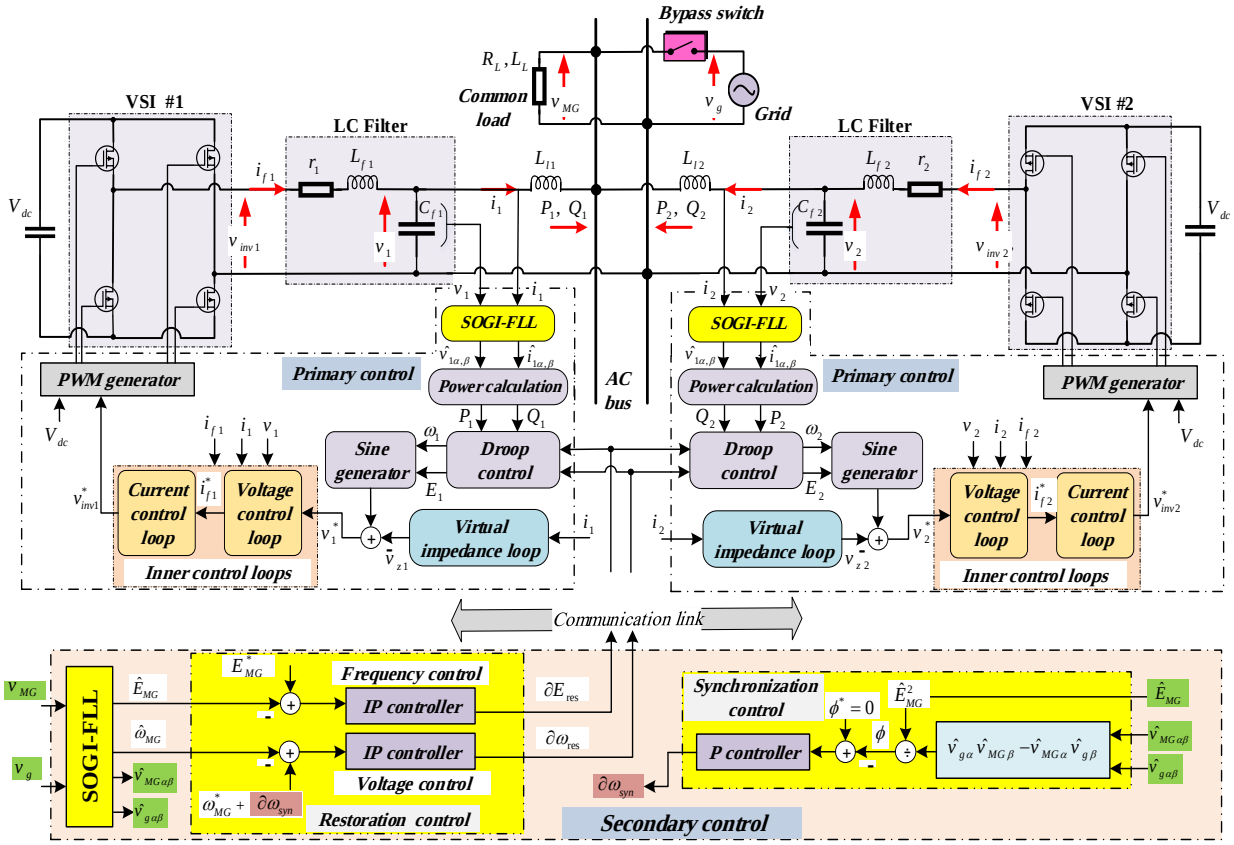

Fig. 4.1. Implemented secondary control for a single-phase islanded MG consists of two droop-controlled paralleled VSIs.

TABLE. 1. POWER STAGE AND CONTROL PARAMETERS

Parameter	Symbol	Unit	Value
Inverters power stage			
Nominal voltage (RMS)	E^* (RMS)	V	220
Nominal frequency	$\omega^* / 2\pi$	Hz	50
DC bus voltage	V_{dc}	V	450
Loads	R_L, L_L	Ω, mH	40, 1
Filter capacitor	C_{f1}, C_{f2}	μF	26
Filter inductor	$r_{1,2}$, $L_{f1,2}$	Ω, mH	0.5, 2.5
DG1 line impedance	L_{l1}	mH	0.9

DG1 line impedance	L_{l2}	mH	1.2
SOGI-FLL scheme			
SOGI gain	k	-	0.7
FLL gain	Γ	s^{-1}	40
Primary control			
Frequency-droop gain	m	W/rad.s	0.0003
Amplitude-droop gain	n	VAr/V	0.003
Virtual impedance	L_v	mH	4
Secondary control			
Voltage proportional gain	$k_{p\text{-}E}$	-	-0.45
Voltage integral gain	$k_{i\text{-}E}$	s^{-1}	1.57
Frequency proportional gain	$k_{p\text{-}f}$	-	-0.22
Frequency integral gain	$k_{i\text{-}f}$	s^{-1}	2.67
Synchronization gain	$k_{p\text{-}\varphi}$	s^{-1}	0.76
Communication delay time	τ	ms	0.5

The following case studies are considered:

- Case 1: This case aims to evaluate the performance of the frequency and amplitude restoration control in the presence of frequent load changes. To this end, the microgrid begins with the no-load operating condition, and next, DG units (1 and 2) start to feed a common inductive load at t = 1 s, while only the primary control is running. At t = 2 s, the frequency and amplitude restoration control are activated, then a load change is realized, by disconnecting and reconnecting a resistive load (40 Ω) from/to the microgrid at t = 5 s and t = 7.5 s, respectively.

- Case 2: This case study aims to test the proposed restoration controller performance under the DG disconnection operating condition. For this purpose, a sudden disconnection of the inverter 2 from the microgrid is programmed at t = 5 s, and only inverter #1 remains to supply the common load, where the same scenarios; as the first case by starting with no-load and next enabling the primary and secondary controls with an inductive load; are considered.

- Case 3: This case study analyses the performance of the synchronization controller. So, this controller is enabled at t = 5 s, to synchronize the microgrid with the main utility grid (50 Hz and 220V).

Fig. 4.2 shows the transient responses of the frequency, amplitude, and active and reactive powers, of DG1, DG2, and the microgrid (or common load bus (CLB)), for the first case study. It can be observed that at no-load operating condition, the frequency and the amplitude of each DG unit and the CLB are at their nominal values. Then, when a load is suddenly connected; while the primary control is running; they drooped with the same amounts in order to share the active and reactive powers of the load, which is also demonstrated. When the restoration process is enabled

(at t = 2 s), the frequency and amplitude static deviations produced by the droop control are removed. Notice that the frequency and voltage inside the microgrid are seamlessly restored to the nominal values, i.e., 50 Hz and 311V. Also, as it is shown, the proposed secondary controller ensures a smooth frequency and voltage recovery when a load change suddenly occurs (at t = 5 s and 7.5 s), and the active and reactive powers-sharing is still guaranteed. We note that the proposed controller provides good transient responses in respect to the desired predefined performance; settling time around 1 s and without overshoots.

The obtained results demonstrating the performance of the proposed restoration control for case 2 are given in **Fig. 4.3**. It can be seen that when the DG2 is disconnected from the microgrid (at t = 5 s), the designed controllers restore successfully the frequency and amplitude of the microgrid, formed only by DG1, to their nominal values. Note that the settling time of the frequency and voltage transient responses is about 1 s. In addition, it can be seen that the DG2 variables are set to the nominal values. It is worth mentioning that the small difference between the voltage amplitude of DG1 and the nominal value is due to the voltage amplitude of the line impedance.

Fig. 4.4 illustrates the obtained results for case 3. It can be observed that, when the synchronization process is enabled (at t = 5 s), the phase angle difference between the microgrid and the main utility grid moves toward zero. Also, the frequency and amplitude of the DG units and CLB are fixed to the grid set points. While the active power remains constant during the synchronization process. We notice that the settling time of the synchronization transient response is around 5 s.

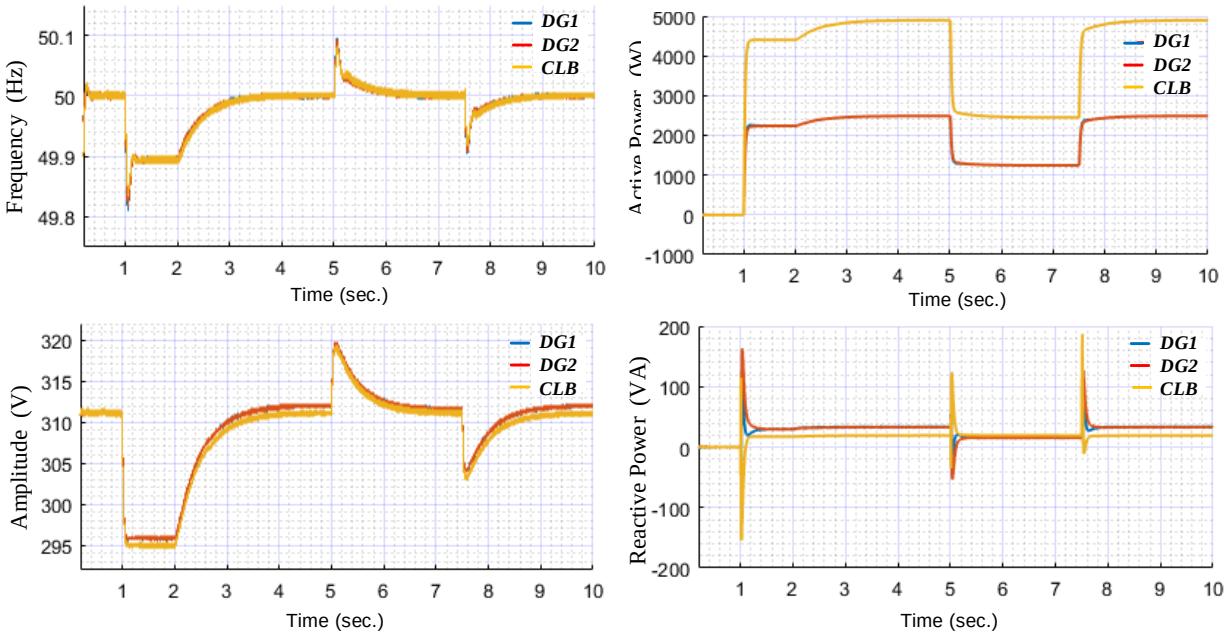

Fig. 4.2. Obtained results in response to case 1.

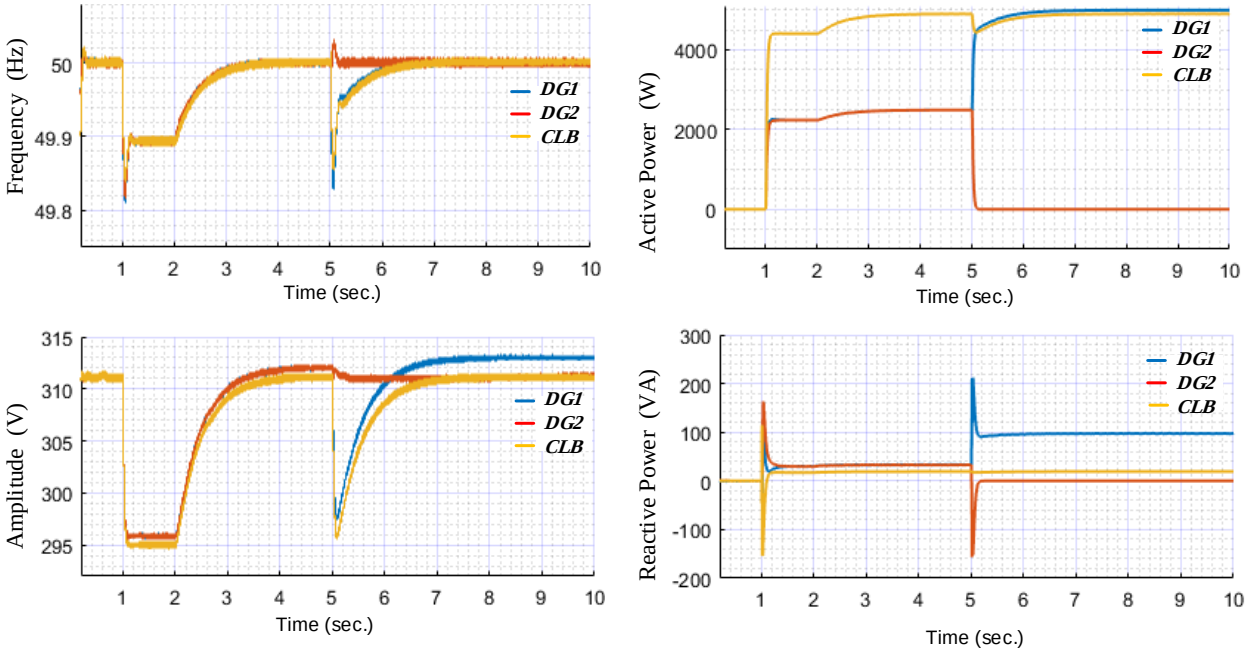

Fig. 4.3. Obtained results in response to case 2.

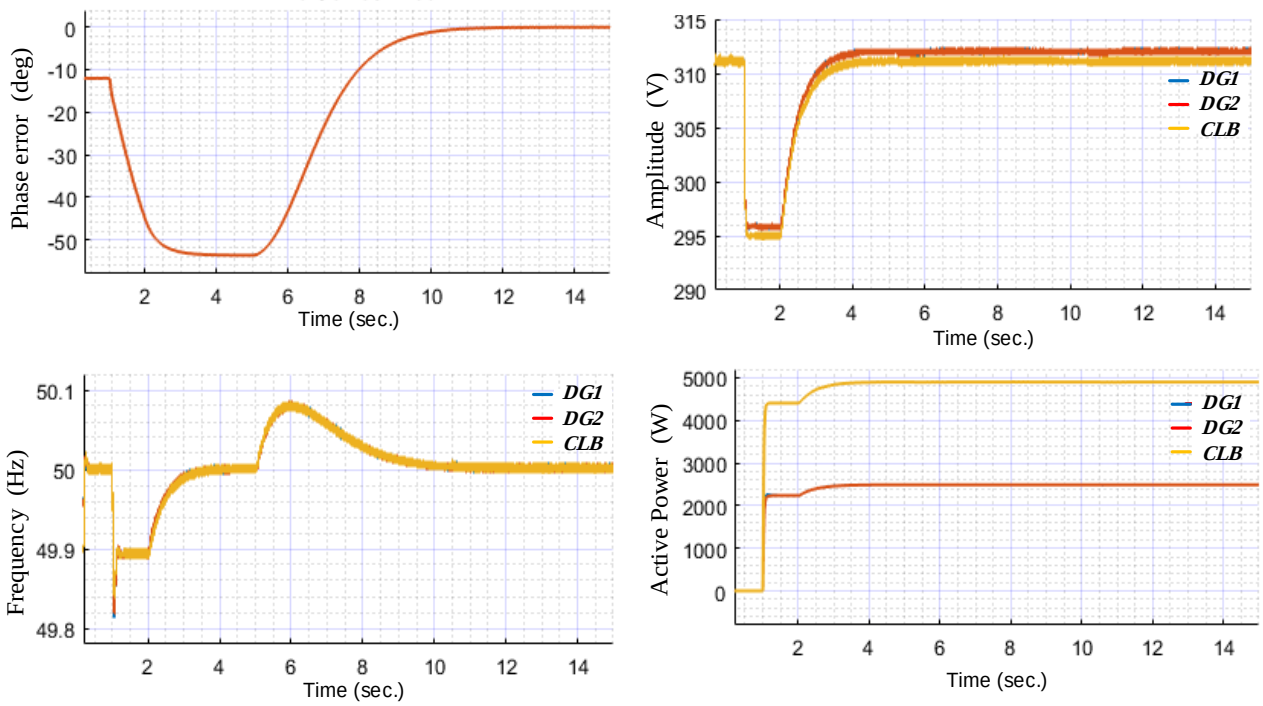

Fig. 4.4. Obtained results in response to case 3.

4.2.2. Experimental Results

In order to verify the theoretical analysis as well as evaluate the performance of the proposed secondary control approach, an experimental setup, as shown in **Fig. 4.5**, is built and tested in the

lab. This experimental setup is similar to the structure presented in **Fig. 4.1**, where two single-phase full-bridge VSIs with LC filter are connected in parallel, forming an islanded microgrid with a power rate of 0.1 kW. The primary control of each DG unit and the designed secondary control are implemented in a separate ARM Cortex microcontroller (STM32F407). RS232 (URAT) protocol is used to communicate between these microcontrollers for the aim of sending the produced control signals by the secondary controller toward the DGs local controllers. In addition, measurement sensors are used to provide the required voltages and currents to the ARM Cortex microcontrollers via signal conditioning circuits. For more details, the algorithms of the primary and secondary control, given in the upper part of **Fig. 4.5**, are implemented in MATLAB/Simulink based STM32F4 Embedded Target and, then, the generated code using Embedded Coder is loaded into the STM32F4 board. The sampling frequencies of the primary and secondary controls are set to 10 kHz and 1 kHz, respectively. The power stage and the control parameters taken in this experiment are summarized in **Table. 2**.

TABLE. 2. EXPERIMENTAL PARAMETERS

Parameter	**Symbol**	**Unit**	**Value**
Inverters power stage			
Nominal voltage (RMS)	E^* *(RMS)*	V	30
Nominal frequency	$\omega^* / 2\pi$	Hz	50
DC bus voltage	V_{dc}	V	60
Loads	R_L	Ω	8
Filter Capacitor	C_{f1}, C_{f2}	µF	16, 18
DG1 Filter inductor	r_1, L_{f1}	Ω, mH	0.3, 2.7
DG2 Filter inductor	r_2, L_{f2}	Ω, mH	0.5, 2.6
DG1 line impedance	L_{l1}	mH	0.8
DG2 line impedance	L_{l2}	mH	0.5
SOGI-FLL scheme			
SOGI gain	k	-	0.7
FLL gain	Γ	s^{-1}	40
Primary control			
Frequency-droop gain	m	W/rad.s	0.003
Amplitude-droop gain	n	VAr/V	0.03
Virtual impedance	L_v	mH	2
Secondary control			
Voltage proportional gain	$k_{p\text{-}E}$	-	-0.69
Voltage integral gain	$k_{i\text{-}E}$	s^{-1}	0.49
Frequency proportional gain	$k_{p\text{-}f}$	-	-0.71
Frequency integral gain	$k_{i\text{-}f}$	s^{-1}	0.58
Synchronization gain	$k_{p\text{-}\phi}$	s^{-1}	0.35
Communication delay time	τ	ms	1

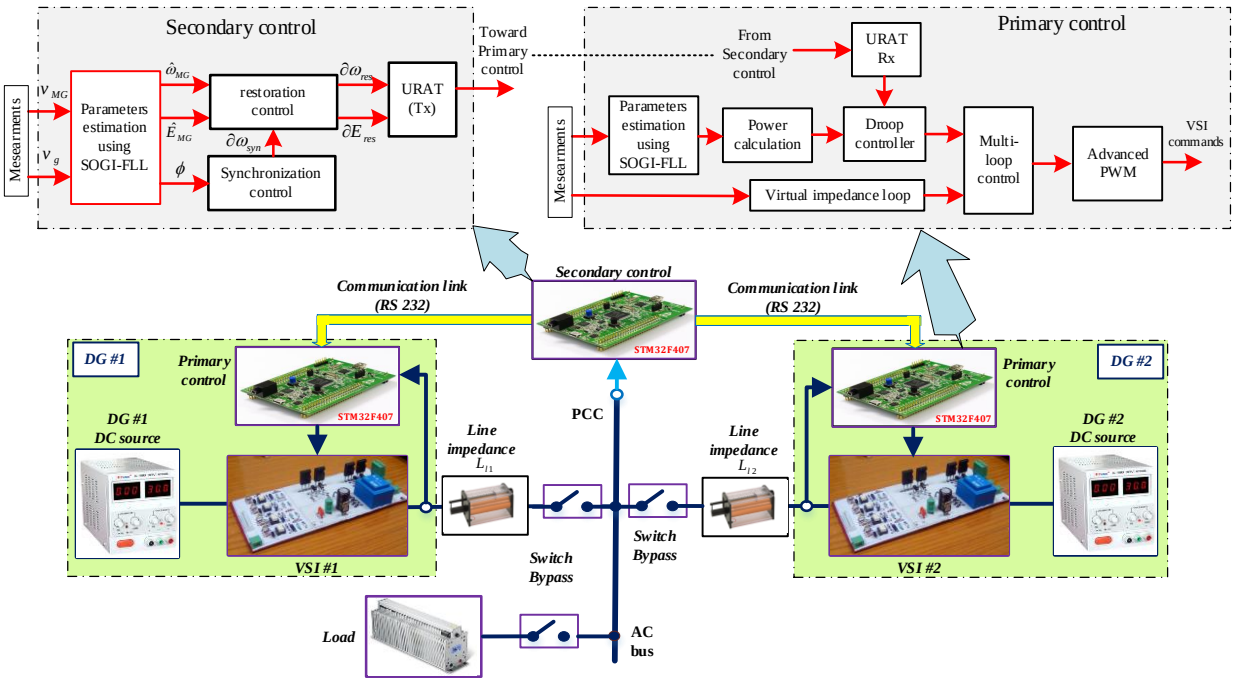

Fig. 4.5. Block diagram of the experimental setup based on ARM Cortex μCs.

It is worth noting that the same cases as the simulation study are considered in the experimental test. However, these tests are carried out at different times and load values. In addition, the obtained results are extracted from ARM microcontrollers and plotted using MATLAB to provide better quality.

In the first experiment, before the secondary control for frequency and voltage restoration is enabled at t = 15 s, only the primary control was running. Next, at t = 25 s and t = 35 s, a resistive load of 8 Ω is suddenly disconnected and reconnected from/to the MG. **Fig. 4.6** shows how the restoration control regulated the frequency and voltage deviation inside the DGs in response to this experiment test. From these figures, it can be seen that frequency and amplitude of both DGs voltage and at the CLB are seamlessly restored to their nominal values when the secondary control is enabled (at t = 15 s), and after, load change as well (at t = 25 s and 35 s). Besides, it can be remarked that the settling time of frequency and amplitude transient response is around 5 s. Notice that the active and reactive powers-sharing between the DG units is still can be observed.

In the second experiment, after activating the secondary control at t = 15 s, the DG2 unit is suddenly disconnected from the MG at t = 26 s. Scopes of **Fig. 4.7** show that the secondary controller is able to regulate successfully the frequency and amplitude to their rated values with the desired transient response (a settling time of 5 s and without overshoot). In the third experiment, the synchronization algorithm is introduced to synchronize the MG to the grid at t = 25 s, after enabling the secondary control at t = 15 s. **Fig. 4.8** depicts the waveforms of the main grid and the

MG voltages and their zooms for each scenario. It demonstrated that these voltages are accurately synchronized when the synchronization control is activated. In addition, it can be observed in **Fig. 4.9**, that the phase angle difference between the main grid and MG is matched to zero after a settling time of 10 s. Moreover, as shown, the voltage frequency and the amplitude of the CLB and the main grid are also matched. It is worth mentioning that the notches appearing in the figures of the experimental results are due to the power supply fluctuations.

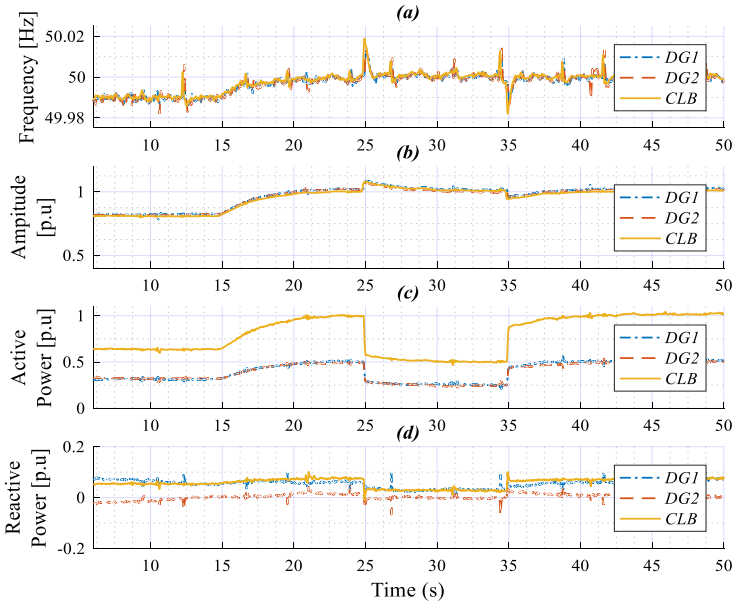

Fig. 4.6. DGs and CLB: ***(a)*** frequency, ***(b)*** amplitude, ***(c)*** active power, and ***(d)*** reactive power in response test 01.

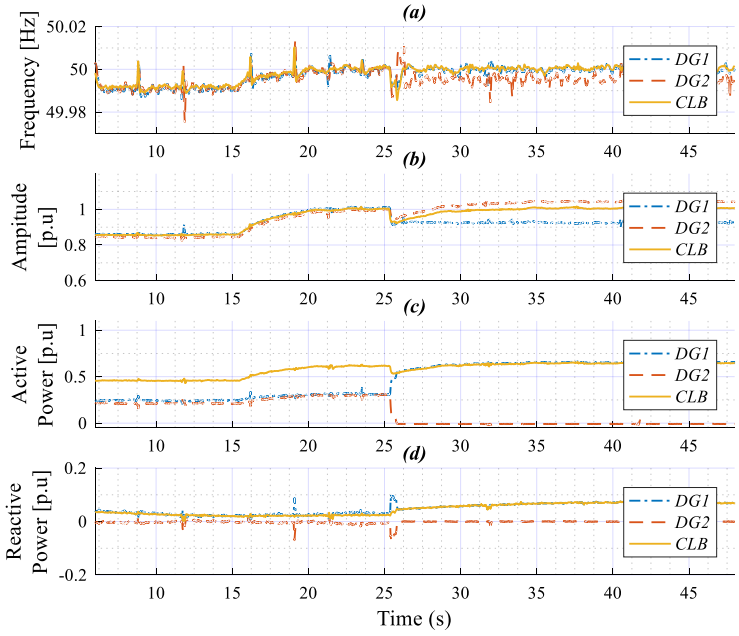

Fig. 4.7. DGs and CLB: ***(a)*** frequency, ***(b)*** amplitude, ***(c)*** active power, and ***(d)*** reactive power in response to test 2.

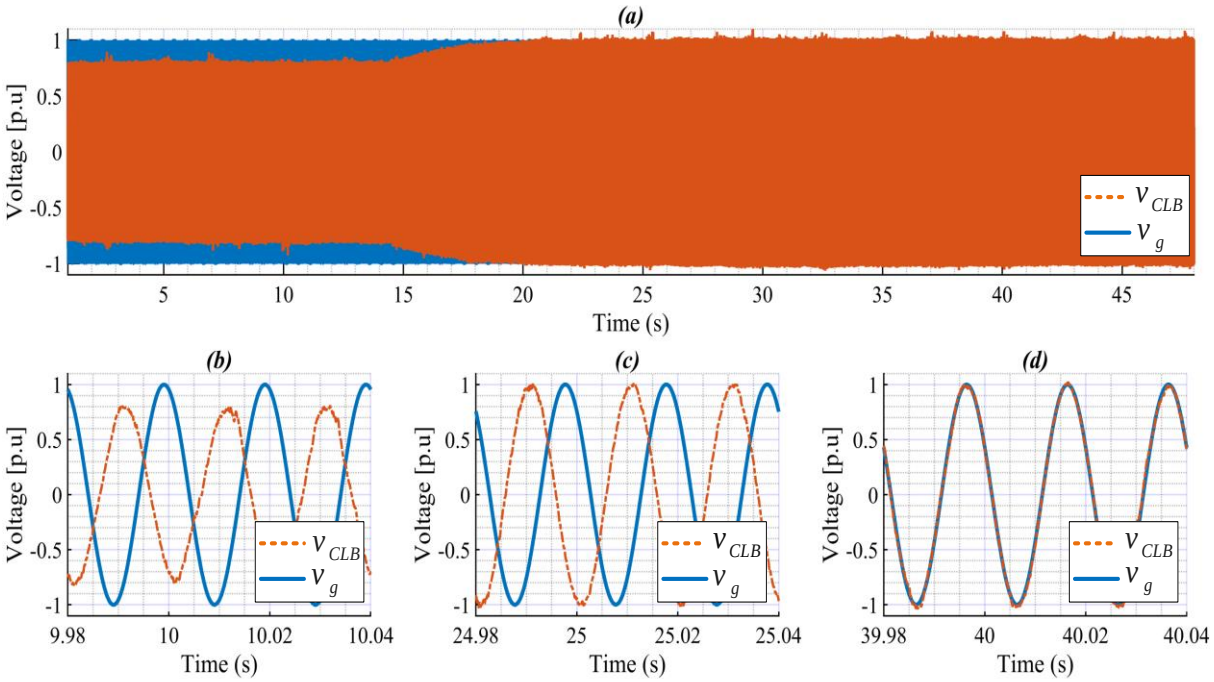

Fig. 4.8. ***(a)*** Grid and CLB voltages and their zooms when: ***(b)*** only the primary control is running, ***(c)*** activating the restoration control, ***(d)*** enabling the synchronization control.

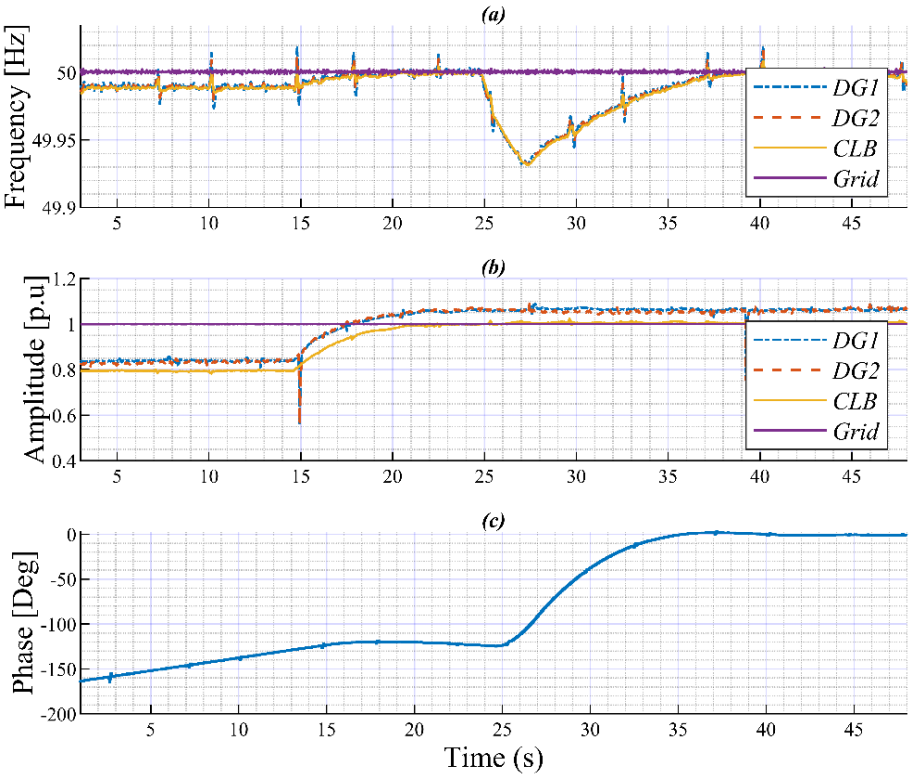

Fig. 4.9. Experimental results: ***(a)*** frequency, ***(b)*** amplitude, and ***(c)*** phase angle in response to test 3.

4.3. Numerical Implementation of the Tertiary Control

The study in this section covers the power flow control of a VSI in grid-connected operation mode. The main function of the proposed controller is to control optimally the real and reactive power exchange (import/export) between a VSI and the utility grid (at the PCC). Numerical results and discussions are also provided in this section.

To demonstrate the effectiveness and the robustness of the proposed tertiary control approach, the system depicted in **Fig. 4.10** is simulated using MATLAB/Simulink/Sim power system. The simulated test system consists of a DG feeding a local load and connected to the main grid thought line impedance and a power flow control based-hierarchical control. The DG includes a DC source, H-bridge inverter, and an LC filter unit and has its own local primary controller. A centralized secondary controller is also considered in this hierarchical control, which receives control input from the tertiary control layer. The proposed tertiary control layer is introduced to ensure optimal power flow of a single-phase droop-operated VSI towards the main grid while supplying the local load. Hence, the power flow controller is expected to control the VSI for feeding the local load and, (a) the injection of the power excess to the main grid if the VSI is able to fulfill the load power demand, or (b) to absorb (export) the needed power form the main grid if the VSI cannot deliver the demand power by the local load.

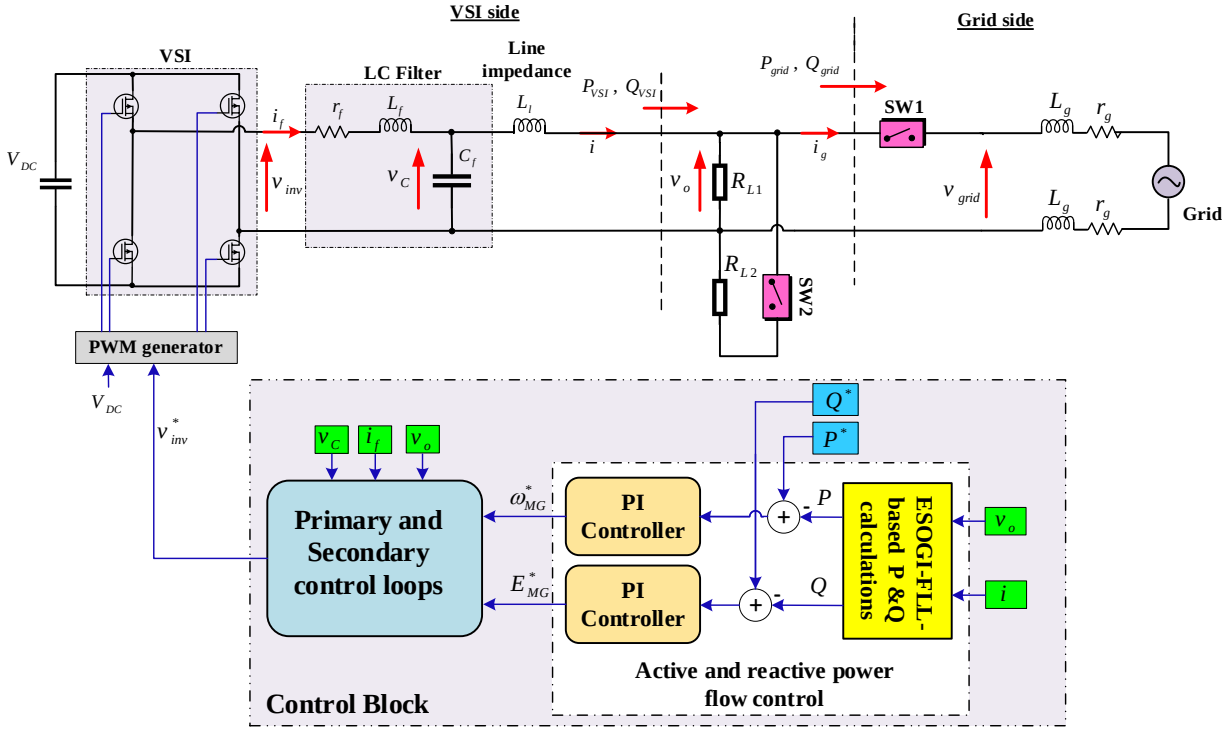

Fig. 4.10. Scheme of a grid-connected single-phase VSI-based MG system feeding a local load, with the proposed tertiary control-based hierarchical control.

It is worth noting that due to the large simulation time (minutes); that cannot be implemented in MATLAB, sim power system environment; the sampling rate of each control level is reduced. Therefore, the sampling frequencies of the primary control, secondary and tertiary control are set to 1 kHz, 10 kHz, and 20 kHz, respectively. Also, the control parameter values of the compensators are adjusted according to the new desired settling time of the transient responses. The simulation parameters are given in **Table. 3**. Note that the value of the DC offset in the measurement devices is not negligible and is set to 5% from the fundamental voltage component.

The performance of the proposed control strategy is examined throughout the numerical tests given below based on suggested operation scenarios. Indeed, the first operation scenario is considered for all the tests, except the last one. At t = 0 s, the microgrid starts operating in island mode feeding a resistive local load of 8 Ω (2 kW), then at t = 0.5 s, the transition process from islanded to grid-tied mode operation is performed, and when the switch (SW1) is closed, the MG is reconnected to the main grid. After this scenario, the next scenarios for the VSI-based MG operating in grid-connected mode are carried out according to the considered tests presented as follows:

- In test 1, a step-change in the active power reference of the DG unit (VSI) from 5 kW to 6 kW is set at t = 1 s.
- In test 2, the grid frequency is varied from 50 Hz to 50.2 Hz at t = 0.75 s and back to 50 Hz at t = 1.1 s.
- In test 3, a symmetrical grid voltage sag of 0.1 p. u (from the grid fundamental amplitude), for 7.5 cycles (form t = 0.85 s to t = 1 s), is set.
- In test 4: the performance of the proposed controller are examined in the event of load changes. Thus, a resistive load of 8 Ω (1 kw) is suddenly added to the local load at t = 1 s.
- In test 5: exporting power from the utility grid is considered. Therefore, at = 0 s the MG is operating in grid-connected with a local load of 16 Ω (4 kw), then at t = 0.4 a resistive load of 16 Ω (4 kw) is suddenly added to the local load, after at t = 0.8, the the added load is disconnected.

TABLE. 3. POWER STAGE AND POWER FLOW CONTROL PARAMETERS

Parameter	Symbol	Unit	Value
Inverters power stage			
Nominal voltage (RMS)	E^* (RMS)	V	220
Nominal frequency	$\omega^* / 2\pi$	Hz	50
DC bus voltage	V_{dc}	V	450
Loads	R_L	Ω	8
Filter capacitor	C_f	µF	26
Filter inductor	r_f, L_f	Ω, mH	0.5, 2.5
Line impedance	L_l	mH	0.9
Grid impedance	L_g, r_g	mH, Ω	0.1,0.001
Grid side load	R_{grid}	Ω	10
SOGI-FLL scheme			
SOGI gain	k	-	0.7
FLL gain	Γ	s^{-1}	40
Power flow control			
P proportional gain	$k_{p\text{-}E}$	-	-0.45
P integral gain	$k_{i\text{-}E}$	s^{-1}	1.57
Q proportional gain	$k_{p\text{-}f}$	-	-0.22
Q integral gain	$k_{i\text{-}f}$	s^{-1}	2.67

The obtained results are given in the figures below, they depict the waveforms of the active and reactive powers generated by the VSI side and injected to the main grid, the frequency and amplitude of the VSI, the grid, and at the PCC voltages, and the grid side voltage and current, and the inverter side output voltage and current and their zooms in response to each test.

Figs. 4.11 and **4.12** display the results in response to active power reference change. Based on these figures the following observations can be made:

- During the islanded operating mode, t = 0 to t = 0.5, the VSI provides the active and reactive powers; of 2 kW, 0 kVar; demanded by the local load (**Fig. 4.11 (a)** and **(b)**, respectively). While the real and reactive power of the grid side are equal to zero (**Fig. 4.11 (c)** and **(d)**). In addition, the frequency and the amplitude of the inverter output voltage are drooped and restored to their nominal values (slight oscillations can be observed due to the droop action), meanwhile, the grid frequency and amplitude are set to 50 Hz and 1 p, u (220 V). Further, **Fig. 4.11 (a)** and **(b)** illustrate that the amount of the VSI current is adjusted corresponding to the local load demand, and the grid current is equal to zero, whereas, the VSI tracks the voltage references produced by the droop controller.
- At t = 0.5, the grid switch (SW1) closes resulting in a seamless transition of the MG-based VSI from islanded to grid-connected mode, in which the inverter voltage and frequency synchronize to their new references received from the tertiary control.

- When the MG begins working in a grid-connected mode, as shown in **Fig. 4.11 (a)** and **(b)**, the proposed tertiary controller forces the inverter VSI to flow successfully the desired values of the active and reactive power provided by the center manager, which set to 5 kW and 0 kVar. A part of the active power, 2 kW, supplies the local load, while the excess of the active power, of 3 kW as demonstrated in **Fig. 4.11 (c)**, is injected into the utility grid. **Fig. 4.11. (e)** and **(d)**, illustrate that the frequency and voltage are matched exactly to the grid frequency and voltage (50 Hz, 1 p. u, i.e. 220 V (RMS)) during the grid-connected mode. According to **Fig. 4.12 (a)**, the VSI side current increases relatively to the new active power reference, while the voltage synchronizes to the grid voltage. In **Fig. 4.12 (b)**, the current amount of the grid side arises, this is injected to the main grid.
- When changing the active power reference at t = 1 s, the proposed controller forces the active and reactive powers to successfully flow the new desired values with a good transient response (6 kW) as shown in **Fig. 4.11 (a)**. Consequently, the grid side active power (power excess) is increased, **Fig. 4.11 (c)**, because the required power of the local load is constant (2 kW). Also, the reactive power remains constant with a slight transient when varying the active power. From **Fig. 4.11 (e)** and **(f)**, the frequency of the VSI tracks the frequency of the main grid during this period, while the voltage amplitude of the VSI and the grid side remain constants. The current of the VSI and the utility grid, shown in **Fig. 4.12 (a)** and **(b)**, are increased according to the active power growth, whereas, the voltage of the VSI and the grid are synchronized and kept with their values constant without any oscillations or transients. Further, the proposed power controller ensures the injection of a proper sinusoidal current into the grid, as illustrated in **Fig. 4.12 (c)**. Moreover, **Fig. 4.12 (c)** demonstrates that the grid current and voltage are in-phase which guarantees a unity power factor.

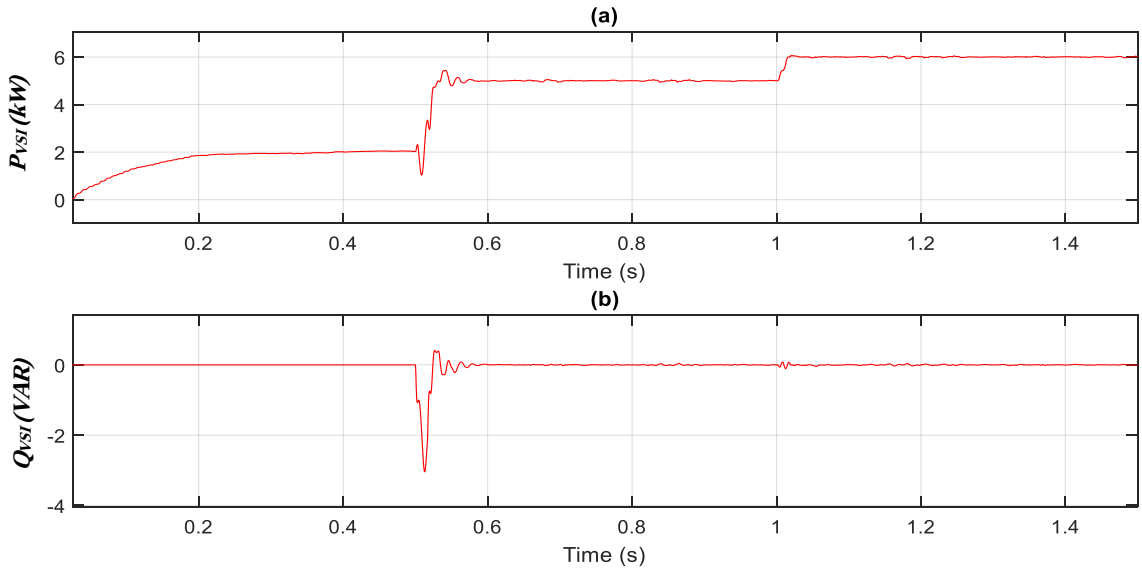

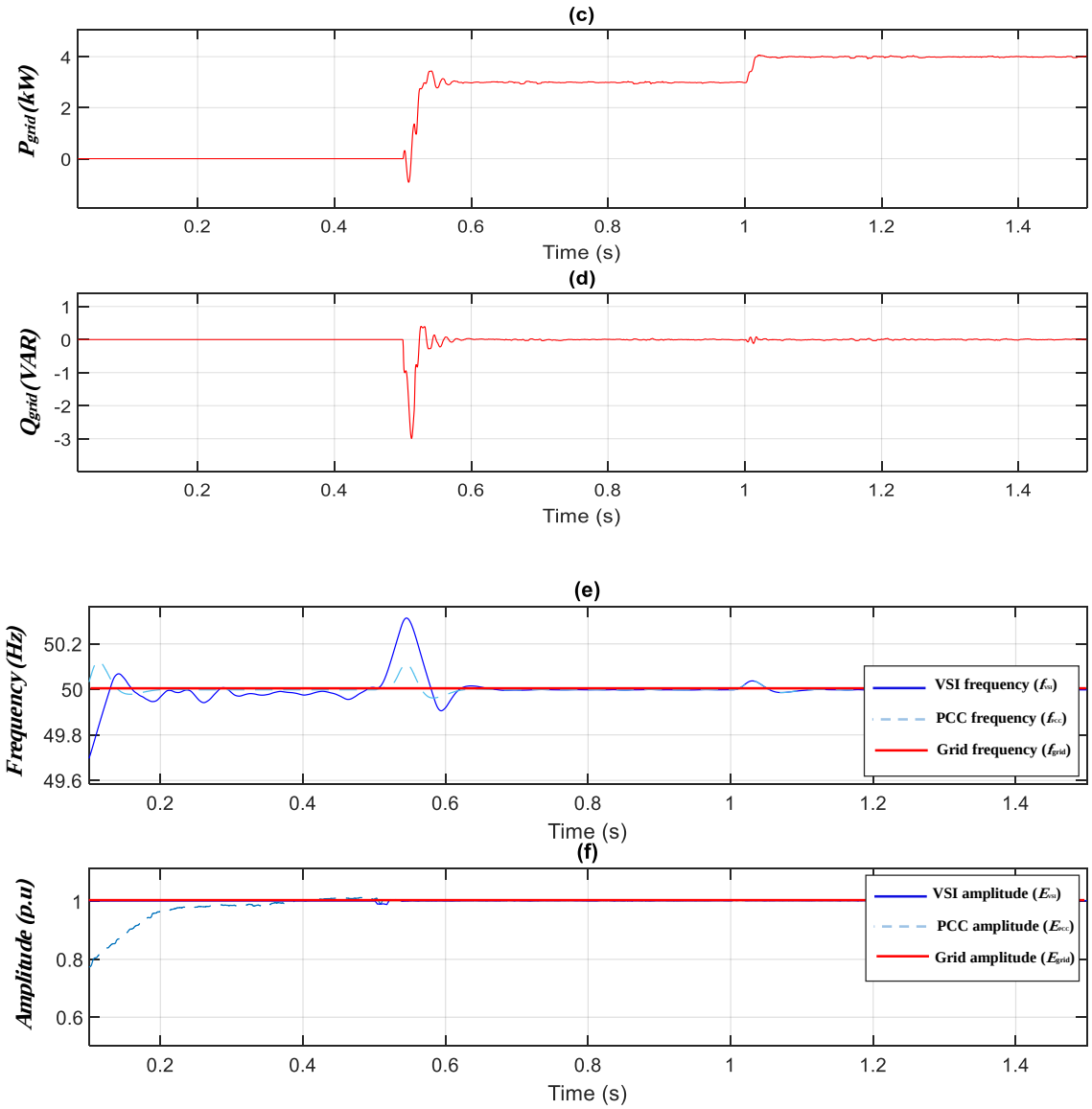

Fig. 4.11. Simulation results acquired with the designed controller in response to test 1.

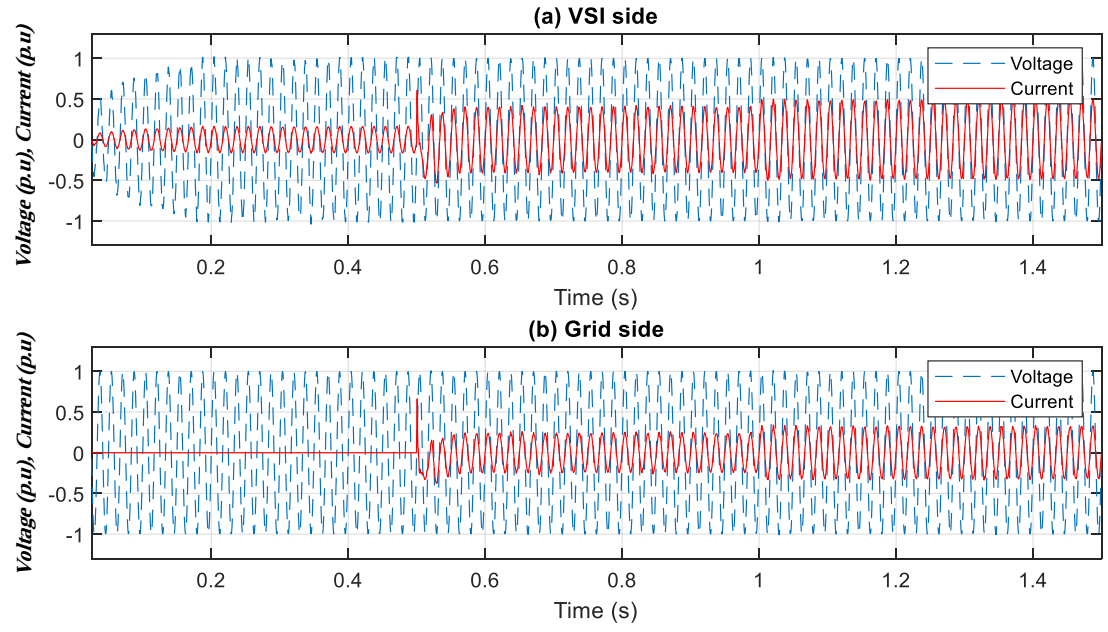

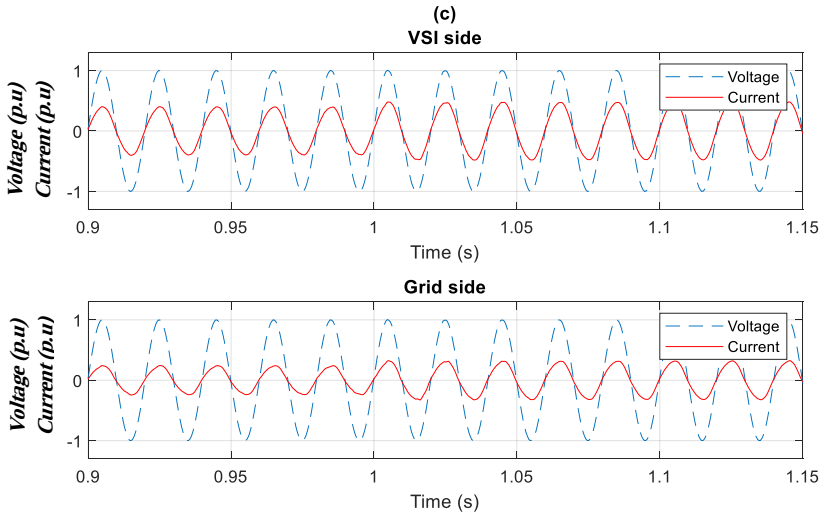

Fig. 4.12. Responses of the voltage and current in test 1; **(a)** inverter side, **(b)** grid side, and **(c)** Zoom.

The results in **Figs. 4.13** and **4.14**, show the performance of the proposed tertiary control in response to the grid frequency variations. The same discussions are considered for the islanded and after the transition mode operation until t = 0.75 s. From **Fig. 4.13 (a)** to **(d)**, one can see that the proposed control fixes the active and reactive power of the VSI to their desired values, and the grid powers, also, remain constant, even when the grid frequency is varied at t = 0.75 s and t = 1.1 s, in which just slight transients can be observed. The transient response presented in **Fig. 4.13 (c)**, illustrates that the frequency of the VSI and at the PCC match with the grid frequency, while in **Fig. 4.13 (b)**, one can notice that the voltage amplitudes do not change during all the rest of the simulation time. Also, the current and voltage of the VSI side and the grid side, shown in **Fig. 4.14**, remain unchanged, just a slight transient, during the grid-connected mode and under frequency variations. Furthermore, one can see that the current injected into the grid has a pure sinusoidal form and in phase with the voltage, hence, a unity power factor is expected.

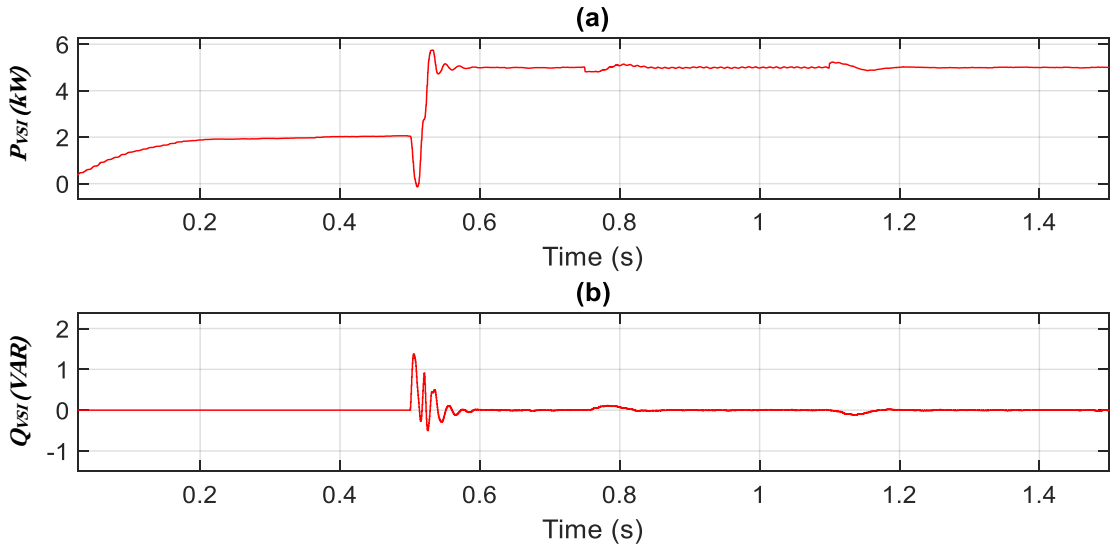

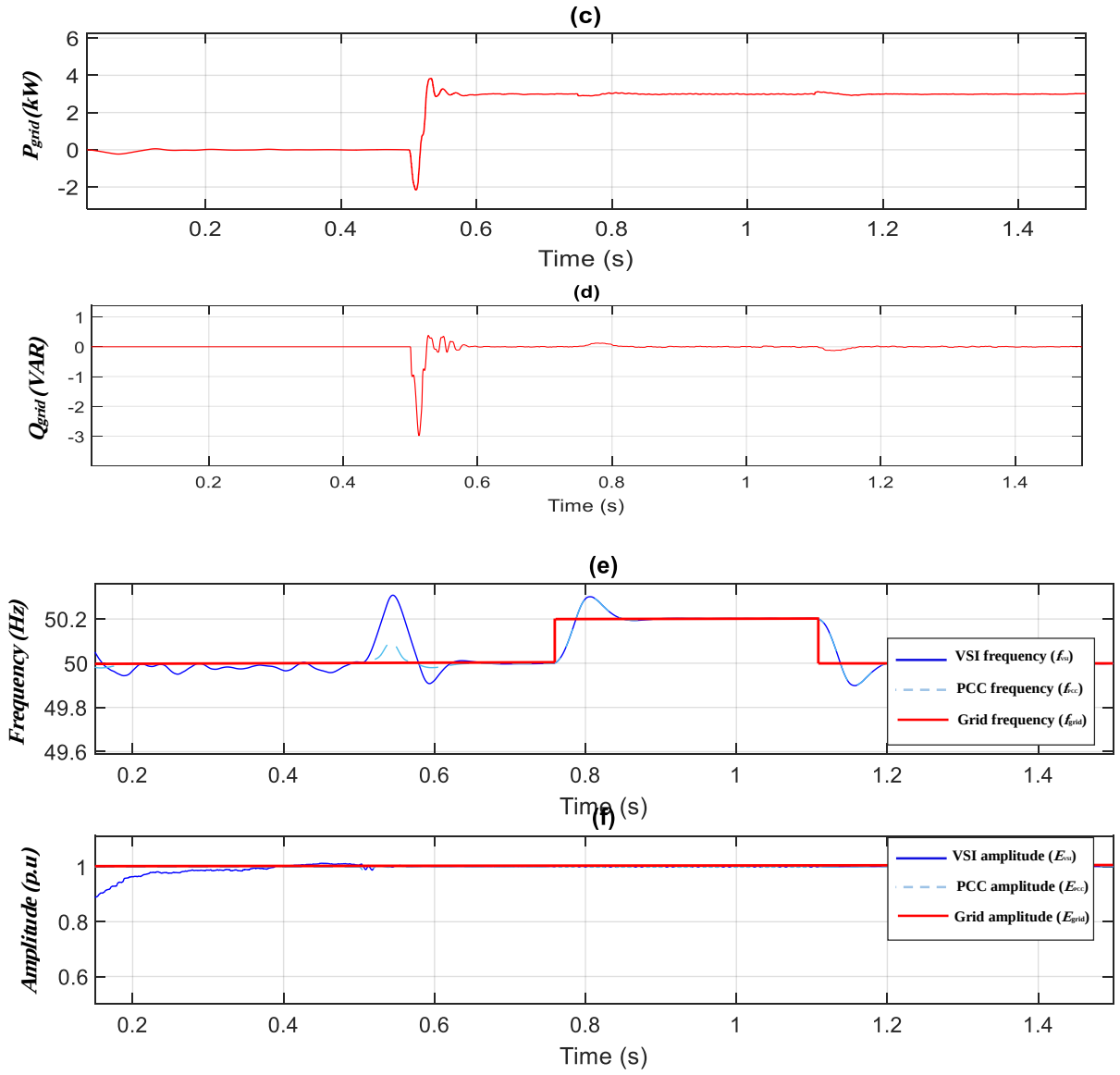

Fig. 4.13. The obtained results in response to grid frequency step change (test 2).

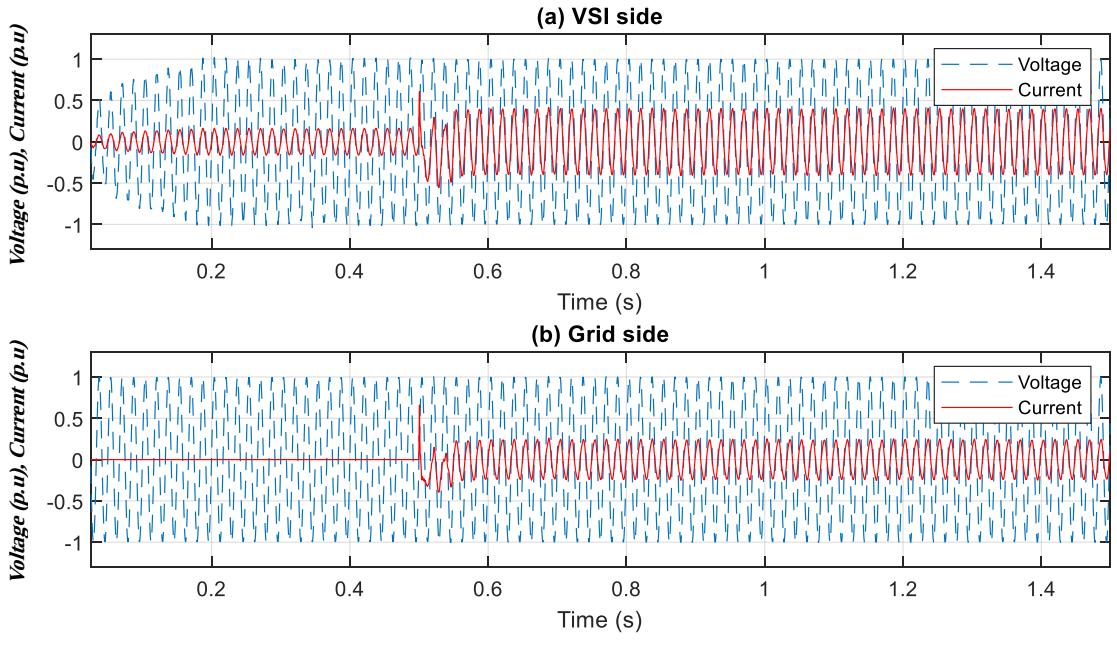

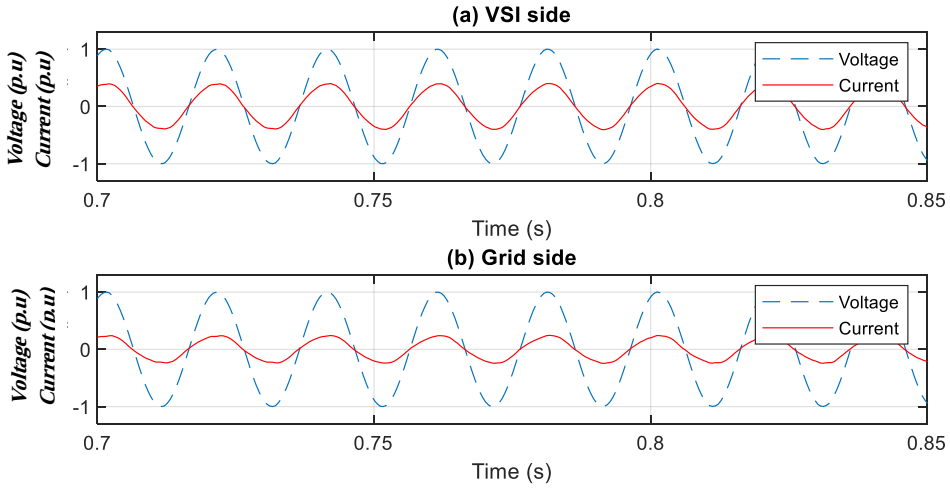

Fig. 4.14. Responses of the voltage and current in test 2; **(a)** inverter side, **(b)** grid side.

The transient responses of the proposed control strategy for grid voltage dip are shown in **Figs. 4.15** and **4.16**. When the grid voltage sag appears at t = 0.8 s, it affects the voltage and the current, of the VSI and the grid, as can be seen in **Figs. 4.15 (b) and 4.16**, hence, the injected active power into the grid side increases, while the active and reactive power of the VSI are fixed by the controller to their references, as shown **Fig. 4.15 (a), (b)** and **(c)**. Whereas, the grid reactive power remain constants with sight transients during voltage sag. From **Fig. 4.15 (e)**, it is can be noticed that the VSI frequency and at the PCC match the grid frequency, where transient in these frequencies is observed under voltage sag. The voltage amplitude transient response of **Fig. 4.15 (f)**, shows that the amplitudes of the inverter and at the PCC track the dripped grid amplitude. According to **Fig. 4.16**, it can be remarked that the voltage of the VSI and the grid are slopped with the same amounts during the voltage sag. Also, it can be seen that the inverter and grid currents increase to generate the expected active power by the inverter and to injected the expected grid power, meanwhile, they keep their sinusoidal forms, as depicted in **Fig. 4.16 (c)**. Furthermore, when the voltage sag is eliminated at t = 1 s, the system is back to operate in normal conditions.

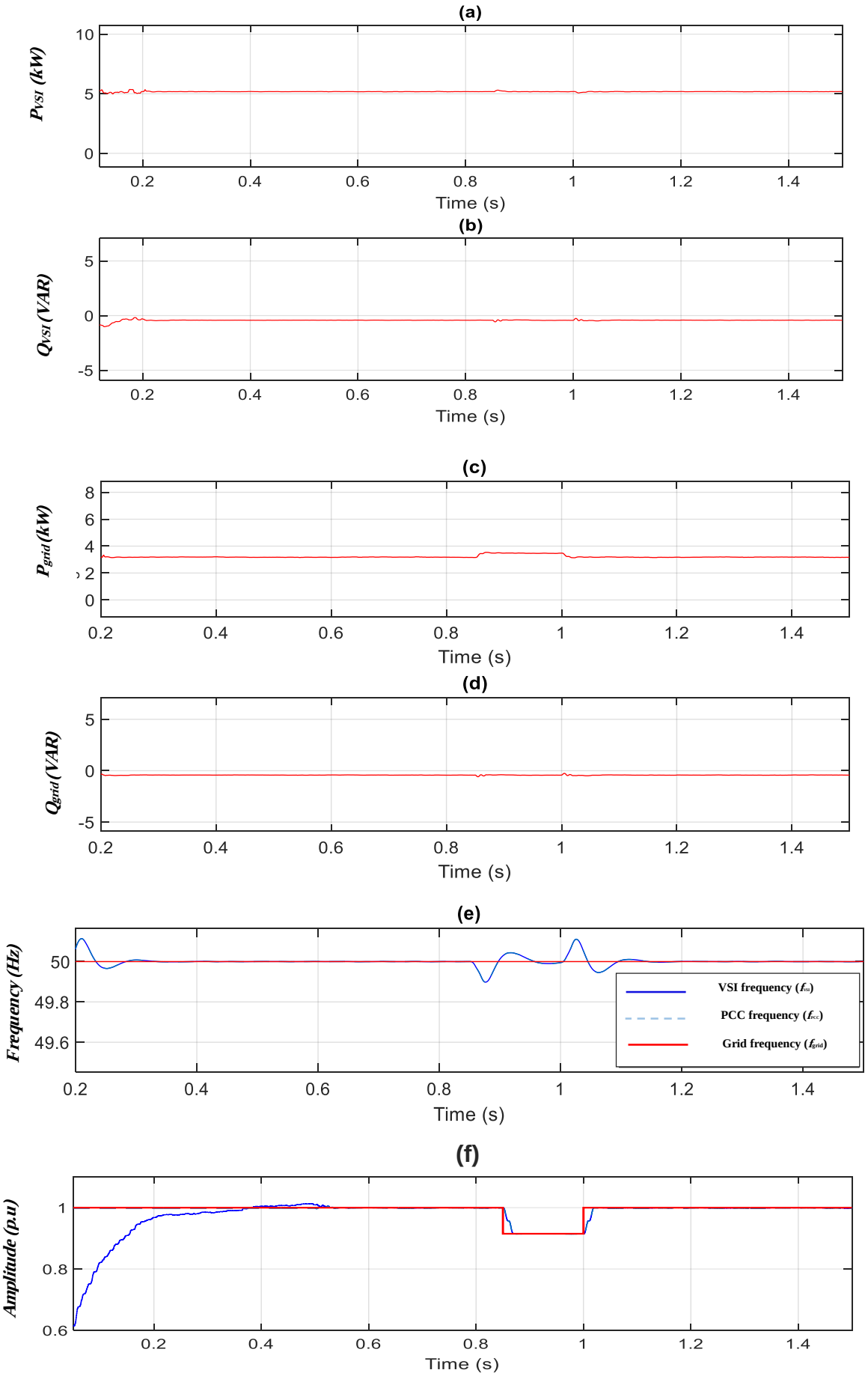

Fig. 4.15. The obtained results in response to grid voltage sag (test 3).

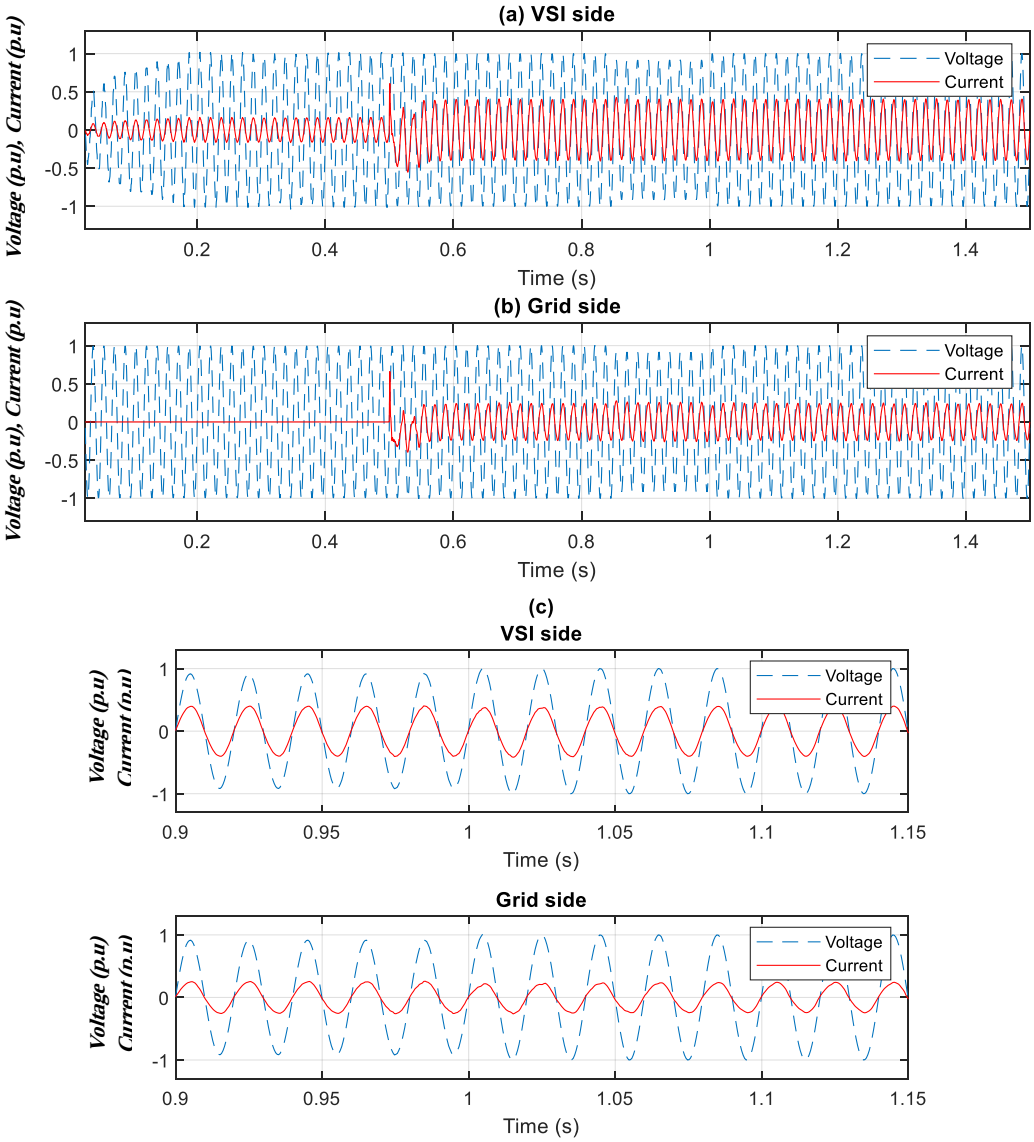

Fig. 4.16. Responses of the voltage and current in test 3; **(a)** inverter side, **(b)** grid side, and **(c)** zoom.

Fig. 4.17 and **4.18** show the performance of the proposed control during load variations. Under this scenario, the proposed controller controls the VSI to operate at its active and reactive powers desired values, as illustrated in **Fig. 4.17 (a)** and **(b)**. According to **Fig. 4.17 (c)**, it can be observed that the active power of the utility grid decreased with an amount of 1 kW, which is the power consumed by the added load. In addition, from **Fig. 4.17 (d)**, one can be noticed that the grid reactive power remains constant, with slight oscillations. Based on **Fig. 4.17 (e)** and **(f)**, it is can be observed that the VSI frequency and amplitude of the VSI are set to the frequency and amplitude of the grid, in which they remain constant, except slight transients, can be noted in the frequencies. **Fig. 4.18 (a)** and **(b)** demonstrate that the output VSI current and voltage, as well as the voltage grid, are remaining constants during the loading condition, while the injected current, with a pure sinusoidal form, into the main grid is reduced due to the added load.

It is worth noting that the grid current and voltage are synchronized, therefore, the unity power factor is ensured.

The results in **Fig. 4.19** and **4.20**, depict the performance of the proposed power flow control when the load demand exceeds the power produced by the inverter side, and the required power is imported from the main grid. At t = 0.4 s, a load of 4kW is added, the inverter is not sufficient to fulfill the load demand, and the needed power is absorbed from the main grid, and after removing the load, it is back to the normal operation, as illustrated in **Fig. 4.19 (c)**. According to this figure, one can see that a negative active power of - 3kW is obtained on the grid side. Also, we note that the designed controller fixe the active and reactive powers produced by the inverter to their the desired references, as shown in **Fig. 4.19 (a)** and **(b)**. Furthermore, in **Fig. 4.19 (d)**, the grid reactive power remains constant, with slight oscillations, during this operating condition. The responses given in **Fig. 4.19 (e**), demonstrate that the inverter and PCC frequenicies are matched with the grid frequency, during adding and removing the load. Form this figure, we noticed, also, that the amplitudes of the inverter, at the PCC, and the grid are matched and remain unchanged during the loading operating conditions.

From **Fig. 4.20 (a)** and **(b)**, it can be observed that the voltage and current of the VSI side and the grid side voltage remain unchanged, while the grid current increases and balances in opposite phase with the grid voltage when a load is added, as it can be seen in **Fig. 4.20 (c)**. After the load is removed at t = 0.8 s, the current returns to its first value and is in-phase with the grid voltage (see **Fig. 4.20 (c)**), which means that VSI injects current into the grid.

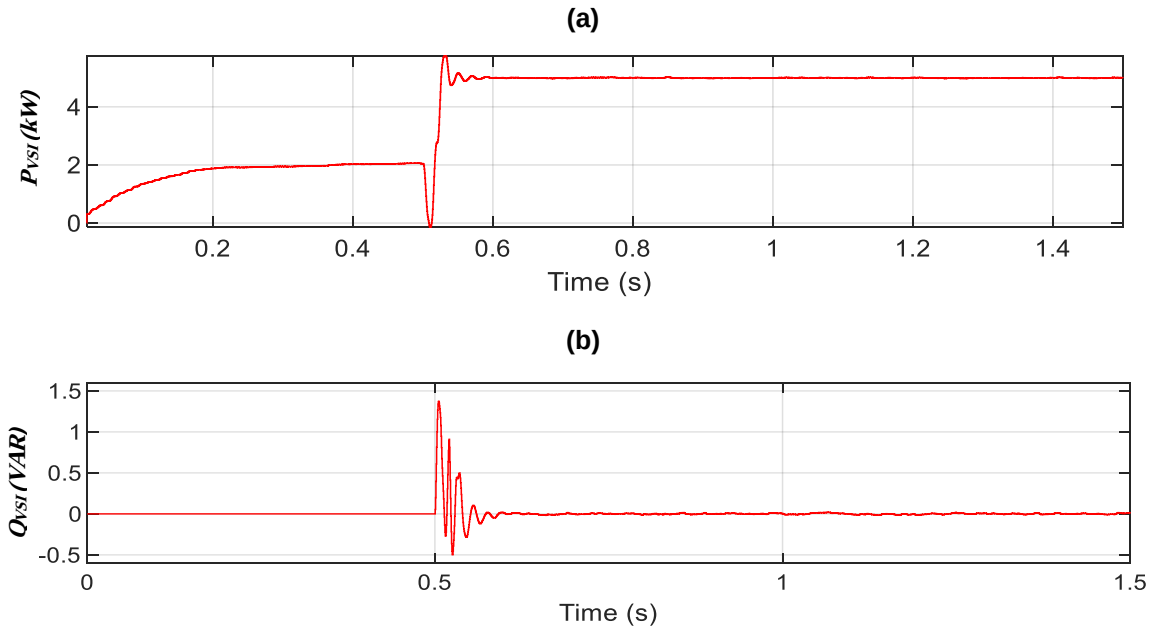

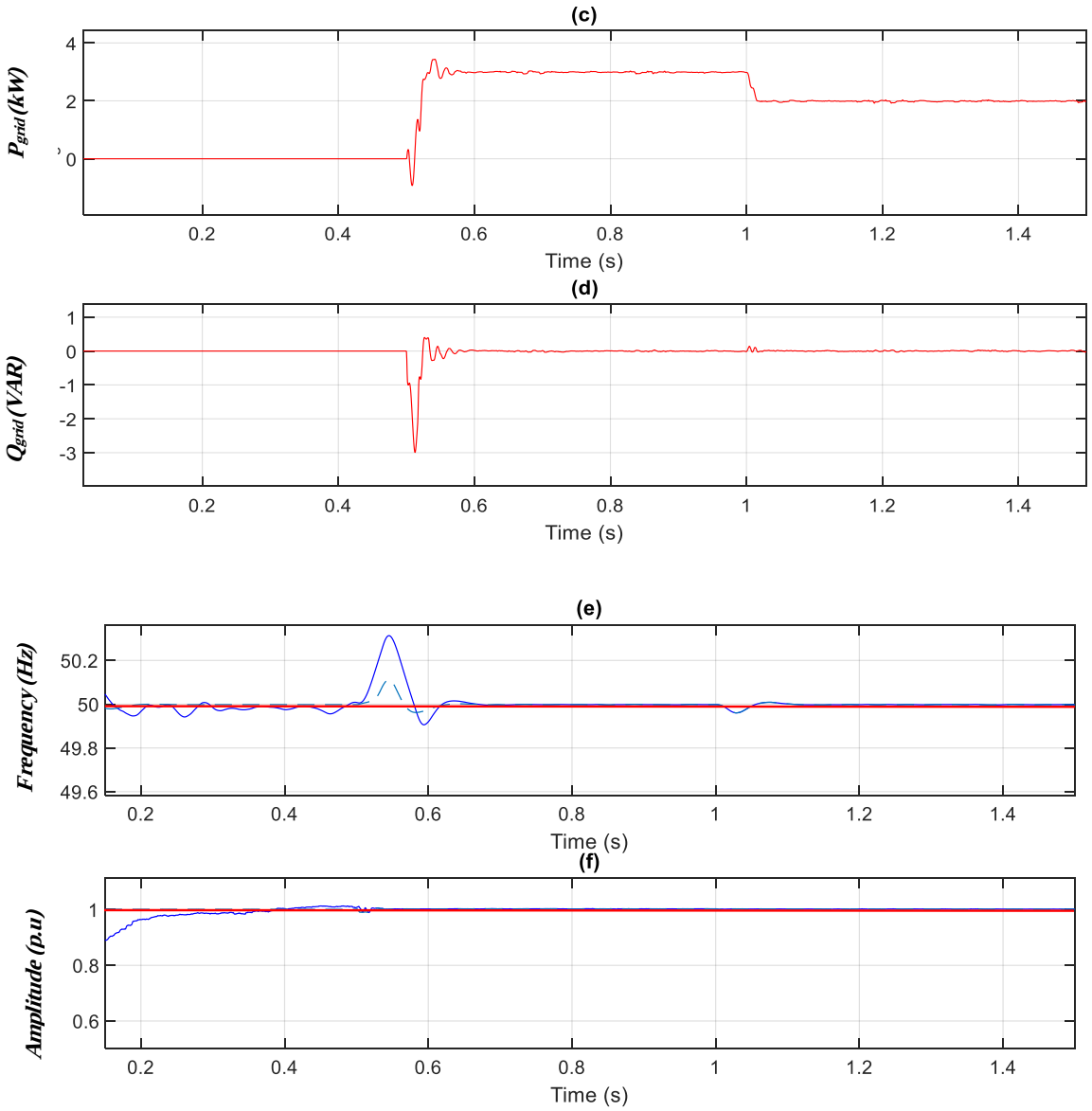

Fig. 4;17. The obtained results in response to load variations (test 4).

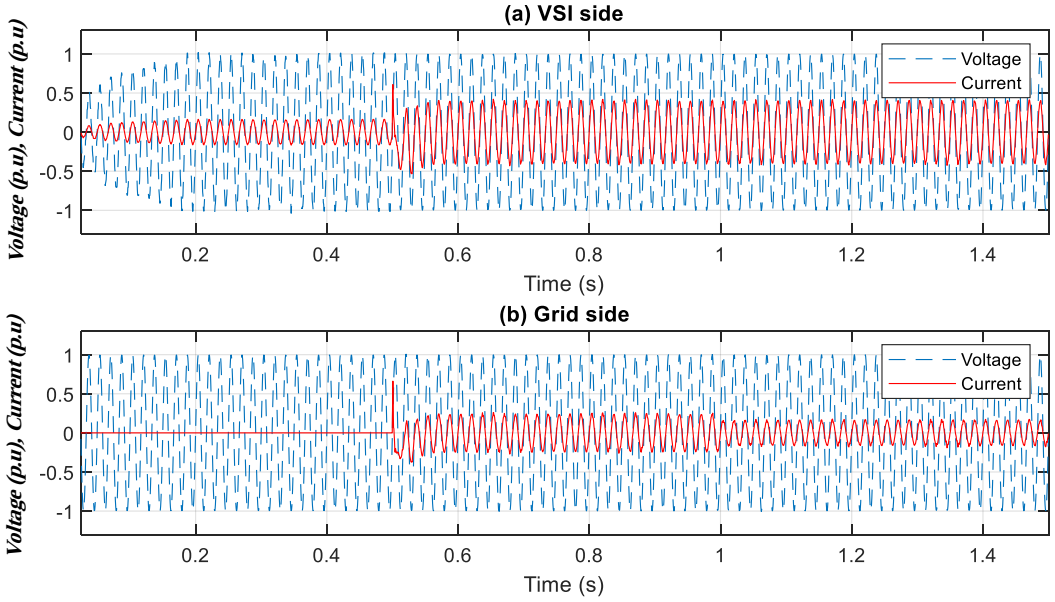

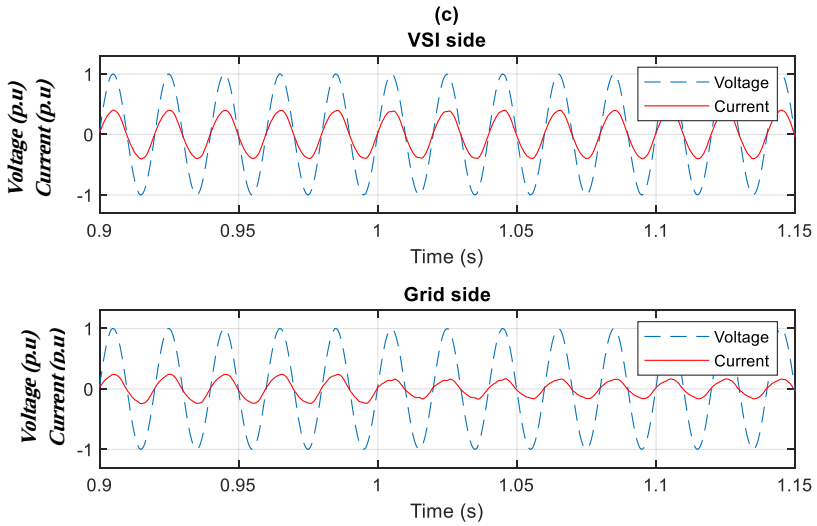

Fig. 4.18. Responses of the voltage and current in test 4; **(a)** inverter side, **(b)** grid side, and **(c)** zoom.

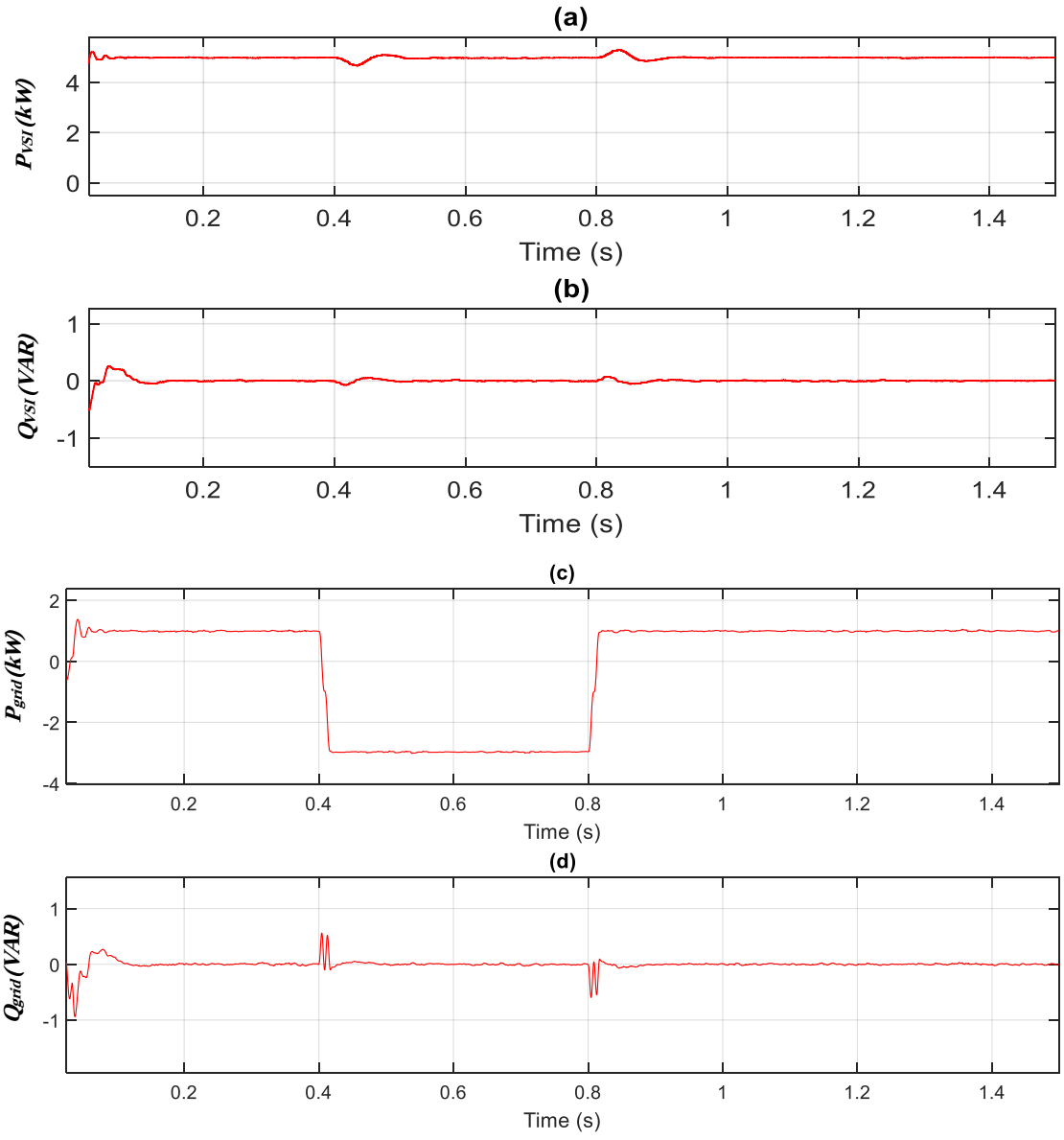

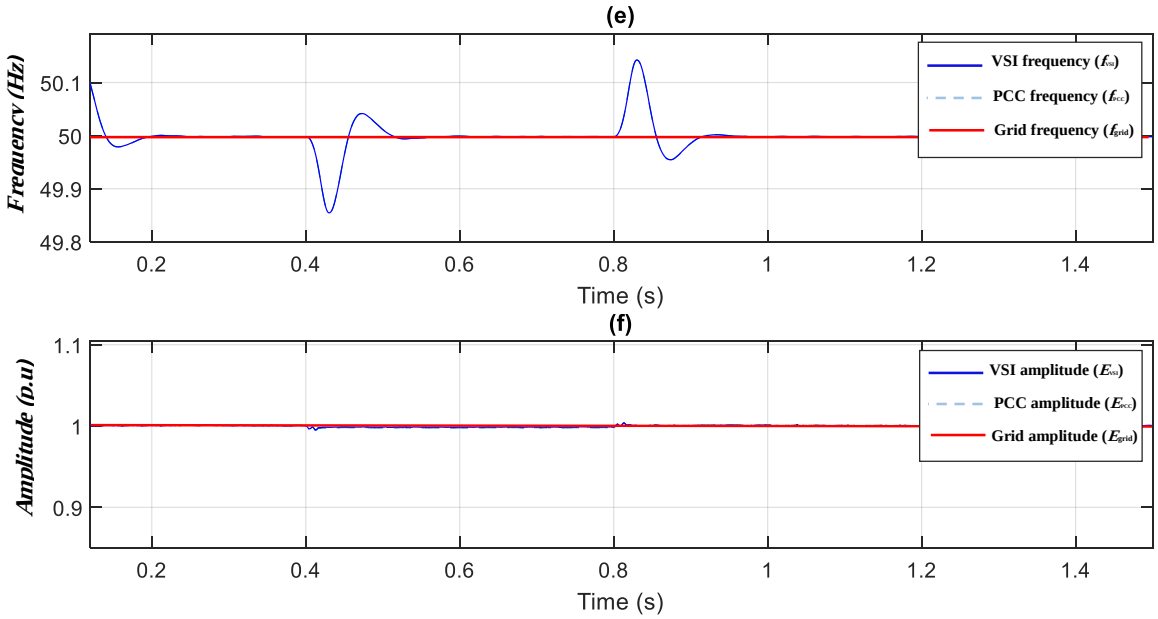

Fig. 4.19. The obtained results in response test 5.

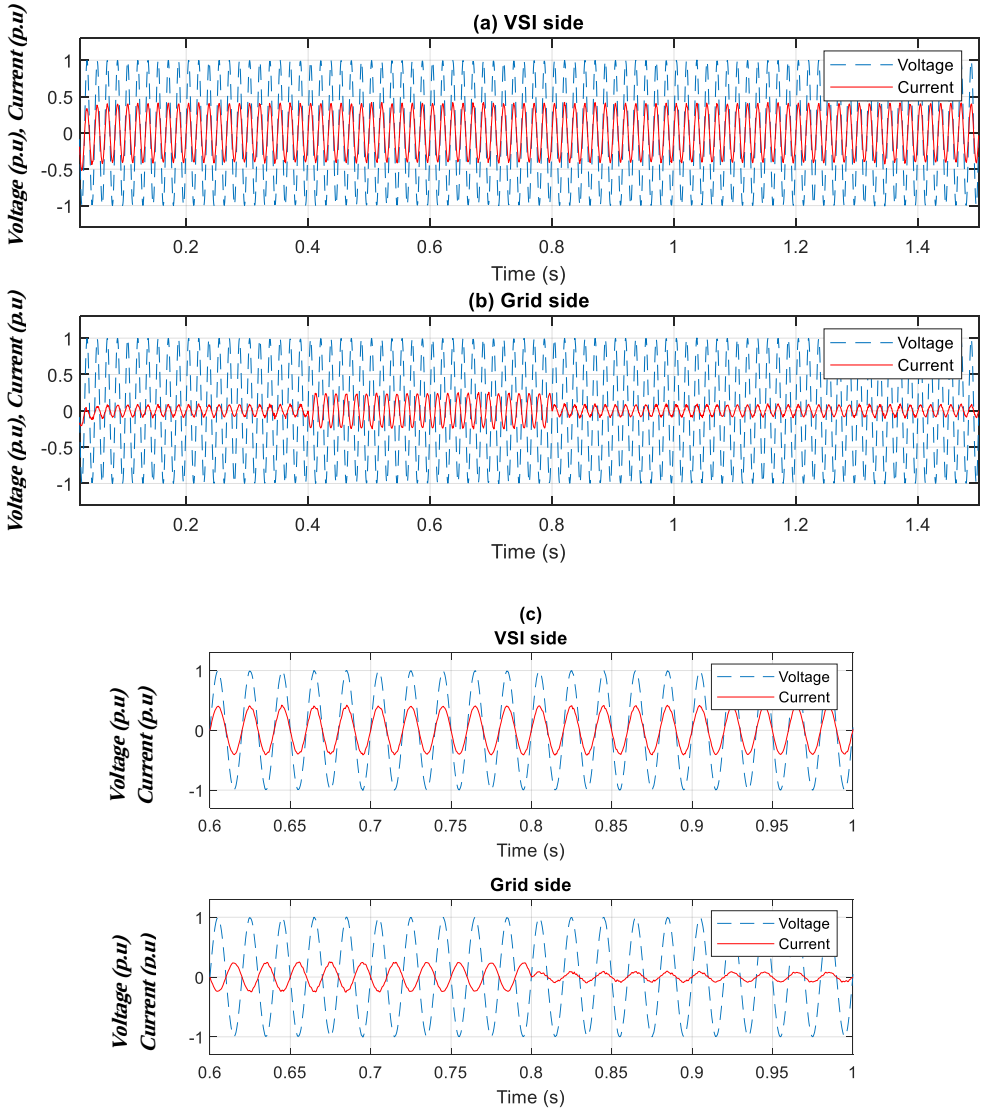

Fig. 4.20. Responses of the voltage and current in test 5; **(a)** inverter side, **(b)** grid side, and **(c)** zoom.

4.4. Conclusion

In this chapter, the implementation of the proposed secondary control and tertiary control of single-phase droop-controlled VSIs-interfaced MG during islanded and grid-connected mode operation was addressed. First, the performance of the suggested secondary control strategy has been examined through simulation case studies and experimental tests. The simulation results and discussions on the outcomes of the proposed secondary control for the MG frequency and amplitude restoration as well as the synchronization with the grid were provided. Besides, the practical results of the secondary control approach for single-phase VSIs-based islanded MG were illustrated and discussed. The results have proved the robustness of the designed secondary control in effectively recovering the frequency and amplitude nominal values with good transient and steady-state responses, even under different load conditions. Secondly, the proposed tertiary control performance for the power flow of single-phase grid-connected VSIs, operated as grid-forming units, towards the main grid was presented in this chapter. The simulation case studies were conducted using the MATLAB/Simulink software framework. The obtained results of the power flow control of VSIs operating in grid supporting mode were provided and discussed. They have demonstrated the effectiveness of the designed controller on providing a system that can respond to changes in load demand and distributed generation output in an effective manner and optimal power flow.

All in all, the presented implementation in this chapter has successfully validated the effectiveness of the proposed secondary and tertiary control schemes. In addition, it confirmed the developed modeling approach and reveals that the expected transient responses are achieved based on the suggested tuning guideline given in the previous chapters.

Conclusions and Future Works

Modeling, analyzing, and designing secondary control and tertiary control schemes intended for a single-phase MG during the islanding and the grid-connection operation was the main objective of the present thesis. The summary and the contributions of the MG control strategies adopted in each chapter are presented in the following.

In chapter 1, a complete overview of the microgrid context was presented, considering background, definition and research interest, different MG configurations, advantages, and architectures, as well as motivation. The hierarchical control of AC microgrid, including primary, secondary, and tertiary control levels were described. The control problem statement of the present thesis was discussed. Literature reviews of the considered secondary and tertiary control strategies and corresponding problems for AC MGs were presented, also, in this chapter. Finaly, the thesis's main contributions, outcomes, and organization were presented.

In chapter 2, a secondary control scheme based on the ESOGI-FLL method for single-phase parallel-connected VSIs-interfaced autonomous AC microgrid was first designed. The ESOGI-FLL method, which has the ability to reject totally the DC componet and its effect, was introduced to ensure accurate estimation the MG voltage amplitude and frequency. Second, a new modeling approach of the designed secondary frequency and amplitude restoration control loops-based MG was proposed. In this approach, the dynamics of ESOGI-FLL were considered, in which the transfer function of the FLL was involved in the frequency restoration model. While applying the dynamic phasor concept, a model that describes the dynamics of the SOGI amplitude estimate was derived, and simplified, and, then, was introduced in the voltage amplitude restoration modeling. The accuracy of the derived models of the ESOGI-FLL frequency and amplitude estimates were confirmed using numerical tests. The results demonstrated that the frequency and the simplified amplitude models can predict accurately the average dynamic behavior of the ESOGI-FLL. Stability analysis based on the obtained models of the MG system incorporating restoration control loops was addressed. Also, systematic tunning guidelines to properly select the restoration control parameters were provided. Finally, the modeling and control design of the synchronization control loop was presented.

The objective of the control proposal, presented in this chapter, is to effectively restore voltages and frequencies of the DGs to their nominal values and optimally manage the power generation among the different DG units, also, offer proper synchronization with the main grid, when the grid-connection mode is expected.

The focus of the third chapter was on designing and modeling a tertiary control scheme equipped with an ESOGI-FLL-based power calculation strategy for a single-phase grid-connected MG. The main aim of this designed control scheme is to ensure efficient and optimal management of the MG power exchange with the main grid. In this scheme, the power calculation based on ESOGI-FLL was involved to provide a precise estimation of the average active and reactive powers. The dynamic phasor modeling of the power flow for a grid-connected VSI-interfaced MG, taking into consideration the dynamics of the ESOGI-FLL-based power calculation was proposed. First, the model of a single-phase VSI connected to the main grid via a line impedance was derived. Second, the model describing the dynamics of the SOGI-FLL-based active and reactive power calculation was extracted and simplified. Third, the open-loop small-signal model of the power flow including the dynamics of the power calculation in state-space was obtained. The accuracy of all obtained models was proved through simulation and HIL tests, and it was discussed that these models are able to predict accurately the system dynamics. The closed-loop small-signal model of the whole MG system incorporating the tertiary control, in state space, was constructed. Stability analysis and effective tunning approaches for selecting the active and reactive controllers' parameters were provided. In addition, the evaluation of the system stability to variations of the controllers' parameters, as well as the robustness assessment of the designed controllers to system parameters variations were carried out.

In chapter 4, the performance of the proposed secondary control and tertiary control schemes-based hierarchical control were tested. In the first part, simulations and experimental implementation of the designed secondary control layer were conducted to verify its effectiveness and robustness. In this part, the considered microgrid testbed for the simulation case was described, it corresponds to an islanded MG which consists of two single-phase parallel-connected VSIs feed a common load. A series of simulations for three case studies with different disturbances were reported and their results were provided and discussed. Next, an experimental setup, similar to the simulation one, for the implementation of the designed secondary based on ARM Cortex μC (STM32F4-Discovery) was presented. The same tests as in the simulation study were considered, and the obtained results and discussions were presented. In the second part, a performed simulation of the designed tertiary control layer for single-phase droop-controlled VSI connected to the main grid was explained. Simulation tests under different grid disturbances were conducted and the corresponding results were given and discussed.

Based on the results' discussions, one can conclude that:

- The designed secondary control achieve voltage amplitude and frequency restoration to

nominal values with the desired transient responses in terms of response time and without overshoot, as well as has improved the reactive power-sharing.

- The effectiveness and the robustness of the designed secondary control are confirmed in ensuring efficient and stable operation of the autonomous MG under different operating conditions and even in the presence of the DC component.
- The experimental tests validate the secondary control proposal in keeping the frequency and voltage amplitude close to their nominal values under various disturbances.
- The synchronization algorithm ensures a seamless transition from islanding mode to grid-connected mode.
- The tertiary can manage optimally the active and reactive exchange between the droop-controlled VSI-based MG and the main grid.
- The proper tracking of the frequency and amplitude of the voltage grid is guaranteed with excellent transient and steady-state performance.
- Stable operation of the grid-connected MG is assured under different grid voltage disturbances which contains the DC component and load changes.

In the future much work will be done by:

- Applying the same design and modeling approaches of the secondary control, for the distributed secondary control for frequency and amplitude restoration intended for single-phase MGs.
- Implementing the designed tertiary control scheme-based hierarchical control in hardware by using ARM cortex μC, for single-phase VSIs connected to the main grid.

Appendices

Appendix A: Gains of the power flow open-loop model at steady-state

Based on the linearized model of the active and reactive power flow, Eq.(3.41) in chapter 3, given by:

$$\begin{bmatrix}\Delta P\\ \Delta Q\end{bmatrix}=\begin{bmatrix}G_1 & G_2\\ -G_2 & G_1\end{bmatrix}\begin{bmatrix}k_{11} & k_{12}\\ k_{21} & k_{22}\end{bmatrix}\begin{bmatrix}\Delta\varphi\\ \Delta E\end{bmatrix} \tag{3.39}$$

Considering power flow decoupling, the equation above yield:

$$\begin{bmatrix}\Delta P\\ \Delta Q\end{bmatrix}=\begin{bmatrix}G_1\times k_{11}+G_2\times k_{21} & 0\\ 0 & -G_2\times k_{12}+G_1\times k_{22}\end{bmatrix}\begin{bmatrix}\Delta\varphi\\ \Delta E\end{bmatrix} \tag{App.A.1}$$

Accordingly, the expression of the gains at steady-state can be obtained as follows:

$$\begin{cases}G_P\big|_{s=0}=G_1\times k_{11}+G_2\times k_{21}\\ G_Q\big|_{s=0}=-G_2\times k_{12}+G_1\times k_{22}\end{cases} \tag{App.A.2}$$

where G_1, G_2; which expected as a function of the system nominal values; are given by Eq.(3.40) in chapter 3, while the expression of the parameters k_{11}, k_{12}, k_{21}, k_{22} can be obtained based on Eq.(3.20) as following:

$$\begin{cases}k_{11}=3V_{gn}E_n\cos(\varphi_n)\\ k_{12}=3V_{gn}\sin(\varphi_n)\\ k_{21}=-3V_{gn}E_n\sin(\varphi_n)\\ k_{22}=3V_{gn}\cos(\varphi_n)\end{cases}$$

Appendix B: Model of the secondary control for STM32F4 Target in MATLAB/Simulink

This appendix presents a guideline for the implementation on MATLAB/Simulink and by using Waijung Blockset of the secondary control algorithm for the STM32F4 platform. The description for each configuration of the STM32F407 modules integrated into the designed model is also provided in this appendix. The designed model is built to be implemented in STM32F407 board for real-time control application intended for a single-phase islanded microgrid.

It is worth noting that Waijung is a Simulink Blockset that is used to generate the C code from MATLAB/Simulink simulation models for specified microcontrollers.

Fig. App.B.1 shows the diagram of the developed model of the secondary control for the STM32F4 Embedded Target in MATLAB/Simulink. As can be seen, this model consists of; i) the embedded target block, ii) the block of the secondary control algorithm developed based on MATLAB function code generation, iii) two analog to digital converters, and iv) two communication modules (UART).

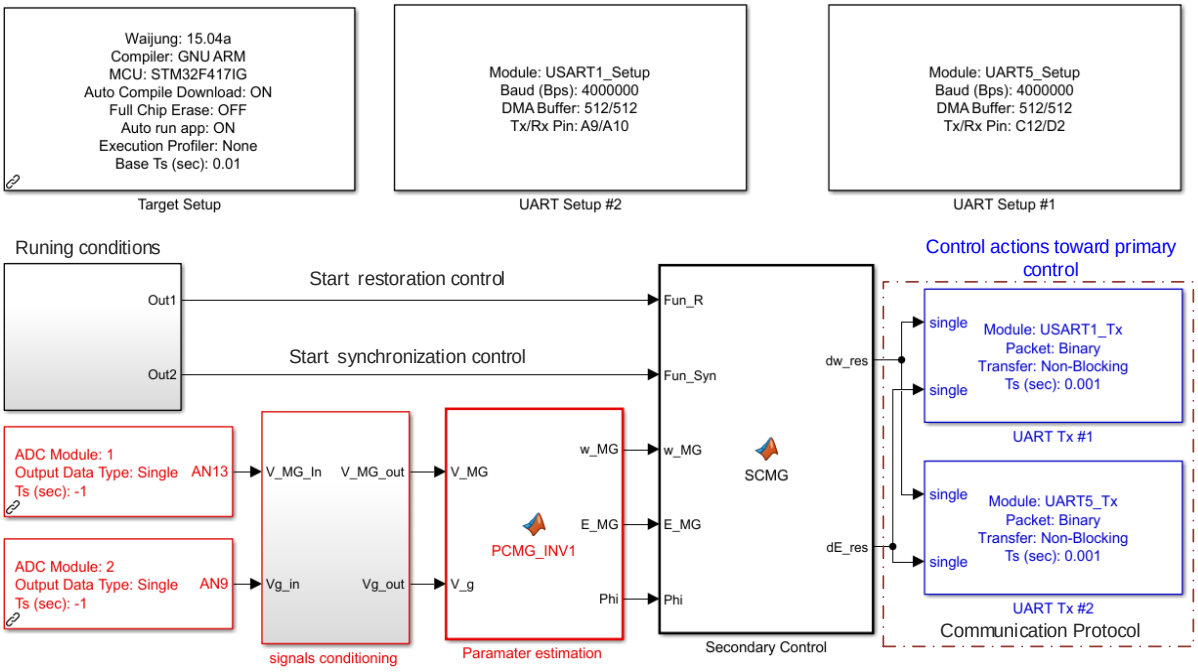

Fig. App.B.1. Model of the secondary control algorithm deployed for STM32F407 target.

- **STM32F4 peripheral configuration:**

1- Target setup:

As shown in **Fig. App.B.2**, two main things should take care of:

a- Choose the target according to the your available board (in our case: STM32F407G);

b- Selection of the compiler; (MDK)

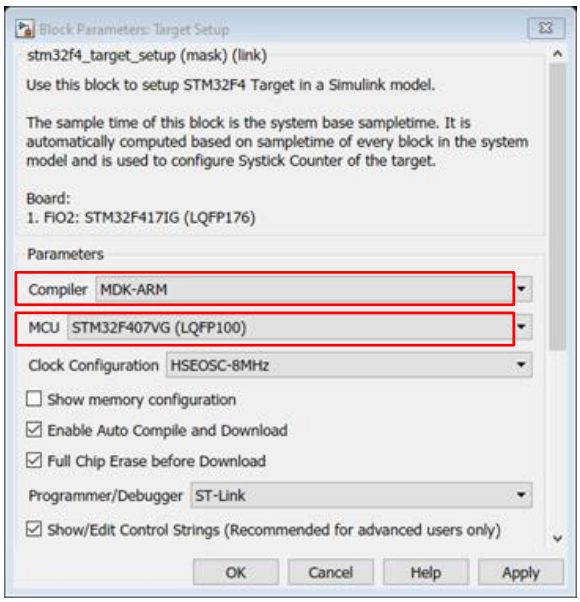

Fig. App.B.2. The STM32F407 Target configuration block.

2- Communication peripheral (URAT setup):

From **Fig. App.B.3**, the thing that should be made for the configuration of the URAT module are:

a- Choose the baud rate (Bps) of the bandwith of transmission.

b- Select the URAT module, and the outputs of the URAT corresponding to the pins of in the STM32F407G board.

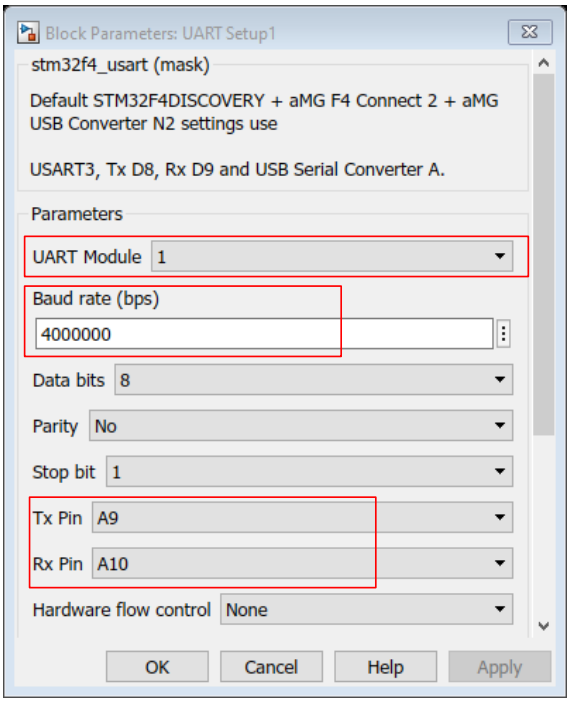

Fig.App.B.3. A dialog box of the communication peripheral.

3- ADC modules:

In this block, the physical ADC, and the type of the manipulated data should be specified, as well as the inputs of the ADC modules (according to the chosen timer) corresponding to the STM32F4 board (see **Fig.App.B.4**).

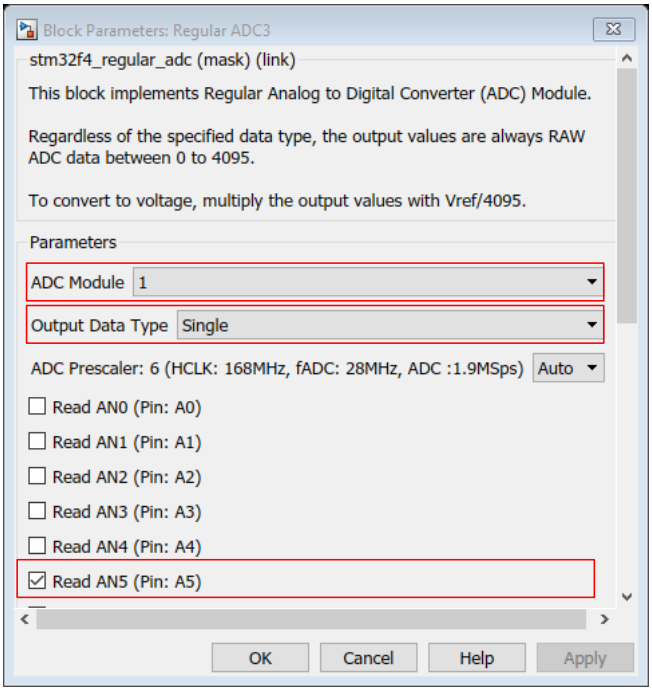

Fig.App.B.4. A dialog box of the ADC block.

In order to load the generated C code in the STM32F4 board, press the bottom “build” illustrated in the MATLAB tools bar.

Bibliography

[1] N. Scarlat, J-F. Dallemand, F. Monforti-Ferrario, M. Banja, and V. Motola, "Renewable energy policy framework and bioenergy contribution in the European Union – An overview from National Renewable Energy Action Plans and Progress Reports," *Renewable and Sustainable Energy Reviews*, vol. 51, pp. 969-985, 2015.

[2] B. Fortunski, "Sustainable Development and Energy Policy: Actual CO2 Emissions in the European Union in the Years 1997–2017, Considering Trade with China and the USA," *Sustainability*, vol. 12, pp. 3363, 2020.

[3] F. Blaabjerg, Y. Yang, D. Yang and X. Wang, "Distributed Power-Generation Systems and Protection," *Proceedings of the IEEE*, vol. 105, no. 7, pp. 1311-1331, July 2017.

[4] F. Katiraei, R. Iravani, N. Hatziargyriou, and A. Dimeas, "Microgrids management," *IEEE Power and Energy Magazine*, vol. 6, no. 3, pp. 4–65, 2008.

[5] A. Hirsch, Y. Parag, J. Guerrero, "Microgrids: A review of technologies, key drivers, and outstanding issues," *Renewable and Sustainable Energy Reviews*, vol. 90, pp. 402-411, 2018.

[6] J. Rocabert, A. Luna, F. Blaabjerg, and P. Rodríguez, "Control of power converters in AC microgrids," *IEEE Transactions on Power Electronics*, vol. 27, no. 11, pp. 4734-4749, 2012.

[7] Y. Sun, X. Hou, J. Yang, H. Han, M. Su, and J. M. Guerrero, "New perspectives on droop control in AC microgrid," *IEEE Transactions on Industrial Electronics*, vol. 64, no. 7, pp. 5741-5745, 2017.

[8] G. Dellile, B. Francois, and G. Malarange, "Dynamic frequency control support by energy storage to reduce the impact of wind and solar generation on isolated power system's inertia," *IEEE Trans. Sustain. Energy*, vol. 3, no. 4, pp. 931–939, Oct. 2012.

[9] X. Liang, "Emerging Power Quality Challenges Due to Integration of Renewable Energy Sources," *IEEE Transactions on Industry Applications*, vol. 53, no. 2, pp. 855-866, Mar.-Apr. 2017.

[10] B. S. Hartono, Y. Budiyanto and R. Setiabudy, "Review of microgrid technology," *2013 International Conference on QIR*, Yogyakarta, Indonesia, 2013, pp. 127-132.

[11] V.K. Sood, H. Abdelgawad, "Microgrids architectures," in: R. K. Chauhan, K. Chauhan, "Distributed Energy Resources in Microgrids", *Academic Press*, 2019, pp. 1-31, Ch1.

[12] B. Yu, J. Guo, C. Zhou, Z. Gan, J. Yu, and F. Lu, "A Review on Microgrid Technology with Distributed Energy," *2017 International Conference on Smart Grid and Electrical Automation (ICSGEA)*, Changsha, 2017, pp. 143-146.

[13] A.R. Singh, D. Lei, A. Kumar, R. Singh, N.K. Meena, "Microgrid System," in: P. Ray, M. Biswal, "Microgrid: Operation, Control, Monitoring and Protection," *Lecture Notes in Electrical Engineering*, *Springer*, vol. 625, pp. 1-13, 2020.

[14] F. Li, L. Ruisheng, and Z. Fengquan, "Microgrid technology and engineering application," *Elsevier*, 2015.

[15] N. Hatziargyriou, "The Microgrids Concept" in: "Microgrids: architectures and control," *John Wiley & Sons*, pp. 1-24, 2014.

[16] N. Hosseinzadeh, A. Aziz, A. Mahmud, et al., "Voltage Stability of Power Systems with Renewable-Energy Inverter-Based Generators: A Review, " *Electronics*, vol. 10, no 2, pp. 115, 2021.

[17] S. Parhizi, H. Lotfi, A. Khodaei and S. Bahramirad, "State of the Art in Research on Microgrids: A Review," *IEEE Access*, vol. 3, pp. 890-925, 2015.

[18] A. Tuladhar, Hua Jin, T. Unger, and K. Mauch, "Control of parallel inverters in distributed AC power systems with consideration of line impedance effect," *IEEE Transactions on Industry Applications*, vol. 36, no. 1, pp. 131-138, Jan.-Feb. 2000.

[19] Dan T. Ton, and Merrill A. Smith, "The U.S. Department of Energy's Microgrid Initiative," *The Electricity Journal*, vol. 25, no. 8, pp. 84-94, 2012.

[20] M.S. Mahmoud, F.M. AL-Sunni, "Control Methods for Microgrids", in: "Control and Optimization of Distributed Generation Systems", *Power Systems*, *Springer*, Cham, pp. 89-157, 2015, https://doi.org/10.1007/978-3-319-16910-1_3.

[21] J. Vasiljevska, J. P. Lopes, and M. A. Matos, "Evaluating the Interest in Installing Microgrid Solutions," *The Electricity Journal*, vol. 25, no. 8, pp. 61-70, 2012.

[22] W. Feng, et al., "A review of microgrid development in the United States–A decade of progress on policies, demonstrations, controls, and software tools," *Applied Energy*, vol. 228, pp. 1656-1668, Mar. 2018.

[23] Alireza Aram, "Microgrid Market in the USA", GLOBAL INNOVATION REPORT, *Hitachi review*, https://www.hitachi.com/rev/archive/2017/r2017_05/Global/index.html.

[24] J. He, Y. W. Li, J. M. Guerrero, F. Blaabjerg and J. C. Vasquez, "An Islanding Microgrid Power Sharing Approach Using Enhanced Virtual Impedance Control Scheme," *IEEE Transactions on Power Electronics*, vol. 28, no. 11, pp. 5272-5282, Nov. 2013.

[25] A. Hossam, M. Gaber, and X. Dianguo, "A new optimal robust controller for frequency stability of interconnected hybrid microgrids considering non-inertia sources and uncertainties," *International Journal of Electrical Power & Energy Systems*, Jan. 2021, 106651, 10.1016/j.ijepes.2020.106651.

[26] J. C. Vasquez, J. M. Guerrero, A. Luna, P. Rodriguez, and R. Teodorescu, "Adaptive Droop Control Applied to Voltage-Source Inverters Operating in Grid-Connected and Islanded Modes," *IEEE Transactions on Industrial Electronics*, vol. 56, no. 10, pp. 4088-4096, Oct. 2009.

[27] Y. A. I. Mohamed and E. F. El-Saadany, "Adaptive Decentralized Droop Controller to Preserve Power Sharing Stability of Paralleled Inverters in Distributed Generation Microgrids," *IEEE Transactions on Power Electronics*, vol. 23, no. 6, pp. 2806-2816, Nov. 2008.

[28] T. Lee and P. Cheng, "Design of a New Cooperative Harmonic Filtering Strategy for Distributed Generation Interface Converters in an Islanding Network," *IEEE Transactions on Power Electronics*, vol. 22, no. 5, pp. 1919-1927, Sept. 2007

[29] K. De Brabandere, B. Bolsens, J. Van den Keybus, A. Woyte, J. Driesen, and R. Belmans, "A Voltage and Frequency Droop Control Method for Parallel Inverters," *IEEE Transactions on Power Electronics*, vol. 22, no. 4, pp. 1107-1115, July 2007.

[30] V. Nasirian, S. Moayedi, A. Davoudi, and F. L. Lewis, "Distributed Cooperative Control of DC Microgrids," *IEEE Transactions on Power Electronics*, vol. 30, no. 4, pp. 2288-2303, April 2015.

[31] T. Dragičević, X. Lu, J. C. Vasquez, and J. M. Guerrero, "DC Microgrids—Part II: A Review of Power Architectures, Applications, and Standardization Issues," *IEEE Transactions on Power Electronics*, vol. 31, no. 5, pp. 3528-3549, May 2016.

[32] Q. Zhou, M. Shahidehpour, Z. Li and X. Xu, "Two-Layer Control Scheme for Maintaining the Frequency and the Optimal Economic Operation of Hybrid AC/DC Microgrids," *IEEE Transactions on Power Systems*, vol. 34, no. 1, pp. 64-75, Jan. 2019.

[33] Y. Karimi, H. Oraee and J. M. Guerrero, "Decentralized Method for Load Sharing and Power Management in a Hybrid Single/Three-Phase-Islanded Microgrid Consisting of Hybrid Source PV/Battery Units," *IEEE Transactions on Power Electronics*, vol. 32, no. 8, pp. 6135-6144, Aug. 2017.

[34] Xuan Liu and Bin Su, "Microgrids — an integration of renewable energy technologies," *2008 China International Conference on Electricity Distribution*, Guangzhou, 2008, pp. 1-7.

[35] A. Vasilakis, I. Zafeiratou, D. T. Lagos and N. D. Hatziargyriou, "The Evolution of Research in Microgrids Control," *IEEE Open Access Journal of Power and Energy*, vol. 7, pp. 331-343, 2020.

[36] P. P. Barker and R. W. De Mello, "Determining the impact of distributed generation on power systems. I. Radial distribution systems," *2000 Power Engineering Society Summer Meeting (Cat. No.00CH37134)*, Seattle, WA, 2000, pp. 1645-1656 vol. 3.

[37] M. Farrokhabadi et al., "Microgrid Stability Definitions, Analysis, and Examples," *IEEE Transactions on Power Systems*, vol. 35, no. 1, pp. 13-29, Jan. 2020.

[38] J. M. Guerrero, J. C. Vasquez, J. Matas, L. G. de Vicuna, and M. Castilla, "Hierarchical Control of Droop-Controlled AC and DC Microgrids—A General Approach Toward Standardization," *IEEE Transactions on Industrial Electronics*, vol. 58, no. 1, pp. 158-172, Jan. 2011.

[39] J. M. Guerrero, M. Chandorkar, T. Lee and P. C. Loh, "Advanced Control Architectures for Intelligent Microgrids—Part I: Decentralized and Hierarchical Control," *IEEE Transactions on Industrial Electronics*, vol. 60, no. 4, pp. 1254-1262, Apr. 2013.

[40] A. Bidram and A. Davoudi, "Hierarchical Structure of Microgrids Control System," *IEEE Transactions on Smart Grid*, vol. 3, no. 4, pp. 1963-1976, Dec. 2012.

[41] T. L. Vandoorn, J. C. Vasquez, J. De Kooning, J. M. Guerrero, and L. Vandevelde, "Microgrids: Hierarchical Control and an Overview of the Control and Reserve Management Strategies," *IEEE Industrial Electronics Magazine*, vol. 7, no. 4, pp. 42-55, Dec. 2013.

[42] E. Kabalci, "Hierarchical Control in Microgrid," in: "Microgrid Architectures, Control, and Protection Methods, " *Springer*, Cham, pp. 381-401, 2020.

[43] L. Meng et al., "Flexible System Integration and Advanced Hierarchical Control Architectures in the Microgrid Research Laboratory of Aalborg University," *IEEE Transactions on Industry Applications*, vol. 52, no. 2, pp. 1736-1749, March-April 2016.

[44] J. C. Vasquez, J. M. Guerrero, M. Savaghebi, J. Eloy-Garcia, and R. Teodorescu, "Modeling, Analysis, and Design of Stationary-Reference-Frame Droop-Controlled Parallel Three-Phase Voltage Source Inverters," *IEEE Transactions on Industrial Electronics*, vol. 60, no. 4, pp. 1271-1280, Apr. 2013.

[45] J. M. Guerrero, L. G. de Vicuna, J. Matas, M. Castilla, and J. Miret, "A wireless controller to enhance dynamic performance of parallel inverters in distributed generation systems," *IEEE Transactions on Power Electronics*, vol. 19, no. 5, pp. 1205-1213, Sept. 2004.

[46] Z. Jiang and X. Yu, "Active power — Voltage control scheme for islanding operation of inverter-interfaced microgrids," *2009 IEEE Power & Energy Society General Meeting*, Calgary, AB, 2009, pp. 1-7.

[47] J. M. Guerrero, Luis Garcia de Vicuna, J. Matas, M. Castilla, and J. Miret, "Output impedance design of parallel-connected UPS inverters with wireless load-sharing control," *IEEE Transactions on Industrial Electronics*, vol. 52, no. 4, pp. 1126-1135, Aug. 2005.

[48] S. Sinha, S. Ghosh, P. Bajpai, "Power-sharing through interlinking converters in adaptive droop controlled multiple microgrid system," *International Journal of Electrical Power & Energy Systems*, vol. 128, 2021, 106649, https://doi.org/10.1016/j.ijepes.2020.106649.

[49] W. Yao, M. Chen, J. Matas, J. M. Guerrero, and Z. Qian, "Design and Analysis of the Droop Control Method for Parallel Inverters Considering the Impact of the Complex Impedance on the Power Sharing," *IEEE Transactions on Industrial Electronics*, vol. 58, no. 2, pp. 576-588, Feb. 2011.

[50] U. B. Tayab, M. A. Bin Roslan, L. J. Hwai, "Muhammad Kashif, A review of droop control techniques for microgrid," *Renewable and Sustainable Energy Reviews*, vol. 76, pp. 717-727, 2017.

[51] R. Hidalgo-León, C. Sanchez-Zurita, P. Jácome-Ruiz, J. Wu and Y. Muñoz-Jadan, "Roles, challenges, and approaches of droop control methods for microgrids," *2017 IEEE PES Innovative Smart Grid Technologies Conference - Latin America (ISGT Latin America)*, Quito, 2017, pp. 1-6.

[52] A. Micallef, M. Apap, C. Spiteri-Staines, and J. M. Guerrero, "Single-Phase Microgrid With Seamless Transition Capabilities Between Modes of Operation," *IEEE Transactions on Smart Grid*, vol. 6, no. 6, pp. 2736-2745, Nov. 2015.

[53] M. Anwar, M. I. Marei, and A. A. El-Sattar, "Generalized droop-based control for an islanded microgrid," *2017 12th International Conference on Computer Engineering and Systems (ICCES)*, Cairo, 2017, pp. 717-722.

[54] H. Ye, Y. Liu, W. Pei, and L. Kong, "Efficient droop-based primary frequency control from variable-speed wind turbines and energy storage systems," *2017 IEEE Transportation Electrification Conference and Expo, Asia-Pacific (ITEC Asia-Pacific)*, Harbin, 2017, pp. 1-5.

[55] A. Bendib, A. Kherbachi, K. Kara and A. Chouder, "Droop controller-based primary control scheme for parallel-connected single-phase inverters in islanded AC microgrid," *2017 5th International Conference on Electrical Engineering - Boumerdes (ICEE-B)*, Boumerdes, 2017, pp. 1-6.

[56] Y. Han, H. Li, P. Shen, E. A. A. Coelho, and J. M. Guerrero, "Review of Active and Reactive Power Sharing Strategies in Hierarchical Controlled Microgrids," *IEEE Transactions on Power Electronics*, vol. 32, no. 3, pp. 2427-2451, March 2017.

[57] H. Han, Y. Liu, Y. Sun, M. Su and J. M. Guerrero, "An Improved Droop Control Strategy for Reactive Power Sharing in Islanded Microgrid," *IEEE Transactions on Power Electronics*, vol. 30, no. 6, pp. 3133-3141, June 2015.

[58] Y. Gupta, K. Chatterjee and S. Doolla, "A Simple Control Scheme for Improving Reactive Power Sharing in Islanded Microgrid," *IEEE Transactions on Power Systems*, vol. 35, no. 4, pp. 3158-3169, July 2020.

[59] Haoming Liu, Yi Chen, Shanshan Li, and Yunhe Hou, "Improved droop control of isolated microgrid with virtual impedance," *2013 IEEE Power & Energy Society General Meeting*, Vancouver, BC, 2013, pp. 1-5.

[60] A. S. Vijay, N. Parth, S. Doolla and M. C. Chandorkar, "An Adaptive Virtual Impedance control for improving Power Sharing among Inverters in Islanded AC Microgrids," *2020 IEEE Energy Conversion Congress and Exposition (ECCE)*, Detroit, MI, USA, 2020, pp. 4621-4626.

[61] R. Moslemi, J. Mohammadpour, "Accurate reactive power control of autonomous microgrids using an adaptive virtual inductance loop," *Electric Power Systems Research*, vol. 129, pp. 142-149, 2015.

[62] J. E. Mariachet, et al. "HIL-assessed fast and accurate single-phase power calculation algorithm for voltage source inverters supplying to high total demand distortion nonlinear loads." *Electronics*, vol. 9, no.10 pp. 1643, 2020.

[63] J. W. Simpson-Porco, F. Dörfler, and F. Bullo, "Synchronization and power-sharing for droop-controlled inverters in islanded microgrids," *Automatica*, vol. 49, no. 9, pp. 2603-2611, 2013.

[64] Z. Shuai, et al., "Droop control method for load share and voltage regulation in high-voltage microgrids," *Journal of Modern Power Systems and Clean Energy*, vol. 4, pp. 76-86, 2016.

[65] J. Kim, J. M. Guerrero, P. Rodriguez, R. Teodorescu and K. Nam, "Mode Adaptive Droop Control With Virtual Output Impedances for an Inverter-Based Flexible AC Microgrid," *IEEE Transactions on Power Electronics*, vol. 26, no. 3, pp. 689-701, March 2011.

[66] J. M. Alcala, M. Castilla, L. G. de Vicuña, J. Miret, and J. C. Vasquez, "Virtual Impedance Loop for Droop-Controlled Single-Phase Parallel Inverters Using a Second-Order General-Integrator Scheme," *IEEE Transactions on Power Electronics*, vol. 25, no. 12, pp. 2993-3002, Dec. 2010.

[67] A. Kherbachi, A. Chouder, A. Bendib, K. Kara and S. Barkat, "Enhanced structure of second-order generalized integrator frequency-locked loop suitable for DC-offset rejection in single-phase systems," *Electric Power Systems Research*, vol. 170, pp. 348-357, 2019.

[68] M. Savaghebi, A. Jalilian, J. C. Vasquez and J. M. Guerrero, "Secondary Control Scheme for Voltage Unbalance Compensation in an Islanded Droop-Controlled Microgrid," *IEEE Transactions on Smart Grid*, vol. 3, no. 2, pp. 797-807, June 2012.

[69] X. Wang, J. M. Guerrero, F. Blaabjerg and Z. Chen, "Secondary voltage control for harmonics suppression in islanded microgrids," *2011 IEEE Power and Energy Society General Meeting*, Detroit, MI, USA, 2011, pp. 1-8.

[70] M. Savaghebi, A. Jalilian, J. C. Vasquez, J. M. Guerrero, and T. Lee, "Voltage harmonic compensation of a microgrid operating in islanded and grid-connected modes," *2011 19th Iranian Conference on Electrical Engineering*, Tehran, 2011, pp. 1-6.

[71] Y. Khayat *et al*., "On the Secondary Control Architectures of AC Microgrids: An Overview," *IEEE* Transactions on Power Electronics, vol. 35, no. 6, pp. 6482-6500, June 2020.

[72] Q. Shafiee, J. C. Vasquez and J. M. Guerrero, "Distributed secondary control for islanded MicroGrids - A networked control systems approach," *IECON 2012 - 38th Annual Conference on IEEE Industrial Electronics* Society, Montreal, QC, 2012, pp. 5637-5642.

[73] L. Meng, J. M. Guerrero, J. C. Vasquez, Fen Tang, and M. Savaghebi, "Tertiary control for optimal unbalance compensation in islanded microgrids," *2014 IEEE 11th International Multi-Conference on Systems, Signals & Devices (SSD14)*, Barcelona, 2014, pp. 1-6.

[74] J. M. Guerrero, J. C. Vasquez, J. Matas, M. Castilla, and L. Garcia de Vicuna, "Control Strategy for Flexible Microgrid Based on Parallel Line-Interactive UPS Systems," *IEEE Transactions on Industrial Electronics*, vol. 56, no. 3, pp. 726-736, March 2009.

[75] X. Zhao, L. Meng, M. Savaghebi, J. C. Vasquez, J. M. Guerrero, and X. Wu, "A dynamic consensus algorithm based low-voltage ride-through operation of power converters in grid-interactive microgrids," *IECON 2016 - 42nd Annual Conference of the IEEE Industrial Electronics Society*, Florence, 2016, pp. 3660-3665.

[76] J. C. Vasquez, J. M. Guerrero, J. Miret, M. Castilla and L. G. de Vicuña, "Hierarchical Control of Intelligent Microgrids," *IEEE Industrial Electronics Magazine*, vol. 4, no. 4, pp. 23-29, Dec. 2010.

[77] M. Savaghebi, A. Jalilian, J. C. Vasquez and J. M. Guerrero, "Secondary Control for Voltage Quality Enhancement in Microgrids," *IEEE Transactions on Smart Grid*, vol. 3, no. 4, pp. 1893-1902, Dec. 2012.

[78] N. B. De Nadai, A. C. Zambroni de Souza, J. G. C. Costa, C. A. M. Pinheiro, and F. M. Portelinha, "A secondary control based on fuzzy logic to frequency and voltage adjustments in islanded microgrids scenarios," *2017 IEEE Manchester PowerTech*, Manchester, United Kingdom, 2017, pp. 1-6.

[79] H. Bevrani, M. R. Feizi, and S. Ataee, "Robust Frequency Control in an Islanded Microgrid: H and μ-Synthesis Approaches," *IEEE Transactions on Smart Grid*, vol. 7, no. 2, pp. 706-717, March 2016.

[80] Z. Yi, Y. Xu, W. Gu and Z. Fei, "Distributed Model Predictive Control Based Secondary Frequency Regulation for a Microgrid with Massive Distributed Resources," *IEEE Transactions on Sustainable Energy*, doi: 10.1109/TSTE.2020.3033320.

[81] E. A. Coelho *et al.*, "Small-Signal Analysis of the Microgrid Secondary Control Considering a Communication Time Delay," *IEEE Transactions on Industrial Electronics*, vol. 63, no. 10, pp. 6257-6269, Oct. 2016.

[82] G. Lou, W. Gu, X. Lu, Y. Xu, and H. Hong, "Distributed Secondary Voltage Control in Islanded Microgrids With Consideration of Communication Network and Time Delays," *IEEE Transactions on Smart Grid*, vol. 11, no. 5, pp. 3702-3715, Sept. 2020.

[83] S. Golestan, M. Monfared, F. D. Freijedo, and J. M. Guerrero, "Design and Tuning of a Modified Power-Based PLL for Single-Phase Grid-Connected Power Conditioning Systems," *IEEE Transactions on Power Electronics*, vol. 27, no. 8, pp. 3639-3650, Aug. 2012.

[84] B. Liu et al., "A Simple Approach to Reject DC Offset for Single-Phase Synchronous Reference Frame PLL in Grid-Tied Converters," *IEEE Access*, vol. 8, pp. 112297-112308, 2020.

[85] D. Wu, T. Dragicevic, J. C. Vasquez, J. M. Guerrero, and Y. Guan, "Secondary coordinated control of islanded microgrids based on consensus algorithms," *2014 IEEE Energy Conversion Congress and Exposition (ECCE)*, Pittsburgh, PA, 2014, pp. 4290-4297.

[86] M. Chen, X. Xiao, "Hierarchical frequency control strategy of hybrid droop/VSG-based islanded microgrids," *Electric Power Systems Research*, vol. 155, pp. Pages 131-143, 2018.

[87] A. Micallef, M. Apap, C. Spiteri-Staines, J. M. Guerrero and J. C. Vasquez, "Reactive Power Sharing and Voltage Harmonic Distortion Compensation of Droop Controlled Single Phase Islanded Microgrids," *IEEE Transactions on Smart Grid*, vol. 5, no. 3, pp. 1149-1158, May 2014.

[88] M. A. Awal, H. Yu, H. Tu, S. M. Lukic and I. Husain, "Hierarchical Control for Virtual Oscillator Based Grid-Connected and Islanded Microgrids," *IEEE Transactions on Power Electronics*, vol. 35, no. 1, pp. 988-1001, Jan. 2020.

[89] O. Palizban, K. Kauhaniemi, and J. M. Guerrero, "Microgrids in active network management—Part I: Hierarchical control, energy storage, virtual power plants, and market participation," *Renewable and Sustainable Energy Reviews*, vol. 36, pp. 428-439, 2014.

[90] K. Vanthournout, K. D. Brabandere, E. Haesen, J. V. D. Keybus, G. Deconinck, and R. Belman, "Agora: distributed tertiary control of distributed resources," *15th Power Systems Computation Conference (PSCC15)*, Liege, Belgium, 2005.

[91] A. Bidram, V. Nasirian, A.Davoudi, and F.L Lewis, "Control and Modeling of Microgrids," in: "Cooperative Synchronization in Distributed Microgrid Control," *Advances in Industrial Control*, *Springer*, Cham, 2017, https://doi.org/10.1007/978-3-319-50808-5_2.

[92] S. Golestan, J. M. Guerrero, J. C. Vasquez, A. M. Abusorrah and Y. Al-Turki, "Modeling, Tuning, and Performance Comparison of Second-Order-Generalized-Integrator-Based FLLs," IEEE Transactions on Power Electronics, vol. 33, no. 12, pp. 10229-10239, Dec. 2018.

[93] G. A.-Tinajero, J. S.-Ramírez, N. V.-Cruz, M. Savaghebi, J. M. Guerrero, and E. Barocio, "Power flow modeling of islanded AC microgrids with hierarchical control," *International Journal of Electrical Power & Energy Systems*, vol. 105, pp. 28-36., 2019.

[94] H. J. Avelar, W. A. Parreira, J. B. Vieira, L. C. G. de Freitas, and E. A. A. Coelho, "A State Equation Model of a Single-Phase Grid-Connected Inverter Using a Droop Control Scheme With Extra Phase Shift Control Action," *IEEE Transactions on Industrial Electronics*, vol. 59, no. 3, pp. 1527-1537, March 2012.

[95] X. Guo, Z. Lu, B. Wang, X. Sun, L. Wang and J. M. Guerrero, "Dynamic Phasors-Based Modeling and Stability Analysis of Droop-Controlled Inverters for Microgrid Applications," *IEEE Transactions on Smart Grid*, vol. 5, no. 6, pp. 2980-2987, Nov. 2014.

[96] Y. Peng, Z. Shuai, X. Liu, Z. Li, J. M. Guerrero, and Z. J. Shen, "Modeling and Stability Analysis of Inverter-Based Microgrid Under Harmonic Conditions," *IEEE Transactions on Smart Grid*, vol. 11, no. 2, pp. 1330-1342, March 2020.

[97] N. Pogaku, M. Prodanovic and T. C. Green, "Modeling, Analysis and Testing of Autonomous Operation of an Inverter-Based Microgrid," *IEEE Transactions on Power Electronics*, vol. 22, no. 2, pp. 613-625, March 2007.

[98] Y. Han, H. Li, L. Xu, X. Zhao, and J. M. Guerrero, "Analysis of Washout Filter-Based Power Sharing Strategy—An Equivalent Secondary Controller for Islanded Microgrid Without LBC Lines," *IEEE Transactions on Smart Grid*, vol. 9, no. 5, pp. 4061-4076, Sept. 2018.

[99] J. G. de Matos, F. S. F. e Silva, and L. A. d. S. Ribeiro, "Power Control in AC Isolated Microgrids With Renewable Energy Sources and Energy Storage Systems," in IEEE Transactions on Industrial Electronics, vol. 62, no. 6, pp. 3490-3498, June 2015.

[100] D. Xua, Y. Daib, C. Yang, and X. Yanc, "Adaptive fuzzy sliding mode command-filtered backstepping control for islanded PV microgrid with energy storage system," *Journal of the Franklin Institute*, vol. 356, no. 4, pp. 1880-1898, Jan. 2019.

[101] M. Aryanezhad, "Management and coordination of LTC, SVR, shunt capacitor and energy storage with high PV penetration in power distribution system for voltage regulation and power loss minimization," *Electrical Power and Energy Systems*, vol. 100, pp. 178–192, Sept. 2018.

[102] A. Mehrizi-Sani and R. Iravani, "Potential-Function Based Control of a Microgrid in Islanded and Grid-Connected Modes," *IEEE Transactions on Power Systems*, vol. 25, no. 4, pp. 1883-1891, Nov. 2010.

[103] A. Bonfiglio et al., "Modeling and Experimental Validation of an Islanded No-Inertia Microgrid Site," *IEEE Transactions on Sustainable Energy*, vol. 9, no. 4, pp. 1812-1821, Oct. 2018.

[104] F. Delfino, G. Ferro, M. Robba, and M. Rossi, "An architecture for the optimal control of tertiary and secondary levels in small-size islanded microgrids," *Electrical Power and Energy Systems*, vol. 103, pp. 75–88, Dec. 2018.

[105] Z. Zhang, C. Dou , D. Yue , B. Zhang, and W. Luo, "A decentralized control method for frequency restoration and accurate reactive power sharing in islanded microgrids," *Journal of the Franklin Institute*, vol. 335, no. 17, pp. 8874–8890, Nov. 2018.

[106] X. Zhao-xia, Z. Mingke, H. Yu, J. M. Guerrero, and J. C. Vasquez, "Coordinated Primary and Secondary Frequency Support Between Microgrid and Weak Grid," *IEEE Transactions on Sustainable Energy*, vol. 10, no. 4, pp. 1718-1730, Oct. 2019.

[107] F. Guo, C. Wen, J. Mao, and Y. Song, "Distributed Secondary Voltage and Frequency Restoration Control of Droop-Controlled Inverter-Based Microgrids," in IEEE Transactions on Industrial Electronics, vol. 62, no. 7, pp. 4355-4364, July 2015.

[108] T. Dragičević, R. Heydari and F. Blaabjerg, "Super-high bandwidth secondary control of AC microgrids," *2018 IEEE Applied Power Electronics Conference and Exposition (APEC)*, San Antonio, TX, 2018, pp. 3036-3042.

[109] R. V. A. Neves, R. Q. Machado, V. A. Oliveira, X. Wang, and F. Blaabjerg, "Multitask Fuzzy Secondary Controller for AC Microgrid Operating in Stand-Alone and Grid-Tied Mode," *IEEE Transactions on Smart Grid*, vol. 10, no. 5, pp. 5640-5649, Sept. 2019.

[110] Q. Shafiee, Č. Stefanović, T. Dragičević, P. Popovski, J. C. Vasquez, and J. M. Guerrero, "Robust Networked Control Scheme for Distributed Secondary Control of Islanded Microgrids," *IEEE Transactions on Industrial Electronics*, vol. 61, no. 10, pp. 5363-5374, Oct. 2014.

[111] Y. Xu, H. Sun, W. Gu, Y. Xu and Z. Li, "Optimal Distributed Control for Secondary Frequency and Voltage Regulation in an Islanded Microgrid," *IEEE Transactions on Industrial Informatics*, vol. 15, no. 1, pp. 225-235, Jan. 2019.

[112] B. Wei, Y. Gui, S. Trujillo, J. M. Guerrero, J. C. Vásquez and A. Marzàbal, "Distributed Average Integral Secondary Control for Modular UPS Systems-Based Microgrids," *IEEE Transactions on Power Electronics*, vol. 34, no. 7, pp. 6922-6936, July 2019.

[113] S. Golestan, J. M. Guerrero, and J. C. Vasquez, "DC-Offset Rejection in Phase-Locked Loops: A Novel Approach," *IEEE Transactions on Industrial Electronics*, vol. 63, no. 8, pp. 4942-4946, Aug. 2016.

[114] S. Golestan, J. M. Guerrero, and G. B. Gharehpetian, "Five Approaches to Deal With Problem of DC Offset in Phase-Locked Loop Algorithms: Design Considerations and Performance Evaluations," *IEEE Transactions on Power Electronics*, vol. 31, no. 1, pp. 648-661, Jan. 2016.

[115] H. Ahmed and M. Benbouzid, "Demodulation type single-phase PLL with DC offset rejection," *Electronics Letters*, vol. 56, no. 7, pp. 344–347, March 2020.

[116] M. Fan, Z. Dai, Y. Yang, M. Xie, L. He and G. Du, "Four-Consecutive-Samples based Frequency Estimation for Single-Phase Grids with DC-offsets," *IEEE Transactions on Industrial Electronics*, doi: 10.1109/TIE.2020.3028805.

[117] B. Liu et al., "A Simple Approach to Reject DC Offset for Single-Phase Synchronous Reference Frame PLL in Grid-Tied Converters," *IEEE Access*, vol. 8, pp. 112297-112308, 2020.

[118] C. Ahumada, R. Cárdenas, D. Sáez, and J. M. Guerrero, "Secondary Control Strategies for Frequency Restoration in Islanded Microgrids With Consideration of Communication Delays," *IEEE Transactions on Smart Grid*, vol. 7, no. 3, pp. 1430-1441, May 2016.

[119] Q. Shafiee, J. M. Guerrero and J. C. Vasquez, "Distributed Secondary Control for Islanded Microgrids—A Novel Approach," *IEEE Transactions on Power Electronics*, vol. 29, no. 2, pp. 1018-1031, Feb. 2014.

[120] R. Heydari, T. Dragicevic and F. Blaabjerg, "High-Bandwidth Secondary Voltage and Frequency Control of VSC-Based AC Microgrid," *IEEE Transactions on Power Electronics*, vol. 34, no. 11, pp. 11320-11331, Nov. 2019.

[121] A. Dehghan Banadaki, F. D. Mohammadi and A. Feliachi, "State-space modeling of inverter-based microgrids considering distributed secondary voltage control," *2017 North American Power Symposium (NAPS)*, Morgantown, WV, 2017, pp. 1-6.

[122] X. Zhou et al., "Robust Grid-Current-Feedback Resonance Suppression Method for LCL-Type Grid-Connected Inverter Connected to Weak Grid," *IEEE Journal of Emerging and Selected Topics in Power Electronics*, vol. 6, no. 4, pp. 2126-2137, Dec. 2018.

[123] Walid Issa, F. Al-naemia, G. Konstantopoulos, S. Sharkh, and M. Abusara, "Stability analysis and control of a microgrid against circulating power between parallel inverters," *Energy Procedia*, vol. 157, pp. 1061-1070, Jan. 2019.

[124] G. M. S. Azevedo, M. C. Cavalcanti, F. Bradaschia, F. A. S. Neves, J. Rocabert and P. Rodriguez, "Enhanced power calculator for droop control in single-phase systems," *2011 IEEE Energy Conversion Congress and Exposition*, *Phoenix*, AZ, 2011, pp. 391-396.

[125] M. Castilla, L.G. de Vicuña, J. Miret, "Control of Power Converters in AC Microgrids", in: A. Zambroni de Souza, M. Castilla, (eds) "Microgrids Design and Implementation", *Springer*, Cham, 2019. https://doi.org/10.1007/978-3-319-98687-6_5.

[126] P. Rodriguez, A. Luna, I. Candela, R. Teodorescu and F. Blaabjerg, "Grid synchronization of power converters using multiple second-order generalized integrators," *2008 34th Annual Conference of IEEE Industrial Electronics*, Orlando, FL, 2008, pp. 755-760.

[127] W.S. Levine, "Design methods," in: "The control handbook," *CRC Press* (vol. 1), Feb. 1996, pp. 169–173. Ch10.

[128] D.G. Zill, "Cross product," in: "Advanced engineering mathematics," Section: 7.4, *Loyola Marymount University, Jones & Bartlett Learning* (6th ed), Sep. 2016, pp. 338–344.

[129] A. A. A. Radwan and Y. A. I. Mohamed, "Modeling, Analysis, and Stabilization of Converter-Fed AC Microgrids With High Penetration of Converter-Interfaced Loads," *IEEE Transactions on Smart Grid*, vol. 3, no. 3, pp. 1213-1225, Sept. 2012.

[130] X. Zhao et al., "Distributed low voltage ride-through operation of power converters in grid-connected microgrids under voltage sags," *IECON 2015 - 41st Annual Conference of the IEEE Industrial Electronics Society*, Yokohama, 2015, pp. 001909-001914.

[131] A. M. Bouzid, J. M. Guerrero, A. Cheriti, M. Bouhamida, P. Sicard, M. Benghanem, "A survey on control of electric power distributed generation systems for microgrid applications," *Renewable and Sustainable Energy Reviews*, vol. 44, pp. 751-766, 2015.

[132] E. A. A. Coelho, P. C. Cortizo and P. F. D. Garcia, "Small-signal stability for single-phase inverter connected to stiff AC system," *Conference Record of the 1999 IEEE Industry Applications Conference. Thirty-Forth IAS Annual Meeting (Cat. No.99CH36370)*, Phoenix, AZ, USA, 1999, pp. 2180-2187, vol. 4.

[133] V. Verma, S. Khushalani-Solanki and J. Solanki, "Modeling and criterion for voltage stability of grid-connected droop controlled inverter," *2017 North American Power Symposium (NAPS), Morgantown*, WV, 2017, pp. 1-5.

[134] S. M. Ashabani and Y. A. I. Mohamed, "A Flexible Control Strategy for Grid-Connected and Islanded Microgrids With Enhanced Stability Using Nonlinear Microgrid Stabilizer," *IEEE Transactions on Smart Grid*, vol. 3, no. 3, pp. 1291-1301, Sept. 2012.

[135] Y. Yang and F. Blaabjerg, "A new power calculation method for single-phase grid-connected systems," *2013 IEEE International Symposium on Industrial Electronics*, Taipei, 2013, pp. 1-6.

[136] S. Golestan, J. M. Guerrero, J. C. Vasquez, A. M. Abusorrah and Y. Al-Turki, "Linear Time-Periodic Modeling, Examination, and Performance Enhancement of Grid Synchronization Systems With DC Component Rejection/Estimation Capability," *IEEE Transactions on Power Electronics*, vol. 36, no. 4, pp. 4237-4253, April 2021.

[137] X. Hou *et al*., "Distributed Hierarchical Control of AC Microgrid Operating in Grid-Connected, Islanded and Their Transition Modes," *IEEE Access*, vol. 6, pp. 77388-77401, 2018.

[138] M. Majidi, A. A. Nazeri, F. M. Ibanez and D. Pozo, "A Guideline for Modeling Voltage and Frequency Controls in AC Microgrids: The Influence of Line Impedance on Transient Time," *2019 IEEE Milan PowerTech*, Milan, Italy, 2019, pp. 1-6.

[139] E. A. A. Coelho, P. C. Cortizo and P. F. D. Garcia, "Small-signal stability for parallel-connected inverters in stand-alone AC supply systems," *Conference Record of the 2000 IEEE Industry Applications Conference. Thirty-Fifth IAS Annual Meeting and World Conference on Industrial Applications of Electrical Energy (Cat. No.00CH37129)*, Rome, Italy, 2000, pp. 2345-2352 vol.4.

[140] Y. Han, H. Li, L. Xu, X. Zhao, and J. M. Guerrero, "Analysis of Washout Filter-Based Power Sharing Strategy—An Equivalent Secondary Controller for Islanded Microgrid Without LBC Lines," *IEEE Transactions on Smart Grid*, vol. 9, no. 5, pp. 4061-4076, Sept. 2018.

[141] B.-J. Kim, H.-J. Kum, J.-M. Park, C.-Y. Won, Analysis, "Design and Implementation of Droop-Controlled Parallel-Inverters Using Dynamic Phasor Model and SOGI-FLL in Microgrid Applications," *Energies*, vol. 11, 1683, 2018.

[142] L. Wang, X. Q. Guo, H. R. Gu, W. Y. Wu and J. M. Guerrero, "Precise modeling based on dynamic phasors for droop-controlled parallel-connected inverters," *2012 IEEE International Symposium on Industrial Electronics*, Hangzhou, 2012, pp. 475-480.

[143] Y. Peng, Z. Shuai, X. Liu, Z. Li, J. M. Guerrero, and Z. J. Shen, "Modeling and Stability Analysis of Inverter-Based Microgrid Under Harmonic Conditions," *IEEE Transactions on Smart Grid*, vol. 11, no. 2, pp. 1330-1342, March 2020.

[144] D. Baimel, J. Belikov, J. M. Guerrero, and Y. Levron, "Dynamic Modeling of Networks, Microgrids, and Renewable Sources in the dq0 Reference Frame: A Survey," *IEEE Access*, vol. 5, pp. 21323-21335, 2017.